Alma Mater Studiorum – Università di Bologna

DOTTORATO DI RICERCA IN

CHIMICA

Ciclo XXXIII

Settore Concorsuale: 03/A1 – Chimica Analitica

Settore Scientifico Disciplinare: CHIM/01 – Chimica Analitica

Newly developed electrosynthesis of Layered Double Hydroxides: application to sensing, energy storage and conversion

Presentata da: Elisa Musella

Coordinatore Dottorato
Prof.ssa Domenica Tonelli

Supervisore
Prof.ssa Domenica Tonelli

Cosupervisore
Prof. Marco Giorgetti

Esame finale anno 2021

A mia madre

ABSTRACT

Layered Double hydroxides (LDHs) have been widely studied for their plethora of fascinating features and applications.

The potentiostatic electrodeposition of LDHs has been extensively applied in the literature as a fast and direct method to substitute classical chemical routes. However, it does not usually allow for a fine control of the M(II)/M(III) ratio in the synthesized material and it is not suitable for large anions intercalation.

Therefore, in this work a novel protocol has been proposed. In particular, the aim was to overcome all the aforementioned constraints using a method based on potentiodynamic reduction of nitrates, which has been demonstrated to be the most effective in obtaining reproducible films with respect to galvanostatic and potentiostatic ones.

In this way, LDHs of controlled composition were prepared using different molar ratios of the trivalent (iron or aluminium) to bivalent (nickel or cobalt) cations in the electrolytic solution ranging from 1:1 to 1:4.

Moreover, we were able to produce electrochemically LDHs intercalated with carbon nanomaterials for the first time. A one-step procedure which contemporaneously allows for the Ni/Al-LDH synthesis, the reduction of graphene oxide (GO) and its intercalation inside the structure has been developed. The electrosynthesised composites display a configuration where the two materials are highly interconnected and create new interfaces that improve the LDHs electrical conductivity. The electrosynthesis started from solutions containing the nickel and aluminium cations as nitrate salts at a fixed concentration and different amounts of GO. The results confirmed that a LDH structure was observed only if the GO concentration was lower than 2 mg mL^{-1}.

All the films have been characterized by a comprehensive multi-technique approach, including the employment of Cyclic Voltammetry, Impedance Spectroscopy, Powder X-Ray Diffraction, Scanning and Transmission Electron Microscopy, Raman, Infra-Red, X-ray Absorption, X-ray Photoemission and Atomic Emission spectroscopies.

The synthesised materials have been applied in several fields of interest.

First of all, Co/Al and Co/Fe-LDHs with a ratio 3:1 were exploited, and displayed good performances as catalysts for 5-(hydroxymethyl)furfural electro-oxidation, thus suggesting to carry out further investigation for applications in the field of industrial catalysis. The same materials, but with different metals ratios, were tested as catalysts for Oxygen Evolution Reaction (OER), obtaining results

comparable to LDHs synthesised by the classical co-precipitation method and also a better activity with respect to LDHs obtained by the potentiostatic approach. We can thus conclude that, to date, the potentiodynamic method has the greatest potential for the rapid synthesis of reproducible films of Co and Ni-based LDHs with controlled composition.

The composite material based on LDH and reduced graphene oxide (RGO) was employed to fabricate a cathode of a hybrid supercapacitor coupled with an activated carbon anode. The device had a starting discharge specific capacity of 880 F g^{-1} which decreased and stabilized at 820 F g^{-1} after 300 cycles. The potential applicability of the supercapacitor was demonstrated by powering a red light-emitting diode.

The preliminary results are very promising and embrace the necessity of development of low environmental impact systems; in fact, the proposed device is binder-free, safe, composed of earth abundant elements and able to work in aqueous electrolyte.

Moreover, a preliminary study has demonstrated the validity of inkjet printing carbon nanotubes on a flexible substrate, followed by their electrochemical modification with a Ni/Al-LDH in order to develop a sensor for the detection of ethanol in alkaline media. In the future, the sensor will be made more compact by printing a RE/CE electrode next to the working electrode to produce a two–terminal device. This assembly will also offer further application possibilities, such as to change the analyte matrix from liquid to gas phase for sensing of ethanol.

Finally, a chemometric technique, the Design of Experiment, has been applied to the field of electrochemistry, with the aim to predict peak intensities and potentials of ternary LDHs, and the preliminary results seem highly interesting. A first model has been proposed for the prediction of OER performances, but its validation and the detailed evaluation of catalytic activity will be carried out in the continuation of this work.

Summary

List of Acronyms and Abbreviations

In the following table the used acronyms and abbreviations are summarized in alphabetic order to facilitate the reading.

Acronym or Abbreviation	Extended Word
AC	Activated Carbon
AES	Auger Electron Spectroscopy
AFM	Atomic Force Microscopy
CA	Chronoamperometry
CC	Carbon Cloth
CME	Chemically Modified Electrode
CNT	Carbon Nanotube
C_S	Specific Capacitance
CV	Cyclic Voltammetry
DOE	Design of experiment
EC	Electrochemical Capacitor
ECSA	Electrochemical Surface Area
EDLS	Electrical double–layer supercapacitor
EDOT	3,4–Ethylenedioxythiophene
EDX	Energy Dispersive X–Rays
EE	Electrocatalytic Efficiency
EIS	Electrochemical Impedance Spectroscopy
ERGO	Electrochemically Reduced Graphene Oxide
EXAFS	Extended X–Ray Absorption Fine–Structure
FE–SEM	Field Emission Scanning Electron Microscopy
FWHM	Full Width at Half Maximum
GC	Glassy Carbon
GCDC	Galvanostatic Charge Discharge Cycle
GO	Graphene Oxide
NMR	Nuclear Magnetic Resonance
HER	Hydrogen Evolution Reaction
HMF	5–Hydroxymethyl–2–furfural
HPLC	High Performance Liquid Chromatography
IR	Infra–Red
LDH	Layered Double Hydroxide
LOD	Limit of Detection

LSV	Linear Sweep Voltammetry
OCP	Open circuit potential
OER	Oxygen Evolution Reaction
PDMS	Polydimethylsiloxane
PEDOT:PSS	Poly(3,4–ethylenedioxythiophene–poly(styrene sulfonate))
PVA	Polyvinyl alcohol
PVdF	Polyvinylidene Fluoride
RDE	Rotating Disk Electrode
RHE	Reversible Hydrogen Electrode
SAED	Selected Area Electron Diffraction
SC	SuperCapacitor
SCE	Saturated Calomel Electrode
TC	ToRay Carbon Paper
TEM	Transmission Electron Microscopy
TOF	Turnover Frequency
XANES	X–Ray Absorption Near–Edge Spectroscopy
XAS	X–Ray Absorption Spectroscopy
XPS	X–Ray Photoelectron Spectroscopy
XRD	X–Ray Diffraction

List of Figures

List of Tables

CHAPTER 1: INTRODUCTION

"The human mind adjusts itself to a certain point of view, and those who have regarded nature from one angle, during a portion of their life, can adopt new ideas only with difficulty."

– Antoine Lavoisier

1.1 Preface and aim of the work

"I continue coupling a plate of silver with one of zinc, and always in the same order... and place between each of these couples a moistened disk. I continue to form a column. If the column contains about twenty of these couples of metals, it will be capable of giving to the fingers several small shocks." – A. Volta.

The study of electricity has fascinated scientists since Volta's time, becoming a fundamental discipline. The interaction between chemistry and electricity has brought to the creation of portable devices, which nowadays are dominating our life. The ability to directly transduce a chemical signal into an electrical one is used by analytical chemists to monitor *in situ* parameters related to the physiological state of people, the environment and food.

Furthermore, electrochemical processes give the chance of directly interconnect chemical energy into electricity. As a matter of fact, electrochemistry could offer solutions to current energy challenges in several ways.

Up to date, the global energy demand doubles every 15 years and all indications suggest it will keep on increasing in the close future: with a growing market for electronic devices and the development of hybrid electric vehicles, there is a growing and urgent demand of high–power energy resources. However, more than 60% of the global electricity production is derived from coal and from natural gas with an associated huge emission of CO_2, which is considered the main contributor to greenhouse effect and global warming[1].

Because of such detrimental environmental effects, replacing fossil fuels with renewable energy sources – primarily with wind and solar energy – has become a moral imperative. The most relevant problem is that they cannot guarantee a continuous flow of energy over the year: since our reliance on renewable energy has to grow, there is an increasing need to store it for the times when the energy cannot be harvested[2].

Among possible alternatives, electrochemical storage and conversion should play a key role. Researchers are focusing their attention on finding new materials in order to boost the performances: environmental sustainability is essential considering the urgent need of large–scale production and diffusion[3,4].

For example, water electrolysis has drawn a lot of attention to store energy from renewables. Its key challenge lies in the high overpotential required to reach the solar flux equivalent

current density, which mainly results from the slow kinetics of oxygen evolution reaction (OER). For this reason, OER catalysts must be employed to low down the overpotential, which thereby increases the water oxidation efficiency. Until now, noble metal–based materials are the most effective electrocatalysts for OER, but the prohibitive cost and the scarcity of noble metals prevent the development of efficient electrocatalysts. To find highly efficient and cost-effective materials remain one of the main topics of the current research in the field of energy production devices[2,5–7]. Similar challenges are faced also by energy storage technologies: new electrode materials are needed since even more and more power density and/or long–term stability are required[1,3,4,7–9].

Moreover, since all harmful substances have to be avoided, new eco–friendly systems need to be proposed, e.g., replacing organic solvents with water or/and eliminating any kind of binder that might be exploited for electrode preparation.

Chemically modified electrodes (CMEs) are conducting or semiconducting materials, coated with a selected film, which confers peculiar chemical, electrochemical, and/or optical properties. CMEs are largely employed for the fabrication of electrochemical devices and systems to be applied in chemical sensing, energy conversion and storage, corrosion protection, biosensing, electrocatalysis, etc.[10,11]. In order to modify electrode surfaces different methods are available: one of the most fascinating routes consists in the electrosynthesis, since it allows both for the synthesis and simultaneous modification of the electrode surface without using an inactive binder.

The focus of my PhD research was to optimize a novel and better performing electrochemical synthesis of several Layered Double Hydroxides (LDHs) onto different electrode supports for catalysis and energy applications. In particular, LDHs based electrodes were studied as sensors, catalysts and in energy storage and conversion devices.

The following researches were carried out and are presented below:

- A novel protocol based on a potentiodynamic reduction of nitrate ions was studied for LDHs based on Co or Ni as M(II) and Al or Fe as M(III). The reproducibility of the method was compared with those based on potentiostatic (mostly used in literature) and galvanostatic conditions. The reproducibility was evaluated from the characterization of the electrochemical behaviour in cyclic voltammetry CV.

  - In order to demonstrate the versatility of the newly developed synthesis various materials with different geometry and porosity (Pt, Ni foam, Grafoil, Carbon Cloth (CC), Toray Carbon Paper (TC)) were evaluated. LDHs based on Co or Ni as M(II) and Al as M(III) were employed.
  - For the first time, we have successfully electro–synthesised LDHs with well–defined M(II)/M(III) ratios in a wide range (from 1:1 to a 4:1) or containing a big molecule (ERGO) in the interlayer. The molar ratios have been chosen on the basis of the limits suggested by the literature for a LDH phase formation. The previously adopted potentiostatic approach displayed a poor reproducibility of the M(II)/M(III) ratio, and allowed only the insertion of small anions, such nitrate, chloride and carbonate.
  - A wide number of ternary LDHs, i.e., based on three metals were also potentiodynamically obtained with the help of chemometrics (DOE).
- The electrochemical behaviour of all LDHs modified electrodes was studied by CV and electrochemical impedance spectroscopy (EIS). The morphologies and composition of the coatings were investigated by field emission scanning electron microscopy (FE–SEM) and energy dispersive spectroscopy (EDX), and the structure was confirmed by recording X–Ray diffraction spectra (XRD), and Infra–Red (IR) or Raman spectroscopy.
- The electrochemical behaviour in CV of Co/Al or Fe modified electrodes was followed *ex–situ*: X–Ray absorption spectroscopy (XAS) and X–Ray photoelectron spectroscopy (XPS) were used due to their complementary features. In particular, the aim was to understand the reactions taking place at the electrode: this objective has been accomplished by applying *ex–situ* XPS/XAS characterization once a potential or current step had been applied.
- LDHs modified electrodes were tested as catalysts and sensors for 5–(hydroxymethyl) furfural (HMF) electro–oxidation. The solution obtained after exhaustive electrolysis was analysed in order to identify the oxidation products.
- LDHs modified electrodes were tested as OER catalysts using a rotating disk electrode or a stationary system in alkaline solutions. The onset potential was

determined by recording polarization curves, and the catalysts stability was checked by chronopotentiometry. The performances in terms of onset potential, Tafel slope and current density of the LDH coatings were estimated.

- LDHs modified electrodes were employed to fabricate hybrid supercapacitors. The specific capacitance and long–term stability of the electrodes was investigated in alkaline media. Several anodes and cathodes were tested. Two configurations have been studied: the capacitor in solution and assembled in a self–standing device. To further demonstrate the real applicability, two SC devices were in series connected and fully charged. The connected SC devices could power and light a red light–emitting diode (LED).

1.2 Chemically modified electrodes

Electrochemical methods traditionally have found important applications in sample analysis and organic and inorganic syntheses. The electrode surface itself can be a powerful tool for a chemist as it is a source of variable free energy electrons depending on the applied potential. As with most measurement tools, however, electrodes encounter specific phenomena that reduce their applicability for analytical and synthetic procedures.

Among the limitations, fouling of the electrode by unwanted precipitation or adsorption processes is likely to happen. Moreover, the slow electrochemical reaction rates of some species require the application of an overpotential for the desired reaction to occur. These phenomena can be often controlled by manipulating the nature of the electrode surface. Until the mid–1970s, however, the only electrodes available were confined to materials such as C, Au, Hg, and Pt[11].

Firstly, introduced by Murray et al.[10] in 1970, chemically modified electrodes (CMEs) are conductive materials whose surface has been modified in order to enhance the electrochemical performances in several applications[12]. They represent a relatively modern approach to electrode systems, and they resulted a useful tool for a wide range of electrochemical investigations. Usually, in a CME a thin film (ranging from a molecular monolayer to a few micrometers–thick multilayer) of a selected compound is deposited on the electrode surface to change its properties according to a targeted application. If the proper reagent is chosen, desirable properties such as reagent–based control of the rates, and selectivity of electrochemical reactions (i.e., electrocatalysis), freedom from adsorption effects, and optical or excited state features might be obtained.

CMEs can be prepared exploiting different techniques for the modifier immobilization; the main routes are described below[11]:

- ***Chemisorption***[13]. It can happen that some species attach spontaneously to the surface of the electrode due to their higher affinity for the conductive material than for the bulk solution. For example, organic species, such as those containing double bonds, are often hydrophobic and strongly adsorb from aqueous solutions on carbon, graphite or platinum. Usually, the amount adsorbed on the electrode surface is almost a monolayer. Self–assembled monolayers (SAM) of organic molecules are molecular

assemblies formed spontaneously on surfaces by adsorption, and are organized into large, ordered domains.

- ***Formation of covalent bond***[14]. In order to create bonds between the substrate and a molecule of interest, chemical reactions can be employed. In particular, electrode materials such as platinum and glassy carbon can be oxidized in order to form hydroxyl groups on the surface which are involved in the formation of the covalent bond. This technique could give rise to a monolayer, but often, the reaction can cause polymerization and thicker layers are formed, especially when organic compounds are used as modifiers.
- ***Physical adsorption***: it has been the first historically employed method. It consists of the adsorption of an electroactive chemical species by means of f an electron interaction with the electrode surface. The major drawback is the difficulty in obtaining a homogeneous and uniform coating. Thus, a trick to overcome this issue is the use of "spin–coating", a technique that consists in the deposition of a drop of the coating material on the centre of the substrate, which is then rotated at high speed in order to spread the material by centrifugal force.
- ***Electrosynthesis***. The modification can be performed synthesising chemical compounds by electrochemical techniques. The main advantages of electrosynthesis are the selectivity, since it is possible to precisely control the applied potentials, the short deposition time, and the good adhesion of the coating to the electrode surface.

1.3 Layered Double Hydroxides (LDHs)

The existence of layered double hydroxides dates back to 1842, when minerals consisting of LDHs were discovered in Sweden[15]. Due to their structural similarities to the hydrotalcites, LDHs are frequently referred to as hydrotalcite–like compounds (HTLCs). Hydrotalcites are hydroxycarbonates of magnesium and aluminium ($Mg_6Al_2(OH)_{16}CO_3{\cdot}4H_2O$) or magnesium and iron ($Mg_6Fe_2(OH)_{16}CO_3{\cdot}4H_2O$). They exist in the form of foliated and twisted plates.

The first studies on the single crystal X–Ray diffraction of minerals revealed that LDHs possessed a layered structure. Each layer consisted of two different cations and the interlayer space was filled with water and carbonate ions. However, at first, this was debated by several researchers. The reason was that, even though the main components of the LDH had been identified, some researchers still felt that the intrinsic details associated with the structural components of LDHs were not yet understood[15].

Synthetically formed LDHs have a highly hydrophilic nature with an amorphous or semicrystalline hexagonal structure. The layered structure of LDHs is based on that of brucite [$Mg(OH)_2$]. It consists of magnesium ions surrounded almost octahedrally by hydroxide ions. These octahedral units form infinite layers by edge–sharing, with the hydroxide ions sitting perpendicular to the plane of the layers. The layers then stack on top of one other to form the three–dimensional structure. From the point of view of packing, the structure is composed of close–packed planes of hydroxyl anions that lie on a triangular lattice. The metal cations occupy the octahedral holes between alternate pairs of OH planes and thus occupy a triangular lattice identical to the one occupied by the OH ions[17].

The basic structure of a LDH may be derived by substitution of a part of the divalent cations in the brucite lattice by trivalent cations so that the layers acquire a positive charge, which is balanced by intercalation of anions (and, usually, water) among the layers. This large family of compounds is also commonly referred as anionic clays indicating a complementarity with the more usual cationic clays whose interlamellar domains contain cationic species[16]. It is the possibility of varying the identity and relative proportions of the di– and trivalent cations as well as the identity of the interlayer ions that gives rise to the large variety of

materials with tunable properties having the general formula $[\mathbf{M^{II}}_{1-x}\mathbf{M^{III}}_{x}\mathbf{(OH)}_2]^{x+}$ $[\mathbf{A}^{n-}]_{x/n} \cdot \mathbf{yH_2O}$ represented schematically in Figure 1_1[17].

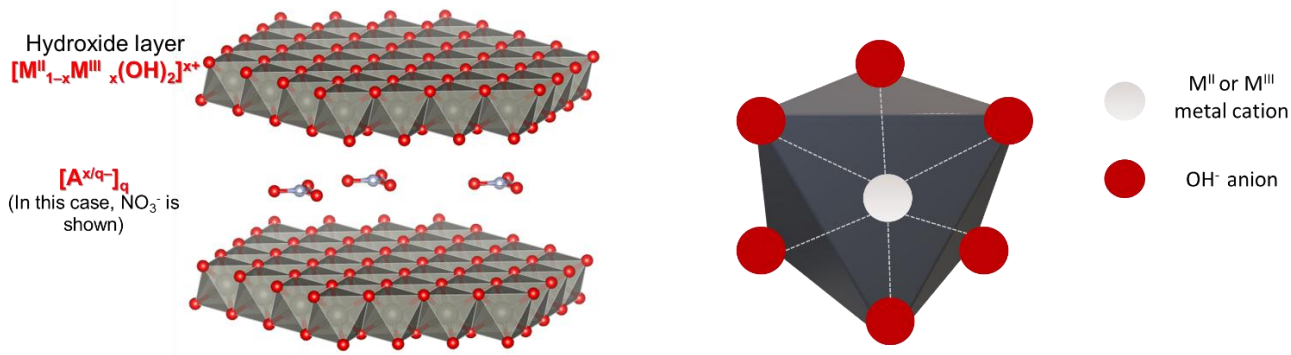

Figure 1_ 1: Schematic representation of a layered double hydroxide structure

Concerning the cations, the only restriction is the size of the radius of M(II) and M(III) ions. Their ionic radii should not differ much from those of the natural LDH (Mg^{2+} and Al^{3+}, respectively) so that they may be accommodated in the octahedral sites of the brucite–like layers. For this reason, good candidates are divalent cations such as Ni^{2+}, Mg^{2+}, Ca^{2+}, Mn^{2+}, Co^{2+}, Cu^{2+} or Zn^{2+} together with trivalent cations such as Al^{3+}, Co^{3+}, Fe^{3+} or Cr^{3+} [18]. The ratio (x) between M(II) and M(III) is also an important feature. Such a x value has been reported to fall in the range $0.1 \leq x \leq 0.5$, but pure LDHs phases only exist for $0.2 \leq x \leq 0.33$. For x values outside this range, compounds with different structures are obtained[19].

The interlayer of LDHs contain typically anions and water molecules which establish a complex network of hydrogen bonds with layer hydroxyl groups. The interlayers are substantially disordered, hydrogen bonds are in a continuous state of flux so that the precise nature of the interlayer is extremely complex to describe[17].

The interactions between layers and interlayers species involves a combination of electrostatic effects and hydrogen bonding. Hydroxyl groups, particularly those bonded to trivalent cations are strongly polarized and interact with the inter–layer anions. Every anion has to satisfy the excess of positive charges on both the sandwiching octahedral layers, which are electrically balanced by two neighbouring interlayers; it has been suggested that charge compensation in LDHs has many of resonance effects characteristics[17].

By virtue of their structural tunability, LDHs and some of their nanocomposites can be employed in an outstanding number of applications, such as electrocatalysts[20], sensors[21,22],

pseudo–capacitors[23,24], drug delivery systems[25], and for intercalation chemistry[19]. The interesting properties of these materials include large surface areas, anion exchange capacities (2–3 meq g^{-1}), comparable to those of anion-exchange resins, recovering of the layered structure after thermal decomposition and low cytotoxicity[18].

1.3 LDHs synthetic methods

Several synthetic methods can be found in the literature for LDHs preparation. The most commonly encountered involve the simple co-precipitation[26] and hydrothermal methods[27], but others include urea hydrolysis[28] glycine-assisted hydrothermal synthesis[29] and reconstruction, which is based on the so–called "memory effect"[30].

In a **co-precipitation method**, typically, a mixed solution of the two metal salts in decarbonated water is added dropwise over hours to an aqueous solution containing guest species under nitrogen atmosphere, with vigorous stirring. During titration, solution pH (7–8) is adjusted with 0.1 M NaOH to induce co–precipitation. Then the precipitate, aged at room temperature for at least 24 h, is filtered, washed with decarbonated water thoroughly, and finally dried under vacuum[26].

A **hydrothermal synthesis**, which is usually employed when organic guest species with low affinity for LDHs have to be intercalated or when the anion–exchange reactions or the co-precipitation using soluble metal salts cannot be applied, is based on the following procedure. The hydroxides precursors and the organic species are mixed together and stirred in deionized water at room temperature. The suspension obtained is then transferred into an autoclave and heated at 100–150 °C for some days. After filtration, the solid is washed with ethanol. The chosen temperature influences the crystal structure of the resulting material: in particular, structures at different temperatures show a different arrangement of water molecules and carbonate groups which are present the interlayer region[27,31].

LDHs can be also prepared by **glycine-assisted hydrothermal method**. In such a case, glycine and sodium sulphate are dissolved in a solution containing the nitrate o salts of the cations in the desired molar ratio**.** After some minutes of stirring a clear solution is obtained. Then 5 M NaOH is added, always under stirring, to increase the pH from ~3.5 to ~13.5. Then the solution is transferred into an autoclave and heated at 120 °C for 24 h. After the

hydrothermal treatment, the autoclave is cooled down to room temperature. The resulting precipitate is recovered by centrifugation, and the supernatant is removed. The precipitate is then washed with deionized water and dried at room temperature[30].

Another method to produce LDHs is rehydration/reconstruction using the structural **"memory effect"**. Firstly, calcination of LDHs (500°C for 4 h under nitrogen) is performed to remove the interlayer water and anions, and structural water, which results in a mixture of metal oxides. They are able to regenerate the LDH layered structure when exposed to water and anions (the latter may differ from the starting ones and thus a new LDH is obtained). The calcined solid is then added to a solution of decarbonated water containing the desired interlayer species. The pH value (between 7 – 8) is adjusted by adding NaOH. Then, the precipitate is aged at room temperature, filtered, washed with decarbonated water thoroughly, and finally dried under vacuum[30].

The major drawbacks of the above-described syntheses are the long time needed for the reaction to occur and the poor adhesion of the LDH to the support material when it works as the coating of electrodes in many electrochemical applications[32].

In such a field, a fascinating synthetic procedure is the **electrodeposition**, since it allows both for the synthesis and simultaneous modification of the electrode surface. Moreover, all the problems related to adhesion are overcome. In 2004 our group first proposed the **potentiostatic electrodeposition** of LDHs[33]. To date, more than hundreds of items result on *Scopus* when searching for "layered double hydroxides electrodeposition" which is certainly the most commonly used method for the direct modification of conductive substrates[33–35].

The electrodeposition is usually carried out in a solution containing the nitrates of the bivalent and trivalent ions, applying to the electrode a cathodic potential (e.g., –0.90 V vs SCE) which promotes the reduction of nitrates and water molecules (Figure 1_2).

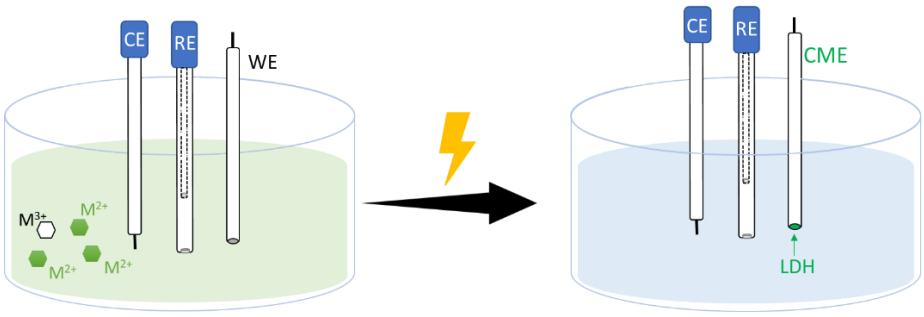

Figure 1_ 2: sketch of the set up in electrosynthesis

The Reactions 1 – 6 either consume H^+ or produce OH^- near the electrode surface, that increases the local pH and leads to the LDH precipitation[33,36,37]:

1. $H^+ + e^- \rightarrow H_{ads}$
2. $2H^+ + 2e^- \rightarrow H_2$
3. $NO_3{}^- + 2H^+ + 2e^- \rightarrow NO_2{}^- + H_2O$
4. $NO_3{}^- + 10H^+ + 8e^- \rightarrow NH_4{}^+ + 3H_2O$
5. $2H_2O + 2e^- \rightarrow H_2 + OH^-$
6. $NO_3{}^- + H_2O + 2e^- \rightarrow NO_2{}^- + 2OH^-$

Of course, some drawbacks must be highlighted also for this approach. First of all, even if it starts from a synthetic bath where the M(II)/M(III) ratio is fixed (generally 3 to 1), the concentration gradients originating during the synthesis hinder a fine control of the final molar ratio in the deposited material, especially when a long potential pulse is applied[38]. In addition, it is widely accepted[39] that a precise control of such a ratio in electrochemically deposited thin films is difficult, because the kinetic mechanisms might be different, depending on the composition of the electrolytic solution. Secondly, when performing the potentiostatic synthesis, the characterization cyclic voltammogram does not always display a reproducible signal of the redox active couple. As to the latter issue, our group[40,41] has recently demonstrated that a **potentiodynamic approach**, where the deposition is stimulated by CV at the cathodic side, provides a reproducibility of the deposit which is much better than the one achieved with either galvanostatic or potentiostatic methods. In fact, the cation concentration gradients in the diffusion layer, which are typical of the potentiostatic approach, are strongly reduced during the application of a potential that does not stimulate electrochemical reactions, thus allowing enough time for the concentrations to be restored at the electrode surface. Thus, the control of the M(II)/M(III) ratio depends only on the composition of the electrolytic bath[42].

1.4 Layered Double Hydroxides applications

As already mentioned in section 3, LDHs have outstanding physical–chemical properties and therefore, their tailor–made behaviour offers extensive applications in different areas. In fact, they are employed in the following fields, such as[43]:

- **Water treatment:** LDHs and thermally activated LDHs have shown potential for the removal of anions and oxyanions of the halogen elements from water: their structure has significant impact on anion uptake. In general, LDHs with high charge density exhibit greater affinity for anions with high charge density (F^-; Cl^-; ClO^-; and BrO_3^-), while LDHs with low charge density are better for the removal of anions with low charge density (Br^- and I^-). This was generally attributed to either the compatibility of the charge density of the adsorbent and adsorbate or to differences in the surface morphology of the LDHs[44,45].
- **Nanomedicine:** LDHs have also gained attention due to their unique features as nanocarriers in drug delivery systems[43]. For this application, materials need to be synthesised from biocompatible metals and should have pH–dependent solubility; in this way, they can be decomposed in the acidic biological environment. Their anion exchange property allows loading of various drugs into the interlayers. Systems have been developed for several active molecules, such as *anticancer drug* (protocatechuic acid, etoposide, methotrexate, camptothecin, gallic acid, 5–fluorouracil, fenbufen, prednisone–cholate, chlorogenic acid, etc.), a*nti–hypertensive drug* (perindopril erbumine, enalapril, lisinopril, captopril, and ramipril), a*nti–inflammatory drug* (salicylic acid, diclofenac, sodium indomethacin), *anti–histamine* (cetirizine), s*unscreen drug* (cinnamic acid, caffeic acid), *anti–tuberculosis* (4–amino salicylic acid), *anti–parkinsonian drug* (levodopa), *vitamins storage and delivery* (folic acid, ascorbic acid) and *antibiotic drug* (ciprofloxacin, chloramphenicol)[43].
- **Anticorrosion agents**: ion exchangers based on LDHs dispersed in polymeric coatings are strong corrosion inhibitors for the metallic substrates. The corrosion is hindered due to the release of an inhibitive anion that diffuses through the pore space of the coating, and it is exchanged for ions in the environment, which are 'entrapped'

into the interlayer space of the layered structure. LDHs have been used as containers for corrosion inhibitors with a two–fold purpose: to release the species that impart active protection and to trap corrosive agents, such as Cl^-, and SO_4^{2-} [46–48].

- **Catalysts**: catalytic applications of LDHs have been reported for the following reactions[18]:
    1. basic catalysis (polymerization of alkene oxides, aldol condensation).
    2. reforming of hydrocarbons (naphthalene and CH_4) with H_2O.
    3. hydrogenation reactions (production of CH_4, CH_3OH, higher alcohols, paraffins and olefins from syngas; hydrogenation of nitrobenzene).
    4. oxidation reactions.
    5. support for Ziegler–Natta catalysts.
- **Flame retardants**: LDHs can be synthesized intercalating organic ions between the lamellas and can be consequently used as nanofillers when developing nanocomposites. It is reported that LDHs can contribute to the flame retardancy in a polymeric matrix, inducing a refractory oxide residue onto the surface of the material. This fact is due to the release of aqueous vapor and carbon dioxide during the decomposition. The endothermic nature of these processes and the dilution of combustible gases of pyrolysis increase the ignition time and reduce the heat release during the combustion[49,50].
- **Electrochemical applications**: LDHs can be employed for the development of devices in the field of sensors, energy storage and conversion (the latter two will be widely discussed in section 7). For these applications LDHs must contain electroactive transition metals (such as Co and Ni) able to undergo an inner redox reaction which confers to the material conductive features. In particular, the redox active centres can act as mediators in the process of electro–catalysis in a suitable potential window in basic media[51]. This property has been exploited for the development of electrochemical amperometric sensors for a wide group of oxidizable analytes, such as alcohols, amines, polyhydric compounds and complex molecules, like pesticides[52,53].

The sensitivity of the measurements depends both on the number of oxidizable sites and on the steric hindrance of the analyte and, thus, on the interlayer spacing. Ni/Al–LDHs show good performance as amperometric sensors for the determination of alcohols, alditols, and sugars, through an electrocatalytic mechanism involving the Ni(III) centres. The substitution of Ni with Co as M(II) induces a selectivity in the electro–oxidation of molecules containing hydroxyl groups; indeed Co/Al–LDH modified electrodes do not display electrocatalytic activity towards monohydric compounds due to the lower redox potential of the Co(III)/Co(II) couple. Therefore, the different behaviour of Co and Ni based LDHs has offered the interesting opportunity to develop an analytical method for the selective determination of alcohols in the presence of polyhydric compounds[53]. The LDH–based sensors show interesting, enhanced performances in terms of sensitivity and detection limit, particularly when the analyte is an anion due to the pre–concentration of the substrate inside the interlayer domains.

However, LDHs employment as sensors has always been restricted by their working conditions involving strong alkaline media. Recently, it has been demonstrated[54] a new sensor, which is effective at neutral pH. In particular, the electrocatalytic performance of a Co/Mn–LDH has been proposed for the detection of hydrogen peroxide, a key molecule in many chemical and biochemical pathways. The distinctive property was attributed to a unique divalent/trivalent transition–metal composition leading to a synergistic electronic coupling between mixed–valent Co(II)/Co(III) and Mn(III) cations, hosted jointly in the octahedral sites of the layered double hydroxide structure.

1.5 Carbon Nanomaterials

Three forms of carbon have been long known: amorphous carbon, graphite, and diamond. In particular, their properties vary depending on the carbon atoms arrangement. For example, graphite represents one of the most common and stable forms of carbon displaying strong covalent bonds in the planes and weak Van der Waals interactions among planes. Diamond is hard and transparent with each carbon atom bound to four other carbon atoms in a regular lattice[55,56].

It is the Nobel Prize–winning discovery of fullerene C_{60} that has started a brand–new chemistry of carbon[56]. Fullerenes are a zero–dimensional form of graphitic carbon that can be visualized as an irregular sheet being curled up into a sphere by incorporating pentagons in its structure. Fullerenes possess various forms and sizes ranging from 20 to 3000 carbon atoms[55,57].

The subsequent discovery of Carbon Nanotubes (CNTs) paved the way for a new era in materials science and for nanotechnology. Conceptually, CNTs are seamless cylinders of single or a few graphene layers with both ends often capped by fullerene–like structures, also containing pentagons, which display a high aspect ratio (i.e., length to diameter ratio) that ranges from 10^2 to 10^7. The structure and the diameter of a single–walled carbon nanotube (SWCNT) are determined by the chiral vector (i.e., roll–up vector) that defines the circumference of the SWCNT with respect to the graphene lattice. Multi–walled carbon nanotubes (MWCNTs) consist of nested, concentric shells of SWCNTs with a spacing between individual walls of 3.4 Å[55,56].

Graphene has been the most recent finding: it is the 2D single–atom–thick carbon nanosheet. It is actually considered the building block of most carbon nanomaterials. In fact, graphene is often viewed as the two–dimensional form of other sp^2 hybridized carbon nanomaterials in that it can be conceptually rolled or distorted to form carbon nanotubes and fullerenes[55,56]. Carbon new allotropes have, in the last decades, emerged as a new class of promising materials which are attractive for a wide range of potential applications, including sensors, energy conversion and storage[55,56].

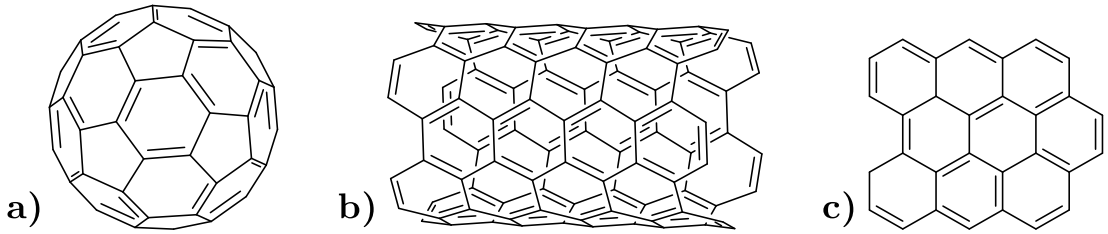

Figure 1_ 3: a) fullerene, b) single walled carbon nanotube and c) graphene.

1.5.1 Graphene and Graphene Oxide

As stated in the previous section, graphene is often viewed as the building block employed to form carbon nanotubes and fullerenes.

The idealized structure of graphene is completely two–dimensional, single layer of carbon atoms with sp^2 hybridized covalent bonds to form a flat hexagonal lattice[58]. Therefore, it can be also viewed as numerous benzene rings connected to each other to form a large–network molecule. Moreover, graphene may simply be described as an individual layer of graphite, a common and widely used mineral that is made up of many graphene layers stacked one atop another and held together by weak Van der Waals forces and $\pi - \pi$ stacking. This last description emphasizes the relationship between graphene and its parent material graphite, which is quite appropriate considering the first works on graphene which used micromechanical cleaving of pyrolytic graphite crystals to isolate those layers[59].

Life is rarely simple, however, and the structure of real graphene tends to be more complex than what one can imagine taking into account what stated above.

In fact, it is highly complicated to produce only single layers of graphene with current fabrication methods. Therefore, what is termed "graphene" can include materials from one-to-many layers, and the exact number of layers, N, critically affects properties especially for low N values[60].

On the other hand, stacks with N>12 or so tend to behave more like thin–film graphite than graphene. Consequently, the literature now embraces terms like single–layer graphene, double – layer or bilayer graphene, few–layer graphene (typically considered 3 – 9 layers) and multilayer graphene. Clearly, there are actually a variety of "graphenes" with different numbers of layers, and each one displays different properties, illustrating the importance of knowing what sort of "graphene" you are working with. Values of N are typically inferred from the peak shapes in Raman spectra, which are characteristic of the specific numbers of

layers in few–layer graphene, or from thickness measurements performed by scanning probe microscopy (SPM) techniques such as atomic force microscopy (AFM)[58,59,61–64].

Another reason for the complexity of graphene structure is that single layers are not completely flat; instead, the flexible sheets have a tendency to fold, buckle and corrugate. This flexibility is related to the out–of–plane phonons (flexural vibrations) that occur in soft membranes, which means that free–standing graphene tends to crumple. Thus, the larger scale distortions like folds and pleats are seen to be an unavoidable by–product of graphite–cleaving techniques. When working with a soft membrane, invariably some of the individual layers will fold and buckle during the process of mechanical peeling and subsequent solution deposition onto the substrate[60].

Graphite oxide instead has a similar layered structure to graphite, but the plane of carbon atoms in graphite oxide is heavily decorated by oxygen–containing groups, which not only expand the interlayer distance but also make the atomic–thick layers hydrophilic[63]. As a result, these oxidized layers can be exfoliated in water under moderate sonication. If the exfoliated sheets contain only one or few layers of carbon atoms like graphene, these sheets are named graphene oxide (GO). The most attractive property of GO is that it can be (partly) reduced to graphene–like sheets by removing the oxygen–containing groups with the recovery of a conjugated structure. The reduced GO (rGO) sheets are usually considered as one kind of chemically derived graphene. Some other names have been also given to rGO, such as functionalized graphene, chemically modified graphene, chemically converted graphene, or reduced graphene. The most straightforward goal of any reduction protocol is to produce graphene–like materials similar to the pristine graphene obtained from direct mechanical exfoliation (i.e., the ‘‘Scotch tape method’’) of individual layers of graphite both in structure and properties. Though numerous efforts have been made, the final target is still a dream. Residual functional groups and defects dramatically alter the structure of the carbon plane; therefore, it is not appropriate to refer to rGO, even today, simply as graphene since the properties are substantially different[63].

At present, in addition to reduction of GO, graphene can be produced by micro–mechanical exfoliation of highly ordered pyrolytic graphite, epitaxial growth, and chemical vapor

deposition (CVD). These three methods can lead to graphene with a relatively perfect structure and excellent properties.

GO has two important characteristics[60,63–65]:

1. it can be produced using inexpensive graphite as raw material by cost–effective chemical methods with a high yield.
2. it is highly hydrophilic and can form stable aqueous colloids to facilitate the assembly of macroscopic structures by simple and cheap solution processes.

Both characteristics are important to the large–scale uses of graphene. As a result, GO and rGO are still hot topics in the research and development of graphene, especially in regard to mass applications. Therefore, the reduction of GO is definitely a key topic, and different reduction processes result in different properties that in turn affect the final performance of materials or devices composed of rGO. Though the final target to achieve perfect graphene is hard to reach, research efforts have continuously made it closer.

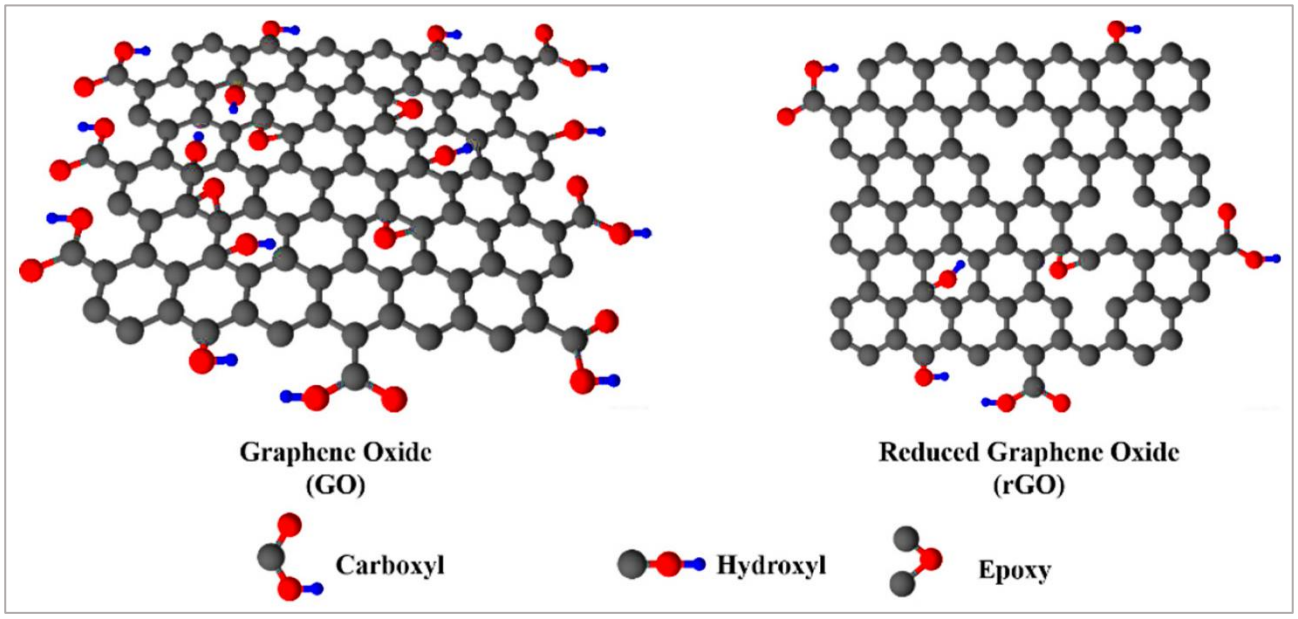

Figure 1_ 4: Representation of GO and rGO structures.

Carbon materials have been widely employed in both analytical and industrial electrochemistry[58].

The graphene era has begun more than ten years ago, and the urge to find new applications for this exciting material is still a hot topic. However, despite the enormous amount of data produced across the globe, it is yet not clear whether graphene has the potential to satisfy the expectation. This is particularly true when it comes to the field of electrochemical energy

storage, where graphene has been widely employed due to the need for new materials that can meet the market's performance requirements[66].

Graphene promises to increase substantially the energy and power–density of practical systems. However, the results obtained so far tend to suggest that real breakthroughs are far. Graphene can be considered an active material when it takes part in an energy–storage mechanism. This can range from hosting ions (such as Li^+ or Na^+ in metal–ion batteries) to store electrostatic charges in the electrode double–layer (as in electrochemical double–layer capacitors) or functioning as a catalyst in metal–air batteries.

1.5.2 Carbon Nanotubes

In 1991, MWNTs were for the first time described by Iijima[67] and the related SWNTs date back to 1993[68]: since then, CNTs have attracted enormous interest because of their unique structural, mechanical, and electronic properties. SWNTs consist in a single graphene sheet "rolled" into a tube, whilst MWNTs contain several concentric tubes sharing a common axis. In addition, MWNTs have shown to display different morphologies (such as "hollow tube", "bamboo" and "herringbone") depending on preparation pathways[69]. Both experimental and theoretical exploration has revealed that CNTs display extraordinary properties including[70]:

- ✓ high aspect ratio (~104),
- ✓ excellent waviness characteristics,
- ✓ lightweight (~2 g cm^{-3}),
- ✓ high thermal properties,
- ✓ good electrical conductivity,
- ✓ high melting point,
- ✓ low density (1.2–2.6 g mL^{-1}),
- ✓ large surface area (~1000 m^2 g^{-1}),
- ✓ excellent hydrogen storage,
- ✓ remarkable biological properties,
- ✓ high corrosion resistance,
- ✓ unique optical properties.

Moreover, CNTs have amazing electronic properties and can be metallic or semiconducting, relying upon their structure (diameter and helicity)[71]. One can fairly imagine that the way

CNTs are grown is crucial: in fact, significant impurity levels can affect the final behaviour of the obtained CNTs for the majority of the proposed syntheses[72]. This is particularly true when it is detected the presence of surface impurities, comprising usually amorphous carbon and metal nanoparticles (NPs), together with charged surface groups from post–growth purification, e.g. acidic functionalities when strong acid cleaning treatments are employed.
Several methods are present in literature for growing CNTs: the most encountered ones are electric arc discharge, laser ablation, high–pressure carbon monoxide (HiPCO), and catalysed chemical vapor deposition (cCVD)[72]. Solid–state carbon sources and carbon vaporization at very high temperatures are employed for the first two pathways. HiPCO produces CNTs from gas – phase reactions of iron carbonyl in carbon monoxide at high pressures. Even if CNTs with high – quality structures are obtained from the first three processes, high amounts of by–products are formed (such as graphitic debris, metal NPs and fullerenes). Consequently, CNTs prepared via these routes require a clean–up procedure after growth. CVD, instead, typically involves the catalytic decomposition of a carbon–based gas with catalytic metal NPs. When CVD conditions are carefully calibrated, CNTs of high crystallinity and low defect density are grown. Amorphous carbon concentration is low and NPs content is limited typically to carbide particles at the end of the nanotubes[72].
Whenever impurities content is high, they need to be removed. Thus, an extensive effort has been devoted into methods of impurities removal from CNTs. Several effective purification strategies have been highlighted, including flocculation, microfiltration, chromatography and centrifugation, and oxidative treatments with strong oxidizing acids (refluxing CNTs into concentrated HNO_3, H_2SO_4, HCl or mixtures of these acids). The secondary effect caused by the acid purification process needs to be considered: typically, CNT are cut, i.e., the ends of CNTs are opened due to oxidative damage of the sidewall. This causes cut ends and defects to form in the CNT sp^2 structure which are functionalized with oxygen–containing groups, such as carboxylic acids, ketones and alcohols. In particular, the presence of sidewall defects causes significant changes in the CNT electronic states near the Fermi level, typically resulting in an increase in resistivity of the CNTs at these points. Thus, the effect of the purification procedure on the resulting structure and electronic properties of the CNTs must be considered carefully when fabricating devices or electrode materials[72].

Considering the already mentioned extraordinary properties, CNTs have attracted incredible research interests and have been considered as the most promising materials for nano–electronics, energy storage devices, composite materials, medicine industry, nano–sensor applications, biological applications, smart materials, water and air purification systems[70]. Restricting the interest to electrochemistry, CNTs play important roles in two major areas: sensors and energy storage. Carbon nanotube electrodes are frequently employed for sensing and biosensing, since their fabrication requires no particular care and their performance are usually sufficient for this application. At the very beginning, CNTs modified electrodes were used, but these were found inappropriate for practical applications because of their mechanical instability. To sustain the mechanical stress, it is necessary to incorporate CNTs in a rigid polymer binder[73]. However, for real–world applications, mass production of cheap electrodes is required. Therefore, there have been many recent efforts to fabricate them using screen–printing technology. Just to make an example, Sanchez et al.[74] incorporated CNTs and immunoreagents on screen–printed electrodes: the resulting electrochemical immunosensor demonstrated five times higher sensitivity towards anti–RIgG than a graphite–based biosensor did. Variations of this scheme were also used for enzymatic detection of other biomarkers such as human chorionic gonadotropin hormone[75] or hydrogen peroxide[76]. The second field of application is energy storage and it is the focus of nowadays research because of its extreme importance. Carbon nanotubes are materials with very high surface area and their structure is analogous to that of graphite: in fact, CNTs can incorporate lithium exactly like graphite[73]. As an example, Wallace et al.[77] have directly grown flexible CNT based electrodes. When employed in a Li^+ ion battery, such electrodes showed high capacity and full reversibility of charge/discharge for 100 cycles. Another route to create flexible energy–storage devices is to couple conducting polymers with CNTs. Polyaniline/CNT papers have also been fabricated[78], which were described as thin, lightweight, and flexible enough to be rolled up or twisted, and displayed excellent electrochemical properties for energy storage.

1.6 Hybrid Materials: LDHs and Carbon Nanomaterials

Even in the presence of redox–active metals in LDHs structure, their performance generally suffers from low electrical conductivity.

To solve this problem, one of the most common strategies is to incorporate carbon nanomaterials inside LDHs. In fact, the introduction of conductive carbon greatly promotes the electron transport and improves the overall electrochemical properties[79]. For example, 2D carbon nanomaterials have been widely studied to develop LDH–based composites. As a matter of fact, graphene exhibits many unique properties such as high electrical conductivity, superior carrier mobility, a high surface area and good stability, which have been already mentioned. However, its cost is quite high, and the reduction of GO is easy to accomplish even if irreversible aggregates may form, which lead to the rapid reduction of surface area and, consequently, to a worse transportation of the electrolyte. In literature, it is possible to highlight different synthetic strategies and different kinds of nanomaterials employed to enhance electrochemical performances of LDHs. In the following, some of the most interesting examples are reported. Werner et al.[80] have proposed exfoliated manganese based LDHs and their composite with GO. This composite was synthesized by flocculating the LDH nanosheets with aqueous GO, which further turned into rGO/LDHs through hydrazine reduction. Compared to the LDHs alone, the rGO/LDH composite exhibited significantly improved pseudocapacitive behaviour. Dong et al.[81] developed Co/Al–LDH/GO films via layer–by–layer assembly method. The composite showed several advantages: first of all, the assembly by electrostatic interaction of GO and LDHs nanosheets guaranteed the complete utilization of the surface area. Moreover, since Co atoms were exposed on the surface of the LDH, the face–to–face assembly increased greatly the accessibility to the redox centres in the electrochemical reaction, and the electrons were able to rapidly move through GO sheets. CNTs have been also widely employed to produce nanocomposites since they display excellent electrical and mechanical properties. The superior performance of the obtained composites can be attributed to the following aspects:

1. CNTs can improve the transport of electrons and ions as a robust and conductive network.

2. their structure largely reduces the electron transfer distance and lowers the charge transfer resistance.
3. the efficient interfacial contact of components reduces the inner resistance of the composite electrode.

It has been also developed a ternary nanocomposite with Ni/Al LDHs, GO and MWCNTs. The nano crystallites of Ni/Al LDH/CNT are self–assembled on the top of GO nanosheets[82]. As an electrode material for supercapacitors, the hybrid material showed outstanding electrochemical performance, including high specific capacitance, good rate capability and excellent cycling stability. Several nanohybrids were proposed by Yu et al.[83] combining Ni/Co/Al LDH nanosheets with carbon nanomaterials such as carbon black, CNTs, rGO, and CNTs/rGO. They investigated and compared the electrochemical performance of the nano–hybrid electrodes. The LDH–CNTs/rGO electrode was proved to be the most performing device which could be attributed to several factors:

1. carbon materials in the nanocomposites are suitable for the transport of charge as channels for electron transmission.
2. Ni/Al LDHs can create mesopores able to shorten the diffusion paths of ions and to facilitate the electrolyte transport in the active material.
3. the nanostructure prevents the agglomeration of components improving their utilization efficiency.

As a new kind of carbon nanomaterial, carbon quantum dots (CQDs) with 0D graphite architectures have drawn much attention due to their advantages such as small particle sizes (∼5 nm), high conductivity, electron reservoir properties, high yield and low cost. In particular, an intense electrostatic interaction can be achieved as CQDs have abundant functional groups on their surface that can nucleate and anchor the pristine nanocrystals. Accordingly, composites made of LDHs and CQDs could increase the load of the active material and strengthen its contact with the conductor, which improves the electrochemical performance and stability[84]. Wei et al.[84] have also fabricated ultrathin nanoplate–like CQD/Ni–Al LDH composites by a simple one–pot solvothermal method, which exhibits a higher specific surface area than the pristine LDH and nanoscale size. The obtained layered structure possesses an enlarged interlayer spacing which not only facilitates the ions diffusion

but also offers continuous electron pathways in the electrochemical reactions. In the presence of CQDs, the Ni/Al LDH nanoplatelets become thinner in the self–assembly process, thus making easier the access of the electrolyte and the exposure of the active sites. In addition, the nanosized CQDs increase the surface roughness and electrical conductivity of the electrode, further promoting the electrochemical performance[84].

A low–cost and one–step scalable synthetic method to fabricate well–designed Co–Mn LDH nano–walls on the flexible carbon fibre (CF) surface have been developed by Zhao et al.[85]. It is desirable to combine promising LDHs with CFs to form a new material with a sophisticated morphology for flexible applications. Firstly, the layer of LDHs supports a stable microenvironment to hold diverse active metal units at the atomic scale for charge transfer. Secondly, due to a 3D flexible conductive network structure, the CF can act as a beneficial scaffold to load active LDHs and achieve bendable and light weight devices. Besides, the hierarchical architecture favours sufficient exposure of the electroactive species and facilitates the transport of ions/electrons in Faradaic reactions. This special architecture and the inherent features of LDHs endow the electrode with remarkable improved pseudocapacitive performance.

1.7 Energy storage and conversion

Energy, in particular electrical energy, is indispensable to maintain our standard of living. Detailed analysis and reports by illustrious institutions (such as the US Department of Energy Information Administration, International Energy Agency, the World Energy Council, ...), indicate that fossil fuels are expected to remain as the dominant energy resources for many long decades to come. Globally, coal was responsible for 40% of electricity produced in 2016 and is expected to provide more than 30% in 2040[4].

Nowadays, the domination of fossil fuels in global electricity production has significantly contributed to atmospheric CO_2 concentration (nearly 25% of the global green–house gas emissions). Fossil fuel–based electricity production has long been indispensable for reliable and cheap base–load power, but it faces significant social, political and environmental pressures to reduce carbon emissions[4].

A strategy that is gaining interest is the shift from fossil fuels to renewables as sources of power generation.

New generations ask for filling the gap between the installed capacities for intermittent sources such as solar and wind, and the actual amounts of electricity they generated: there is the urgent need for utility–scale storage technologies. This is particularly true also looking at nowadays politics. From the European elections of May 26, 2019, what is most surprising is the result obtained by the parties enrolled in the *Green Party*. The rise of the ecological movement in Europe has been recorded for some time in various countries and has been consolidated in this round with the conquest of 74 seats in the European Parliament (almost 10% of the total – https://www.europarl.europa.eu/election–results–2019/en).

This exploit of the environmentalist parties in the last European elections is perhaps precisely due to a greater sensitivity to the issues of climate change and environmental sustainability. Not only youth movements have found space in the public debate, such as that of *Fridays for Future* launched by Greta Thunberg (https://fridaysforfuture.org/), but also the international organizations themselves (such as the United Nations with their campaign on the *Sustainable Development Goals* (https://sdgs.un.org/goals)) have been able to convey messages which have been translated, especially among young people, into greater proximity to *Green Parties*.

Our responsibility as scientist is to find new strategies to pursue a common goal: a greener future.

In general, the variety of electrical storage technologies and approaches can be organized into four general categories:

- mechanical,
- chemical,
- electrochemical,
- electrical.

They exhibit a wide range of discharge characteristics and power ratings. However, the options for large–scale storage are low. Only pumped–hydro and compressed air energy storage systems are commercially available for bulk storage at utility scale (figure 1_5). The maturity levels of more advanced technologies, such as electrochemical storage, are still under active development and further require demonstration and deployment at utility scale. Moreover, the utility industry, which relies on low cost, scalability, and reliability, is typically averse to risk–taking. So, they are understandably sceptical about many of these technologies due to cost, scale–up issues, and lack of track records on safe and reliable operation for prolonged use at industrial scale[4].

However, over the past several decades, many efforts have been made in developing alternative technologies to harvest and use clean, sustainable energy: in particular in the exploitation of solar energy, wind power, biofuels, and hydrogen, as well as in energy technologies, such as fuel cells and lithium–ion batteries. Although these types of energy sources have played a marginal role up to now, new technologies and materials are the focus of basic resource, in order to make alternative energy more practical and competitive than fossil fuels.

For the future, employing electrochemical energy storage devices might allow the storage of this energy when electricity supply is higher than demand (typical of the above-mentioned intermittent power sources) and for its release when demand becomes higher than supply.

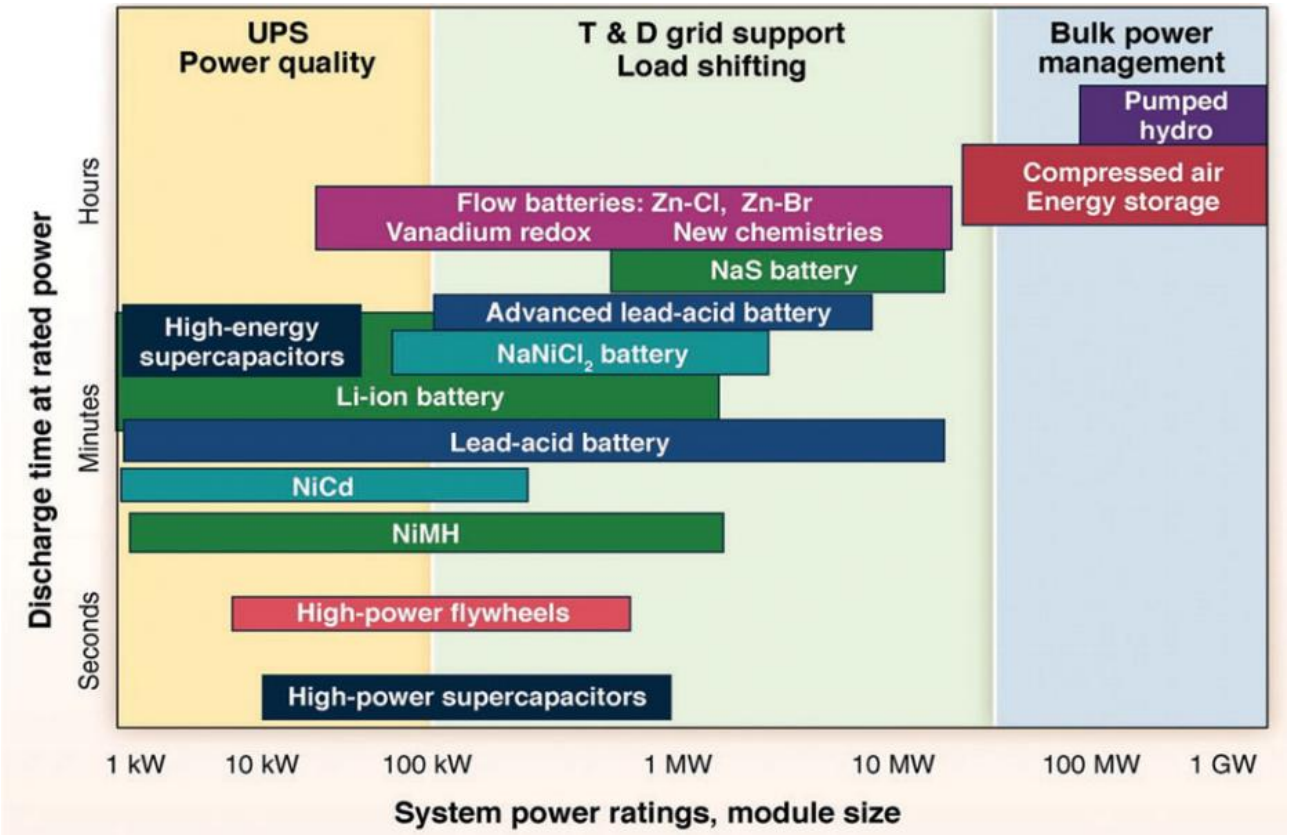

Figure 1_ 5: Comparison of power ratings and discharge time scales of various electrical energy storage systems (figure has been taken from ref. 3).

From this point of view, water electrolysis can play a fundamental role in the development of a sustainable energy system. These systems are electrochemical energy conversion devices producing hydrogen. The hydrogen energy represents probably the most attractive alternative to electricity storage in batteries since its reconversion into electricity via fuel cells opens–up independent scaling of power and energy due to the separation of the hydrogen storage from the conversion device.

In many application areas, beside fuel cells and batteries, the most employed electrical devices for energy conversion and storage are the electrochemical supercapacitors. In recent years, these devices have attracted considerable interest, mainly due to their high–power density and long lifecycle. The performance of such devices depends intimately on the properties of the functional materials; for this reason, currently the challenge is to address the demand of new functional materials with higher and faster storage and conversion efficiency.

1.7.1 Energy storage: Classification

As previously mentioned, systems for electrochemical energy storage include batteries, fuel cells, and electrochemical capacitors (ECs). The major difference among these three classes of devices lies in the mechanisms by which the energy is stored and converted. On the contrary, common features encounter those processes taking place at the interface which exists between an electrode and the electrolyte; moreover, electron and ion transport are separate.

When considering batteries and fuel cells, energy is generated through redox reactions at the anode and cathode. In general, the more negative electrode is designated as anode, whereas the cathode is the more positive one. Batteries are closed systems, in which the electrodes are the charge–transfer medium which takes an active role in the redox reaction. Fuel cells instead are open systems where the active masses undergoing the redox reaction are delivered from outside the cell, either from the environment, for example, oxygen from air, or from a tank, for example, fuels such as hydrogen and hydrocarbons[4]. In electrochemical capacitors, energy can be either delivered via redox reactions or not. By orientation of electrolyte ions at the electrode/electrolyte interface, the so–called electrical double layers (EDLs) are formed and released. In comparison to capacitors and fuel cells, batteries have found by far the most application markets and have got an established market position. Whereas capacitors have found niche markets as memory protection in several electronic devices, fuel cells are basically still in the development stage. Fuel cells have established their usefulness in space applications with the advent of the Gemini and Apollo space programs[4].

To compare the power and energy capabilities, a representation known as the Ragone plot has been developed. A simplified Ragone plot (Figure 1_6) discloses that fuel cells can be described as high–energy systems, whereas capacitors are considered high–power systems. Batteries have intermediate power and energy characteristics. There is some overlap in energy and power of capacitors, or fuel cells, with batteries. Indeed, batteries with thin film electrodes exhibit power characteristics similar to those of capacitors. Moreover, there are also hybrids such as metal/air batteries (or, in other words, metal/air fuel cells), which contain a battery electrode (metal anode) and a fuel cell electrode (air cathode). High power and high energy (and thus a competitive behaviour in comparison to combustion engines

and turbines) can best be achieved when the available electrochemical power systems are combined.

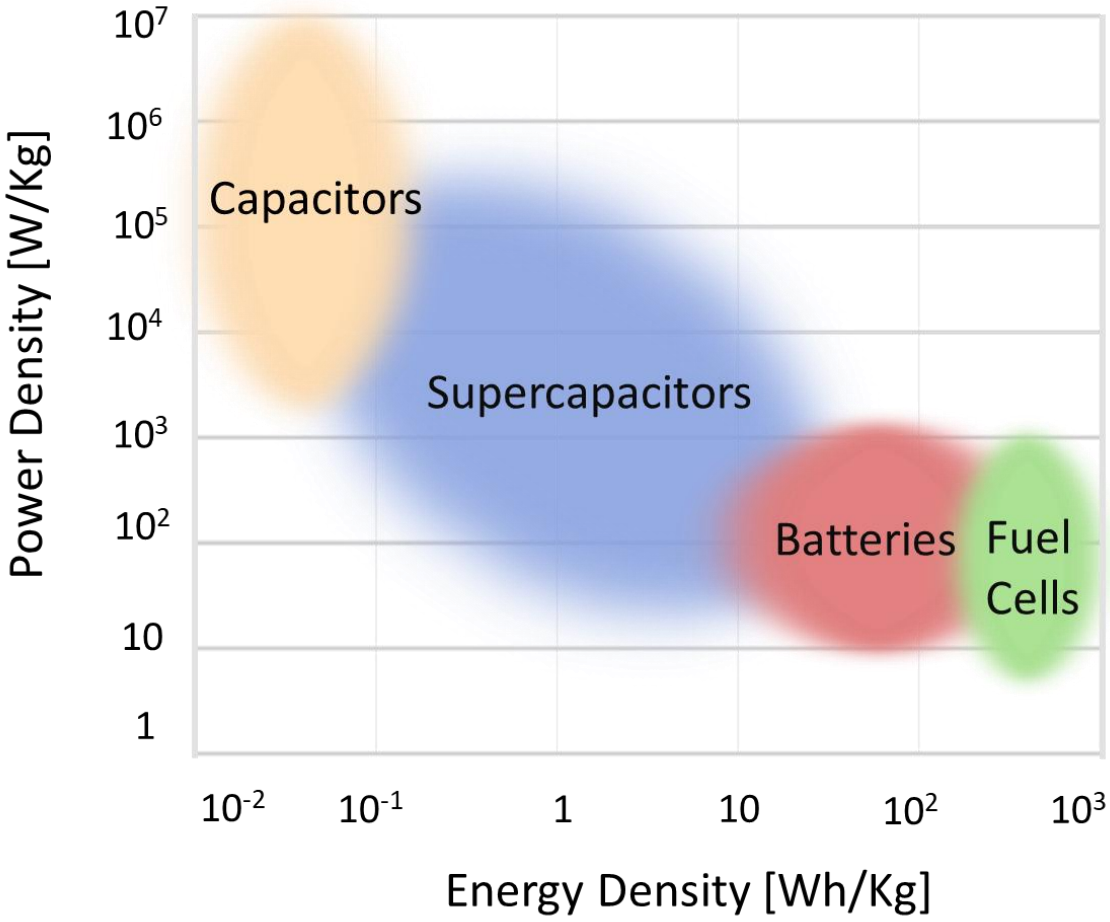

Figure 1_ 6: Simplified Ragone plot of the energy storage domains for the various electrochemical energy conversion systems and conventional capacitors.

Particular attention is hereby posed on ECs (also called supercapacitors or ultracapacitors). Conventional electrostatic and electrolytic capacitors physically store charge. Typically, they store it in an electric double layer constituted by ions at the interface between a high–surface–area carbon electrode and a liquid electrolyte.

More recently, aside from conventional capacitors, pseudo–capacitors and hybrid capacitors have also entered the energy storage scenario.

The term "pseudocapacitance" indicates a behaviour of electrode materials that have the electrochemical signature of a capacitive electrode, i.e., a linear dependence of the charge stored with changing potential within the window of interest, but in which charge storage

originates from electron–transfer mechanisms, rather than simply relying on the accumulation of ions in the electrochemical double layer[86].

Despite this clear definition, many battery–type electrodes or other materials that exhibit Faradaic behaviour have been called in the literature pseudocapacitive materials, leading the scientific community to confusion due to the concept of "pseudocapacitance", which cannot be applied to purely Faradaic behaviour. The term "hybrid" supercapacitor should be used instead: when pairing two electrodes with different charge–storage behaviour, i.e. one capacitive and one Faradaic, the resulting device is as a matter of fact a hybrid between a supercapacitor and a battery[86].

Anyway, nowadays, researchers are focusing their attention on finding new electrode materials in order to boost the performances of all these kinds of electrochemical capacitors. Environmental sustainability is essential considering a possible large–scale production and diffusion. Since all harmful substances should be avoided, new eco–friendly devices are proposed in literature replacing, for example, the organic solvent with water or/and eliminating the binder that is used for electrode preparation.

Until now, the electrode materials for supercapacitors can be generally divided into three categories. Carbon–based materials (graphene, carbon aerogels, carbon nanotubes, etc.)[87–89], conducting polymers (polyaniline, polythiophene, and polypyrrole)[65,90,91], and transition metal oxides/hydroxides[92–94].

Unfortunately, the above–mentioned materials are facing some challenges in broader applications. Carbon–based materials mostly have been used because of their high specific surface area, good electrical conductivity, and excellent stability but they may only physically store limited charges without any electrochemical reactions, hence displaying low specific capacitance.

Transition metal oxides have a high specific capacitance and rate capability, but they tend to display low specific surface area, poor electrical conductivity, partial dissolution during cycling, and sometimes they exhibit high cost and can be a potential harm to the environment[95].

Conducting polymers offer the advantages of low cost in comparison with metal oxides, a higher charge density than carbon–based materials and they often have good intrinsic

conductivity. However, they may suffer from severe swell and shrink during the charge–discharge process, which leads to the decline of mechanical strength of the electrode and deterioration of the specific capacitance during cycling[24].

In particular, increasing research efforts are centred onto the effective utilization of earth abundant elements and natural resources achieving attractive electrochemical performance of supercapacitor with the lowest environmental impact. In this scenario, LDHs are promising materials that can easily work in aqueous environment.

1.7.1.1 LDHs in hybrid capacitors

LDHs have become ideal candidates as supercapacitor materials because of the varying oxidation states of transition metals and their unique layered structures. Interesting materials contain Ni or Co as divalent cations: the advantages rely on their low cost and relatively environmentally friendly nature. In addition, these materials show good conductivity, and several structure types exist containing water in the host structure with high proton mobility[96].

However, the power density and cycling stability of these materials are usually unsatisfactory due to the redox kinetics limited by the low electron transfer and mass diffusion rates[79].

In order to solve these problems, several strategies have been proposed. Usually, LDHs crystallites have a relatively large diameter (ranging from 0.2 to 5 mm) and thickness (6 – 40 nm) causing only surface atoms to be exposed: in the Faradaic redox reactions, surface atoms play a crucial role in controlling active sites and electron transfer rate. Therefore, one of the adopted approaches involves the design of nanoarchitectures with large surface area and suitable pore–size distribution, where all species are active in the redox reaction process and which can ensure rapid mass and electron transport[79].

A few examples are hereby reported for Ni–based LDHs:

- Shao et al.[97] synthesized several microspheres of Ni/Al–LDHs with different structure (yolk–shell, core–shell, and hollow) leading to different specific surface areas and pore size distribution. Among them, the hollow Ni/Al–LDH shows the best electrochemical performances: high specific capacitance, excellent rate capability and stable cycling stability which is superior to the other structures. The increased number of exposed active species gave rise to a higher capacitance along repeated charge/discharge cycles.

- Zhao et al.[79] produced Ni^{3+} doped single–layer Ni/Ti–LDH nanosheets through an in–situ growth method. The characterization revealed the presence of a LDH monolayer with a particle size of about 20 nm. The monolayer holds highly exposed pseudocapacitance active facets that ensure efficient supercapacitive reactions. In addition, the Ni^{3+} defects in the monolayer facilitated electron accumulation and transportation, and meanwhile buffered huge volume changes of the active sites with repeated charge/ discharge cycles.

As already mentioned in section 6, the performance of nanostructured LDHs generally suffers from a low electrical conductivity as well as a strong tendency to stack together in the solid state.

To solve these problems, great efforts have been made through incorporating the LDHs with zero–three–dimensional carbon nanomaterials. The introduction of conductive carbon greatly promotes LDHs electron transportation and improves the overall electrochemical properties. Again, some examples are reported:

- Li et al. proposed a 3D Ni/Co–LDH@CNT composite which delivered a capacitance as high as 2046 F g^{-1} at 1 A g^{-1}. As the current density reached up to 15 A g^{-1}, it still retained high capacitance (1335 F g^{-1})[98].
- Chen et al.[99] have assembled the high–density Ni/Co–LDH on a 2D conductive CNT network, which can serve as a high performance and low–cost scaffold for ECs. The Ni/Co LDH nanoflakes have been grown on a large–diameter CNTs. The specific surface area of the composite is greatly improved. As a result, it was directly used for the assembly of a binder–free compact electrode. The electrode exhibits a high specific capacitance as well as excellent rate performance. Moreover, the hierarchical nanostructure assures the electrode from serious structural damage and capacitance loss after a hundred of cycle.
- Wang et al.[100] have synthesized an electrode nanocomposite with an innovative strategy via layered assembly of Co/Al–LDH nanosheets and single layer GO sheets. The specific capacitance was 1031 F g^{-1}. After 6000 cycles, the specific capacitance was retained with no obvious decrease.

1.7.2 Water splitting: Oxygen Evolution Reaction (OER)

Renewable energy is plentiful but tends to be intermittent and unpredictable. Since our reliance on renewable energy needs to grow, there is an increasing necessity to store this energy[2].

One of the most attractive alternatives is to use renewable power (when it is available) to split water into hydrogen and oxygen according to the equation:

$$2H_2O \rightarrow 2H_2 + 2O_2$$

In fact, the hydrogen produced by the reaction can be stored and then oxidized (by burning in air or in a fuel cell) to release energy and regenerate water, giving a carbon–neutral fuel production and consumption cycle.

The reaction in the above–mentioned equation is a thermodynamically unfavoured process and requires an energy input of 286 kJ mol^{-1} at room temperature and pressure[2]. Electrochemical methods are viewed as efficient and scalable tools in order to carry out this conversion.

Under acidic conditions, water is oxidized at the anode according to the equation (also known as oxygen evolution reaction (OER)):

$$2H_2O \rightarrow 2O_2 + 4e^- + 4H^+$$

At the cathode, the hydrogen evolution reaction (HER) is carried out:

$$4e^- + 4H^+ \rightarrow 2H_2$$

The minimum theoretical voltage difference necessary for the water splitting reaction occurrence is 1.23 V at room temperature. However, additional energy is required if we want these reactions to actually proceed (activation energy). The faster we want the water splitting to proceed (measured as current density), the greater amount of activation energy must be supplied. The term "overpotential" (symbol η) describes the additional voltage which must be applied to obtain a given current density.

In this scenario, the role of electrocatalysts is to lower this overpotential as much as possible. Under acidic conditions, the best electrocatalysts are precious metals (Pt at the cathode and IrO_2 or RuO_2 at the anode).

On the contrary, when basic media are employed, the HER and OER proceed according to the following equations:

$$\text{HER: } 4H_2O + 4e^- \rightarrow 2H_2 + 4OH^-$$

$$\text{OER: } 4OH^- \rightarrow O_2 + 4e^- + H_2O$$

In this case, excellent HER and OER catalysts are the first–row transition metals (and their alloys) and oxides, respectively.

Solar power is by far the largest source of renewable energy (~ 1.2×10^{14} kJ impinge earth every second). Therefore, it is perhaps natural that there is considerable interest in the coupling of solar irradiation to electrochemical water splitting. Two general routes are available for this process[2]:

- the employment of conventional solar panels to run conventional electrolysers ("indirect" solar–to–hydrogen production). This approach benefits from the use of conventional, tried–and–tested technologies but suffers from efficiency losses since additional steps are involved (electricity is first generated in the photovoltaic cell and then consumed in a electrolysis step in a separate device).
- the development of a single device able to perform at the same time light absorption and water splitting ("direct" solar–to–hydrogen production). In recent years, an explosion of research targeting the development of direct solar–to–fuels devices has been recorded. Such direct solar–to–fuels devices can be considered to perform artificial photosynthesis, whereby the energy of sunlight is captured and stored in the form of chemical bonds in a "solar fuel" product (in this case, hydrogen). Some limitations are intrinsic to this approach: the current densities that can be obtained are limited by the power of the incident sunlight (0.1 W cm^{-2} at most), which means that realistic current densities are about the order of 10 mA cm^{-2} for artificial photosynthesis.

In order to compete with undirect methods, the electrocatalysts employed for artificial photosynthesis systems will have to be both very cheap and widely available, thus restricting the choice to the first-row transition metals and their compounds.

1.7.2.1 LDHs as catalysts for OER

Co and Ni–based oxides and hydroxides are known to be promising OER catalysts in alkaline media and are thus appealing for large–scale usage because of their high abundance on earth and low cost[2,101].

In particular, Subbaraman et al.[101] systematically investigated four different types of 3d transition metal (oxy)hydroxides. Their OER activities were demonstrated to be in the order Ni > Co > Fe > Mn, in accordance with the OH_{ad}–M^{2+d} energetic strength order of Ni < Co < Fe < Mn. Among these transition metal based OER catalysts, layered bidimensional materials family have attracted increased attention for OER because of numerous advantages such as large surface–to–bulk ratio, much more efficient exposure of catalytic active sites in comparison with the 0D and 1D materials, controllable layered structure adjustment (intercalation, topological transformation, and assembly of other functional materials), tuneable chemical composition with different cations ratio, hierarchical porosity facilitating the diffusion of water molecules and release of gaseous products, strong electrostatic interactions between layers and interlayer anions to offer an ordered arrangement of interlayer species and a tailorable orientation of active sites, as well as the increase of structural stability. Yet, it remains challenging to solve the poor conductivity, low electron and charge transfer ability and insufficient active edge sites, especially for the bulk form of LDHs[2,39,101–104]. The most encountered reaction processes of LDH electrocatalysts in alkaline solution are listed below:

1. $[M] + OH^- \rightarrow [M-OH] + e^-$
2. $[M\text{-}OH] + OH^- \rightarrow [M-O] + H_2O + e^-$
3. $2[M\text{-}O] \rightarrow 2[M] + O_2$
4. $[M\text{-}O] + OH^- \rightarrow [M-OOH] + e^-$
5. $[M\text{-}OOH] + OH^- \rightarrow [M-OO] + H_2O + e^-$
6. $2[M\text{-}OO] \rightarrow 2[M] + 2O_2$

This corresponds to multiple electron–transfer steps involved. Each step needs to overcome the relative Gibbs free energy barrier (ΔG_n, n=1, 2, 3 and 4). The adsorption–desorption processes initiate at the active sites, i.e., transition metal elements ([M]), subsequently generating the [M–OH], [M–O] and [M–OOH] intermediates.

The ΔG_3 (reaction 4) was found to be the step thermochemically least favourable for the real OER catalyst, in which the OOH species is weakly bound to the catalyst. The transformation of M–OOH intermediates result in slow kinetics of OER and thus a high overpotential is usually required to prompt OER reactions[103].

Figure 1_7 summarizes the reaction scheme.

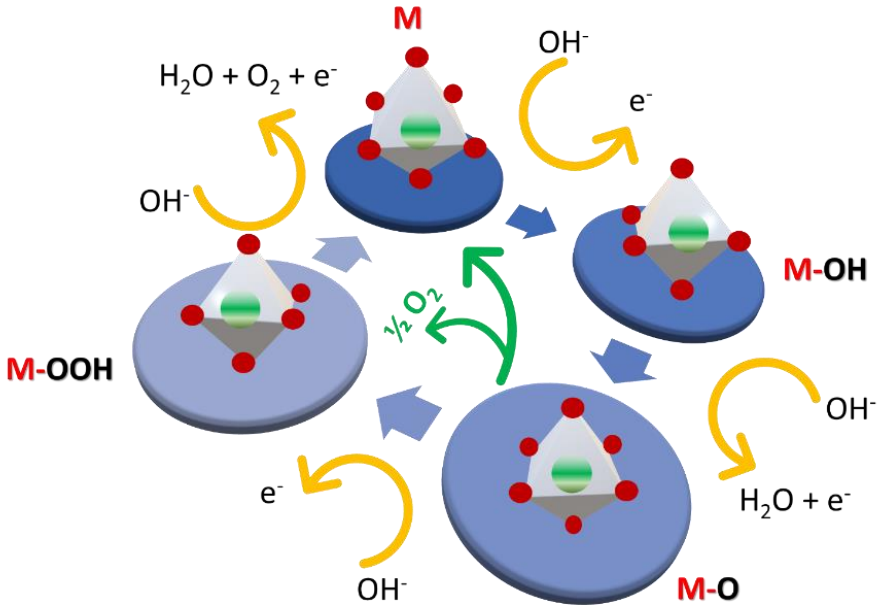

Figure 1_ 7: The OER mechanism of LDHs in alkaline conditions. The green line means the possible sideway of O_2 formation instead of M–OOH

More recently, Ni/Fe and Co/Fe LDHs have been structurally studied with a combination of electrochemical measurements, operando X–Ray scattering and absorption spectroscopy, and density functional theory calculations (DFT) with the aim to elucidate the catalytically active phase, reaction centre and the OER mechanism[105]. Dionigi et al.[105] has reported that, under the application of anodic potentials, M(II)–Fe LDHs oxidize from as–prepared α–phases to activated γ–phases. In particular, the γ–phases are characterized by about 8% contraction of the lattice spacing and switching of the intercalated ions. DFT calculations revealed also that the OER proceeds via a Mars van Krevelen mechanism: the reactions start from the deprotonation of the surface OH of the *in–situ* surface phase, instead of starting from OH adsorption, as generally assumed in many previous studies.

For the newly proposed mechanism, the authors have found that the oxidation of two–metal coordinated bridge OH moieties is more favourable than that of one–metal coordinated atop OH due to the synergy of the two nearest–neighbour metal sites in stabilizing the potential limiting OER reaction intermediates (O• radicals) by forming an O–bridged reaction center[105].

As a matter of fact, LDHs can also be seen as metal–doped monometallic hydroxides. Therefore, some examples about the mono–metallic hydroxides are briefly analysed hereby.

Conventional syntheses of hydroxides catalysts (such as Ni and Co hydroxides) are not typically conducted under inert atmosphere, so the reaction environment is commonly exposed to air. As a result, an inevitable oxidation process is carried out by the dissolved oxygen in solutions or coming from air.

During the crystal growth, Ni^{2+} or Co^{2+} could be oxidized to the trivalent counterparts without any subsequent oxidation process. This means that Ni^{3+}–doped $Ni(OH)_2$ or Co^{3+}–doped $Co(OH)_2$ can be obtained under the normal conditions and these monometallic hydroxides should not be charge–balanced as usual. Strictly speaking, these hydroxides synthesized under air atmosphere are substantially "self–doped monometallic LDHs," and numerous previous reports have demonstrated that Ni^{3+}/Co^{3+} exists in their monometallic hydroxides counterparts through traditional synthesis, thus forming self–doped monometallic LDHs[6].

As nickel and cobalt hydroxides possess similar structures, $Ni(OH)_2$ is taken as an example to discuss the structural features. There are two polymorphs of $Ni(OH)_2$: hydrotalcite–like phase (also called α-phase) and brucite–like phase (β-phase): the difference can be highlighted looking at the interlayer distances, which are reported to be about 8.0 and 4.6 Å, respectively[106,107]. The difference is due to the fact that the interlayer space of the former contains anions like nitrate, carbonate, sulphate and water molecules, whereas the latter displays well-oriented $Ni(OH)_2$ layers which are stacked perfectly along the c-axis.

The electrochemical activities by α– and β–$Ni(OH)_2$ are quite divergent: in particular the first one can be considered an active phase whilst the second a stable phase. The reason of such a phenomenon arises from the difference in interlayer distances which leads to changed ion transfer characteristics. Hall et al. highlighted the fact through in situ Raman spectroscopy: α–$Ni(OH)_2$ was spontaneously transformed to β–$Ni(OH)_2$ in alkaline solution[108].

Although numerous studies have been dedicated to $Ni(OH)_2$ or $Co(OH)_2$–based catalysts for OER, the performances of single $Ni(OH)_2$ or $Co(OH)_2$–based materials are too unsatisfactory to be considered as relevant in the field of water splitting[6].

Incorporating metal elements with different valent states into monometallic hydroxide is considered as an interesting strategy to greatly enhance the intrinsic electrocatalytic activity:

in fact, the redistribution of localized π–symmetry electrons via bridging O^{2-} (π–donation) endows favourable adsorption/desorption of oxygenated species[6].

However, it is still unclear which is the real function of metal centres, how the chemical states can be verified, and which surface effect they may induce along with the OER process. Beyond that, substituting lattice oxygen in metal hydroxide with nonmetal (e.g., sulphur, phosphorus, fluorine, and boron) is a plausible and alternative strategy to modify electronic structure of hydroxides as well[6].

Incorporation of other metal or nonmetal elements could actually improve the low conductivity of LDHs; since a series of M(II)–M(III) LDH groups can be regulated by M(III) species within the hydroxide matrix, the conventional LDHs can be also seen as n–type semiconductor.

Generally, other transition metals incorporation increases the active sites of LDHs and regulates the electronic structure of pristine metal hydroxides enhancing the OER performance. Chen et al.[109] illustrated that a heteroatom such as Cu or Mn can act as dopant into $Co(OH)_2$ and well modulate the electronic structure of $Co(OH)_2$, improving remarkably OER performance. A similar phenomenon has also been demonstrated by Jia et al.[109]: they boosted OER performance by tuning the metal composition of M(II) (M(II) = Ni or Co)/Mn–LDHs. In particular, effort has been made with the aim to elucidate the role of Mn in the adsorption of oxygenated species, which consequently formed the Mn–OOH intermediate.

Particular attention has also been devoted to engineered micro– and nanostructured, porous materials: this because hollow structure of LDHs was reported to display highly efficient behaviour toward OER. Microstructures of LDHs have certain impacts on specific properties such as specific surface area, and hydrophilicity which influence the electrocatalytic performance.

For example, Zhang et al.[110] proposed the fabrication of hierarchical Ni/Fe–LDH hollow microspheres, which exhibited diameters of around 250 nm and were composed of ultrathin nanoplatelets. The ultrathin hollow structure of Ni/Fe–LDH offered an enhanced performance compared with regular Ni/Fe–LDH nanoparticles because of their higher specific surface area and better hydrophilicity for ion/electron transport.

Among the tremendous effort devoted to boost the catalytic performance of LDHs toward OER, the Fe–incorporation in Ni based catalyst has been reported as the best method for stimulating OER. For this reason, Ni/Fe–LDHs have been the most investigated material among all the nanostructured LDHs.

In fact, this strategy can drastically enhance the unsatisfactory OER activity of $Ni(OH)_2$, i.e., by forming Ni/Fe–LDHs. It has been prevalently explored and regarded as one of the most active OER catalysts; however, the role of Fe–incorporation and the mechanism of how its incorporation affects the OER activity are still under debate, even if to investigate the dynamic OER process catalysed by Ni/Fe–LDH, powerful *operando* or *in–situ* techniques are employed to directly detect the changes of chemical states, structure, or morphology of the intermediates[5,6,39,105,111,112].

Moreover, also Co/Fe based LDHs have recently gained tremendous attention because of the electronic configuration of Co^{2+} ($t_{2g}^6e_g^1$), close to the optimal e_g filling. Yang et al.[39] have synthesized Co–based LDH catalysts with Fe and Al contents in the range of 15 to 45 % through a co-precipitation method. It has been highlighted that Fe^{3+} or Al^{3+} ions play an essential role as trivalent species to stabilize the LDH structure: in fact OER activity decreased upon increasing the Al content for the Co– and Al–based LDH catalysts, whereas a synergistic effect in Co– and Fe– based LDHs was observed, which resulted in an optimal Fe content of 35 at%.

As aforementioned, due to the high tunability of the composition of LDHs, a great number of active centres can be introduced into their structure to modify cations and electronic structure. However, the OER activity of LDHs is still not even close to an optimal performance, which could be further boost through insertion of a third metal–doping. The additional metal centre can regulate the electronic structures of LDH resulting in further synergetic effects between the doped and host metals, forming ternary LDHs with higher electrocatalytic activities[6].

At first, efforts have been centred on the incorporation of Co in a controllable manner into Ni/Fe–LDH host layers to modulate the electronic structures, to promote the generation of higher valence of the metal elements, and to reduce the thickness of the nanosheets, thus enriching the active sites and boosting the catalytic activities[6].

For example, Cao et al.[113] successfully prepared sulphur–doped Ni/Co/Fe–LDH porous nanosheets through a sacrificial template, and the intrinsic OER activity was greatly improved due to the exposure of more active sites and the enhanced electric conductivity.

1.8 References

1 M. D. Leonard, E. E. Michaelides and D. N. Michaelides, *Renew. Energy*, 2020, **145**, 951–962.

2 I. Roger, M. A. Shipman and M. D. Symes, *Nat. Rev. Chem.*, 2017, **1**, 0003

3 B. Dunn, H. Kamath and J. M. Tarascon, *Science*, 2011, **334**, 928–935.

4 T. M. Gür, *Energy Environ. Sci.*, 2018, **11**, 2696–2767.

5 Z. Cai, X. Bu, P. Wang, J. C. Ho, J. Yang and X. Wang, *J. Mater. Chem. A*, 2019, **7**, 5069–5089.

6 L. Lv, Z. Yang, K. Chen, C. Wang and Y. Xiong, *Adv. Energy Mater.*, 2019, **9**, 1–29.

7 M. Tahir, L. Pan, F. Idrees, X. Zhang, L. Wang, J. Zou and Z. Lin, *Nano Energy*, 2017, **37**, 136–157.

8 M. Conte, P. P. Prosini and S. Passerini, *Mater. Sci. Eng. B Solid-State Mater. Adv. Technol.*, 2004, **108**, 2–8.

9 G. A. Elia, K. Marquardt, K. Hoeppner, S. Fantini, R. Lin, E. Knipping, W. Peters, J. F. Drillet, S. Passerini and R. Hahn, *Adv. Mater.*, 2016, **28**, 7564–7579.

10 C. M. Elliott and R. W. Murray, *Anal. Chem.*, 1976, **48**, 1247–1254.

11 R. W. Murray, A. G. Ewing and R. A. Durst, *Anal. Chem.*, 1987, **59**.

12 R. W. Murray and Kenan, *Acc. Chem. Res.*, 1980, **13**, 135–141.

13 D. K. Schwartz, *Annu. Rev. Phys. Chem.*, 2001, **52**, 107–137.

14 A. J. Downard, *Electroanalysis*, 2000, **14**, 1085–1096.

15 X. Wang, Y. Lin, Y. Su, B. Zhang, C. Li, H. Wang and L. Wang, *Electrochim. Acta*, 2017, **225**, 263–271.

16 J. He, M. Wei, B. Li, Y. Kang, D. G. Evans and X. Duan, *Layer. Double Hydroxides*, 2006, **119**, 89–119.

17 X. Duan, D. G. Evans, *Layered Double Hydroxides,* 2006, Vol. **119**, *Springer Science & Business Media.*

18 F. Cavani, F. Trifirò and A. Vaccari, *Catal. Today*, 1991, **11**, 173–301.

19 A. I. Khan and D. O'Hare, *J. Mater. Chem.*, 2002, **12**, 3191–3198.

20 P. Benito, M. Monti, W. De Nolf, G. Nuyts, G. Janssen, G. Fornasari, E. Scavetta, F. Basile, K. Janssens, F. Ospitali, D. Tonelli and A. Vaccari, *Catal. Today*, 2015, **246**, 154–164.

21 E. Scavetta, A. Casagrande, I. Gualandi and D. Tonelli, *J. Electroanal. Chem.*, 2014, **722–723**, 15–22.

22 I. Gualandi, E. Scavetta, Y. Vlamidis, A. Casagrande and D. Tonelli, *Electrochim. Acta*, 2015, **173**, 67–75.

23 L. Zhang, K. N. Hui, K. S. Hui and H. Lee, *Electrochim. Acta*, 2015, **186**, 522–529.

24 Y. Zhang and S. Wei, *J. Nanoparticle Res.*, 2019, **21**.1: 14..

25 H. Asiabi, Y. Yamini, M. Alipour, M. Shamsayei and S. Hosseinkhani, *Mater. Sci. Eng. C*, 2019, **97**, 96–102.

26 P. Nalawade, B. Aware, V. J. Kadam and R. S. Hirlekar, 2009, **68**, 267–272.

27 M. Ogawa and S. Asai, Chemistry of materials, 2000, **12**, 3253–3255.

28 M. Adachi-pagano, C. Forano, J. Besse, L. Mate, C. No and B. Pascal, J. Mat. Chem. 2003, **13**, 1988–1993.

29 V. Prevot, N. Caperaa, C. Taviot-gue and C. Forano, Crystal Growth & Design, 2009, **9**, 8, 3647

30 K. L. Erickson, T. E. Bostrom and R. L. Frost, Materials Letters 2005, **59**, 226–229.

31 M. Nayak, T. R. Kutty, V. Jayaraman and G. Periasanny, *J. Mater. Chem.*, 1997, **7**, 2131–2137.

32 S. Miyata, *Clays Clay Miner.*, 1983, **31**, 305–311.

33 E. Scavetta, B. Ballarin, M. Giorgetti, I. Carpani, F. Cogo and D. Tonelli, *J. New Mater. Electrochem. Syst.*, 2004, **7**, 43–50.

34 Y. Vlamidis, E. Scavetta, M. Giorgetti, N. Sangiorgi and D. Tonelli, *Appl. Clay Sci.*, 2017, **143**, 151–158.

35 I. Gualandi, E. Scavetta, S. Zappoli and D. Tonelli, *Biosens. Bioelectron.*, 2011, **26**, 3200–3206.

36 E. Scavetta, I. Gualandi, D. Tonelli, C. Mousty, V. Prevot and M. Monti, *Electrochim. Acta*, 2014, **152**, 75–83.

37 E. Scavetta, B. Ballarin, C. Corticelli, I. Gualandi, D. Tonelli, V. Prevot, C. Forano and C. Mousty, *J. Power Sources*, 2012, **201**, 360–367.

38 E. Bernardi, M. Monti, D. Tonelli, P. H. Ho, P. Benito, A. Vaccari, L. Nobili, G. Fornasari and E. Scavetta, *Electrochim. Acta*, 2016, **222**, 1335–1344.

39 F. Yang, K. Sliozberg, I. Sinev, H. Antoni, A. Bähr, K. Ollegott, W. Xia, J. Masa, W. Grünert, B. R. Cuenya, W. Schuhmann and M. Muhler, *ChemSusChem*, 2017, **10**, 156–165.

40 I. Gualandi, Y. Vlamidis, L. Mazzei, E. Musella, M. Giorgetti, M. Christian, V. Morandi, E. Scavetta and D. Tonelli, *ACS Appl. Nano Mater.*, 2019, **2**, 143–155.

41 E. Musella, I. Gualandi, E. Scavetta, A. Rivalta, E. Venuti, M. Christian, V. Morandi, A. Mullaliu, M. Giorgetti and D. Tonelli, *J. Mater. Chem. A*, 2019, **7**, 11241–11249.

42 E. Musella, I. Gualandi, E. Scavetta, M. Gazzano, A. Rivalta, E. Venuti, M. Christian, V. Morandi and D. Tonelli, *Chem. - A Eur. J.*, 2019, **25**, 16301–16310.

43 F. Barahuie, M. Z. Hussein, S. Fakurazi and Z. Zainal, *Int. J. Mol. Sci.*, 2014, **15**, 7750–7786.

44 F. L. Theiss, S. J. Couperthwaite, G. A. Ayoko and R. L. Frost, *J. Colloid Interface Sci.*, 2014, **417**, 356–368.

45 K. H. Goh, T. T. Lim and Z. Dong, *Water Res.*, 2008, **42**, 1343–1368.

46 Y. Wang and D. Zhang, *Mater. Res. Bull.*, 2011, **46**, 1963–1968.

47 Z. Yang, H. Fischer, J. Cerezo, J. M. C. Mol and R. Polder, *Constr. Build. Mater.*, 2013, **47**, 1436–1443.

48 Z. Yang, H. Fischer and R. Polder, *Mater. Corros.*, 2013, **64**, 1066–1074.

49 M. Zammarano, M. Franceschi, S. Bellayer, J. W. Gilman and S. Meriani, *Polymer (Guildf).*, 2005, **46**, 9314–9328.

50 S. Xu, L. Zhang, Y. Lin, R. Li and F. Zhang, *J. Phys. Chem. Solids*, 2012, **73**, 1514–1517.

51 E. Scavetta, B. Ballarin, M. Berrettoni, I. Carpani, M. Giorgetti and D. Tonelli, *Electrochim. Acta*, 2006, **51**, 2129–2134.

52 A. Khenifi, Z. Derriche, C. Forano, V. Prevot, C. Mousty, E. Scavetta, B. Ballarin, L. Guadagnini and D. Tonelli, *Anal. Chim. Acta*, 2009, **654**, 97–102.

53 E. Scavetta and D. Tonelli, *Electroanalysis*, 2005, **17**, 363–370.

54 H. Farhat, C. Taviot-Gueho, G. Monier, V. Briois, C. Forano and C. Mousty, *J. Phys. Chem. C*, 2020, **124**, 15585–15599.

55 L. Dai, D. W. Chang, J. B. Baek and W. Lu, *Small*, 2012, **8**, 1130–1166.

56 D. Jariwala, V. K. Sangwan, L. J. Lauhon, T. J. Marks and M. C. Hersam, *Chem. Soc. Rev.*, 2013, **42**, 2824–2860.

57 Z. Wang, X. Ke, Z. Zhu, F. Zhu, M. Ruan, H. Chen, R. Huang and L. Zheng, *Phys. Lett. Sect. A Gen. At. Solid State Phys.*, 2001, **280**, 351–356.

58 D. A. C. Brownson and C. E. Banks, *Analyst*, 2010, **135**, 2768.

59 M. Pumera, *Chem. Soc. Rev.*, 2010, **39**, 4146.

60 K. R. Ratinac, W. Yang, J. J. Gooding, P. Thordarson and F. Braet, *Electroanalysis*, 2011, **23**, 803–826.

61 V. V. Sharma, I. Gualandi, Y. Vlamidis and D. Tonelli, *Electrochim. Acta*, 2017, **246**, 415–423.

62 T. Kuila, S. Bose, P. Khanra, A. K. Mishra, N. H. Kim and J. H. Lee, *Biosens. Bioelectron.*, 2011, **26**, 4637–4648.

63 S. Pei and H. M. Cheng, *Carbon N. Y.*, 2012, **50**, 3210–3228.

64 A. Shalaby, D. Nihtianova, P. Markov, A. D. Staneva, R. S. Iordanova and Y. B. Dimitriev, *Bulg. Chem. Commun.*, 2015, **47**, 291–295.

65 A. Alabadi, S. Razzaque, Z. Dong, W. Wang and B. Tan, *J. Power Sources*, 2016, **306**, 241–247.

66 R. Raccichini, A. Varzi, S. Passerini and B. Scrosati, *Nat. Mater.*, 2015, **14**, 271–279.

67 S. Iijima, *Nature*, 1991, **354**, 56–58.

68 S. Iijima and T. Ichihashi, *Nature*, 1993, **363**, 603–605.

69 R.L. McCreery, *Chem. Rev.*, 2008, **108**, 2646–2687.

70 S. K. Soni, B. Thomas and V. R. Kar, *Mater. Today Commun.*, 2020, **25**, 101546.

71 M. Elrouby, *J. Nanotechnol. Adv. Mater.*, 2013, **38**, 23–38.

72 I. Dumitrescu, P. R. Unwin and J. V. Macpherson, *Chem. Commun.*, 2009, **7345**, 6886.

73 M. Pumera, *Chem. - A Eur. J.*, 2009, **15**, 4970–4978.

74 S. Sánchez, M. Pumera and E. Fàbregas, *Biosens. Bioelectron.*, 2007, **23**, 332–340.

75 S. Sánchez, M. Roldán, S. Pérez and E. Fàbregas, *Anal. Chem.*, 2008, **80**, 6508–6514.

76 S. Sánchez, M. Pumera, E. Cabruja and E. Fàbregas, *Analyst*, 2007, **132**, 142–147.

77 J. Chen, A. I. Minett, Y. Liu, C. Lynam, P. Sherrell, C. Wang and G. G. Wallace, *Adv. Mater.*, 2008, **20**, 566–570.

78 C. Meng, C. Liu and S. Fan, *Electrochem. commun.*, 2009, **11**, 186–189.

79 M. Zhao, Q. Zhao, B. Li, H. Xue, H. Pang and C. Chen, *Nanoscale*, 2017, **9**, 15206–15225.

80 S. Werner, V. W. H. Lau, S. Hug, V. Duppel, H. Clausen-Schaumann and B. V. Lotsch, *Langmuir*, 2013, **29**, 9199–9207.

81 X. Dong, L. Wang, D. Wang, C. Li and J. Jin, *Langmuir*, 2012, **28**, 293–298.

82 W. Yang, Z. Gao, J. Wang, J. Ma, M. Zhang and L. Liu, *ACS Appl. Mater. Interfaces*, 2013, **5**, 5443–5454.

83 C. Yu, J. Yang, C. Zhao, X. Fan, G. Wang and J. Qiu, *Nanoscale*, 2014, **6**, 3097–3104.

84 Y. Wei, X. Zhang, X. Wu, D. Tang, K. Cai and Q. Zhang, *RSC Adv.*, 2016, **6**, 39317–39322.

85 J. Zhao, J. Chen, S. Xu, M. Shao, D. Yan, M. Wei, D. G. Evans and X. Duan, *J. Mater. Chem. A*, 2013, **1**, 8836–8843.

86 T. Brousse, D. Bélanger and J. W. Long, *J. Electrochem. Soc.*, 2015, **162**, A5185–A5189.

87 H. Pan, J. Li and Y. P. Feng, *Nanoscale Res. Lett.*, 2010, **5**, 654–668.

88 K. Xia, G. Wang, H. Zhang, Y. Yu, L. Liu and A. Chen, *J. Nanoparticle Res.*, 2017, **19**, 254

89 C. Li, X. Yang and G. Zhang, *Mater. Lett.*, 2015, **161**, 538–541.

90 A. Sumboja, X. Wang, J. Yan and P. S. Lee, *Electrochim. Acta*, 2012, **65**, 190–195.

91 D. P. Dubal, S. H. Lee, J. G. Kim, W. B. Kim and C. D. Lokhande, *J. Mater. Chem.*, 2012, **22**, 3044–3052.

92 S. Yao, P. Li, L. Wang, G. Chen and Y. Jiao, *New J. Chem.*, 2019, **43,** 3139–3145.

93 U. M. Patil, S. B. Kulkarni, V. S. Jamadade and C. D. Lokhande, *J. Alloys Compd.*, 2011, **509**, 1677–1682.

94 Z. Yu, B. Duong, D. Abbitt and J. Thomas, *Adv. Mater.*, 2013, **25**, 3302–3306.

95 H. Wang, X. Xiang and F. Li, *J. Mater. Chem.*, 2010, **20**, 3944–3952.

96 X. M. Liu, Y. H. Zhang, X. G. Zhang and S. Y. Fu, *Electrochim. Acta*, 2004, **49**, 3137–3141.

97 M. Shao, F. Ning, Y. Zhao, J. Zhao, M. Wei, D. G. Evans and X. Duan, *Chem. Mater.*, 2012, **24**, 1192–1197.

98 X. Li, J. Shen, W. Sun, X. Hong, R. Wang, X. Zhao and X. Yan, *J. Mater. Chem. A*, 2015, **3**, 13244–13253.

99 H. Chen, F. Cai, Y. Kang, S. Zeng, M. Chen and Q. Li, *ACS Appl. Mater. Interfaces*, 2014, **6**, 19630–19637.

100 L. Wang, D. Wang, X. Y. Dong, Z. J. Zhang, X. F. Pei, X. J. Chen, B. Chen and J. Jin, *Chem. Commun.*, 2011, **47**, 3556–3558.

101 R. Subbaraman, D. Tripkovic, K. C. Chang, D. Strmcnik, A. P. Paulikas, P. Hirunsit, M. Chan, J. Greeley, V. Stamenkovic and N. M. Markovic, *Nat. Mater.*, 2012, **11**, 550–557.

102 Y. Vlamidis, E. Scavetta, M. Gazzano and D. Tonelli, *Electrochim. Acta*, 2016, **188**, 653–660.

103 Z. Cai,a X. Bu, P. Wang, J. C. Ho, J. Yang, X. Wang, *J. Mater. Chem. A*, 2019, **7**,

5069-5089

104 J. Wang, L. Wang, X. Chen, Y. Lu and W. Yang, *J. Solid State Electrochem.*, 2015, **19**, 1933–1948.

105 F. Dionigi, Z. Zeng, I. Sinev, T. Merzdorf, S. Deshpande, M. B. Lopez, S. Kunze, I. Zegkinoglou, H. Sarodnik, D. Fan, A. Bergmann, J. Drnec, J. F. de Araujo, M. Gliech, D. Teschner, J. Zhu, W. X. Li, J. Greeley, B. R. Cuenya and P. Strasser, *Nat. Commun.*, 2020, **11**, 1–10.

106 K. I. Pandya, W. E. O'Grady, D. A. Corrigan, J. McBreen and R. W. Hoffman, *J. Phys. Chem.*, 1990, **94**, 21–26.

107 A. Szytula, A. Murasik and M. Balanda, *Phys. status solidi*, 1971, **125**, 0–3.

108 D. S. Hall, D. J. Lockwood, S. Poirier, C. Bock and B. R. MacDougall, *ACS Appl. Mater. Interfaces*, 2014, **6**, 3141–3149.

109 L. Chen, H. Zhang, L. Chen, X. Wei, J. Shi and M. He, *J. Mater. Chem. A*, 2017, **5**, 22568–22575.

110 C. Zhang, M. Shao, L. Zhou, Z. Li, K. Xiao and M. Wei, *ACS Appl. Mater. Interfaces*, 2016, **8**, 33697–33703.

111 C. Taviot-Guého, P. Vialat, F. Leroux, F. Razzaghi, H. Perrot, O. Sel, N. D. Jensen, U. G. Nielsen, S. Peulon, E. Elkaim and C. Mousty, *Chem. Mater.*, 2016, **28**, 7793–7806.

112 J. Jiang, F. Sun, S. Zhou, W. Hu, H. Zhang, J. Dong, Z. Jiang, J. Zhao, J. Li, W. Yan and M. Wang, *Nat. Commun.*, 2018, **9**, 1–12.

113 L. M. Cao, J. W. Wang, D. C. Zhong and T. B. Lu, *J. Mater. Chem. A*, 2018, **6**, 3224–3230.

CHAPTER 2: EXPERIMENTAL SECTION

"Numero pondere et mensura Deus omnia condidit."

– Sir Isaac Newton

In this section the preparation of the modified electrodes, and the experimental setup for the measurements will be described.

2.1 Chemicals

In Table 2_1, the list of employed chemicals is reported.

Table 2_ 1: List of all the chemicals employed.

Reagent	Chemical formula or abbreviation	Proprieties	Brand / manufacturer
Cobalt(II) nitrate hexahydrate	$Co(NO_3)_2 \cdot 6H_2O$	98 % pure	Sigma–Aldrich
Nickel(II) nitrate hexahydrate	$Ni(NO_3)_2 \cdot 6H_2O$	99.999 % pure	Sigma–Aldrich
Aluminum nitrate nonahydrate	$Al(NO_3)_3 \cdot 9H_2O$	> 96 % pure	Sigma–Aldrich
Iron(III) nitrate nonahydrate	$Fe(NO_3)_3 \cdot 9H_2O$	99 % pure	Riedel–de Haen
Graphene Oxide	GO	4 mg mL^{-1}	Sigma–Aldrich
Sodium hydroxide	NaOH	98 % pure	Sigma–Aldrich
Potassium hydroxide	KOH	98 % pure	Sigma–Aldrich
Sulfuric acid	H_2SO_4	95–98 % w/w	J. T. Baker
Hydrochloric acid	HCl	37 % (w/w)	Merck
Acetone	CH_3COCH_3	≥ 98.8% pure	Sigma–Aldrich
3,4–Ethylenedioxythiophene (EDOT)	$C_6H_6O_2S$	MW=142.15 g mol^{-1} d=1.334 g cm^{-3}	Aldrich
5–Hydroxymethyl–2–furfural	$C_6H_6O_3$	99% pure	Sigma–Aldrich
Poly-styrene-sulfonate sodium salt (PSS)	$-(C_8H_7O_3SNa)_x-$	MW∼70000	Sigma–Aldrich
Poly–dimethyl–siloxane (PDMS)	$-(C_2H_6OSi)_x-$	/	Sigma–Aldrich
Polyvinyl alcohol	$-(C_2H_4O)_x-$	99 % pure	Sigma–Aldrich
Polyvinylidene fluoride	$-(C_2H_2F_2)_x-$	/	Sigma–Aldrich
Activated Charcoal	C	/	Sigma–Aldrich
Acetylene Black	C	99 % pure	Alfa Aesar
Potassium chloride	KCl	99 % pure	Fluka
Ethanol	C_2H_5OH	96–97.2 %	Sigma–Aldrich

2.2 Chemical Laboratory equipment

- General laboratory glassware
- Analytical balance (AT21 Comparator, Mettler Toledo, accuracy: ± 0.001 mg, capacity up to 22 g).
- Analytical balance (SCALTEC SPB32, error: ± 0.0001 g, capacity up to 120 g).
- Micropipettes 0.5–10, 10–100, 100–1000 μL (Pipetman Gilson).
- The electrochemical deposition and characterization were performed by using a CH Instrument Mod. 660 C, controlled by a personal computer via CH Instrument software, connected to a PINE Research Instrumentation Modulated Speed Rotator (MSR).
- Galvanostatic cycling with potential limitation in constant current mode was performed by using a battery cycler (Neware Battery Testing System).
- All the graphs were elaborated using the software Origin 9.0 or Microsoft Office Excel 2010.
- The majority of electrochemical experiments were carried out using a single compartment, three–electrode cell composed by the following electrodes:
    - Working electrodes:
        - GC rotating disk electrode (0.5 mm diameter) for the applications of the LDH modified electrodes as OER catalysts.
        - Pt electrodes (BASi, up to 2.5 cm diameter).
        - Grafoil GTJ (purchased by VED)
        - Nickel Foam (Xiamen Tob New Energy Technology Co., Thickness: 1.60mm)
        - Toray Carbon Paper Gas Diffusion Layer (Quintech, Thickness: 0.190mm, bulk density: 0.44 g cm^{-3})
        - Carbon Cloth Gas Diffusion Layer (Quintech, Thickness: 0.38mm, bulk density: 1.75 g cm^{-3})
        - Ink–jet printed Carbon Nanotubes

- Reference electrodes:
  - Hg/HgO electrode (Amel Instruments) to carry out the characterizations in alkaline solutions.
  - Saturated calomel electrode (SCE, Amel Instruments), for the other measurements (electrosynthesis, electrodes pretreatments, etc).
- Counter–electrode: Pt wire (Sigma Aldrich).

2.3 Electrode modification

During the experimental work, several electrode supports were employed and different LDHs were electro–synthesised in order to evaluate materials performances.

2.3.1 Cleaning of electrode surface

Cleaning the electrode is a critical step to achieve a well adherent coating.

- **Platinum treatment**: as previously reported[1], the Pt surfaces are strongly influenced by the electrochemical pre-treatments. In particular, the electrochemical tests performed in a KNO_3 solution indicated that the nitrate reduction, responsible for the OH^- generation necessary for the LDH deposition, needs a lower overvoltage when Pt surfaces were submitted to an electrochemical pre-treatment. Therefore, Pt was firstly polished to a mirror–like surface by mechanical cleaning, using sandpaper, and then the electrode was submitted to an electrochemical treatment which consists in three steps:
    - 250 CV cycles between –0.25 and +1.30 V vs SCE, in 0.1 M H_2SO_4 at a scan rate of 1 V s^{-1}.
    - polarization at –0.90 V vs SCE for 300 s in 1 M H_2SO_4 (under stirring in order to remove H_2 bubbles).
    - 250 CV cycles in between –0.25 and +1.30 V vs SCE, in 0.1 M H_2SO_4 at a scan rate of 1 V s^{-1}.
- **GC treatment**: the electrode surface was polished to a mirror–like surface by a mechanical cleaning with SiC sandpaper and aqueous alumina (0.05 μm) slurry on a wet polishing cloth.

For the following electrodes, the first step is to obtain the desired geometry and dimension before the polishing treatment. If not stated otherwise, the shape of the electrode is a rectangle of 3·1 cm. Then the active area is delimited to 1·1 cm with Teflon, as shown in figure 2_1.

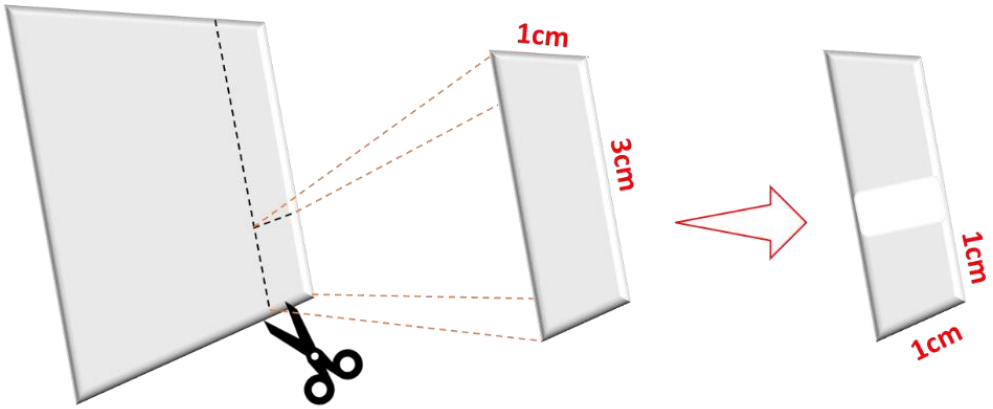

Figure 2_ 1: first step in the preparation of the electrodes

- **Grafoil treatment**: the surface was rinsed in ethanol for 10 min, and then dried to a constant weight.
- **Carbon Cloth treatment**: the electrode was rinsed in acetone for 5 min, afterward in ethanol for 5 min and then in distilled water for 5 min. Finally, it was dried to a constant weight.
- **Toray Carbon Paper treatment**: the surface was rinsed in ethanol for 10 min, and then dried to a constant weight.
- **Ni–foam treatment**: the electrode was immersed in acetone for 10 min at 50°C under sonication, then in distilled water for 10 min at 50°C, under sonication, and finally dried to a constant weight.

2.3.2 Contact Angle

The contact angle was statically measured by a home–made set–up (Fig. 2_2 A) which is composed of a photo camera, a stage with a variable height, a syringe mounted on a support. A droplet was carefully deposited on the investigated substrate by a syringe which is positioned above the sample surface. The photo camera was aligned to the substrate and captured an image from the profile of the droplet and the substrate. The contact angle was measured by using a software.

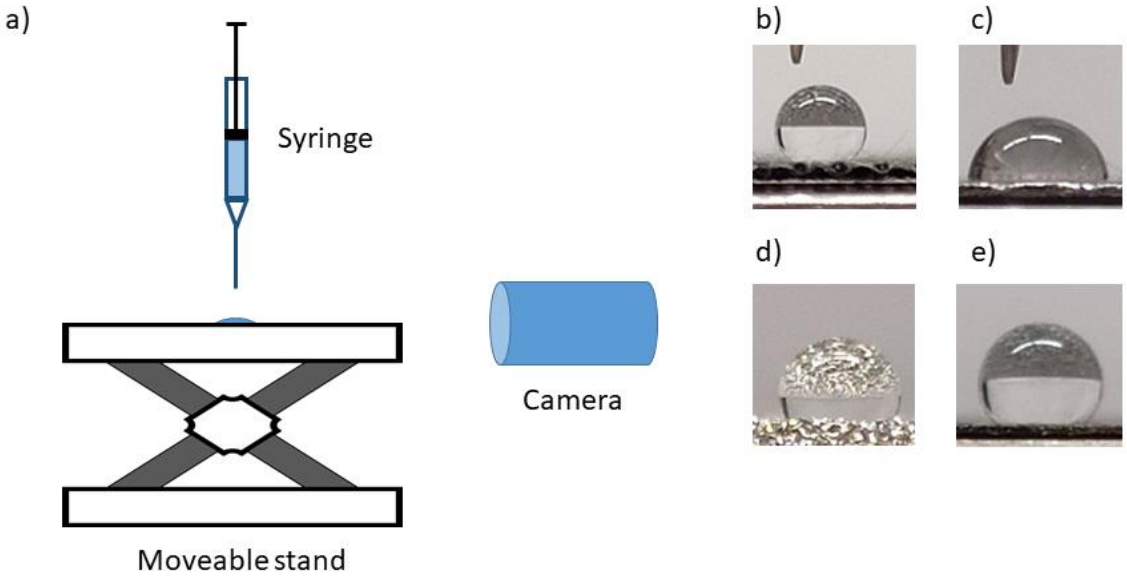

Figure 2_ 2: (a) Home–made set up for the statical measure of the contact angle. Pictures refer to Carbon Cloth (b), Grafoil (c), Nickel Foam (d) and Toray Carbon Paper (e).

2.3.3 Potentiodynamic LDHs synthesis

The LDH films were deposited on the electrode surface by cathodic reduction of a freshly prepared 0.03 M solution containing M(II) and M(III) at variable molar ratios in distilled water.

The electrochemical reaction was carried out by CV (2 cycles). After performing the modification, the electrode was immediately rinsed with water.

Hereby, all the parameters of LDHs potentiodynamic synthesis on the different substrates are reported (potentials are measured vs SCE).

Table 2_ 2: CV parameters for the potentiodynamic syntheses

	Pt	**GC**	**Grafoil**	**CC**	**TC**	**Ni–Foam**	**Ink–jet printed CNTs**
Ni/Al	–1.3 and 0.0 V 0.025 V s^{-1}	–1.3 and 0.0 V 0.025 V s^{-1}	–1.3 and 0.0 V 0.025 V s^{-1}	–1.3 and 0.0 V 0.03 V s^{-1}	–1.4 and 0.0 V 0.03 V s^{-1}	–1.3 and 0.0 V 0.03 V s^{-1}	–1.3 and 0.0 V 0.025 V s^{-1}
Ni/Al–ERGO	–1.3 and 0.0 V 0.025 V s^{-1}	/	–1.3 and 0.0 V 0.025 V s^{-1}	/	/	/	/
Co/Al	–1.3 and 0.0 V 0.02 V s^{-1}	–1.3 and 0.0 V 0.03 V s^{-1}	–1.3 and 0.0 V 0.03 V s^{-1}	–1.3 and 0.0 V 0.03 V $s^{-1}s$	–1.4 and 0.0 V 0.03 V s^{-1}	–1.3 and 0.0 V 0.03 V s^{-1}	/
Co/Fe	–1.1 and 0.0 V 0.03 V s^{-1}	–1.1 and 0.0 V 0.04 V s^{-1}	–1.1 and 0.0 V 0.04 V s^{-1}	/	/	/	/

Co/Al–ERGO	–1.3 and 0.0 V 0.02 V s^{-1}	/	–1.3 and 0.0 V 0.03 V s^{-1}	/	/	/	/
3 Metals LDH (Al)	–1.3 and 0.0 V 0.02 V s^{-1}	/	–1.3 and 0.0 V 0.03 V s^{-1}	/	/	/	/
3 Metals LDH (Fe)	–1.1 and 0.0 V 0.03 V s^{-1}	/	–1.1 and 0.0 V 0.04 V s^{-1}	/	/	/	/

2.3.2 Potentiostatic LDHs synthesis

All the parameters of LDHs potentiostatic synthesis on the different substrates are reported (potentials are measured vs SCE).

Table 2_ 3: Parameters for the potentiostatic syntheses

	GC	**Grafoil**	**CC**	**TC**	**Ni–Foam**
Ni/Al	–1.1 V 30 s	–1.3 V 30 s	–1.2 V 30 s	–1.2 V 30 s	–1.2 V 30 s
Co/Al	/	–1.3 V 30 s	–1.2 V 30 s	–1.2 V 30s	–1.2 V 30 s

The galvanostatic deposition has been studied only for Ni/Al–LDH on GC. The electrosynthesis was performed in five steps in which a current of − 0.5 mA was applied for 5 s. Between every cathodic pulse, a zero current step was performed for 5 s.

In general, the procedures employed for all depositions were optimized after a preliminary investigation that was devoted to obtaining the highest reproducibility. However, only in the case of GC support, the procedure already described in the literature for the potentiostatic deposition has been employed.

2.3.4 Electrodeposition of PEDOT: PSS

The starting solution for the electrochemical deposition of PEDOT:PSS contained 0.1 mM polystyrene sulfonate (PSS) and 10 mM 3,4-ethylenedioxythiophene (EDOT). The mixture of EDOT and PSS was stirred for 45 min until complete dissolution. The electrochemical deposition was carried out using 25 CV cycles from 0.00 V to +1.20 V at 0.100 V s^{-1}.

2.3.5 Modification of the electrode with a slurry based on AC

Activated Carbon (AC), Acetylene Black (AB) and the binder (chosen between polyvinylalcohol (PVA) or polyvinylidene–fluoride (PVDF)) were weighed in a beaker in order to obtain a solid total mass of 1 g, then approximately 4.5 mL of dispersant were added

gradually, under continuous stirring. The slurry was stirred until the desired consistency was obtained.

Different types of slurries were prepared to evaluate the best formulation (ratios are given in weight):

1. AC: AB: PVA = 8: 1: 1, in deionized H_2O
2. AC: AB: PVDF = 7: 2: 1, in deionized H_2O
3. AC: AB: PVDF = 8: 1: 1, in EtOH
4. AC: AB: PVDF = 7: 1: 2, in deionized H_2O

The considerations that led to the choice of the optimal formulation are widely described below. The electrochemical tests used for the characterization of the electrodes suggested to use formulation 2 as it guarantees the highest adhesion of the modifier to the substrate.

Before the electrode modification with the slurry, it was necessary to keep it under magnetic stirring for at least two hours, in order to obtain a homogeneous suspension. Once the preparation of the anode was completed, the electrodes were dried for at least 12 hours, before being employed. As a support, Grafoil was used. The desired area was delimited on the plate using Teflon tape. 300 µl of the slurry were taken with a micropipette, and deposited on the Grafoil plate, taking care to obtain a homogeneous coverage. The electrode area for the set–up "capacitor in solution" was 3·3 cm^2, whereas for the set–up "assembled capacitor" it was 2·2 cm^2.

2.4 Procedure for the hybrid capacitor fabrication

The asymmetric hybrid supercapacitor (SC) was composed of two different electrodes:

- LDH from one side
- AC based electrode on the other side.

When the SC performances were evaluated in solution, the two electrodes were immersed in 6M KOH in a two terminal device setting (Figure 2_3a) under nitrogen flow. When the SC device was assembled, a solid polyelectrolyte was used. The solid polyelectrolyte was prepared by the following procedure:

1. weight 1 g of PVA, 0.001 mol of KOH and 0.001 mol of KCl
2. transfer the reagents in a 10 mL flask and fill with distilled water
3. stir the solution for 10 minutes at 100–150 °C
4. transfer on a Petri dish and let it dry overnight.

Then a squared poly–dimethyl–siloxane mask of 3·3 cm^2 area was prepared, and the central part was removed, leaving an internal square of 2·2 cm^2 area. The mask was fixed on a 3·6 cm^2 Grafoil sheet, and the internal part was filled with the AC slurry. After drying, the remained void space was filled with the solid polyelectrolyte. Then the electrode was fixed on the upper part of the Grafoil sheet modified with the electrodeposited LDH or LDH/ERGO0.05 (figure 2_3b).

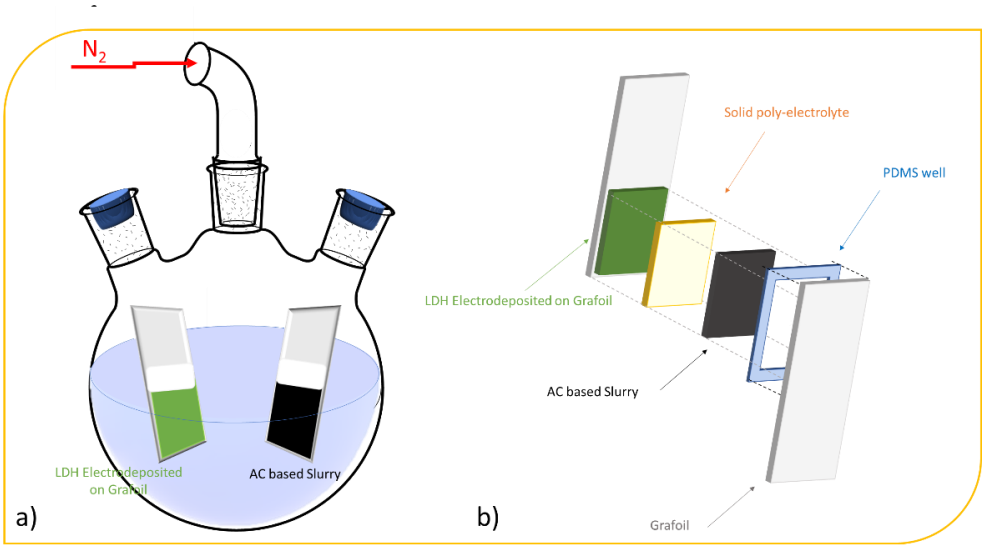

Figure 2_ 3: a) sketch of the set–up of the hybrid SC in solution and b) schematic representation of the assembled hybrid SC

2.5 Electrode characterizations

The synthesised materials were characterized by several methods. The electrochemical behaviours were studied by cyclic voltammetry. Structural characterizations were performed in order to confirm the LDH phase and get further knowledge on the oxidation states of metals and how they change upon oxidation. The morphology and the adhesion of the material were investigated by SEM.

2.5.1 Structural Characterization

- **X–ray diffraction**:

X–ray diffraction analysis was carried out by means of a PANalytical X'Pert PRO powder diffractometer equipped with a fast X'Celerator detector. Cu Kα radiation was used (40 mA, 40 kV). The 2–theta range was investigated from 5° to 60° with a step size of 0.066° and a time/step of 250 s. Size was estimated with Scherrer equation:

$$Crystallite\ size\ (average) = \left(\frac{k\lambda}{Bcos\theta}\right)$$

where k is the shape factor (= 1), λ is the wavelength (= 0.154 nm), B is the full width at half maximum of the reflection (instrumental broadening was considered), and θ is the diffraction angle of the reflection (= 4.85°).

- **X–ray Absorption Spectroscopy**:

XAS experiments were performed at ELETTRA Synchrotron Radiation Laboratory (Basovizza, Trieste), through the ELETTRA proposal 20180220 (Principal Investigator: Marco Giorgetti) and through the CERIC proposal 20172042 (Principal Investigator: Marco Giorgetti). Spectra were recorded at the XAFS beam line 11.1, in fluorescence mode using a large area Si drift diode detector (KETEK) at the Co and Fe K–edge (7709 eV and 7112 eV, respectively) using a Si(111) double crystal monochromator. Extended X–ray absorption fine structure (EXAFS) curves were recorded at room temperature. X–Ray absorption spectroscopy spectra were deglitched, calibrated, and normalized using the Athena program. The pre–edge background was removed by subtraction of a linear function extrapolated from the pre–edge region, and the XANES spectra were normalized at the unity by extrapolation of the atomic background. The EXAFS analysis was performed by using the GNXAS package that considers Multiple Scattering (MS) theory. Briefly, the method is based on the

decomposition of the EXAFS signals into a sum of several Single Scattering (SS) and Multiple Scattering (MS) contributions, i.e., the n–body terms. It allows for the direct comparison of the raw experimental data with a model theoretical signal. The procedure avoids any filtering of the data and allows for a statistical analysis of the results. The theoretical signal is calculated ab initio following a previously published structural model for LDHs that has been adapted to this set of samples and contains the relevant two–body γ(2), three–body γ(3) and four body γ(4) MS terms. For the case of the Co–edge the following n–body terms have been included in the fitting procedures: the two–atom contributions γ(2) Co–O with degeneracy of six and the two–atom contributions γ(2) Co–Co with degeneracy of four, and a γ(2) Co–Fe with degeneracy of two. Also, the following n–body terms have been included in the fitting procedures for the Fe Kedge case: the two–atom first shell contribution γ(2) Fe–O with degeneracy of four plus a γ(2) Fe–O with degeneracy of two; the two–atom contributions γ(2) Fe–Co with degeneracy of four plus the two–atom contributions γ(2) Fe–Fe with degeneracy of two. Data analysis was performed by minimizing a χ^2–like residual function that compares the theoretical signal, α mod(E), to the experimental one, α exp(E). The phase shifts for the photoabsorber and backscattered atoms were calculated ab initio according to the muffin–tin approximation and allowing 5–15% overlap between the muffin–tin spheres. The Hedin– Lundqvist complex potential was used for the exchange correlation potential of the excited state. The core hole lifetime was fixed to the tabulated value and included in the phase shift calculation. The experimental resolution in the fitting analysis was about 1 eV, in agreement with the stated value for the beamline used.

- **Morphology characterization**

The morphological, and structural characterization, and chemical compositions of the LDH films were investigated by Field Emission–Scanning Electron Microscopy (FE–SEM) using a LEO 1530 ZEISS instrument equipped with Schottky emitter, operated at an acceleration voltage variable from 5 to 15 keV, and Everhart–Thornley and In–lens detectors for secondary electrons imaging. Energy Dispersive X–ray Spectroscopy (EDS) measurements were performed with an Oxford INCA system equipped with a

30 mm^2 Silicon Drift Detector. The Transmission Electron Microscopy (TEM) analyses were performed with a FEI TECNAI F20 microscope equipped with Schottky emitter and operated at 200 keV. The instrument is also equipped with EDS and Scanning Transmission Electron Microscopy (STEM) detectors. The TEM images were acquired in phase contrast mode while STEM images were recorded using a High Angle Annular Dark Field (HAADF) detector and show an intensity I that is proportional to $Z^{1.7}t$, where Z is the mean atomic number and t is the thickness of the specimen (the so–called Z–contrast).

- **IR/RAMAN Spectroscopy**

Infrared spectra were recorded on a Perkin Elmer Spectrum 2000 FT–IR spectrophotometer. Raman spectra were recorded with a Renishaw System RM1000. The spectrometer was coupled to a Leica DMLM microscope equipped with 50×, 20× and 5× objectives which allowed, with the 50× objective, a nominal spatial resolution <2 mm in xy and 4 mm in z. The excitation wavelength was from an argon laser tuned at 514.5 nm. The laser output power was around 25 mW, but when needed the light intensity impinging on the film was reduced by neutral density filters to avoid sample damage.

- **X–ray Photoelectron Spectroscopy**

X–ray Photoelectron Spectroscopy (XPS) was performed with a VG ESCALAB 220 iXL spectrometer. The X–Ray source was non–monochromatized Al Kα. During the experiment, the base pressure was 1×10^{-8} mbar. Detail spectra of relevant core levels were scanned four times at a pass energy of 10 eV with a step width of 0.1 eV and a dwell time of 300 ms. The detail spectra were corrected by subtraction of excitation satellites before peak fitting due to the non–monochromatized Al anode. Data analysis was performed by UNIFIT 2020 (https://www.unifit–software.de/). The background of the detail spectra was fitted using a combination of polynomial and Shirley background. Peak shapes were simulated combining Lorentzian and Gaussian functions by convolution (Voigt profile). The binding energy scale was calibrated to the C 1s signal of adventitious hydrocarbons at 285.0 eV.

- **Atomic Emission Spectrometry**

The elemental analysis was performed using an Agilent 4210 Atomic Emission Spectrometer MP–AES, controlled by a computer via Agilent MP Expert software.

2.6 Electrochemical characterization

The CVs were recorded in order to study the redox activity of the synthesized materials and determine the stability of the modified electrodes.

- **Cyclic Voltammetry**

The electrochemical behaviour of the electrodes was studied by CV in a suitable potential window at different scan rate (0.001, 0.005, 0.010, 0.025, 0.050, 0.100, 0.250, 0.500 V s^{-1}), in 0.1, and 1.0 M NaOH, and in 0.1, 1.0, and 6.0 M KOH.

In each experiment, CV curves were recorded until the cycles resulted superimposable.

- **Electrochemical Impedance Spectroscopy**

Impedance spectra were recorded for each LDH in the potential range of the anodic wave comprising also potentials higher than the onset of the oxygen evolution reaction and were plotted in different plots.

- **Evaluation of performances as catalysts**

The catalytic activity of the electrodes was investigated in alkaline solution (0.1, and 1.0 M NaOH or KOH) by linear sweep voltammetry (LSV) or by CV, recording iR–corrected polarization curves at the scan rate of 0.010 V s^{-1}.

When OER was evaluated, the procedure proposed by McCrory et al. was followed[2,3]. As a preliminary test, the determination of the Electrochemical Surface Area (ECSA) for electrodes has been carried out, following these steps:

1. Determine the open circuit potential and wait until stability (usually at least 10 minutes in 1M NaOH).
2. Record CVs in a potential window of 0.1 V centred in the OCP (OCP ± 0.05 V) at the scan rate of 0.005, 0.010, 0.025, 0.050, 0.100, 0.200, 0.400 V s^{-1}.

3. Point out the anodic and cathodic currents at the OCP and plot the results as current (mA) as a function of the scan rate. Using the linear fitting, obtain the interpolation lines, one for the cathodic and the other for the anodic current. The average slope of each line is the capacity of the double layer ($C_{DL,}$ mF).
4. ECSA is obtained dividing the C_{DL} for the specific capacity (C_S) of an atomic planar layer of the investigated material in the condition used in the procedure (1M NaOH, C_S=0,040 mF cm^{-2}).

$$ECSA = \frac{C_{DL}}{C_S}$$

5. The roughness factor (RF) is obtained dividing the ECSA by the geometrical area of the electrode.

$$RF = \frac{ECSA}{Geometrical\ Area}$$

The OER activity was evaluated primarily by performing CVs at 10 mV s^{-1} scan rate; this scan rate is slow enough to ensure a steady–state behaviour at the electrode surface. The durability of the material was studied recording chronopotentiometric curves by applying a current density of 10 mA cm^{-2} for at least two hours. When OER was evaluated using GC–RDE, the WE was constantly rotated at 1600 rpm in order to remove the oxygen bubbles from its surface during LSV and chronopotentiometric experiments. The Tafel slopes, onset potentials and overpotentials were determined. When exhaustive electrolysis was carried out, the conversion (%) and the selectivity for the oxidation products were calculated using the following equations:

$$HMF\ conversion\,(\%) = \frac{Mol\ of\ reagent\ consumed}{Mol\ of\ initial\ reagent} \cdot 100$$

$$Selectivity\,(\%) = \frac{Mol\ of\ product}{Mol\ of\ reagent\ converted} \cdot 100$$

The Faradaic efficiency (FE) of product was calculated by:

$$FE\,(\%) = \frac{Mol\ of\ product\ formed}{Mol\ of\ total\ electrons\ passed} \cdot 100$$

- **Evaluation of performances as capacitor**

The specific capacitances of materials were calculated by different methods: from CVs, recorded at different scan rates, and from charge/discharge curves, recorded at different current densities. The electrochemical measurements were conducted in alkaline solution (0.1 M NaOH or KOH, and 1 M or 6 M KOH).

The specific capacitance (F g^{-1}) can be evaluated from the CV, since the charge accumulated inside the material is related to the area under the cyclic voltammogram in a proper potential window. From the CVs the specific capacitance can be obtained by the following equation:

$$C_S = \frac{2I}{m\nu}$$

where I (A) is the current value, m (g) is the mass and ν is the scan rate (V s^{-1}).

The materials were tested by performing galvanostatic charge–discharge tests, in a stable potential window under the charging condition of constant current density (1.0, 2.0, 5.0 and 10.0 A g^{-1} (alternatively A cm^{-1})). The discharge was performed with the same constant current density. The specific capacitance was calculated by the equation:

$$C_S = \frac{I\Delta t}{m\Delta V}$$

Where I (A) represents the discharge current, m (g) is the mass, Δt and ΔV are the total discharge time and the potential drop during discharge, respectively.

Long–term cycling stability was investigated carrying out at least 10,000 cycles at a current density of 2.5 A g^{-1}.

Capacitance retention (%) can be calculated as the ratio of initial to final cycles specific capacitance. Of course, a series of retentions in % form can be determined over all cycles as:

$$C_{Retention} = \frac{C_{n+1}}{C_n} \cdot 100$$

where n is the number of a cycle.

Discharge/Charge efficiency (%) has been calculated for each cycle as:

$$E_{D/C} = \frac{C_D}{C_C} \cdot 100$$

- **Evaluation of performances as sensors**

The as–prepared LDHs were stabilized in 0.1 M KOH. The stabilization was carried out in order to activate the redox systems; the current slowly increases from the very first cycles and the last ones, when the cycles become superimposable.

The analytical performances of the LDHs were studied in 0.1 M KOH; the electrode responses were evaluated recording CV curves at different scan rates for increasing ethanol additions to establish the working potential. After each addition, the solution was stirred for a few minutes and then a CV cycle was recorded.

Also, chronoamperometric curves were recorded for subsequent ethanol additions, keeping the solution under stirring. From these curves the calibration graphs (current vs concentration) were obtained.

From the slope of the calibration, it was possible to directly obtain the sensitivity values.

The limit of detection (LOD), instead, was calculated as:

$$y_{LOD} = y_b + 3\sigma_b$$

Where y_b is the white signal and σ_b its standard deviation. The intercept of the calculated calibration curve is taken as an estimation of y_b. The standard deviation of the regression has been employed as σ_b.

2.7 References

1 I. Gualandi, A. G. Solito, E. Scavetta and D. Tonelli, *Electroanalysis*, 2012, **24**, 857–864.

2 C. C. L. McCrory, S. Jung, I. M. Ferrer, S. M. Chatman, J. C. Peters and T. F. Jaramillo, *J. Am. Chem. Soc.*, 2015, **137**, 4347–4357.

3 C. C. L. McCrory, S. Jung, J. C. Peters and T. F. Jaramillo, *J. Am. Chem. Soc.*, 2013, **135**, 16977–16987.

CHAPTER 3: RESULTS AND DISCUSSION

"Science is constantly proved all the time. If we take something like any fiction, any holy book, and destroyed it, in a thousand years' time, that would not come back just as it was. Whereas if we took every science book and every fact and destroyed them all, in a thousand years they'd all be back because all the same tests would be the same result."

– Ricky Gervais

This section contains parts of the published works and some of the same used sentences. (Reproduced with permission)

3.1 Novel electrochemical synthesis and characterization of LDHs

To date, more than two hundred of items result on Scopus when searching for "layered double hydroxides electrodeposition". Nowadays, this is certainly one the most commonly used method for the direct modification of conductive substrates[1–4].

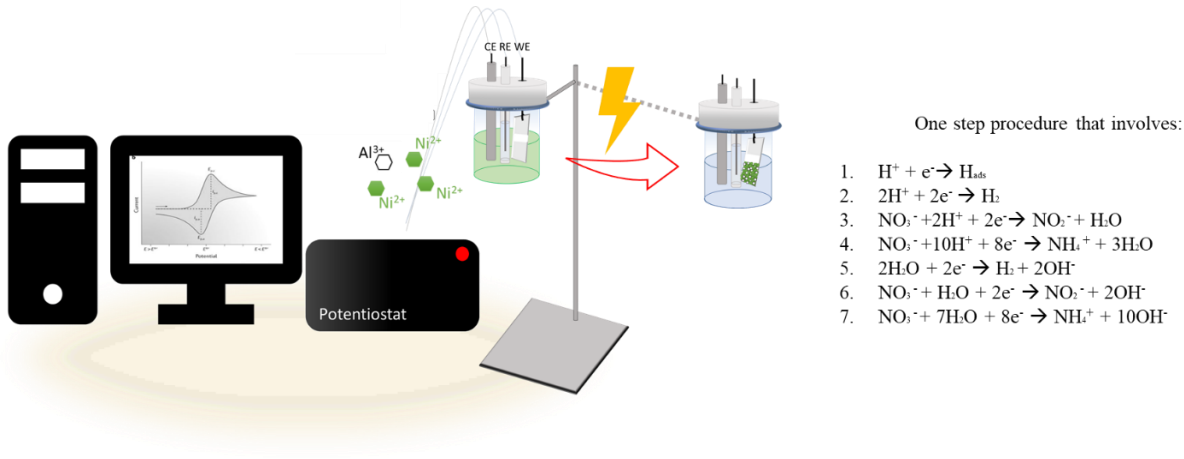

Figure 3_ 1: sketch of the experimental set up and reactions taking place during the deposition.

As already mentioned in chapter 1, the electrosynthesis of LDHs is usually performed by applying a cathodic potential to the working electrodes while they are immersed in a solution containing the nitrate salts of the divalent and trivalent metals. KNO_3 can also be added to the electrolyte bath to boost the nitrate reduction reaction. The negative polarization induces the occurrence of reactions 1–7 in figure 3_1. The OH^- production and H^+ depletion lead to a pH change from a weakly acidic to a basic value that causes LDH precipitation on the electrode surface. Although this kind of procedure has been widely used, some weak points can be identified by studying the literature:

1. **Kinetics of electrochemical OH^- generation.** NO_3^- reduction is usually preferred as OH^- source instead of H_2 evolution since the latter generates bubbles on the electrode surface which can eventually interfere with the LDH film formation. Nitrate reduction is a very complex multistep process under a strong kinetic control[5]. The rate of the overall electrochemical reaction depends on the activity of the surface. For example, the activity of Pt can be varied by an electrochemical treatment and it highly affects the nature of the electrodeposited LDH films[6].

2. **LDH precipitation**. LDH precipitation relies on both the nucleation and the growth of crystals, as typical of all the solubility equilibria. Therefore, the rate of the process is controlled by the oversaturation degree of the solution and by the presence of defects on the electrode surface that can act as nucleation centres. Furthermore, the precipitation of Al containing LDHs can follow two different pathways depending on the rate of pH increase[7,8]. If the pH slowly increases, $Al(OH)_3$ precipitation takes place first, and when all Al^{3+} has been completely consumed, the bivalent cations can be inserted into the amorphous structure of $Al(OH)_3$ to form the layered structure. When a quick pH variation occurs instead, direct precipitation occurs.
3. **Reagent diffusion.** LDH precipitation involves at least three reagents: M(II), M(III), and OH^-. The cations diffuse from the solution bulk to the electrode surface, while the hydroxide ions are generated next to the electrode surface and diffuse toward the solution. LDH precipitation should take place on the electrode, and it occurs when the OH^- production exactly equalizes the OH^- removal by LDH precipitation[9]. If the OH^- production is slow enough that its concentration is less than the one which can be consumed by Al^{3+}, only $Al(OH)_3$ formation occurs. The reason is that $Al(OH)_3$ precipitates at a lower pH with respect to the LDH, and Al^{3+} is continuously renewed by diffusion from the solution bulk.

   On the other hand, when the OH^- production is too fast, OH^- ions diffuse toward the bulk of the solution, leading to LDH precipitation also far from the electrode surface. Furthermore, the concentration profiles that are generated close to the electrode surface can lead to a variation of the molar ratio of M(II) and M(III) as a function of the distance from the conductive material, when long potential pulses are applied.

Considering all these factors, small variations of the electrode surface can significantly affect the LDH deposition because they modify both the electrochemical activity and the surface density of defects that can act as nucleation sites. Therefore, a very robust procedure is necessary to obtain reproducible results during LDHs electrosynthesis.

The first electrochemical procedure adopted for the synthesis of LDHs was proposed by Tonelli's group in 2004 consisting in a potentiostatic reduction of nitrates. Even if some great advantages were highlighted (such as a short time for electrode modification and well–

adhered coatings), when performing the potentiostatic synthesis, the characterization CVs did not always display a reproducible signal of the redox active couple. Moreover, even if in the electrolytic bath used for the electrodeposition the M(II)/M(III) ratio was known, the concentration gradients originating during the synthesis hindered a fine control of the final ratio in the deposited material, especially when a long potential pulse was applied. Lastly, an electrochemical route able to even partially intercalate a big molecule inside the LDH interlayers has never been accomplished, and this is to the detriment of
one of the most fascinating features of LDHs which is the interlayer tunability.

To summarize, the aim of section 3.1 is to study and compare three different electrochemical synthetic protocols (Galvanostatic, Potentiostatic and Potentiodynamic) and to demonstrate that the last one is able to overcome all the previously mentioned issues. Moreover, great efforts have been devoted to the characterization of the obtained films: in fact, the newly developed synthesis will be demonstrated to ensure also good phase formation for all cases studied, differently from the previously employed methodologies.

3.1.1 Comparison of electrochemical syntheses: Preliminary tests[I]

To find the best electrodeposition procedure, three approaches have been tested:

1. ***Potentiostatic deposition***. The potentiostatic approach, which is the most commonly employed in the literature, is performed by applying a constant potential to the working electrode (usually between −1.1, and −0.9 V, vs SCE). In this case, it is possible to control the thermodynamics of the system and the kinetics through the overpotential. Consequently, the applied potential rules the processes that can or cannot occur at the electrode. A process that should be avoided when choosing the deposition potential is water reduction because hydrogen evolution can damage the LDH film, as already stated. However, the use of this approach does not ensure a fine control of the rate of OH^- production.
2. ***Galvanostatic deposition***. In galvanostatic deposition a constant current flows between the working and the counter electrodes. In this way, the rate of the overall electrochemical processes is forced by the potentiostat, and consequently, the rate of OH^- production should be finely controlled. On the other hand, the applied potential must be varied to guarantee the instrument operation, and thus, it is more difficult to control the side processes.
3. ***Potentiodynamic deposition***. In a potentiodynamic approach, the deposition is stimulated by performing a cyclic voltammetry on the cathodic side, for example from 0 to −1.3 V. The most anodic potential is fixed far from the onset potential of the deposition to have enough time to restore the cation concentration close to the electrode surface by diffusion. Moreover, the value of the most cathodic potential can be fixed to avoid the occurrence of side reactions.

[I] Reprinted from Ni/Al layered double hydroxide and carbon nanomaterial composites for glucose sensing. I. Gualandi, Y. Vlamidis, L. Mazzei, E. Musella, M. Giorgetti, M. Christian, V. Morandi, E. Scavetta, D. Tonelli, ACS Applied Nano Materials, 2019, 2 (1), 143-155.

The different synthetic strategies were performed using the electrode modified with Ni/Al–LDH as benchmark and the characterization CVs of three different depositions are reported in figure 3_2.

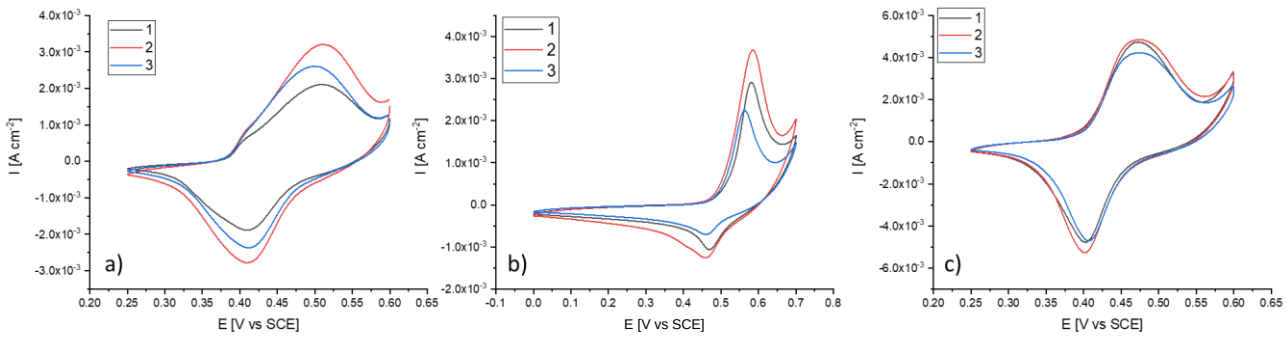

Figure 3_ 2: CVs (scan rate = 0.01 V s−1) recorded in 0.1 M NaOH for electrodes resulting from potentiostatic a), galvanostatic b), and potentiodynamic c) electrodepositions.

The reproducibility of the procedures was tested by evaluating the peak currents associated with the redox signal of Ni centres according to the following reaction 8 [10,11]:

$$8.\ Ni(II) - LDH + OH^- \rightarrow Ni(III)(OH) - LDH + e^-$$

The potentiostatic deposition exhibits the worst robustness (since it displays both difference in peak intensities and shape) probably because it does not allow for a fine control of the OH^- production and, thus, of the amount of precipitated LDH (Figure 3_2a). Also, in the case of the galvanostatic synthesis, the reproducibility of the deposit is scarce, with a standard deviation higher than 15% (Figure 3_2b). On the other hand, when the synthesis is performed by a potentiodynamic procedure, the results display good reproducibility with a standard deviation of the peak current equal to 3% (Figure 3_2c).

The potentiodynamic synthesis was chosen for subsequent experiments as it shows the best reproducibility. Furthermore, the results obtained were compared (next section) with those relevant to the potentiostatic synthesis.

It is worth mentioning that the conditions chosen for the potentiodynamic deposition led to a LDH film with higher peak currents than the potentiostatic one. The key point is that when the films are obtained by the potentiostatic approach, the variation range of the peak currents is very high and is often of the same order of magnitude of the peak currents.

3.1.2 Potentiostatic VS Potentiodynamic synthesis: different supports at comparison[II]

Supports

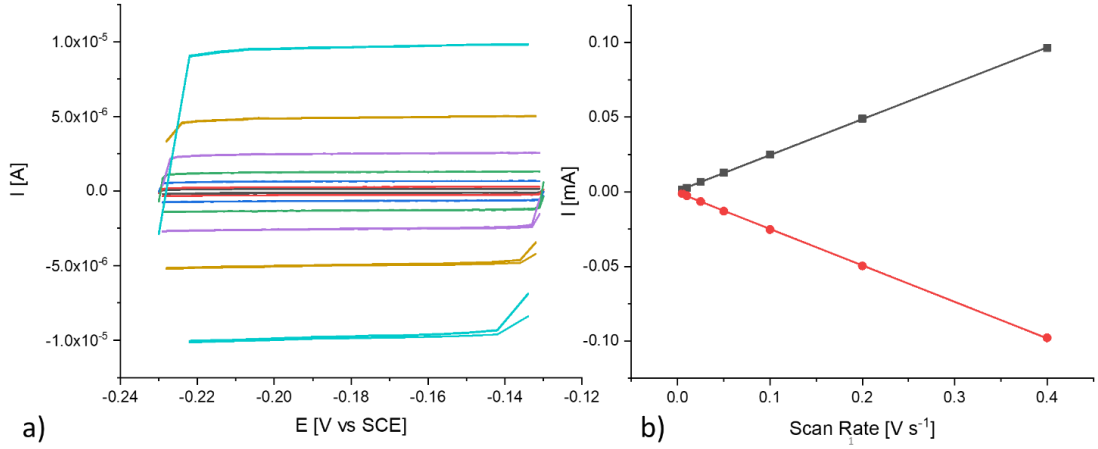

Figure 3_ 3: a) Double–layer capacitance measurements to determine ECSA for TC support from CV in 1 M NaOH. Cyclic voltammograms were measured at the following scan rates: 0.005 (black line), 0.01 (red line), 0.025 (blue line), 0.05 (green line), 0.1 (purple line), 0.2 (dark yellow line), and 0.4 V s^{-1} (light blue line). (b) Cathodic (red circle) and anodic (black square) currents measured at the OCP value plotted as a linear function of the scan rate.

The electrochemically active areas (ECSAs) of four different supports were evaluated in 1 M NaOH employing the protocol introduced by McCrory et al.[12,13]. This method considers the double–layer capacitance of the system from CVs, measuring currents recorded at potentials close to the open circuit value (OCP) (Figure 3_3a which refers to TC as an example). The charging current, I_c, is equal to the product of the double layer electrochemical capacitance (C_{DL}) and the scan rate (ν): $I_c = \nu C_{DL}$. C_{DL} is calculated as the slope of the line obtained by plotting I_c versus the scan rate ν (Figure 3_3b).

[II] Reprinted from Electrosynthesis and characterization of Layered Double Hydroxides on different supports. E. Musella, I. Gualandi, M. Giorgetti, E. Scavetta, F. Basile, A. Rivalta, E. Venuti, F. Corticelli, M. Christian, V. Morandi, D.Tonelli, Applied Clay Science, 2020, 105949.

The ECSA value is obtained by dividing C_{DL} by the specific capacitance of the sample (Cs), which is reported by McCrory for 1 M NaOH (0.040 mF cm^{-2}). In all cases investigated, the same geometrical area has been considered. The highest ECSA was registered for Grafoil, with a value of 5 followed by TC, NiF and CC with 3, 0.45 and 0.4, respectively.

Moreover, the contact angle was evaluated. The ability to evaluate the wetting of solids by liquids is an important feature for many applications, including the capability to coat a surface. Wettability is obtained by measuring the contact angle formed between a liquid drop and a solid surface. The calculated values are reported in Table 3_1, and confirm that the most hydrophilic support is Grafoil, whereas the most hydrophobic one is Carbon Cloth. For comparison, literature values for contact angles are reported in the same table: the results obtained are quite in line with what previously stated.

Table 3_ 1: Values of contact angle for the analysed supports

	G	**CC**	**NiF**	**TC**
Value	82 ± 2	140 ± 1	110 ± 7	127 ± 6
	75 ± 4 [14]	144.7 ± 0.5 [15]	> 120 [16]	135± 5 [17]

Electrochemical deposition and characterization of LDHs

Independently of the synthetic approach chosen, the experimental conditions were varied in order to obtain a LDH film which displayed the highest reproducibility, evaluated through the CV characterization. The electro–synthesis was carried out on the above–mentioned supports, and parameters such as the scan rate and the potential window were investigated for the potentiodynamic approach, whilst only the applied potential for the potentiostatic one. In the latter case, time was not considered as a variable and thus was set at 30 s because the concentration gradients hinder the control of cations ratio in the final material when a long potential pulse is applied[9], as already said. It is worth repeating that the electrochemical synthesis involves the reduction of a nitrate solution, which is dominated by a strong kinetic control where the rate of the electrochemical reaction strongly depends on the activity of the electrode surface: in particular, the presence of defects can affect the rate of these processes. As already said, even small variations of the electrode surface can significantly alter the LDH deposition: therefore, a very robust procedure is necessary to obtain reproducible results

during the electrosynthesis. The deposition curves recorded during the synthesis of the Co/Al–NO_3 and Ni/Al–NO_3 LDHs are displayed in Figure 3_4. In all cases studied, the absolute highest current has been observed for the NiF support independently of the LDHs deposited, followed by CC, G and TC.

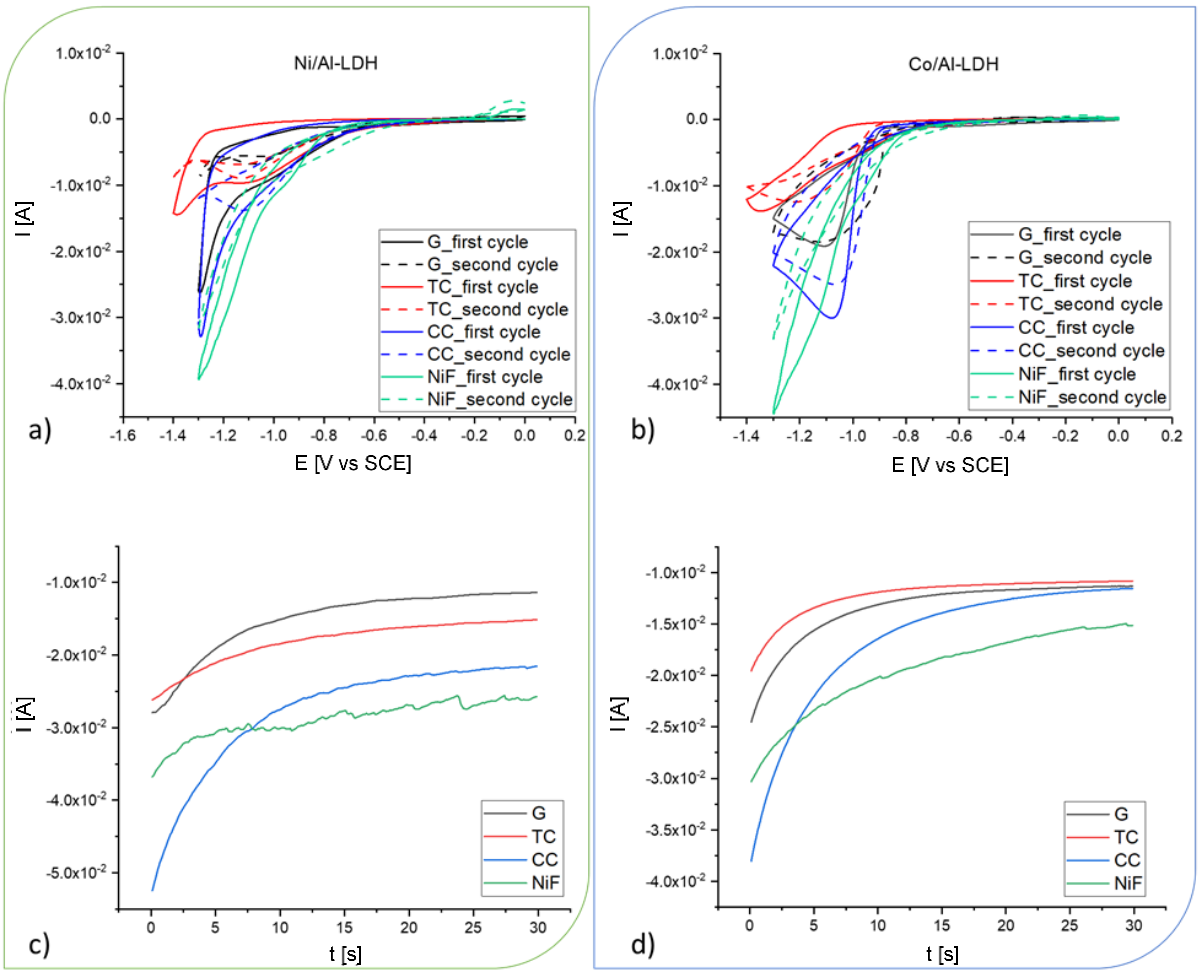

Figure 3_ 4: Comparison between the electrosynthetic approaches. (a) potentiodynamic protocol for Ni/Al–LDH, and (b) for Co/Al–LDH (c) potentiostatic protocol for Ni/Al–LDH and (d) for Co/Al–LDH. The parameters for the deposition are reported in tables 2.2 and 2.3. Total concentration of cations is 30 mM and the ratio between M(II) and M(III) is 3 to 1.

The two approaches were used to modify the four supports and the reproducibility of the procedures was tested by evaluating the peak currents associated with the redox signal of metal centres (Figure 3_5 a,b). The typical peaks, observed in the potential window between +0.35 and +0.6 V are related to the quasi reversible redox couple Ni(III)/Ni(II). The partial irreversibility is due to the oxidation of the Ni(II) centres to Ni(III), characterized by a cooperative Jahn–Teller effect, which could induce a chemical/structural instability[18].

The Co/Al–LDH, instead, is supposed to undergo the reactions 9–10 (Figure 3_5 c,d)[19]:

9. $Co(II)\text{-}LDH + OH^- sol \rightarrow Co(III)(OH)\text{-}LDH + e^-$
10. $Co(III)(OH)\text{-}LDH + OH^- sol \rightarrow Co(IV)(OH)\text{-}LDH + e^-$

The Co based LDH coating displays a broad feature due to the closeness of the formal potentials of the reactions 9 and 10, which hinders the resolution of the two peaks. Anyway, the behaviour can be considered quasi reversible since the ratio of the anodic to the cathodic charge of the feature is very close to 1. Figures 3_5 a − d show the CVs relevant to the optimized procedures to obtain the best results in terms of reproducibility of the electrochemical signal for the CC support. Generally, the potentiostatic deposition exhibits the lowest robustness independently of the support adopted, as it does not allow for a fine control of the OH^- production, and, consequently, of the amount of precipitated LDH. On the other hand, when the synthesis is performed by the potentiodynamic procedure, the results display good reproducibility with a relative standard deviation of the CV area always below 10%, and often less than 5% (as displayed in figures 3_5 e, f). Moreover, the current intensities and CV areas recorded for the potentiodynamic syntheses are higher than those of the potentiostatic one, which means that a higher amount of material has been deposited. Therefore, it is clear that the potentiodynamic approach is more satisfying in all the cases studied. In addition, it can be inferred that the reproducibility is mainly affected by the nature of the substrate and not by the nature of the bivalent cation present in the brucitic layers since a univocal trend is recognizable for both LDHs. The effect of the substrate is again evident comparing the characterization signals of LDHs (Figures 3_5 g, h). In the case of films obtained with the dynamic syntheses, which are shown in the figures, the same current trend recorded for the deposition curves is observed: the highest current intensities are measured for the NiF support independently of the LDH deposited, followed by CC, G and TC. Finally, it is possible to argue that the main contribution to the rate of the electrochemical deposition reaction is due to the activity of the electrode surface, independently of the synthetic strategy adopted.

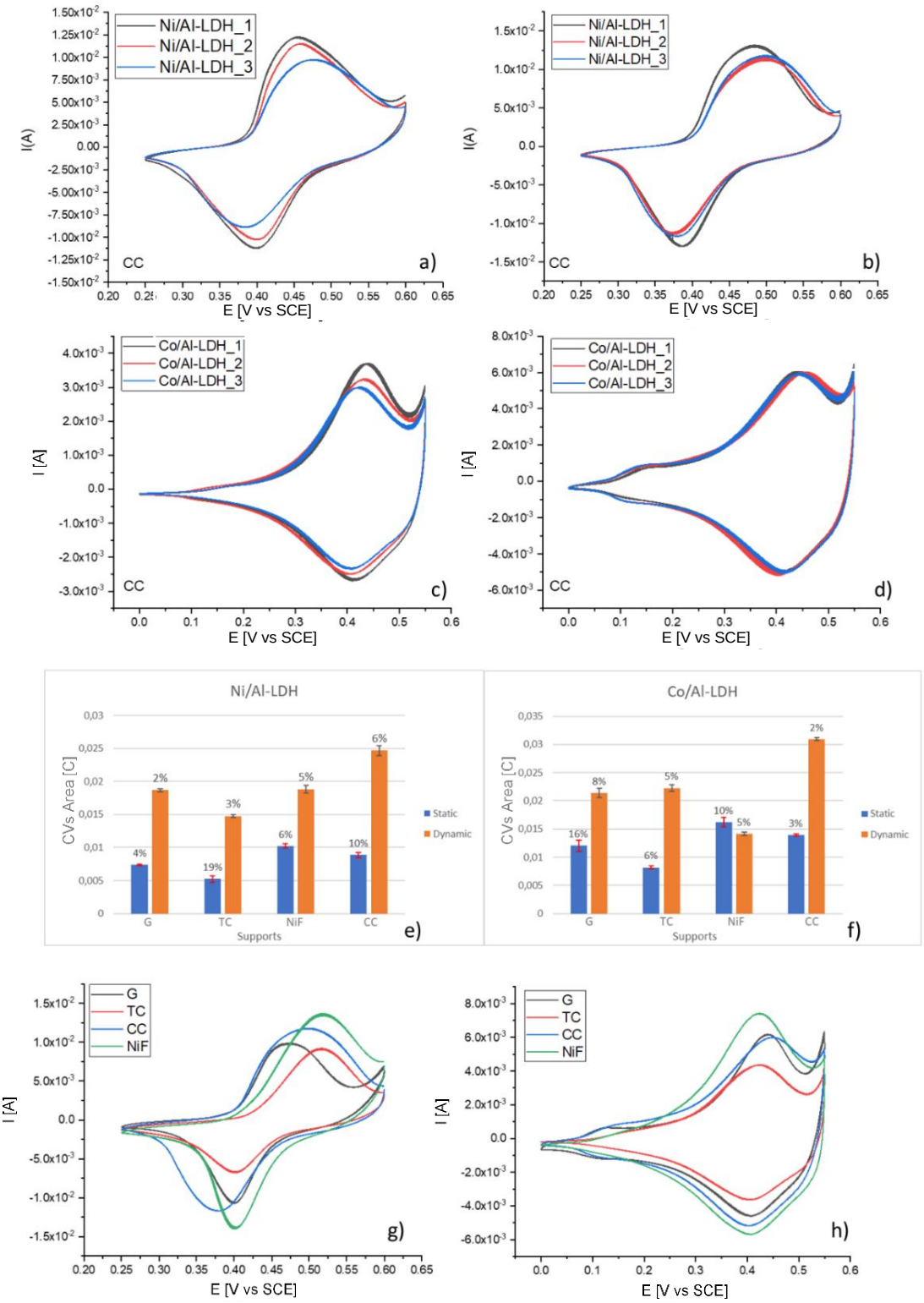

Figure 3_ 5: Comparison of CVs recorded at 0.01 V s^{-1} for the electrosynthetic approaches in 0.1 M KOH. (a) potentiostatic protocol for Ni/Al–LDH, (b) potentiodynamic protocol for Ni/Al–LDH (c) potentiostatic protocol for Co/Al–LDH (d) potentiodynamic protocol for Co/Al–LDH. (e) areas with ***relative standard deviation*** *for Ni/Al–LDH (f) areas with* ***relative standard deviation*** *for Co/Al–LDH (g) comparison among supports for Ni/Al–LDH_D, and (h) for Co/Al–LDH_D*

Morphologies

The morphology of the LDH films has been investigated by means of FE–SEM (Figure 3_6). Figures 3_6_1–4a show the micrographs of the bare substrates. These images have been recorded at a lower magnification (the length scale, 100 µm, is shown) to highlight the bulk structures than the images of the LDHs (the length scale, 1 µm, is shown) to gain major details of film morphologies.

Grafoil displays a wrinkled surface, which is typical of graphite sheets (Fig. 3_6_1a). In fact, it is produced from natural or synthetic flaky graphite by means of an oxidizing agent to form a compound with and between the layers of the graphite structure constituting the particles. Subsequently, heating at high temperatures abruptly produces its rapid expansion. Defects, as wrinkles and folded graphite layers, are clearly shown (bright lines in the image)[20] as well as impurities and contaminants (round shaped bright particles).

Toray Carbon Paper is made of carbon fibres stacked and inter–crossed together (Figure 3_6_2a). Its structure is very complex: three different areas are displayed, where two solid regions and voids appear. One solid region consists of long, thin randomly distributed fibres. The other one looks like a thin sheet binding the fibres of the paper. These fibres are supposed to be good electron conductors; hence they are typically employed to transport electrons to and from the layers[21].

Carbon Cloth is a woven textile material consisting of carbon fibres oriented in two directions, as shown in Figure 3_6_3a. It can be described as a twill weave and it looks like a wicker basket with good conductivity[22].

Figure 3_6_4a shows that the Nickel Foam has a 3D, cross–linked grid structure, with considerable and uniform wrinkles on its surface. This porous skeleton should, in principle, provide electrolyte accessible channels for ion transportation, and shorten the distance for ion diffusion[23].

As far as the LDHs films are concerned, we can say that when the potentiodynamic approach is employed, the substrate is homogeneously covered, and no detachment of the film is highlighted in any case, viceversa if the potentiostatic synthesis is performed the deposit shows breakages and detachments.

When Grafoil is the support, a nanostructured film is obtained, which can be described as highly homogeneous and compact with a thickness of 0.8 – 1 μm for the potentiodynamic synthesis, and of 500 nm for the potentiostatic one (Figure 3_6_1 b–e). In the case of Toray Carbon Paper (Figure 3_6_2b–e) and Carbon Cloth (Figure 3_6_3b–e), the classical desert rose structures are visible for both syntheses. However, in the case of 3_6_2c and 3_6_2e the morphology is not the same throughout the deposit (static synthesis) and, in particular, the substrate is not homogeneously covered. In all cases, the film is nanostructured with thicknesses ranging from 300 to a maximum of 500 nm. When Nickel Foam is employed as a substrate, a great variety of morphologies are recorded (Figure 3_6_4b–e). A "desert rose" like morphology appears only in the case of Co/Al LDH synthesized via the potentiostatic route while the potentiodynamic one gives rise to a film which is very compact with nanosized particles. The synthesis of Ni/Al LDH on this substrate generates a poorly resistant film, which tends to show grooves and cracks in the case of potentiostatic synthesis. With the potentiodynamic one, instead, spherical nanometric particles are observed. Thicknesses are around 1–1.5 μm for the potentiodynamic synthesis, while for the potentiostatic one they are around 700 nm. In general, the thickness values furtherly confirm that a lower amount of LDH is deposited with the potentiostatic method. For the supports characterized by the highest contact angles (CC and TC) the predominant morphology is the "desert rose". This result is explicable with the weak interactions between the polar brucitic layers (which can be easily assumed similar to water) and the hydrophobic surface of these supports which induces a directional growth of the deposit toward the solution bulk.

As to the potentiodynamic approach, the deposits with the highest thickness are obtained when the support is NiF, while the thickness decreases in the following order: G, CC and TC. This result is in good agreement with the current values recorded during LDHs deposition and with the CV characterization curves: in fact, the current intensities are usually related to the amount of material.

Elemental analysis was also carried out by EDS for all the electrosynthesised films (spectra not reported). The presence of the expected elements (Co/Al/O and Ni/Al/O) plus carbon coming from the substrates was evinced. The obtained results, expressed as M(II)/M(III) ratios, are shown in Table 3_2.

Table 3_ 2: Molar M(II)/M(III) ratios of the electrosynthesised LDHs

	Ni/Al_D	**Ni/Al_S**	**Co/Al_D**	**Co/Al_S**
G	3	5	3	4
TC	2	1	2	1
CC	3	5	3	3
NiF	–	–	4	1

In the case of NiF, it is not possible to distinguish the Ni coming from the substrate and the one coming from the deposit, and this is the reason why the ratio M(II)/M(III) was not determined. In general, the potentiodynamic synthesis produces films whose compositions are more similar to that of the starting electrolytic solution (M(II)/M(III) = 3). The largest deviations are displayed by the Toray Carbon Paper substrate, even if also in the case of NiF the synthetic bath composition has not been reproduced. To understand these results, it is necessary to remind that LDHs can be deposited by two possible mechanisms. The first involves the precipitation of $Al(OH)_3$ followed by the insertion of the bivalent cation generating the brucitic structure, the second one consists in the direct precipitation of the LDH on the electrode. It is possible to infer that when the M(II)/Al ratio is lower than 3, the deposition follows the first mechanism, but the insertion of M(II) is not efficient, and Al amount is higher than expected.

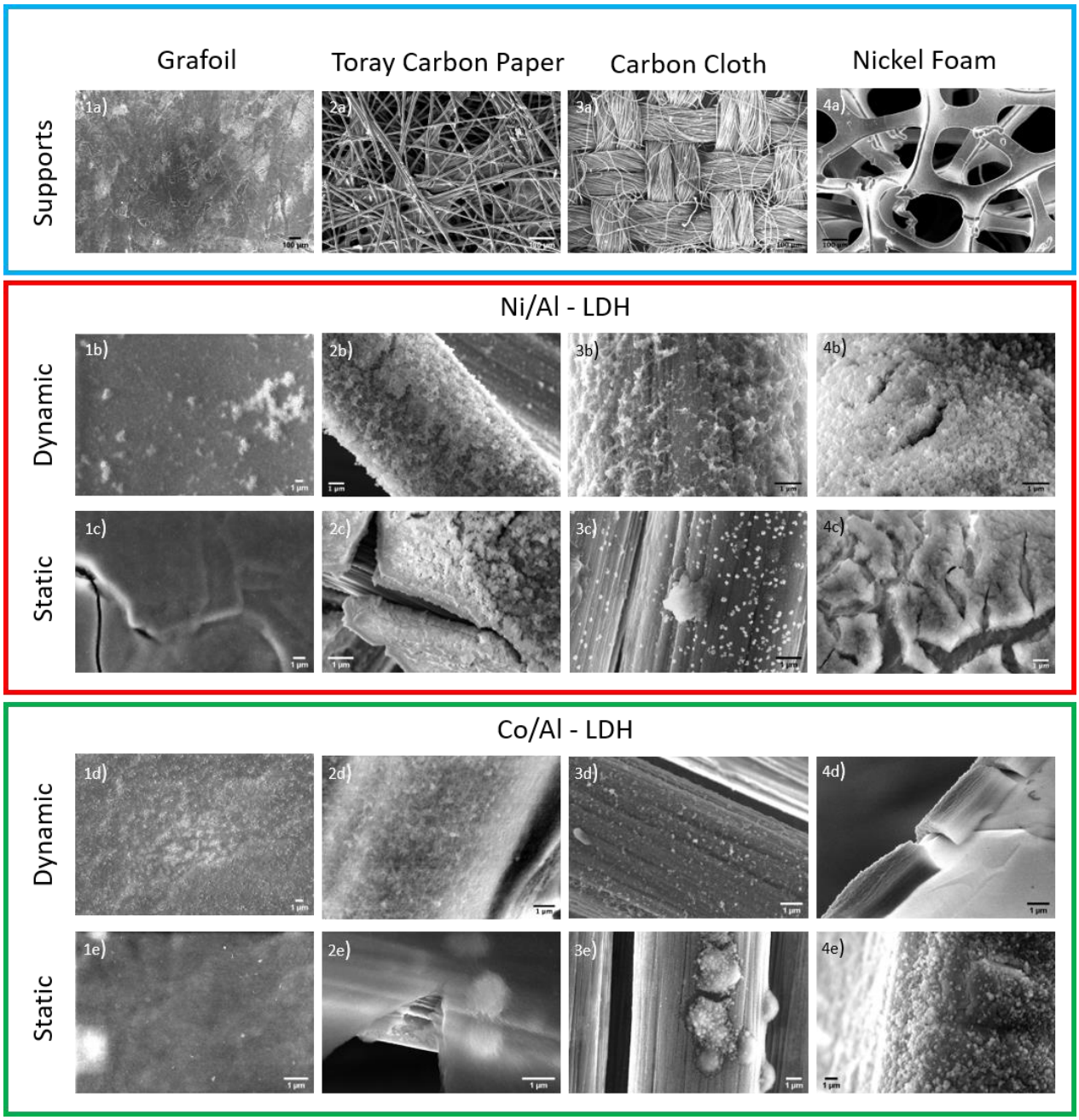

Figure 3_ 6: SEM images at different magnifications of all analysed samples. Columns are numerated from 1 to 4 and are related to the kind of support employed. Rows are numerated from b to e and are related to LDHs and the synthetic procedure, with the exception of the first row which shows the images of the bare supports. (1a) G (2a) TC (3a) CC (4a) NiF. (1b) Ni/Al–LDH_D@G (2b) Ni/Al–LDH_D@TC (3b) Ni/Al–LDH _D@CC (4b) Ni/Al–LDH_D@NiF. (1c) Ni/Al–LDH_S@G (2c) Ni/Al–LDH_S@TC (3c) Ni/Al–LDH_S@CC (4c) Ni/Al–LDH_S@NiF. (1d) Co/Al–LDH_D@G (2d) Co/Al–LDH_D@TC (3d) Co/Al–LDH_D@CC (4d) Co/Al–LDH_D@NiF. (1e) Co/Al–LDH_S@G (2e) Co/Al–LDH_S @TC (3e) Co/Al–LDH_S@CC (4e) Co/Al–LDH_S@NiF.

Raman and FT–IR Spectroscopies

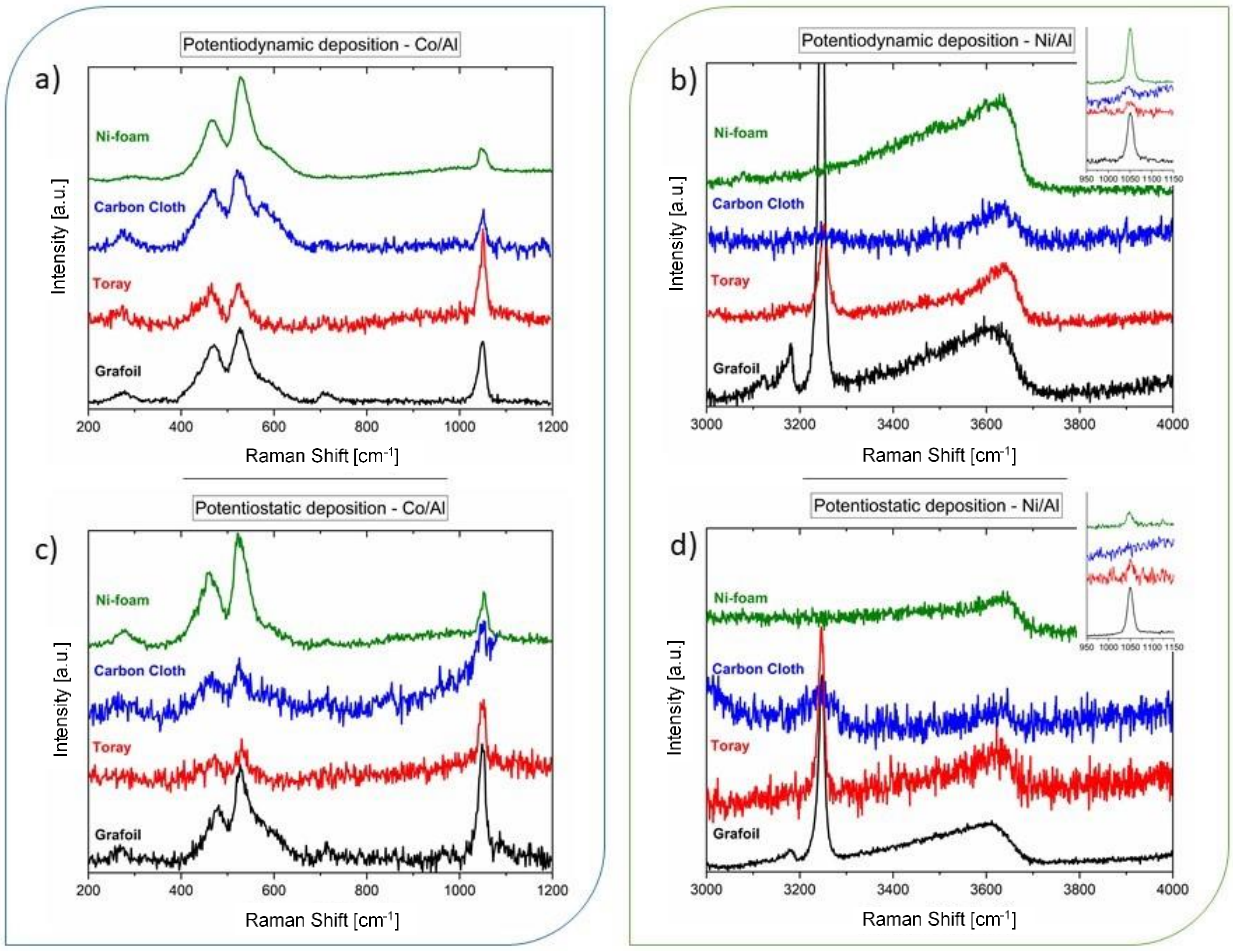

Figure 3_ 7: Raman spectra of (a,c) Co/Al–LDH and (b,d) Ni/Al–LDH on Grafoil, Toray paper, Carbon Cloth and Nickel Foam.

The Raman spectra of the Co/Al and Ni/Al–LDHs on the various substrates and relevant to the two synthetic methods are shown in Figure 3_7 in the wavenumber regions which allow for their identifications. The main spectral features over the wavenumber range 200–1200 cm^{-1} of the Co/Al LDHs are the broad Raman shift at 472 cm^{-1}, with a shoulder at lower wavenumbers, and the sharper bands at 528 and 1050 cm^{-1} (Fig. 3_7 a, c). Much weaker features appear below 300 cm^{-1} and at 711 cm^{-1}. Peak assignments for this LDH have been widely discussed in the literature and we have recently reviewed them[24-28]. The agreement with the data previously obtained confirms the chemical nature and the structural characteristics of the deposited material[27,29].

The most relevant spectroscopic feature of the Ni/Al–LDHs samples is the very broad band centred around 3630 cm^{-1} (Fig. 3_7 b, d), in agreement with the literature findings, which corresponds to OH stretching of the $Ni(OH)_2$ [30]. At lower wavenumbers, the only band observed is the nitrate stretching at 1050 cm^{-1}, detected for all LDHs with the exception of the sample obtained by the potentiostatic method on Carbon Cloth, as reported in the inset of Figure 3_7 d. Other spectral peaks are found to belong to the substrate. We can conclude that, independently of the details of the spectral analysis, the Raman measurements efficiently probe the chemical identity of the materials obtained on all the four different supports. Both for Co/Al and Ni/Al–LDHs, the spectra on each substrate are virtually the same and, therefore, we can assume that the structure and the composition of the LDH do not depend on the nature of the support. Generally, for a given support the Raman spectra of the samples prepared by potentiodynamic electrodeposition display a stronger intensity than those obtained by the potentiostatic method. Although a quantitative estimate is not possible, such a behaviour closely mirrors the findings of the morphology study, which suggests that when the potentiodynamic approach is used the obtained film is thicker with a better degree of crystallinity, and the substrate is more homogeneously covered. Nickel Foam and Grafoil are the substrates which yield the most intense Raman signal, again in agreement with the morphology results for these systems.

To further confirm the chemical nature of the sample, IR spectra were also performed (Figure 3_8). The bands below 800 cm^{-1} are assigned to the bending vibrations of metal–oxygen (M–O)[31]. The ν_3 stretching mode of nitrate appears centred at 1343 cm^{-1} as the strongest band of the IR spectrum of both Co/Al and Ni/Al–LDHs. A symmetry lowering of the intercalated anion, the presence of defects or of different geometries or, finally, contaminations of other anions, can explain the shoulders at 1300 and 1390 cm^{-1} [29]. A small peak at 1630 cm^{-1} may be due to C=C vibrations resulting from graphitic domains of graphene and bending vibration of H_2O[32].

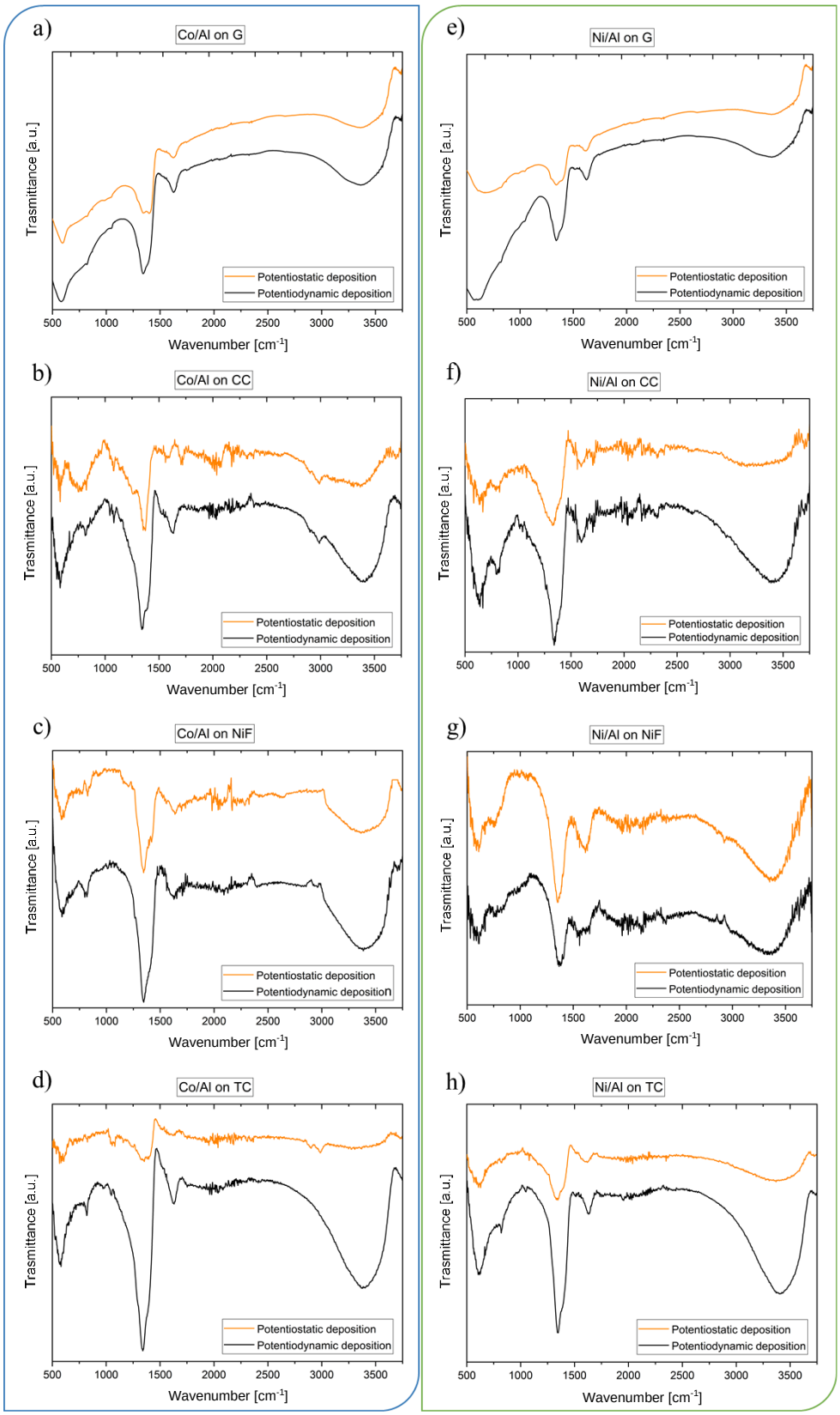

Figure 3_ 8: Infrared spectra of Co/Al–LDH (left), and Ni/Al–LDH (right) on Grafoil (a,e), Carbon Cloth (b,f), Nickel Foam (c,g) and Toray carbon paper (d,h), both synthesised by the potentiostatic (orange traces) and potentiodynamic (black traces) depositions.

3.1.3 Variation of the LDHs film composition[III]

One of the major drawbacks that must be highlighted for the classically adopted potentiostatic approach is the following: even if the electrolytic bath has a composition for which the M(II)/M(III) ratio is known, the concentration gradients originating during the synthesis hinder a fine control of the final ratio in the deposited material, especially when a long potential pulse is applied[33]. In fact, it is widely accepted[24] that a precise control of such a ratio in electrochemically deposited thin films is difficult, because the kinetic mechanisms might be different, depending on the composition of the electrolytic solution. The cation concentration gradients in the diffusion layer, which are typical of the potentiostatic approach, are strongly reduced when the electrode is biased with a potential that does not stimulate electrochemical reactions, allowing enough time for the concentrations to be restored at the electrode surface. Thus, the control of the M(II)/M(III) ratio should remain dependent on the composition of the electrolytic bath.

In the following section, we have investigated a wide range of concentrations in the deposition bath, with M(II)/M(III) ratios from 1:1 to a 4:1, to verify whether the potentiodynamic method could accomplish the synthesis of Co/Fe– and Co/Al–based LDHs with well–defined molar ratios. The molar ratios have been chosen on the basis of the limits suggested by the literature for LDH phase formation[34]. To the best of our knowledge, no systematic study has been carried out before on the correlation between M(II)/M(III) ratio and composition of the starting solution for any electrochemically synthesised LDHs.

[III] Reprinted from Electrochemical Approach for the Production of Layered Double Hydroxides with a Well-Defined Co/Me[III] Ratio. Elisa Musella, Isacco Gualandi, Erika Scavetta, Massimo Gazzano, Arianna Rivalta, Elisabetta Venuti, Meganne Christian, Vittorio Morandi, Domenica Tonelli, Chemistry – A European Journal, 2019, 25 (71), 16301-16310.

Structural characterization

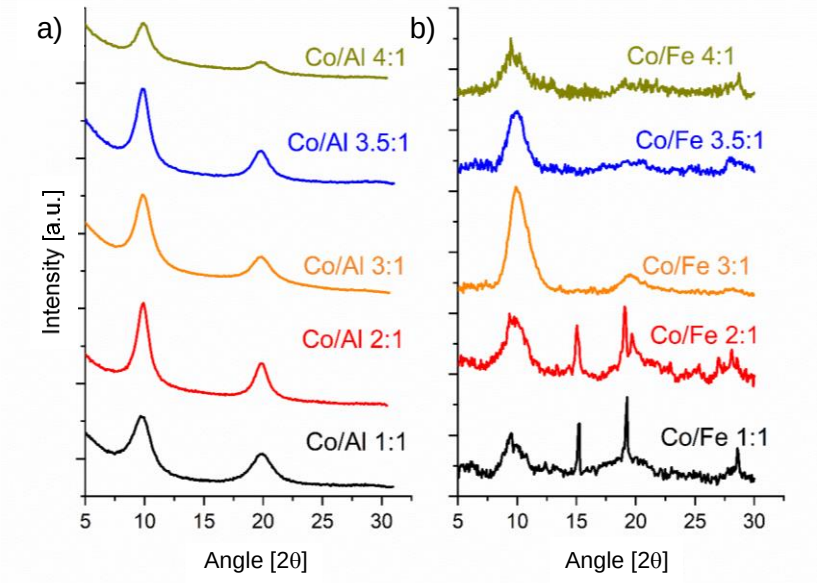

Figure 3_ 9: PXRD patterns of the electro–synthesised LDHs. a) Co/Al and b) Co/Fe in different molar ratios. The analysis was carried out directly on Pt electrodes. The presence of the extremely intense peaks due to substrate diffraction hinders the observation of the full pattern. The two 003 and 006 reflections of LDH–like phase are detectable as they are the most intense and furthermore, they could also be strengthened by a preferential orientation effect due to deposition of 00l layers on the electrode surface.

With the aim to verify the structure of the LDHs, Powder X–Ray diffraction (PXRD) analysis has been carried out directly on the electrodes. The patterns of all Al based samples, reported in Figure 3_9 a, show the main peaks typical of LDH phase, indexed as 003 and 006 reflections[35]. On the contrary, for Fe based materials reflections are definitely less evident. To enhance the diffraction effects of LDH phase, patterns are plotted in Figure 3_9 b after the background subtraction. Samples Co/Fe 2:1 and Co/Fe 1:1 show in addition sharp peaks due to segregation of iron oxide/hydroxides. Peak positions are substantially the same for all the samples, and corresponding to an interlayer of 0.89 nm; the widths, used as markers of structure quality, are broader in iron containing samples, as reported in Table 3_3. The size of the coherent domains as calculated by the Scherrer formula along the c–axis direction is very small and is equivalent to about three–unit cells (c= 2.65 nm) for aluminium and two cells for iron, respectively. This evidences a lower ability of Co/Fe system to pack into hydrotalcite like layers.

Table 3_ 3: peak width measured on the reflection 003 and size calculated by Scherrer equation.

	Co/Al		**Co/Fe**	
	FWHM (°)	Size (nm)	FWHM (°)	Size (nm)
1:1	1.3	7	2.1	4
2:1	1.2	7	1.9	5
3:1	1.3	7	1.8	5
3.5:1	1.2	7	2.1	4
4:1	1.6	6	2.1	4

Morphological characterization

The morphological characterization of the LDHs electro–synthesised on Grafoil was performed using FE–SEM. All the supports appeared homogeneously covered and no detachment of the film was observed. A more thorough investigation displayed different compactness and thicknesses of the coatings. Figure 3_10 illustrates the differences among the morphologies of the materials based on M(II)/M(III) different molar ratios. In the Co/Al LDHs, the nanoparticles appear spherical and display a larger size than those of Fe based LDHs. When the Co/Al molar ratio is 1:1 (Figure 3_10 a), the morphology consists of well–defined spherical small particles (about 20 – 40 nm). Co/Al LDHs 2:1 and 3:1 (Figures 3_10 c and 3_10 e, respectively) are quite similar: they result in a real compact structure and the particles are fused each other. The Co/Al 3.5:1 (Figure 3_10 g) shows a more complex morphology consisting of a flower–like architecture growing on a more compact LDH structure (similar to those relevant to the 2:1 and 3:1 ratios). Finally, Co/Al 4:1 (Figure 3_10 i) shows spherical nanoparticles with a diameter of about 40–50 nm. As to the Co/Fe LDHs (Figures 3_10 b, d, f, h, l), the films present a different and somehow more porous morphology which leads to a minor compactness with respect to the Co/Al LDHs. Nevertheless, all the electrodeposited films are uniform, and show a high compactness in depth, with the particles that still have the spherical morphology discussed above, but appear almost fused each other in all cases studied, with no noteworthy differences related to the molar ratios.

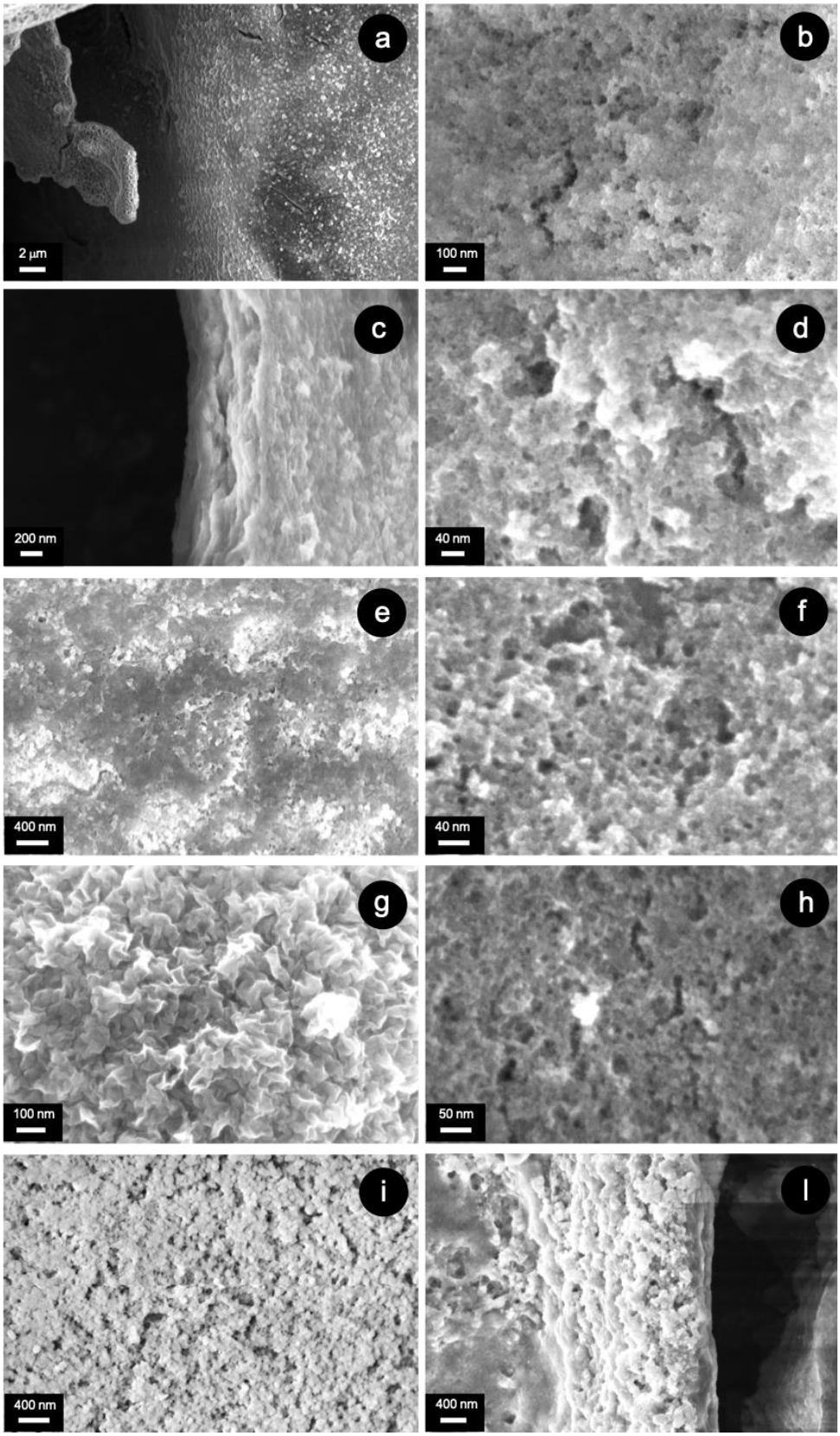

Figure 3_ 10: SEM images of a) Co/Al 1:1, b) Co/Fe 1:1, c) Co/Al 2:1, d) Co/Fe 2:1, e) Co/Al 3:1, f) Co/Fe 3:1, g) Co/Al 3.5:1, h) Co/Fe 3.5:1, i) Co/Al 4:1, l) Co/Fe 4:1

The LDH films were also characterized both by semi–quantitative SEM/EDX analysis (Figure 3_11) and by MP–AES experiments to determine the M(II)/M(III) atomic ratios. The results of the MP–AES experiments are reported in Table 3_4. The values resulting from the two techniques are quite similar, close to the molar ratio of the salts present in the electrolytic solutions used for the syntheses, and compatible with a LDH stoichiometry. This result suggests that it is possible to precisely control the composition of the Co–based LDHs electrosynthesised by the newly proposed potentiodynamic method.

Table 3_ 4: Estimated M(II)/M(III) ratio from AES.

	Ratio				
Co/Al–LDH	**1**	**2**	**3**	**3.5**	**4**
AES	1.13 ± 0.05	2.22 ± 0.08	2.98 ± 0.01	3.67 ± 0.02	4.13 ± 0.03
	Ratio				
Co/Fe–LDH	**1**	**2**	**3**	**3.5**	**4**
AES	0.93 ± 0.03	1.92 ± 0.06	3.07 ± 0.02	3.49 ± 0.06	4.57 ± 0.07

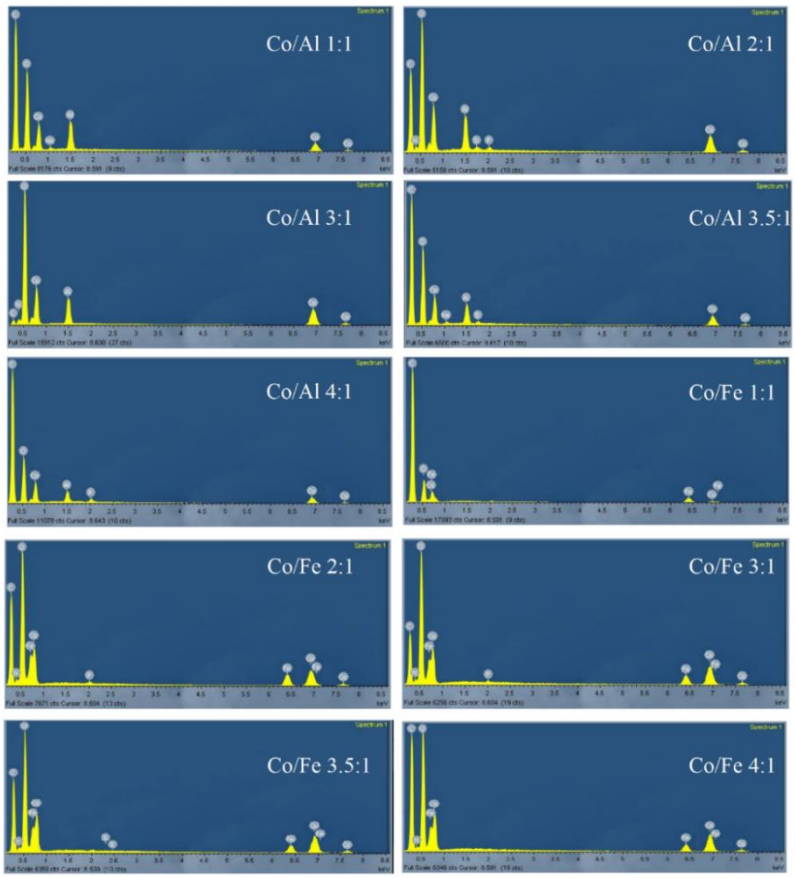

Figure 3_ 11: EDX spectra of all sets of samples.

Raman and FT–IT spectroscopies

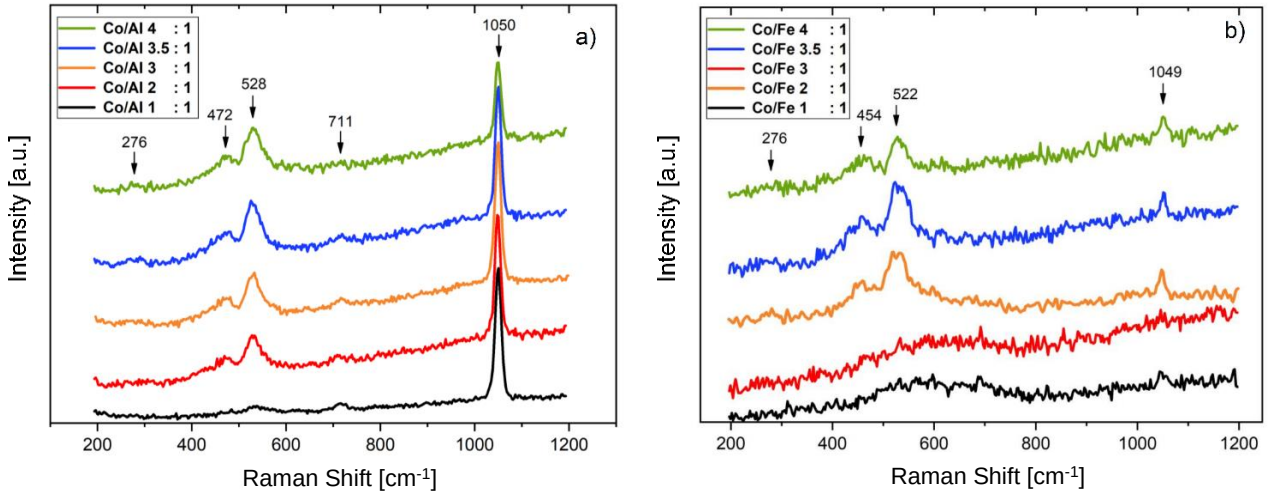

Figure 3_ 12: Raman spectra of the Co/Al a) and Co/Fe–LDHs b) in the 200–1200 cm^{-1} wavenumber region.

Figure 3_12 shows the Raman spectra of the Co/Al (a) and Co/Fe–LDHs (b) in the 200–1200 cm^{-1} wavenumber region, where information about the anions intercalated in the structure and the framework vibrations can be obtained. The main features of the Co/Al LDHs are the band around 472 cm^{-1}, with a shoulder at lower wavenumbers, and the stronger bands at 528 and 1050 cm^{-1}. Weaker features appear at 711 cm^{-1} and below 300 cm^{-1}. Even though in the literature[24,36,37] there is no general agreement about the assignments of the bands at 472 and 528 cm^{-1}, they can be assumed to be originating from the MOM linkage in the structural units of LDHs, with shifts depending on the nature of the cation[34]. In particular, the intensity of the one at higher frequency, described as a lattice vibration of the brucite octahedral layers[39], has been related in a number of systems[39,40] to the degree of crystallization. Such a band appears in all the Co/Al LDHs with almost constant intensity, with the only exception of the 1:1 LDH spectrum, dominated by the ν_1 nitrate vibration (vide infra). This is likely an indication of a permanence of the crystal structure along the series. Also in the IR spectrum (Fig. 3_13 a), strong lattice vibration bands, describing cation–oxygen motions, are observed below 700 cm^{-1} [18]. The Raman band at 1050 cm^{-1} is assigned to the ν_1 symmetric stretching of the intercalated nitrates. Accordingly, its intensity has been found to decrease proportionally to the Co/Al ratio, as a result of the changing content in the divalent cation. The same trend has been detected for the signal at 711 cm^{-1}, although less evident due to its lower intensity, confirming the assignment of this band to

an in–plane bending of the nitrate ion. Note that the ν_3 stretching mode of the nitrate appears centered at 1343 cm^{-1} as the strongest band of the IR spectrum of the Co/Al LDHs (3_13 a, c). A symmetry lowering of the intercalated anion, the presence of defects or of different geometries or, finally, contaminations of other anions, can explain the shoulders at 1293 and 1390 cm^{-1}. Also assigned to the intercalated nitrates is the band of the ν_2 bending vibrations at 822 cm^{-1} of the IR spectrum. Like the Co/Al–LDHs, the Co/Fe–LDHs show bands at 454 and 522 cm^{-1} only up to a 3:1 Co/Fe ratio (Figure 3_13 b). This is accompanied by the virtual absence of absorptions due to lattice modes in the same energy range of the IR spectrum (3_13 b, c). Rather than ascribing this evidence to the lack of a specific vibration involving the Co cations, we suggest that this hints to a lower crystallinity of the sample, induced by the distortion effect due to the presence of the iron cation. Also, as a general observation, all the Raman spectra of the Co/Al–LDHs display a stronger intensity with respect to those of Co/Fe–LDHs, regardless of the Co content. Such a behaviour is often related to a higher degree of crystallinity of the system. In agreement with what reported previously[24,27,29], the ν_1 nitrate band at 1049 cm^{-1} is barely detected in any of the Co/Fe LDH samples. In the IR spectrum a broad band centred at 1334 cm^{-1} appears, with a shoulder at 1293 cm^{-1} and a side band at 1395 cm^{-1}. As previously noticed for the Co/Al LDHs, the presence of more peaks can be interpreted as a symmetry lowering of the nitrate ion and reflects the occurrence of defects. However, also the signals of other possible intercalating anions should fall in this interval, so that the contamination of carbonate and hydroxide ions cannot be ruled out.

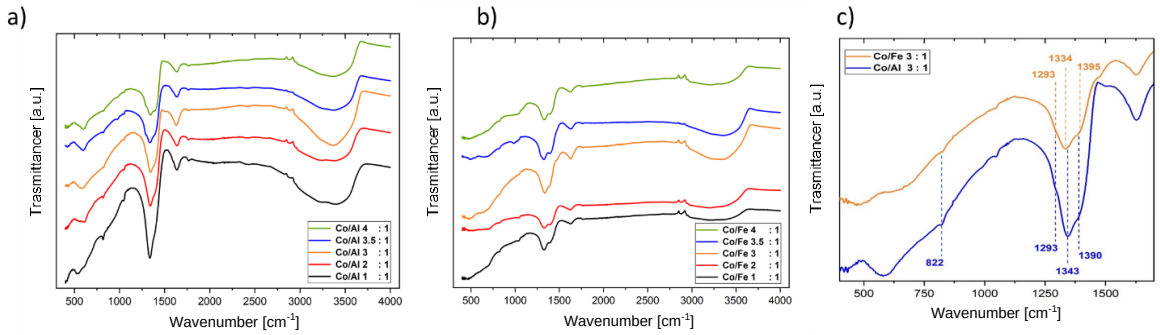

Figure 3_ 13: Infrared spectra of the a) Co/Al and b) Co/Fe–LDHs in the 400–4000 cm^{-1} wavenumber region. c) Infrared spectra in the 400–1700 cm^{-1} wavenumber region of the Co/Al and Co/Fe–LDHs 3:1, displaying the bands used as diagnostic.

Electrochemical characterization

The electrochemical behaviour of the LDHs was studied by CV in 0.1 M NaOH. The stability of each film was evaluated by performing several voltammetric curves, and the responses were superimposable for hundreds of cycles, thus confirming a good adhesion of all materials to the support and a satisfactory stability. Representative CVs are reported in Figure 3_14. The curves are related to Co redox system (reactions 9, 10).

All the CVs of Co/Al LDHs exhibit very broad features both in oxidation and reduction throughout the examined voltage range, from 0 to +0.55 V. This could be characteristic of an electric double layer capacitance or a Faradaic pseudocapacitance. It is possible to observe that, if the amount of Al decreases, i.e., for the Co/Al LDHs 3:1, 3.5:1, and 4:1, a peaks couple in the range of 0 – 0.1 V appears, and the resistive behaviour becomes less evident.

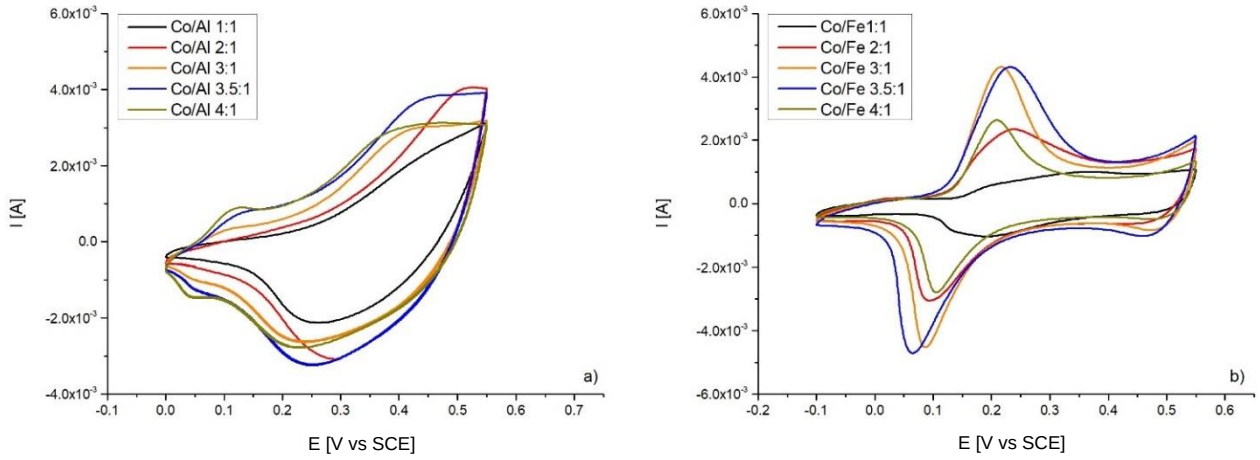

Figure 3_ 14: Electrochemical characterization of a) Co/Al–LDHs set of samples and b) Co/Fe–LDHs set of samples on Grafoil in 0.1 M NaOH.

A possible explanation for this kind of behaviour can be found from the Marcus theory for the variable–range hopping in semiconductors[41]. As already reported by Schuhmann *et al.* for similar systems[24], considering redox–hopping–type conduction and the presence of mixed $Co^{2+/3+}$ valences[42], the use of an electrochemically inactive cation (such as Al^{3+}) in the crystal lattice compromises the redox hopping, and the minimal distance for an electron to overcome would be the distance between two Co ions separated by an Al^{3+} ion. Since this distance is remarkably larger than the one between two adjacent Co ions, the charge–transfer rates slow down. Hence, this feature might indicate that the presence of increasing amount

of Al^{3+} ions suppresses the electrochemical activity by diluting the Co sites in the Co/Al LDHs and making the CV shapes always more resistive.

It is also possible that the presence of Al^{3+} limits the oxidation of Co^{2+} to Co^{3+} since it is not possible for Al^{3+} to reduce itself and, therefore, in order to maintain the structure, not all the Co sites participate to the reaction.

In contrast to Al^{3+}, Fe^{3+} is a redox–active species that can participate in the redox–hopping–type charge transfer with Co[24] and, therefore, the Fe based LDHs display a typical Faradaic and quasi–reversible contribution in the range 0 – 0.3 V, and a very interesting capacitive component up to ~0.55 V. The only exception can be made for the Co/Fe LDH 1:1 that can be better described as a Faradaic pseudocapacitance.

3.1.4 Variation of the interlayer: combining LDHs with nanomaterials[IV]

In this section, we have explored the new protocol for the electrosynthesis of Ni/Al LDH intercalated with electrochemically reduced graphene oxide. The procedure has been optimized by varying the bath composition. The ERGO intercalation has been proven by a comprehensive multi–technique approach demonstrating for the first time the possibility of electrosynthesis of LDH intercalated with big anions.

[IV] Reprinted from Electrosynthesis of Ni/Al layered double hydroxide and reduced graphene oxide composites for the development of hybrid capacitors. E. Musella, I. Gualandi, G. Ferrari, D. Mastroianni, E. Scavetta, M. Giorgetti, A. Migliori, M. Christian, V. Morandi, R. Denecke, M. Gazzano, D. Tonelli. Electrochimica Acta, 365, 137294

Electrosynthesis

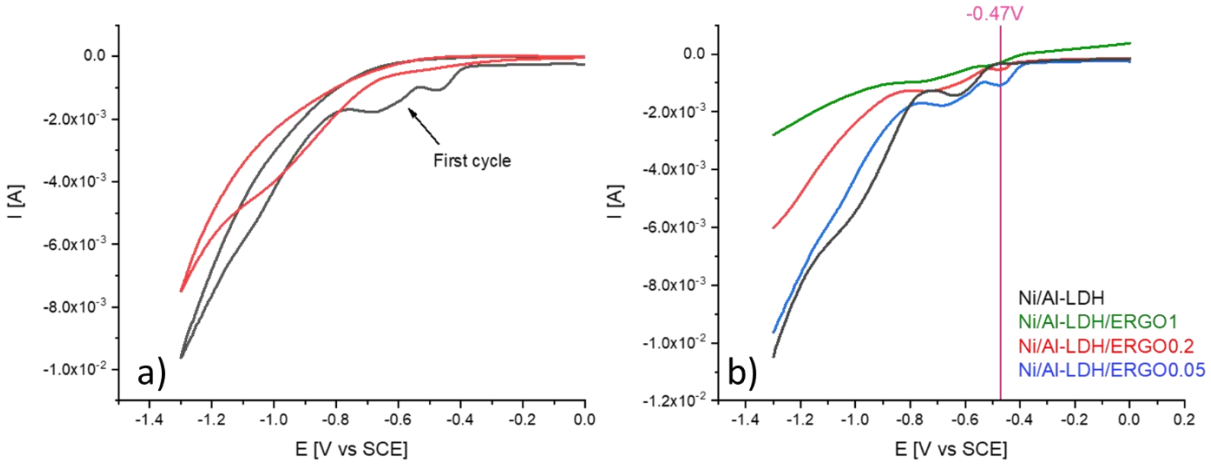

Figure 3_ 15: a) CV curves recorded during the electrodeposition of the Ni/Al–LDH on Pt in the presence of 0.05 mg mL-1 GO concentration. b) Comparison of the first sweeps recorded during the electrodeposition of the Ni/Al–LDH, Ni/Al–LDH/ERGO0.05, Ni/Al–LDH/ERGO0.2, and Ni/Al–LDH/ERGO1.

The LDH/ERGO electrodeposition was performed by applying a variable potential to the electrodes while they were immersed in a solution containing the nitrate salts of the metals Ni^{2+} (or Co^{2+}) and Al^{3+} and GO. The M(II)/M(III) ratio is 3:1. The negative polarization has hereby a dual purpose:

i) to induce the reduction of nitrates and water according to reactions[43] 1 – 7 in Figure 3_1;

ii) to reduce graphene oxide present in the solution in order to restore its conductivity properties.

The voltammograms recorded during the deposition of Ni/Al–LDH/ERGO0.05 are displayed in figure 3_15 a. It is important to highlight that, in the cathodic sweep of the first cycle, it is possible to observe three peaks, two of them already present in the deposition trace recorded for the LDH alone (at about –0.65 and –1 V, figure 3_15 b. The third peak is located at –0.47 V vs SCE, and it can be ascribed to the reduction of GO to ERGO. Moreover, in the first sweeps of all the CVs relevant to the electrosynthesis of the composites, the current decrease is proportional to the quantity of GO in solution (this is also true for the second cycle). In particular, it is reasonable to guess that the reduction of GO competes with the one of nitrates: considering a concentration of 1 mg/mL, the reduction peak at –

0.47 V is barely detectable. Therefore, the argument behind the hypothesis is that in this condition the reduction of the GO does poorly take place and it hinders the nitrate reduction necessary for the pH increase and, therefore, for the LDH electrodeposition. This hypothesis is confirmed by PXRD (see below). Moreover, the molar ratio Ni/Al has been evaluated by means of MP–AES and resulted: 3.03 for the pure LDH, 2.93 for Ni/Al–LDH/ERGO0.05, 1.63 Ni/Al–LDH/ERGO0.2 and 0.95 for Ni/Al–LDH/ERGO1. These data suggest that only in case of the highest GO concentration the Ni/Al ratio is not compatible with a LDH structure. Therefore, it is clear that for the electrosynthesis of a LDH/ERGO composite, it is fundamental to choose the proper GO concentration in solution. In fact, the reduction of GO should interfere as less as possible with reduction of nitrates, thus guaranteeing the adequate pH for LDH precipitation. If this would not occur an amorphous phase containing $Al(OH)_3$, where only a partial insertion of Ni^{2+} has occurred, precipitates on the electrode instead of a LDH.

Structural characterization

The thin films obtained by the potentiodynamic synthesis were characterized by PXRD to confirm the formation of a LDH structure. The diffractograms of all the composite materials are plotted in figure 3_16 a. All of them, except for LDH/ERGO1, display the two typical reflections, indexed as 003 and 006, and reveal good phase formation.

Peak positions are all different one each other. As already reported in literature[31], the intercalation of ERGO into the LDH is confirmed by a decreased interlayer distance. In particular, d values are calculated to be 0.88 nm for Ni/Al–LDH, whilst 0.83 nm for LDH/ERGO0.02 and 0.81 nm for LDH/ERGO0.05. The same trend has been observed, for a Ni/Al–LDH graphene composite synthesized by a chemical synthesis based on layer by layer stacking of the two materials[31].

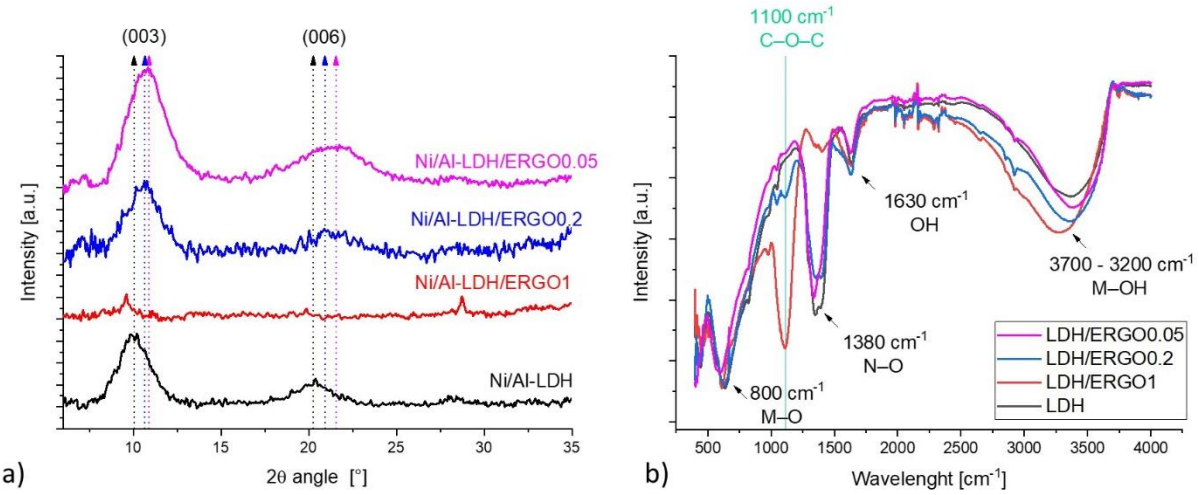

Figure 3_ 16: a) PXRD and b) FT–IR spectra of all set of samples

As stated above, our results might suggest that the lower GO concentration is in the synthesis solution the higher is its degree of reduction and also its interlayer intercalation, due to the strong electrostatic interaction between ERGO and LDH sheets, leading to a thinner spacing between the brucite–like layers. Figure 3_16 b shows that all samples present almost the same absorption peaks in the FT–IR spectra. The relatively strong and broad peak between 3700 and 3200 cm^{-1} is related to the O–H stretching vibration of Ni–O–H, and the broad adsorption peak at 1630 cm^{-1} is associated to the O–H bending vibrations of the interlamellar water molecules due to the formation of hydrogen bonds. The weak bands below 800 cm^{-1} are assigned to lattice vibrations of metal–oxygen (M–O) in the brucite–like layers[25,36]. The band at 1100 cm^{-1} can be ascribed to the epoxy bonding C–O–C, and, therefore, is the most suitable to point out the presence of GO at different extent of reduction[31]. As a matter of fact, it is possible to notice that the intensity of this band increases with GO concentration in the starting solution. Independently from the real structure of the composite Ni/Al–LDH/ERGO this observation leads to furtherly confirm that when the GO concentration is at the highest value (1 mg mL^{-1}) the electrochemical reduction of the oxygen containing functionalities is not so efficient as when the concentration is lower (0.05 and 0.2 mg mL^{-1}), as already discussed in the previous section. A possible explanation to this behaviour can be seen in the low conductivity of graphene oxide itself. In fact, when the GO concentration is the highest, the conductivity of the overall system could be negatively affected, thus requiring a higher overpotential for the reduction occurrence. Moreover, GO might also be adsorbed on the electrode surface causing a decrease

in its active area. The obvious conclusion is that the concentration of 1 mg mL^{-1} is too high for the preparation of a composite LDH/ERGO, since it both hinders the LDH precipitation and the GO reduction. Finally, the absorption bands located at about 1380 cm^{-1} correspond to the stretching vibrations of N–O (nitrate ions) and are present in all the materials, except for LDH/ERGO1, although with different relative intensities[18]. In any case, the presence of interlayer nitrate anions is not in conflict with PXRD data: the reflections are so broad that a contribution of the nitrate could not be neglected. Indeed, also GO has absorption bands[44] at 1387.5 and 1418.8 cm^{-1} and, actually, they are detectable in the spectrum of LDH/ERGO1, so furtherly confirming that, in these synthesis conditions, the GO reduction practically does not occur.

Morphological Characterization

The morphology of the LDH films was investigated by FE–SEM. Figures 3_17 a–d show the images of the electrodeposited thin films coming from the three electrolytic solutions with GO different concentrations. Figure 3_17 a shows that the pure Ni/Al–LDH displays a homogeneous and compact layer with a textured surface due to the very small LDH crystallites (around 40 nm). The thickness of the layer can also be estimated to be around 200 nm. LDH/ERGO1 exhibits a structure typical of a graphitic like nanomaterial on which an inorganic compound has been deposited in a non–homogeneous way. In fact, it is possible only to observe some aggregates of the aluminium rich amorphous material, whose existence has been already widely discussed. The presence of GO, due to the poor reduction, is predominant here. (Figure 3_17 b) At higher magnifications, it can be also observed some inorganic material under a layer of GO. From the cross–sectional image of LDH/ERGO0.2 composite (Figure 3_17 c), it is possible to point out a complex structure. In fact, starting from the electrode surface (bottom) it visible a uniform LDH layer, covered with ERGO flakes on which a thick deposit of LDH has grown, and finally another ERGO sheet on the top. Looking at the thick deposit it is possible to notice the presence of ERGO flakes strongly interconnected with the LDH particles. ERGO is recognizable by its wrinkled surface, which is due to the rearrangements occurring after the removal of the hydroxyl and epoxy functionalities from the GO and the consequent recovery of the conjugated systems during the reducing process. This feature is even more evident in the case of LDH/ERGO0.05

(Figure 3_17 d) where the two materials seem to exhibit the highest interpenetration and ERGO seems to display the highest reduction degree. As far as TEM analysis is concerned (Figure 3_17 e–f), the pure LDH displays again a granular structure in the thin border (Figure 3_17 e), which is typical of this material, and a uniform distribution. In addition, even if the ordered structure is not clearly visible in the image, the Selected Area Electron Diffraction (SAED) pattern shows that two diffraction rings are detected with d=0.25 nm and d=0.15 nm, which furtherly confirms the LDH phase (not reported)[4]. Figure 3_17 f displays Ni/Al–LDH/ERGO0.05 sample: the presence of both ERGO and Ni/Al–LDH is again evident. SAED diffraction pattern (not reported) shows four diffraction rings: d=0.25 nm, d=0.21 nm, d=0.15 nm and d=0.12nm. The rings with d = 0.21 and 0.12 nm (also in the Fast Fourier Transform, FFT, in the bottom left inset) can be indexed as the (1,–1,0) reflection of ERGO (or graphite – like compounds)[45]. Figure 3_17 g reports a phase contrast TEM image recorded on the border of a fragment which clearly displays a layered structure. Several EDS spectra were collected in the thinnest parts on the border. The seven positions are indicated with numbers from 1 to 7. The ratios C_K to Al_K, and C_K to Ni_K counts, as shown in the table, depend on the beam position, suggesting that the layers composition varies. This fact confirms that the compound is made up of layers having a different composition. Summarizing, these data relevant to Ni/Al–LDH/ERGO0.2 and 0.05 support the hypothesis that a layer by layer growth of LDH and ERGO takes place, with also an interpenetration of ERGO sheets inside the inorganic material. Moreover, no nitrogen can be detected in this area, highlighting the nitrate absence.

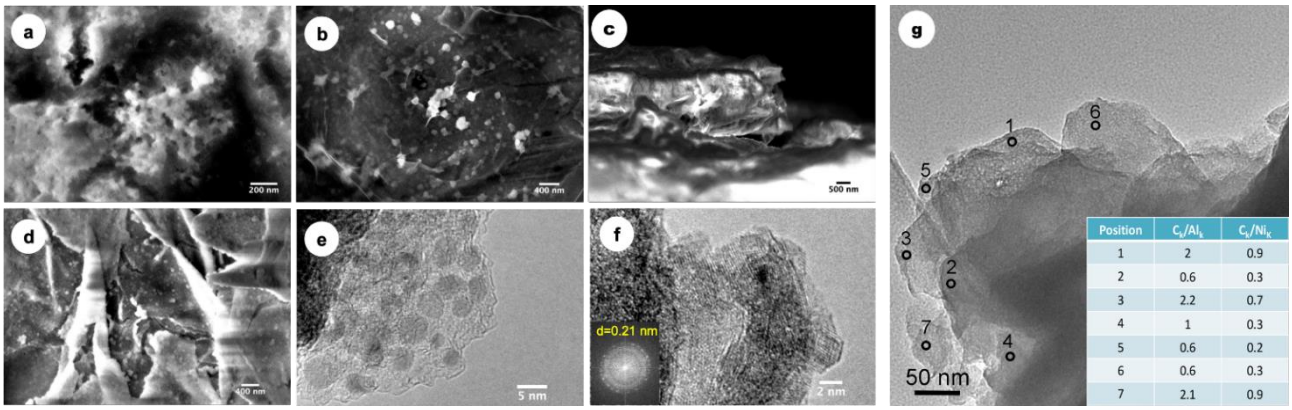

Figure 3_ 17: SEM images of a) Ni/Al–LDH b) Ni/Al–LDH/ ERGO1 c) cross–sectional view of Ni/Al–LDH/ ERGO0.2, and d) Ni/Al–LDH/ ERGO0.05. HREM–TEM images of e) Ni/Al–LDH,

and f) Ni/Al–LDH/ ERGO0.05, inset: SAED pattern of ERGO g) TEM images of Ni/Al–LDH/ ERGO0.05; the open circles indicate the positions were the EDS spectra were collected. In the table the ratios of C_k/Al_k and C_k/Ni_k counts are shown.

XPS Characterization

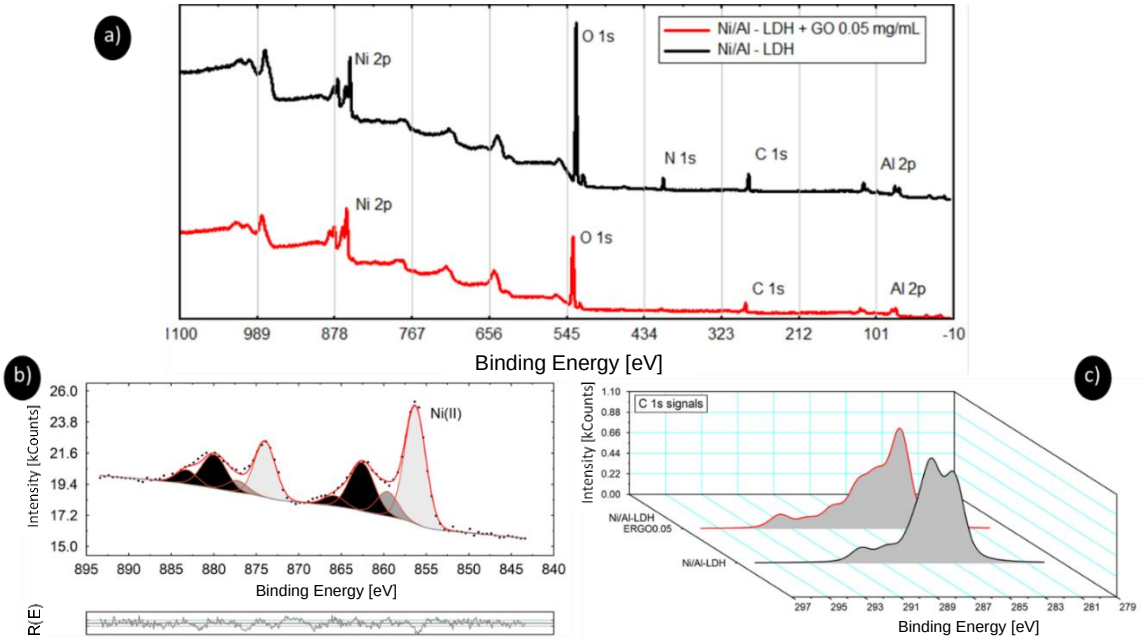

Figure 3_ 18: XPS data of a) normalized survey spectra of Ni/Al–LDH and Ni/Al–LDH/ERGO0.05 b) Ni 2p site of Ni/Al–LDH and c) comparison between C 1s of the pure LDH and the one of LDH/ERGO0.05 composite (spectra have been normalized)

Figure 3_18 shows the XPS survey and high–resolution Ni 2p and C 1s spectra of the pure LDH and the composite Ni/Al–LDH/ERGO0.05. A first difference between the materials can be seen already from the survey spectra: the signal of N 1s is practically absent when GO is present in the electrolytic solution. This should be due to the fact that nitrate is not predominant in the first outer interlayer regions, having been replaced by ERGO. The Ni 2p spectrum exhibits two main peaks at 856.4 and 874.0 eV, corresponding to Ni $2p_{3/2}$ and Ni $2p_{1/2}$, and the satellites. Of course, all Ni 2p peaks are subject to spin–orbit coupling, which produces $2p_{3/2}$ and $2p_{1/2}$ peaks. In the case of $Ni(OH)_2$, the other most important effect is multiplet splitting, which occurs because the unpaired core electron ($2p^5$) couples with the unpaired Ni^{2+} valence electrons ($3d^8$)[42]. The spin–energy separation of 17.6 eV and the main peak located at 856.4 eV (Figure 3_18 b) suggests the presence of Ni^{2+}, in good agreement with previously reported values for $Ni(OH)_2$ [43–46]. The structure can be compared to the one of β–$Ni(OH)_2$,which is isostructural with brucite, $Mg(OH)_2$ [46].

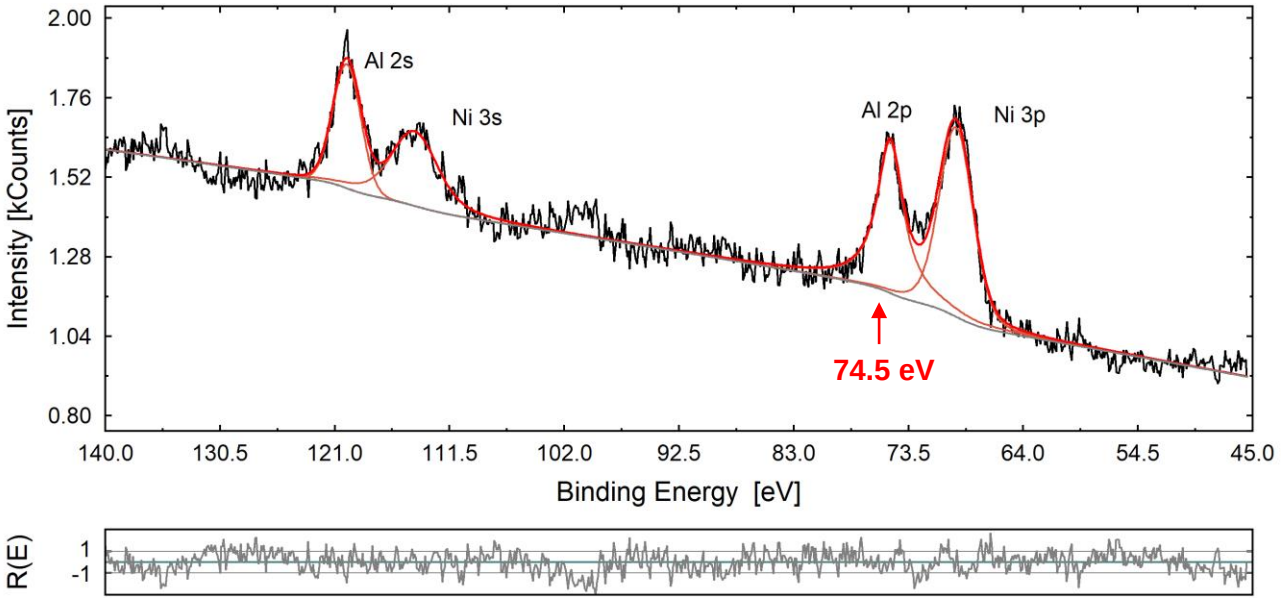

Figure 3_ 19: spectrum displaying the presence of Al 2p and Al 2s peaks in Ni/Al–LDH. The position of Al 2p is 74.5 eV, which is typical al Al^{3+}.

Al 2p detailed spectrum exhibits a peak at 74.5 eV (Figure 3_19), which is in the reported binding energy range of $Al(OH)_3$ [51,52]. In particular, this position is related to gibbsite–type $Al(OH)_3$, which is structured in hexagonal closed packed sheets in which Al cation is octahedrally coordinated by 6 OH groups[51]. All these findings confirm the presence of Ni/Al–LDH. Ni 2p and Al 2p signals show no major difference for the material obtained in the presence of GO or for the pure LDH.

The C1s spectra are expected to show a clear difference for the sample containing or not containing ERGO. As can be seen in Fig. 3_20, this is indeed the case. However, as it is evident from the deconvolution of the peaks into different contributions (Fig. 3_20), both samples exhibit a complex structure. Most of the features correspond to carbon containing contaminations. The clearest evidence for the presence of ERGO is the strong contribution at about 285 eV (characteristic of C–C bonds in sp^2 configuration) but still C–O derived features above 286 eV (and even CO_2 or carbonate species around 292 eV) are present[31,53-55].

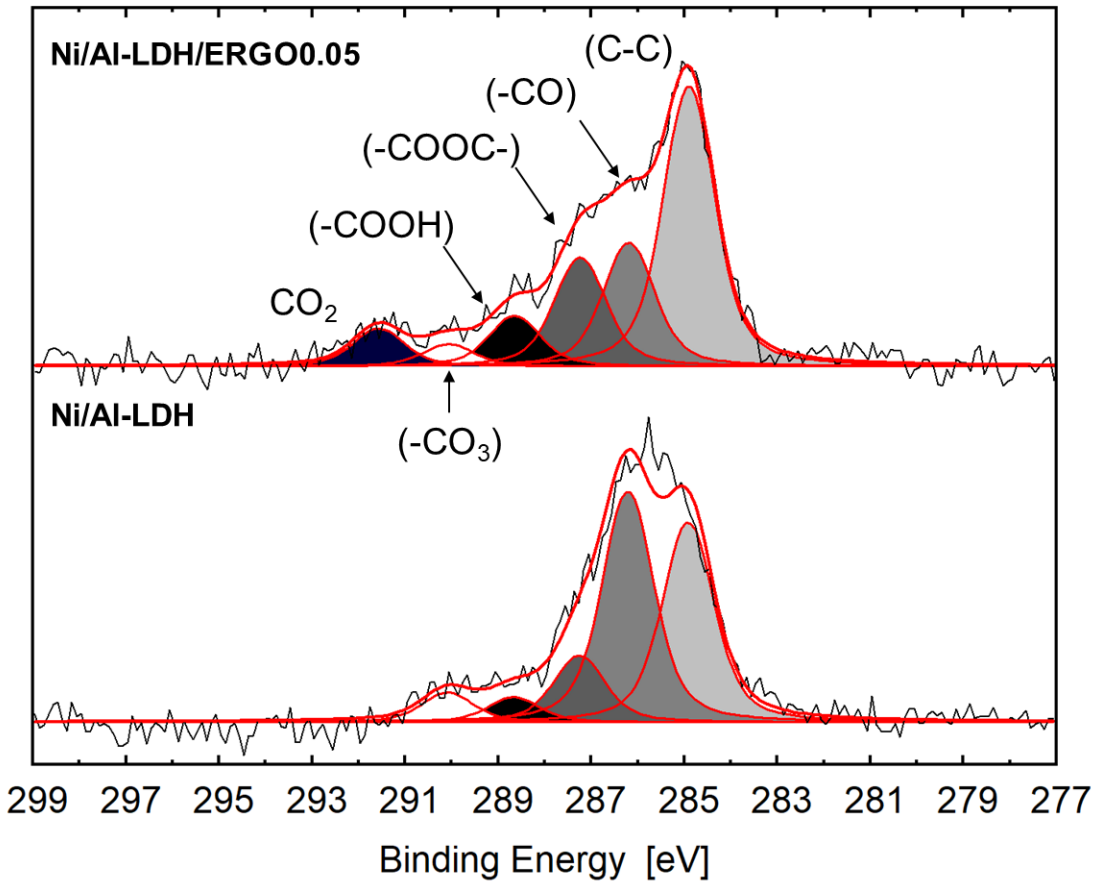

Figure 3_ 20: comparison between C 1s signal of Ni/Al–LDH (bottom) and Ni/Al–LDH/ERGO0.05 (top)

Discussion on the LDH/ERGO structure

On the basis of all the characterization data, the synthesised composites display a peculiar structure that should enhance the overall electrical conductivity. The PXRD data exclude the LDH formation in the case of the composite named LDH/ERGO1. All the observations suggest that the reduction process of graphene oxide, even if occurring with low efficiency at the concentration of 1 mg mL^{-1} (visible from the intense peak of epoxy group in IR spectrum), hinders the reduction of nitrates. The latter is responsible for the precipitation of LDH: as stated before, if the pH increases slowly at the electrode/solution interface, first amorphous $Al(OH)_3$ precipitation takes place and only when all the Al^{3+} has been completely consumed, it is possible for Ni^{2+} to enter the structure. Considering the resulting Ni/Al molar ratio, not compatible with a LDH structure (0.93), it is reasonable to conclude that this pathway has started but the nickel ion insertion in $Al(OH)_3$ has in large extent failed due to the too low pH value reached in the experimental conditions adopted for the preparation of this composite. In the other two cases, PXRD suggests the formation of a poorly crystalline

LDH/ERGO phase, where single ERGO foils are alternated with the brucite layers (from the decreased interlayer distance). However, the reflections are so broad that a contribution of the nitrate presence in the interlayer region might not be neglected. In fact, as evident from IR data, NO_3^- is still present both in LDH/ERGO0.05 and in LDH/ERGO0.2. However, no nitrogen has been detected either by XPS on the outer surface (5–10 nm) of material on the electrode or by EDS analysis. A plausible explanation can be suggested thinking about the electro–synthetic mechanism: it is a complex multistep process. When the fast electrosynthesis is blocked, and thus the production of hydroxyl ions, the still growing film can be somewhere contaminated by intermediate products which cannot be converted into LDHs. Since their structure is amorphous, they might have entrapped some NO_3^- inside. As stated before, the efficiency of the reduction processes increases with decreasing GO concentration in solution, as confirmed both from deposition CVs and from the signal of epoxy–groups in IR spectra. Even though an intensive characterization effort has been performed it is hard to fully explain the two LDH/ERGO composite structures, due to the several competing processes involved in their synthesis. Combining PXRD data, CVs and SEM images, it is possible to highlight two different growth mechanisms. On one hand, ERGO is intercalated in the interlayer of the LDHs, on the other hand, ERGO acts as nucleation center for the growth of the LDH. The lower is the concentration of GO in solution, the higher is the degree of reduction obtained and also ERGO intercalation in the interlayers. It is possible to guess that the predominant mechanism for LDH/ERGO0.05 synthesis is the intercalation, whilst for LDH/ERGO0.2 is the crystallite growth of the LDH on the ERGO flakes. A simplified sketch of the two limit structures is reported in figure 3_21 a and b, respectively.

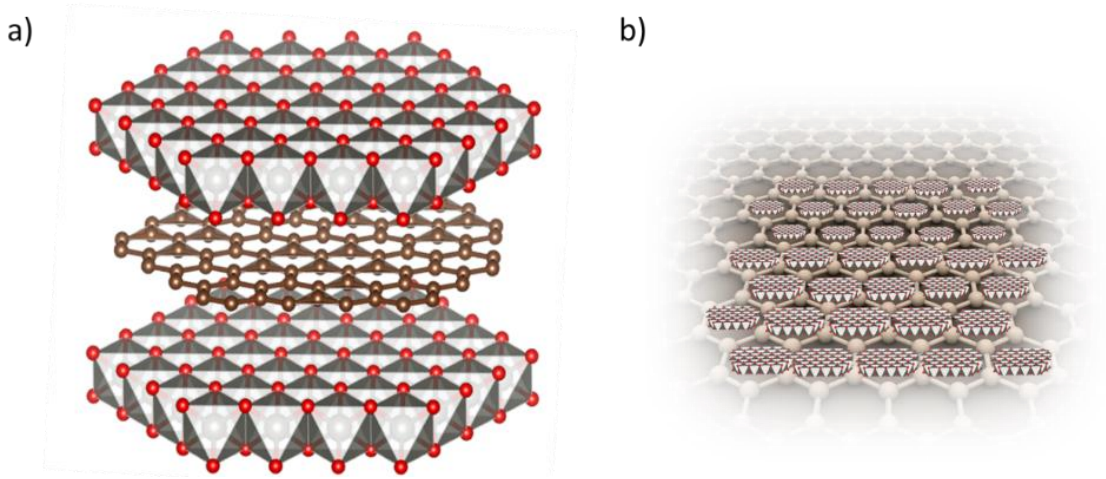

Figure 3_ 21: a) 3D sketch of the structure of ERGO intercalated LDH b) sketch of the structure of LDH growing on ERGO flakes (relative sizes of LDH sheets and ERGO are not respected in the figures)

Electrochemical Characterizations

The CV characterization curves of the pure LDH and the two composites LDH/ERGO are reported in Figure 3_22 a. Cyclic–voltammograms display a typical reversible signal in the potential range between 0.25 and 0.6V, relevant to the redox couple Ni(II)/Ni(III). The presence of ERGO decreases the overpotential needed for the occurrence of Ni(II) oxidation with respect to the LDH alone. In fact, the anodic peak potential (E_{pa}) shifts from 0.52V toward 0.48 V. However, the amount of nanomaterial present in the electrolytic solution used for the synthesis does not seem to affect the performances: just a really low amount of ERGO (0.05 mg mL^{-1}) causes an enhancement of the reversibility of the system, suggesting that a further study on the comparison between Ni/Al–LDH and Ni/Al–LDH/ERGO0.05 can be very interesting. The crucial role of nanomaterials is demonstrated by the difference between the anodic and cathodic peak potentials (ΔE_p) of Ni/Al–LDH/ERGO0.05 that is lower than the value recorded for Ni/Al–LDH, at all investigated scan rates (1, 5, 10, 25, 50 and 100 mV s^{-1}). Since the charge transfer kinetics plays a key role in fast power release, a study was performed to estimate the effect of intercalated ERGO. The LDH is combined with ERGO to increase its charge transfer rate with the electrode surface because ERGO sheets in close contact with the LDH layers enhance the electron exchange between the two materials, so increasing the LDH electrical conductivity.

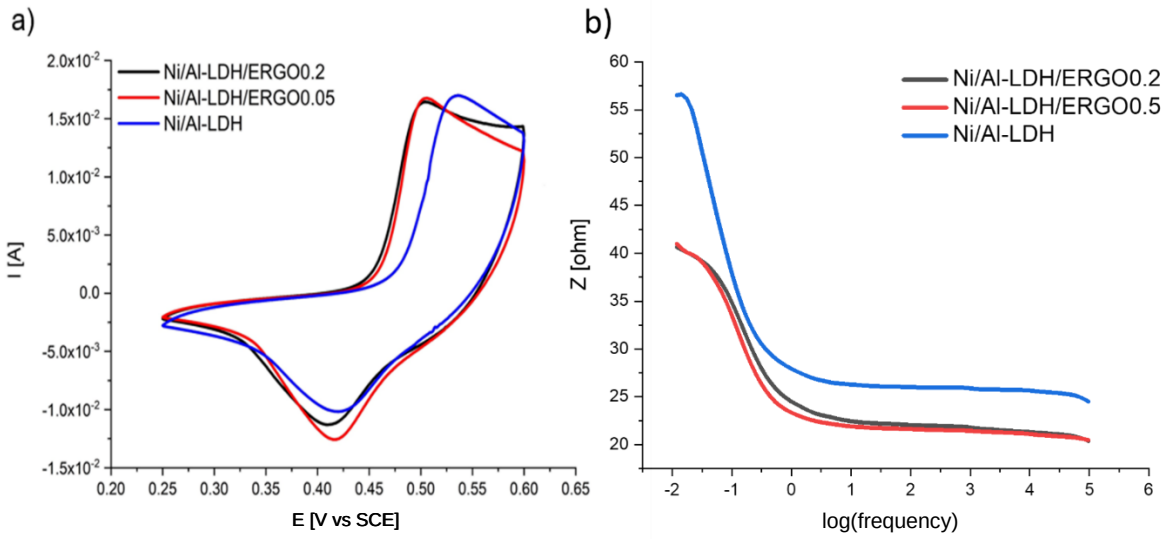

Figure 3_ 22: a) CVs of pure LDH and the composites Ni/Al–LDH/ERGO0.05 and Ni/Al–LDH/ERGO0.2 recorded in 0.1 M KOH at 0.01 mV $s^{-1;}$ b) Bode plot for the same materials recorded when the applied potential corresponds to the peak maximum.

The effect of ERGO is qualitatively demonstrated, as already stated above, by the higher reversibility of Ni(III)/Ni(II) redox behaviour in Ni/Al–LDH/ERGO0.05 that exhibits a lower ΔE_p values at each scan rate than the pure LDH. Since Ni/Al–LDH/ERGO0.05 is a complex composite material and modelling every process that occurs during charge transfer is beyond the aim of this work, we estimate the heterogeneous rate constant (k_s) with a simplified approach in order to get a numerical estimation of the ERGO effect on the performance of the composite material. The comparison between k_s apparent values was carried out considering the equations valid for an under diffusion control process (in our case for scan rate values equal or higher than 25 mV s^{-1}). Therefore, it is possible to use the formula:

$$log_{10}\left(k_S\sqrt{\frac{RT}{nF\nu D}}\right) = 0.294\left(\frac{nF}{RT}\Delta E_p - 2.218\right)^{-1} - 0.0803 - 0.108\left(\frac{nF}{RT}\Delta E_p - 2.218\right)$$

Were n, R, T, F, ν and D are the number of exchanged electrons, the ideal gas constant, the absolute temperature, the Faraday constant, the scan rate, and diffusion coefficient, respectively. From the formula, it is possible to calculate $\frac{k_S}{\sqrt{D}}$ for Ni/Al–LDH/ERGO0.05 and Ni/Al–LDH. Considering that the diffusion coefficient inside the LDH should be the

same (calculated to be roughly 2×10^{-8} cm^2 s^{-1} [56]), the ratio between the two k_S can be directly obtained by the equation:

$$\left(\frac{k_{S\,Ni/Al-LDH/ERGO\,0.05}}{D_{Ni/Al-LDH/ERGO\,0.05}}\right) \cdot \left(\frac{k_{S\,Ni/Al-LDH}}{D_{Ni/Al-LDH}}\right)^{-1} = \frac{k_{S\,Ni/Al-LDH/ERGO\,0.05}}{k_{S\,Ni/Al-LDH}}$$

The ratio results equal to 25, so highlighting the superior features of Ni/Al–LDH/ERGO0.05. Electrochemical Impedance Spectroscopy (EIS) tests were also performed at the anodic peak position, where the response is ruled by Ni redox process (equations 8), to gain more insights about the ERGO effects on the charge transfer processes taking place at Grafoil modified electrodes. Figure 3_22 b, reports |Z| vs log (frequency) for Ni/Al–LDHs (blue curve), Ni/Al–LDH/ERGO0.2 (black curve) and Ni/Al–LDH/ERGO0.05 (red curve) to explicitly show the dependence of the overall impedance on the frequency. Looking at the graph, it is evident that ERGO presence lowers the impedance, especially in the low frequency region, that is connected to the kinetics of interfacial charge transfer reactions. This result confirms that ERGO, independently from its concentration (the curves obtained for 0.05 and 0.2 mg mL^{-1} ERGO concentration are practically superimposable) helps to improve the kinetics of Ni centres redox reaction.

3.2 Application of LDHs

3.2.1 HMF electro–oxidation[V]

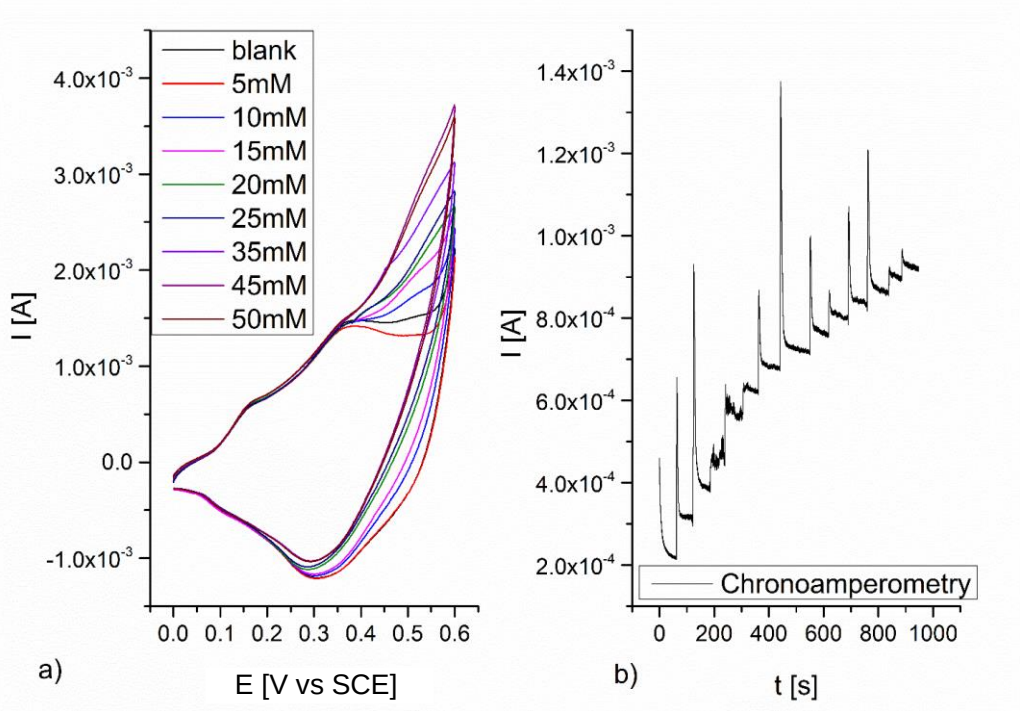

Figure 3_ 23: a) CVs recorded at Co/Al–LDH coated Grafoil in 0.1 M NaOH, containing HMF at different concentrations, ν = 0.01 mV s^{-1}; b) I vs. time plot obtained for the same Co/Al–LDH at +0.5 V in 0.1 M NaOH under magnetic stirring, while the HMF concentration was increased by progressive additions of a concentrated solution

A preliminary study of the oxidation of HMF was carried out by CV employing Co based LDHs as mediators. Firstly, the suitable experimental working conditions were explored in terms of applied potential. As an example, Fig. 3_23 shows the CVs recorded at Grafoil coated with Co/Al–LDH following the addition of different amounts of HMF to a 0.1 M NaOH solution. An increase of the anodic current is recorded which is proportional to HMF concentration.

[V] Reprinted from Newly developed electrochemical synthesis of Co-based layered double hydroxides: toward noble metal-free electro-catalysis. E. Musella, I. Gualandi, E. Scavetta, A. Rivalta, E. Venuti, M. Christian, V. Morandi, A. Mullaliu, M. Giorgetti, D. Tonelli, Journal of Materials Chemistry A, 2019, 7 (18), 11241-11249.

The chronoamperometric response was obtained by setting the potential at +0.5 V (Fig. 3_23b). The same experiments were carried out using Pt as the support and all of them were repeated also for the Co/Fe–LDH. The sensitivities and the LOD values of the four calibration lines are reported in Table 3_5. The Co/Al–LDH displays a slightly better performance as to the sensitivity in respect to the Co/Fe–LDH, independently of the support. As expected, the same material on the two supports displays the same LOD, and the values are similar for both LDHs. Moreover, the reproducibility of the sensitivity values for the HMF determination, as expressed by the slopes of the calibration lines, is satisfactory, as expected by the good reproducibility of the newly proposed electrodeposition.

Table 3_ 5: LOD values and sensitivities obtained from the calibration lines for HMF determination by chronoamperometry.

	Sensitivity (AM^{-1} cm^{-2})	**LOD (M)**
Co/Al–LDH on Pt	0.417 ± 0.008	$1.69 \cdot 10^{-4}$
Co/Al–LDH on Grafoil	0.394 ± 0.006	$1.73 \cdot 10^{-4}$
Co/Fe–LDH on Pt	0.070 ± 0.002	$2.23 \cdot 10^{-4}$
Co/Fe–LDH on Grafoil	0.069 ± 0.004	$2.12 \cdot 10^{-4}$

As a proof of concept, Co/Al–LDH on Grafoil has also been submitted to an exhaustive electrolysis (E = +0.5 V, t = 72 h, nitrogen atmosphere). Nowadays, research efforts are devoted in developing processes for production of 2,5–furandicarboxylic acid (FDCA) to be employed as a monomer in industrial synthesis. In this scenario, the proposed system results in a complete noble metal–free catalyst. Moreover, the support must also be considered in a process development, since a catalyst prepared with the same metal active phase might display different catalytic performances depending on the support used. Thus, in this wide range of studies on innovative processes aiming at the preparation of metal–supported catalysts, it is here proposed Grafoil as a support since it is low cost, environmentally friendly, and easy to handle, as already mentioned. The solution coming from the exhaustive electrolysis was analysed by HPLC equipped with diode array detector (Fig. 3_24) and ^{1}H–NMR (Fig 3_25) in order to identify the oxidation products. Neither HPLC nor ^{1}H–NMR shows presence of HMF, confirming a 100% virtual conversion. 5–Hydroxymethyl–2–furancarboxylic acid (HMFCA) and FDCA are formed as major products, and an

unidentified aliphatic product can be also detected. This product was investigated also with ESI–MS spectrometry giving a molecular weight of 242.

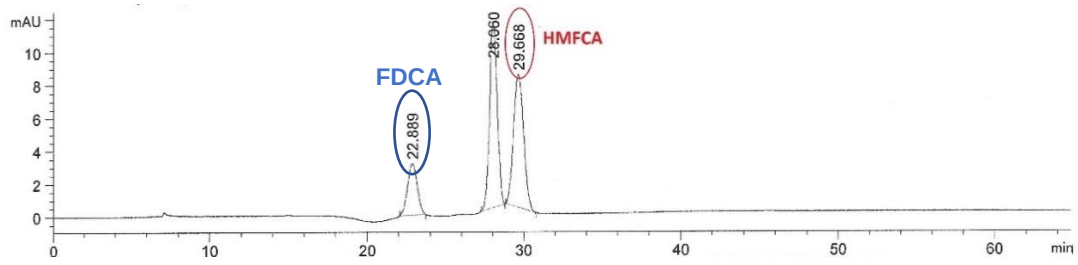

Figure 3_ 24: HPLC analysis of electro–oxidation products of HMF

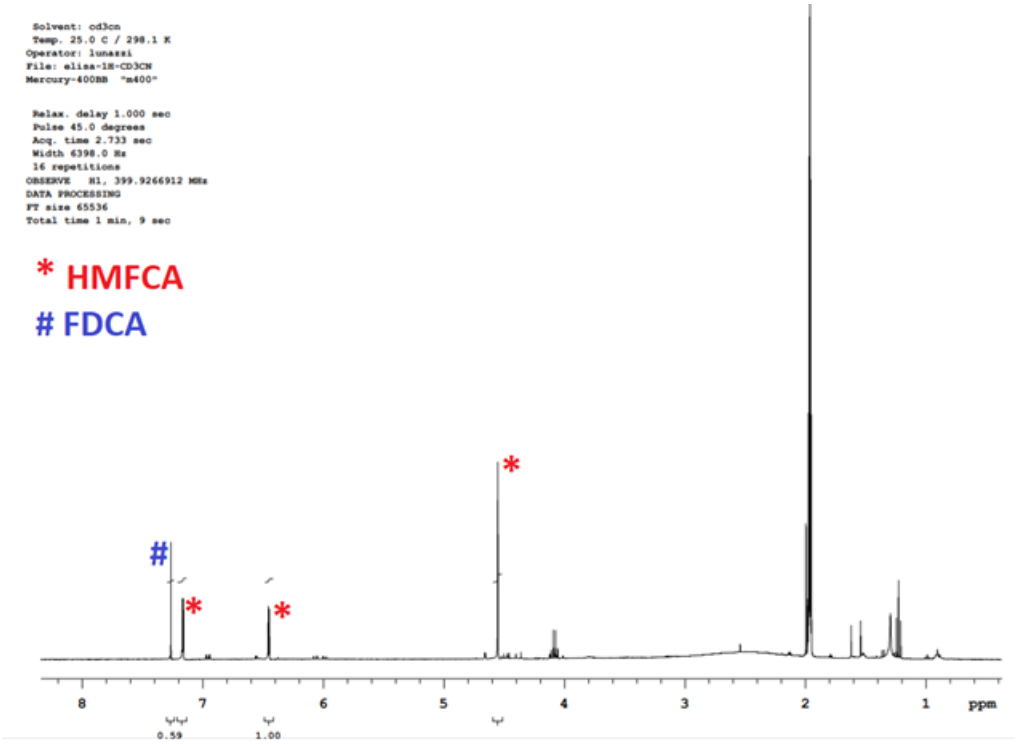

Figure 3_ 25: 1HNMR spectrum of the mixture of HMFCA and FDCA

The selectivity toward FDCA, calculated from HPLC, results 49%, while toward HMFCA is 37%. The Faradaic efficiency was calculated to be 40.8%. When analysing the FE, it must be noticed that the oxygen evolution reaction competes with the electrocatalytic oxidation of HMF to FDCA in alkaline media, probably causing also a decrease of the selectivity. Summarizing, the above reported results suggest that the proposed chemically modified electrodes can be considered an interesting approach to produce FDCA from HMF catalytic oxidation.

3.2.2 Oxygen evolution reaction[III]

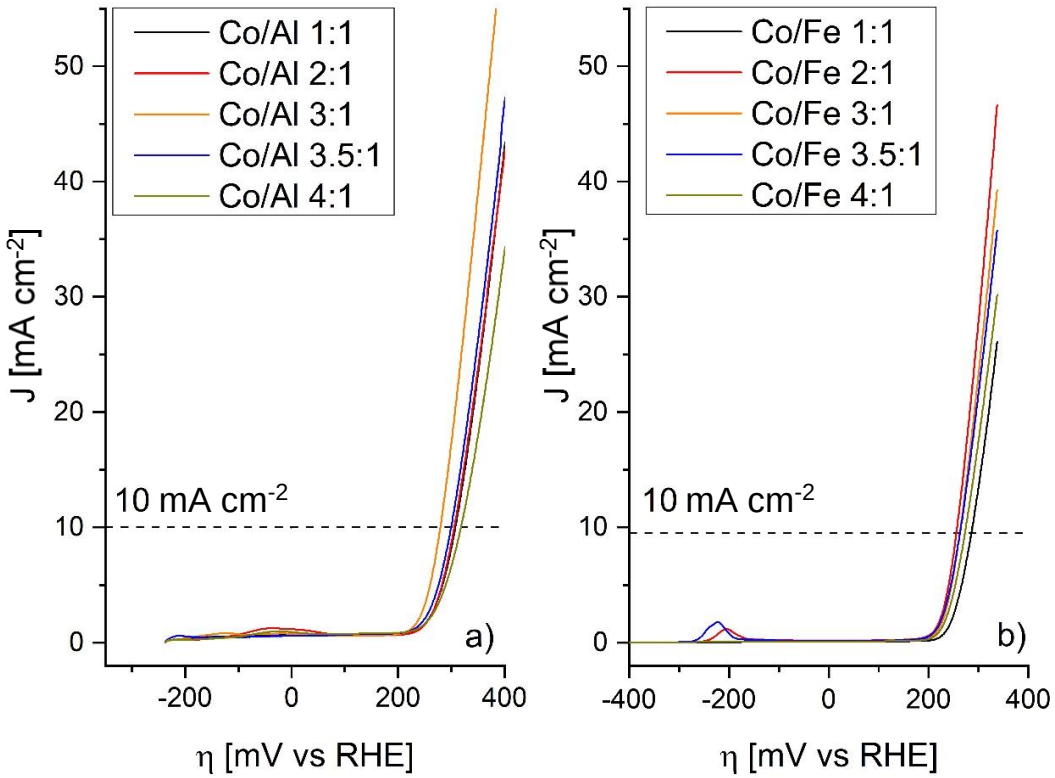

Figure 3_ 26: Evaluation of OER activity for the investigated molar ratios in 1 M NaOH,

The OER activities of the Co/Al and Co/Fe–LDHs were also determined by electrosynthesising the catalysts directly on glassy carbon rotating disc electrodes (GC–RDE) so to obtain thin films. The RDE electrode allows for the evaluation of the material properties avoiding the formation of O_2 on the surface. This can be considered the first step for the scaling up of an OER process. As shown in Figure 3_26a, the OER activity has a maximum for the Co/Al LDH 3:1 for which also the best performances in terms of Tafel slope and onset potential are achieved (Table 3_6). This trend is analogue to the one recorded for ECSA values, suggesting the existence of a correlation between the parameters OER activity and ECSA. The result confirms that a correct molar ratio is crucial to guarantee the best performance for OER activity.

In Figure 3_26b, which displays the Co/Fe–LDHs performances, the OER activity has a maximum for the Co/Fe 2:1 Also in this case, this material shows the best performances in terms of Tafel slope and onset potential (Table 3_6). The main difference between Al^{3+} and

Fe^{3+} is that iron is a redox–active species able to participate in the electron hopping charge transfer with Co, resulting in a synergic effect[24].

In particular, it is noteworthy that Co based LDHs exhibit reasonable intrinsic activity for the OER, as it has been demonstrated by this and several previous works, in absence of Fe. However, when Fe is incorporated, the activity is drastically enhanced, which emphasizes the hypothesis of a synergic effect between Co and Fe as two cooperating active sites. It is reported[24] that Co^{4+} species have been observed in OER–active catalysts under oxygen evolution conditions and are widely accepted to be a vital intermediate in the OER catalytic cycle of Co–based catalysts. As a matter of fact, according to the OER pathway proposed by Ullmann et al.[57], the Co^{4+} species are able to coordinate the oxo groups and, therefore, facilitate the proton–coupled electron–transfer (PCET) steps. This leads to radicals formation on the Co^{3+} sites. It is also true that Fe is oxidized at a lower potential than Co, thus Fe can substitute Co in Co/Fe LDHs to produce oxo species at lower potentials, which may facilitate the PCET steps and, ultimately, enhance the overall OER catalysis.

This is the reason why Co/Fe LDHs show much better OER activities than the Co/Al ones. As already mentioned, another important parameter is the overpotential required to reach a current density of 10 mA cm^{-2}, whose values are also reported in Table 3_6.

Table 3_ 6: Tafel slope, onset potential and overpotential at a current density of 10 mA cm^{-2} of all the investigated LDHs

	Co/Al			**Co/Fe**		
Ratio	*Tafel slope (mV dec^{-1})*	*Onset overpotential (mV vs RHE)*	*Overpotential (mV vs RHE)*	*Tafel slope (mV dec^{-1})*	*Onset Potential (mV vs RHE)*	*Overpotential (mV vs RHE)*
1:1	47.91	330	360	49.36	260	330
2:1	47.51	300	350	**36.89**	**230**	**310**
3:1	**45.03**	**290**	**340**	**38.69**	**240**	**320**
3.5:1	**46.81**	**280**	**350**	39.15	250	310
4:1	47.85	300	350	42.30	250	320

All the parameters investigated hint a very satisfactory OER performance of the Co/Fe LDHs 2:1 and 3:1, in good agreement with the previous literature[24], where the Co/Fe LDHs

with different Fe atomic contents were obtained by chemical route. Noteworthy, the most performing material for OER resulted that containing 35% Fe, which virtually corresponds to the LDH with Co/Fe 2:1 ratio. Accordingly, we may conclude that the impurity present in such a system, in the form of segregated Fe oxide/hydroxides phase, does not play any significant role in the observed enhanced OER activity.

EIS tests were also performed operating at two different potentials, and precisely at E = 0.3 V, far from OER evolution (at oxidation peaks of Co), and at E = 0.6 V where OER proceeds, to gain more insights on the charge transfer processes taking place at Grafoil electrode modified with all the tested LDHs. The data are presented in Figure 3_27 in Bode form (|Z| vs log frequency, and phase angle vs log frequency) for Co/Al LDHs (red curves), and Co/Fe LDHs (black curves) to explicitly represent the spacing on the frequency scale[57].

When the EIS experiments are carried out at a potential far from the OER reaction the response is ruled by Co electrochemical reactions (equations 9 and 10). Examining the phase angle vs log frequency curves (Figure 3_27c), it appears that a resistive like behaviour is observed for all the Al containing LDHs in the frequency region $10^{3.5}$ – 1 Hz, while this frequency interval is more limited ($10^{3.5}$–10 Hz) when the trivalent metal is Fe.

Phase angles higher than 60°, indicative of a capacitive domination of the impedance response, are noted below 10^{-2} Hz for Co/Al LDHs, and 10^{-1} Hz for Fe containing LDHs. Being this frequency range connected to the kinetics of the interfacial charge transfer reactions, our results prove that this process is more efficient for Al – containing LDHs, resulting in lower overall impedance values (Figure 3_27a). On the contrary, when the EIS measurement was performed at 0.6 V (OER conditions in all cases), the overall impedance for Fe containing LDHs at low frequencies decreases remarkably compared with the values recorded at 0.3 V, becoming even lower than that recorded for Al based LDHs. Looking at the |Z| vs log frequency plots (Figure 3_27b), we observe that Fe containing LDHs display one section of constant negative slope (in the frequency range between 1 and 10^2 Hz), between two flat shelf sections at the high and low frequency extremes. The inspection of the phase angle vs log frequency curves (Figure 3_27d) reveals a very small variation of the phase angle over the entire frequency range (the maximum value of the phase angle is 5°) suggesting a resistive like behaviour. For Al LDHs the relaxation process occurs on a longer

time scale (10^{-2}–1 Hz) and the phase angle values indicate a capacitive domination in this zone.

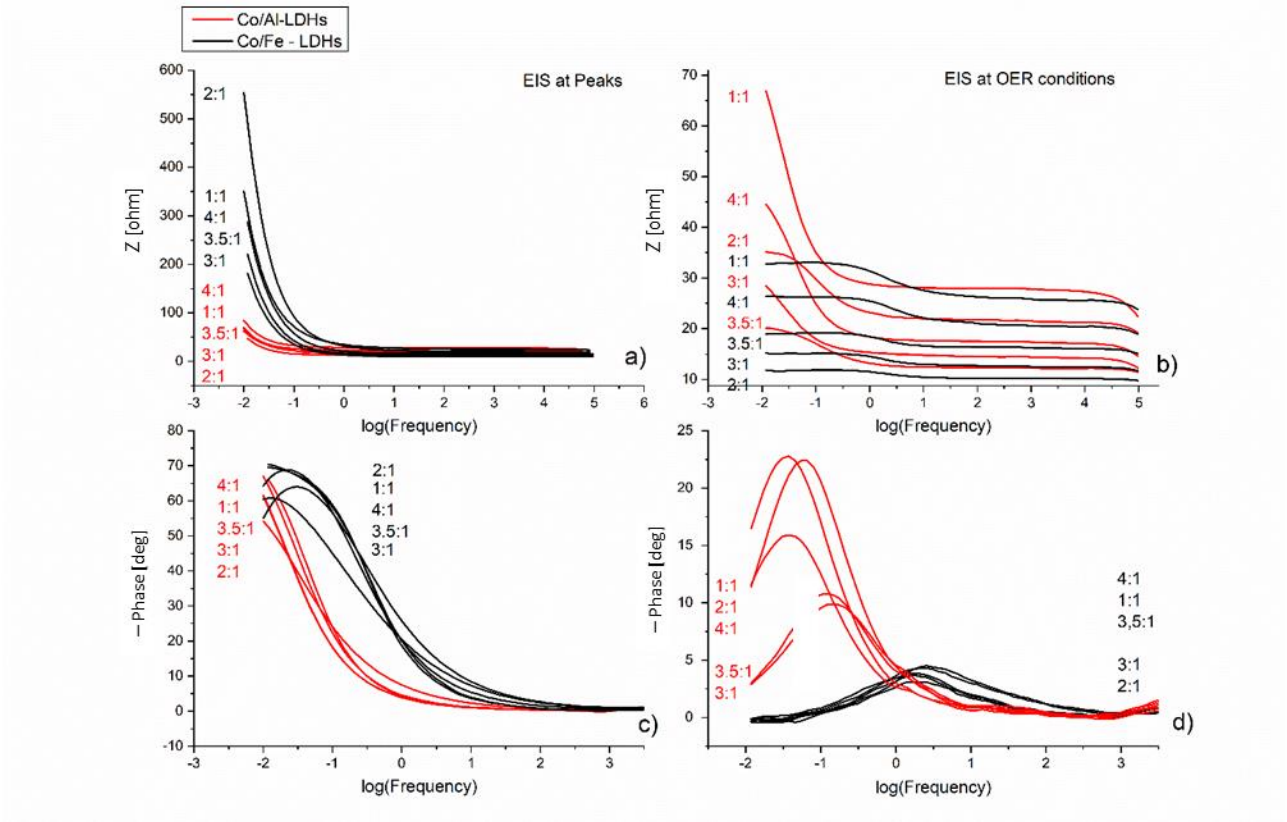

Figure 3_ 27: EIS for all the investigated LDHs (red Co/Al, and black Co/Fe samples,) recorded in 0.1 M NaOH. a) plot of the total impedance vs the logarithm of the frequency when the applied potential is far from OER condition. b) EIS experiments were performed at the potential of 0.6 V vs SCE, c) Bode plot when the applied potential is far from OER condition. d) EIS experiments were performed at the potential of 0.6 V vs SCE.

This result highlights the synergistic effect of Fe – containing LDHs in OER conditions. The redox behaviour is surely ruled by the Co couple of the LDH, but the presence of Fe significantly improves the performance of the electrode modifier for OER, lowering the overall impedance and improving the kinetics of OER reaction. The lowest |Z| value is recorded for the LDH with a Co/Fe molar ratio 2:1.

Moreover, for each set of LDHs, we chose the two best catalysts (data in bold in Table 3_6) to be further investigated with the stationary system based on Grafoil, a substrate that is much greener compared to Ni foam.

Following the McCrory et al. procedure[12,13], the OER activity was evaluated primarily by performing CVs at the 0.01 V s^{-1} scan rate; this scan rate is slow enough to ensure a steady–

state behaviour at the electrode surface. The results of 30 s chronopotentiometric steps (red circles) and chronoamperometric steps (blue triangles) are shown for comparison, and the close overlay of the data suggests the achievement of steady–state conditions (Figure 3_28a). In Figure 3_28b, LSVs of all the catalysts are plotted for comparison. Interestingly, the overpotentials obtained on Grafoil do not differ much with respect to the ones achievable with the RDE; in fact, for Co/Al 3:1 the value is 370 mV, while for Co/Al 3.5:1 is 380 mV. Furthermore, the overpotential necessary to obtain 10 mA cm^{-2} current density for Co/Fe 2:1 is 330 mV while for the 3:1 is 340 mV.

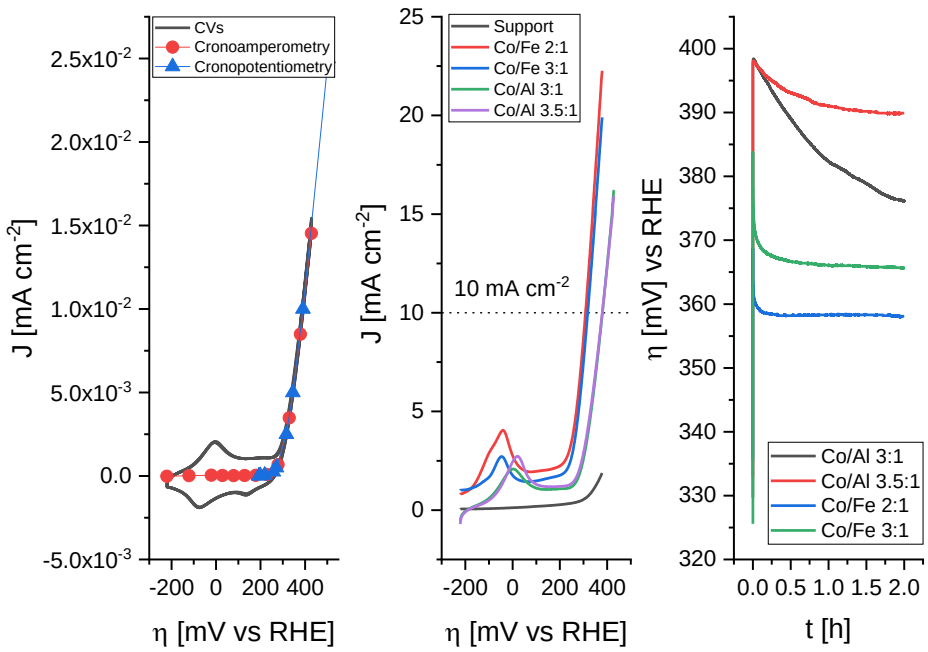

Figure 3_ 28: a) Co/Al–LDH 3:1 on Grafoil. The OER activity was evaluated by CVs at 0.01 V s−1 in 1 M NaOH. The results of 30 s chronopotentiometric steps (red circles) and chronoamperometric steps (blue triangles) are shown. b) comparison of best performing LDHs c) long term stability (2h)

This feature can be considered as an important result when scaling up an industrial process, since it is a clear indication of the robustness of the synthetic protocol. The long–term stability of the four catalysts considered the best performing ones was further investigated under conditions closer to real applications by galvanostatic stability (GSS) tests. The ohmic drop (iR)–corrected potential applied to the working electrode at 10 mA cm^{-2} is plotted as a function of time (Figure 3_28c). As suggested by McCrory et al.[12,13] procedure, the 2h

stability test is reported for all the selected catalysts. The potential during the polarization of the electrode at 10 mA cm^{-2} firstly decreases and then stabilizes at a defined value (355 mV for Co/Fe 2:1, the best performing one). The worst stability is displayed by the Co/Al 3:1 system. Finally, Table 3_7 summarizes the OER activities in terms of overpotential reported in the literature for similar LDHs synthesised by chemical route and by the potentiostatic approach.

Table 3_ 7: Comparison of the electrocatalytic performance of the chosen catalysts in this work with the Co LDH–related catalysts reported in the literature. (Co 3:1 corresponds approximately to Co45, while Co 2:1 to Co35)

Catalyst	Synthetic route	Overpotential	Catalyst	Synthetic route
Co/Al 15 – LDH	Coprecipitation	400	83	24
Co/Al 25 – LDH	Coprecipitation	/	83	24
Co/Al 35 – LDH	Coprecipitation	/	83	24
Co/Al 45 – LDH	Coprecipitation	450	102	24
Co/Fe 15 – LDH	Coprecipitation	390	70	24
Co/Fe 25 – LDH	Coprecipitation	360	70	24
Co/Fe 35 – LDH	Coprecipitation	350	49	24
Co/Fe 45 – LDH	Coprecipitation	360	47	24
Co/Fe 3:1 – LDH	Electrosynthesis: potentiostatic	410	29	58
Co/Al 3:1 – LDH	Electrosynthesis: potentiostatic	460	30	58

They demonstrate that the results obtained in this work are comparable or even better than those previously reported. It is important to highlight that the electrochemically synthesized Co/Fe 2:1 gives the same performance as the one chemically synthetized with a similar molar ratio[24]. Moreover, comparing the results obtained in this work using the potentiodynamic deposition with those relevant to a potentiostatic electrosynthesis[58] we can point out the major difference between the two methods. The OER turns out to be especially enhanced in terms of overpotential when the potentiodynamic route is used (350 vs 410 mV for M(II)/M(III) ratio of 3:1). This is probably due to the higher porosity and ECSA typical of

the LDHs obtained with such an electrosynthesis, which produces a higher amount of Co (and Fe when present) sites accessible for the OER.

3.2.3 Electrochemical hybrid capacitors development[II, IV]

Cathode development

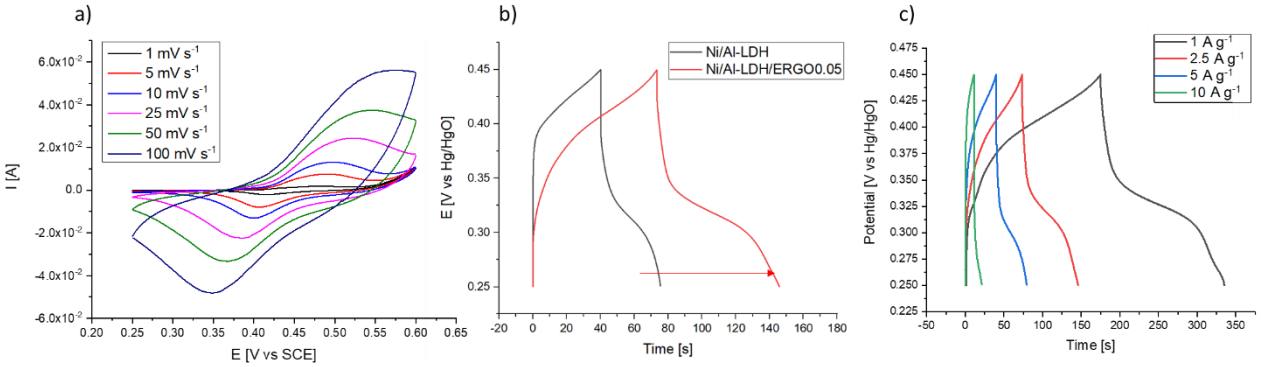

Figure 3_ 29: a) CVs at different scan rates of Ni/Al–LDH/ERGO0.05; b) comparison of GC–D curves of Ni/Al–LDH/ERGO0.05 and Ni/Al–LDH at 2.5 A g^{-1} c) GC–D curves recorded at different current densities for Ni/Al–LDH/ERGO0.05. All the tests were performed in 0.1 M KOH.

In addition to the Faradaic process described in the above section, we have explored the charge storage characteristics of the deposited films to verify their possible application in hybrid electrochemical capacitors, as already reported for other layered double hydroxide materials[53,59–61].

The electrochemical properties of the electrodes were initially investigated in a three–electrode cell using 0.1 M KOH as the supporting electrolyte. Figure 3_29a shows CVs at different scan rates. The power–law relationship with the scan rate is:

$$i = a\nu^b$$

where i is the average current of anodic and cathodic peaks, ν the scan rate, and a and b are adjustable parameters. b values are calculated to be 0.76 for Ni/Al–LDH, and 0.78 for Ni/Al–LDH/ERGO0.05. These values indicate that the electrochemical behaviour of the two materials is controlled by both capacitive (b=1) and diffusive (b=0.5) processes. The potential window at which they work can be considered narrow, limited to approximately 0.45 V. Figure 3_29b shows the galvanostatic charge/discharge (GC–D) curves that are recorded in 6 M KOH at the electrodes exploiting the pure LDH and LDH/ERGO0.05 in the potential range of 0 – 0.50 V. The LDH exhibits a voltage response deriving not only from a Faradaic process (voltage plateau behaviour) but also a linear portion of the time

(and thus the charge) variation with potential. In addition, the charge increases in the presence of ERGO, underlying the merit of the present synthetic approach. At the current density of 2.5 A g^{-1}, the specific capacitances (Cs) of Ni/Al–LDH and Ni/Al–LDH/ERGO0.05 are 550 F g^{-1} and 650 F g^{-1}, respectively. The GC–D curves at different energy densities are reported in Figure 3_29c for the composite Ni/Al–LDH/ERGO0.05. Cs values result to be 745, 649, 600, 585 F g^{-1} at current densities of 1, 2.5, 5, and 10 A g^{-1}. It can be noticed that they decrease gradually with increasing current density, due to diffusion which limits the movement of the electrolyte ions[1]. Nevertheless, the materials retain a good rate in their performances. In all studied cases, when the current is reversed from charge to discharge, an ohmic drop occurs due to the internal resistance. The IR drop is slightly decreased in the case of Ni/Al–LDH/ERGO0.05 in respect with pure Ni/Al–LDH (see Figure 3_29b).

Anode development

In this part, the development of an anode composed of activated carbon (AC) or PEDOT:PSS is discussed. These materials have been found to be suitable to be coupled with cathodes based on LDH and ERGO in hybrid supercapacitors.

Activated carbon–based electrodes

The anode is prepared with activated carbon, carbon black, and a polymer binder. To evaluate the best composition of the modifier, the Grafoil support was modified with various formulations of the slurries. In the preliminary evaluation of the anode materials, the employed solvent was 1 M KOH. In particular, different mass ratios between the constituents, different types of polymeric binders (PVDF or PVA), and different dispersing liquids were investigated as follows:

1. AC:AB:PVA=8:1:1, in H_2O
2. AC:AB:PVDF=7:2:1, in H_2O
3. AC:AB:PVDF=8:1:1, in EtOH
4. AC:AB:PVDF=7:1:2, in H_2O

The slurries were dispersed either through drop–casting or spin–coating. To define the optimal modifier and deposition method, the first test which was carried out was the immersion of the electrode in water to verify the adhesion of the modifier to Grafoil.

Following these tests, it was observed that, especially in the case of electrodes prepared by drop–casting, those with PVA as a binder released much more material into water than the ones prepared with PVDF. This observation led to:

- Choose the PVDF as binder for the preparation of the electrodes.
- Deposit a smaller amount of modifier.

In addition to the physical tests, the electrodes were also characterized by CV, recorded at a scan rate of 10 mV s^{-1}, which is shown in figure 3_30.

As regards the CV, it can be noted that the current intensities are higher when the binder is PVDF, despite a smaller amount of the deposited material.

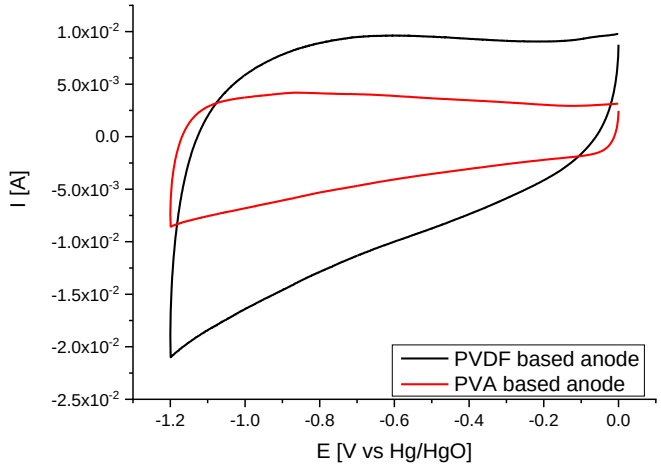

Figure 3_ 30: comparison of CVs between PVDF and PVA based electrodes

In a similar way, the effectiveness of the deposition technique was evaluated in terms of adhesion of the material to the electrode support, noting that the method that released the minimum amount of modifier in water was that performed by spin–coating. Once the most suitable binder was determined, the percentage to be used in the slurry was studied, again on the basis of water resistance, since all the characterization tests of both single and coupled electrodes in the supercapacitor were carried out in solution. The percentage of 10% of PVDF was chosen since it led to the best results, which were confirmed both by CVs and charge and discharge cycles, as can be seen in Figure 3_31.

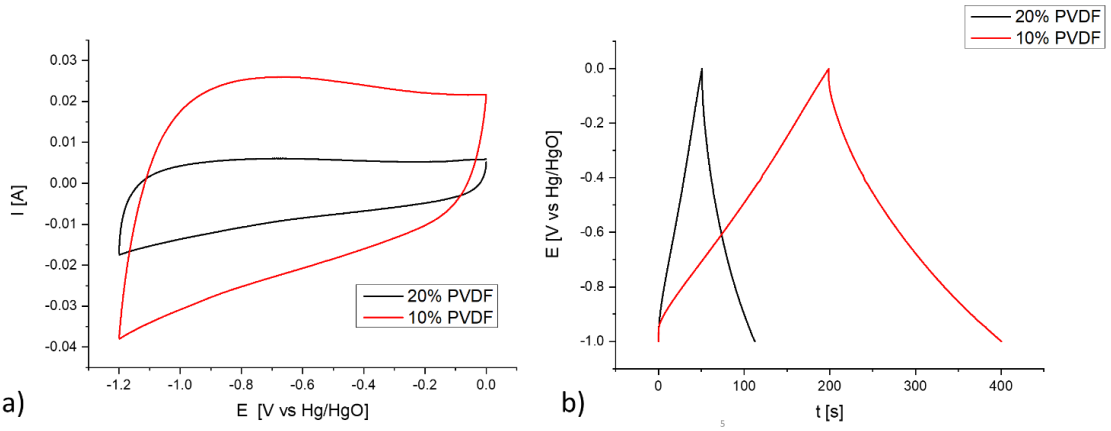

Figure 3_ 31: comparison of a) CVs and b) GC-D–curves for two slurries containing different amounts of PVDF

A final parameter that was evaluated was the kind of dispersant liquid. Although deionized water had already shown to provide good results, ethanol was also tested. As can be seen in figure 3_32, although electrodes prepared with ethanol have longer charging and discharging times, with the same current compared to electrodes prepared with water (a feature that would theoretically make them more suitable for the application), they present other relevant drawbacks:

- high loss of material
- gas production between the electrode and modifying support.

This is why the potential range used in the CV characterization was restricted using –0.9 V as cathodic limit, in order to avoid the disruption of the modifier during the execution of the voltammogram. Other reasons that suggested not to use EtOH as a dispersant are due to the fact that this solvent seems to impregnate the supports, with damage to the support itself, and to its volatility which, making it evaporate very quickly, prevents an uniform coverage of the Grafoil during the spin–coating.

Once the composition of the modifier was optimized, the anodes were characterized by CV between –1.2 and 0 V, at different scan rates, in order to evaluate their electrochemical behaviour. As can be seen in Figure 3_32, the voltammetric curve does not show any peak indicating redox reactions, suggesting a purely capacitive behaviour: the charge is constant for the entire analysed potential range. Even the galvanostatic charge / discharge cycles do not show plateaus due to redox reactions, and the curve is purely triangular.

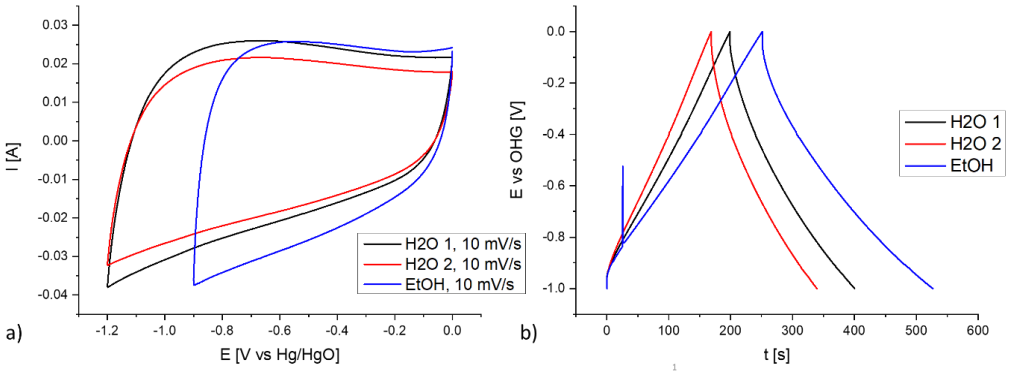

Figure 3_ 32: comparison of the performances of modifiers obtained with different slurries through a) CV and b) GC-D–curves

The characterizations were carried out in a nitrogen atmosphere to avoid the reduction of oxygen at the anode and, therefore, a decrease in capacity. Consequently, nitrogen was bubbled into the electrolytic solution, then a gas head was maintained during characterizations.

PEDOT:PSS electrode

In the case of PEDOT:PSS, both CVs (Figure 3_33a) and GC-D curves (Figure 3_33b) display a purely capacitive behaviour in the potential range investigated, thus evidencing the charge storage capabilities in 6 M KOH. The average specific capacitance calculated from the CVs is 0.2 F cm^{-2}. Considering the GC-D curves, the obtained values are 0.25, 0.23, 0.7 and 0.1 F cm^{-2} at current densities of 3, 7.5, 16 and 35 mA cm^{-2}, respectively.

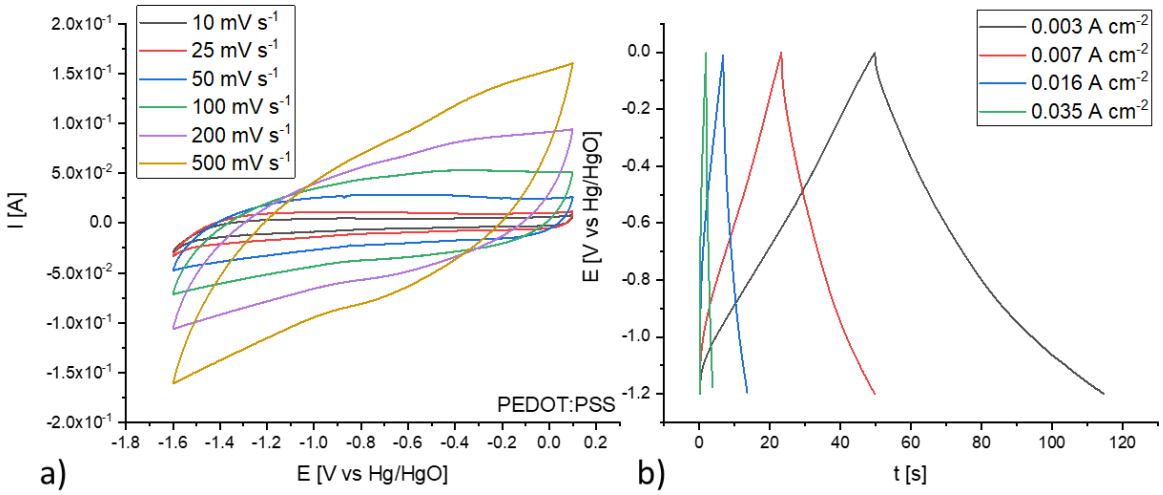

Figure 3_ 33: a) CV characterization of PEDOT:PSS at different scan rates and (b) charge/discharge curves of PEDOT:PSS in 6 M KOH.

Hybrid capacitor: in solution set–up and assembled device

The LDH–based electrodeposited material was coupled to an AC electrode and tested in solution in a glass cell and in an assembled device as well. Figure 3_34a describes the configuration in solution, where the two electrodes, namely AC and Ni/Al–LDH/ERGO0.05, are immersed in 6 M KOH under nitrogen, whereas Figure 3_34b displays the CV responses recorded at different scan rates for this set up.

All the CVs display a nearly capacitive behaviour in the potential range investigated, thus evidencing the charge storage capabilities of the hybrid supercapacitor when operating in solution. In figure 3_34c the specific discharge capacitance is plotted against the cycle number in a glass cell configuration by using the Ni/Al–LDH or Ni/Al–LDH/ERGO0.05 at one terminal side. Tests were made with a current density of 2.5 A g^{-1}.

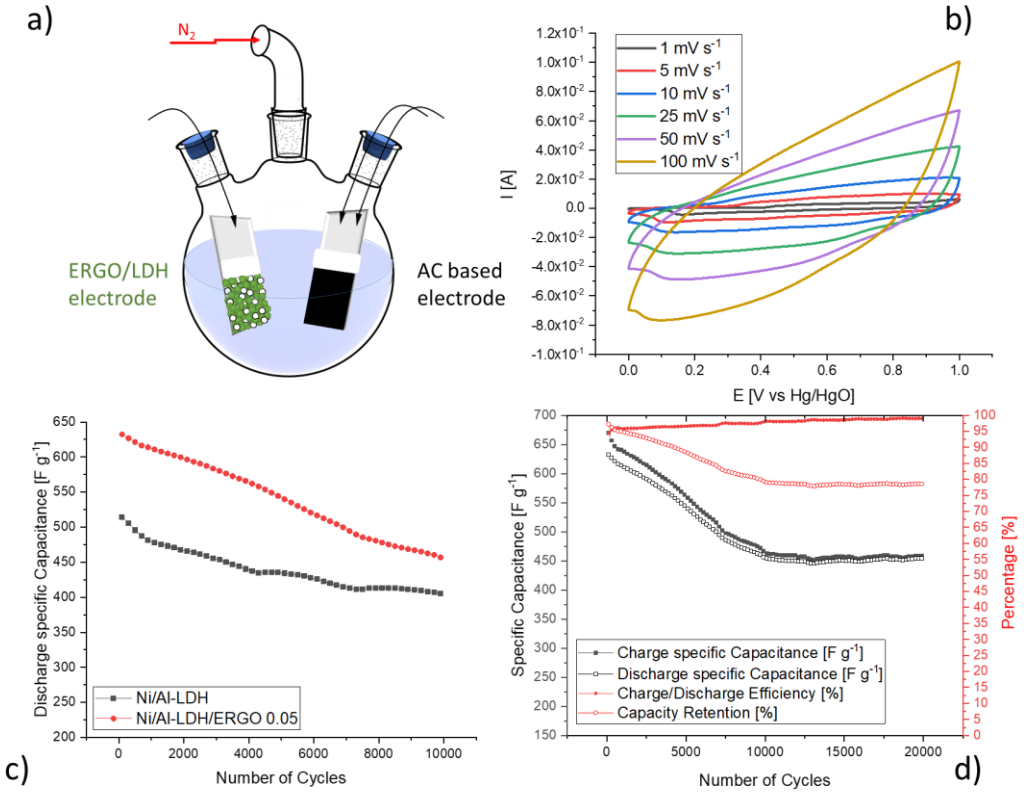

Figure 3_34: a) sketch of the set–up of the hybrid SC in solution; b) CVs at different scan rates of the asymmetric capacitor based on AC and Ni/Al–LDH/ERGO0.05 in 6 M KOH; c) comparison of the specific capacitance of Ni/Al–LDH and Ni/Al–LDH/ERGO0.05 during the continuous charge discharge cycling test at 2.5 A g^{-1}; d) capacitance retention of Ni/Al–LDH/ERGO0.05 at 2.5 A g^{-1} for 20,000 cycles in solution. Tests were performed in 6 M KOH.

From this figure, a superior performance of Ni/Al–LDH/ERGO0.05 with respect to the pure LDH is evident. In both cases the specific capacitance decreases during the first 10,000 cycles but, as pointed out in figure 3_34d which shows also the charge capacity (black trace), it reaches a plateau after about 11,000 cycles at a value of 450 F g^{-1} for Ni/Al–LDH/ERGO0.05.

Table 3_8 compares the performances of different Ni/Al–based LDHs with and without the addition of carbon nanomaterials, as supercapacitors in solution. Ni/Al–LDH alone has a specific capacitance in line with that of other chemically synthesized LDHs. Their C_s can be enhanced producing materials with peculiar morphology (such as hollow microspheres or petal–like structures) in order to favour the ion diffusion. The morphology effect is evident both for pure LDHs and composites.

The best capacitances are observed when nanostructured LDHs are produced in combination with 0D or 1D nanomaterials (nanoplates with quantum dots, nanosheets, etc...).

Anyway, the composite here proposed shows better performances than LDHs combined with graphene or reduced graphene oxide as obtained in the form of bulk porous films (i.e., without controlled morphology).

The results of this work suggest that LDHs obtained with the proposed method display capacitances that are definitively analogous to the chemically synthesized ones with uncontrolled morphology. It is worth highlighting that our systems are particularly stable and long–lasting: they were still functioning after 20,000 cycles with respect to a maximum of 10,000 for other cases reported in the literature.

Ni/Al–LDH/ERGO0.05 displayed 80% of capacitance retention after 20,000 cycles which is the best stability obtained among all the compared materials. This high stability can be attributed to the strong adhesion to the supports, as already demonstrated for the LDHs electrosynthetic procedure[62].

Table 3_ 8: Comparison of the capacitive performances of the electrosynthesised Ni/Al–LDH and Ni/Al–LDH/ERGO0.05 with analogous chemically synthesized LDHs and C nanomaterials composites reported in the literature.

	Specific Capacitance F g^{-1} (at a specific current density A g^{-1})	**Capacity Retention (cycle numbers)**	**Electrolyte**	**Ref**
Pure LDHs				
NiAl–LDH petal–like	795 (2.5)	80% (1000)	1 M KOH	63
Hollow NiAl–LDH microspheres	735 (2)	116.5% (1000)	1 M KOH	64
NiAl–LDH	482 (10 mA cm^{-2})	94% (400)	6 M KOH	65
NiAl–LDH	140 (0.4)	–	6 M KOH	66
NiAl–LDH	550 (2.5)	69% (20000)	6 M KOH	This Work
LDHs combined with carbon nanomaterials				
Quantum dots – NiAl–LDH nanoplates	1794 (2)	93% (1500)	6 M KOH	67
NiAl–LDHs – graphene nanosheets	1255.8 (1)	106% (1500)	6 M KOH	32
NiAl LDHs/g–C3N4	714 (0.5)	82% (10 000)	6M KOH	68
Flower–like NiAl LDH–NF/Graphene	214.7 (1)	80% (5000)	6M KOH	69
Ni/Al–LDH and rGO	39.55 (1.04)	67.4% (10000)	6 M KOH	70
Ni/Al–LDH/ERGO0.05	650 (2.5)	80% (20000)	6 M KOH	This work

In addition, Ni/Al–LDH has been also evaluated together with the electrosynthesised conductive polymer (PEDOT:PSS,) to obtain an all–binder–free system. When coupling the two electrodes, the obtained hybrid capacitor had a starting discharge C_s of 0.72 F/cm^2 which decreases and stabilizes at 0.65 F/cm^2 after 20 cycles. The capacity retention is 86% after 1000 cycles (Figure 3_35).

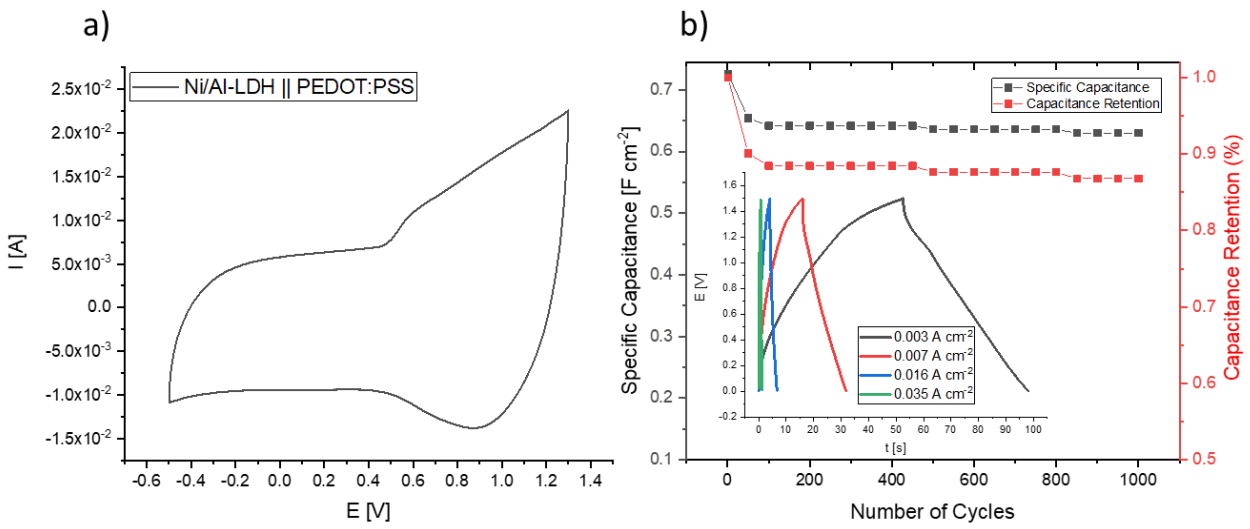

Figure 3_ 35: a) CV characterization of Ni/Al–LDH || PEDOT:PSS, b) long term stability test at 0.003 A cm^{-2} of Ni/Al–LDH || PEDOT:PSS, inset: charge/discharge curves at different current densities. Tests were performed in 6 M KOH.

At last, Figure 3_ 36 a displays the first attempted device based on Ni/Al–LDH/ERGO0.05 electrode and AC which can be described as an all solid–state hybrid supercapacitor. In Figure 3_36 b, the first 1,500 cycles of the assembled hybrid supercapacitor are displayed as proof of concept. The capacitor has a starting discharge C_s of 880 F g^{-1}, which decreases and stabilizes at 820 F g^{-1} after 300 cycles. The capacity retention is 88% and the charge/discharge efficiency is around 95%. To further demonstrate the potential applications, two fabricated SC devices were in series connected and fully charged (Figure 3_36 c) to 2.4 V. The connected SC devices could power and switch on a red light–emitting diode (LED, whose required voltage and current are 1.8 V and 10mA, respectively). In Figure 3_36 d the light time of the LED is plotted against the charge time of the two SCs. It can be noticed that, until 1,000 s, there is a linear correlation between the charge time and the light–time (when the LED is switched on). For longer charge times, a plateau of light time is recorded. Therefore, it is shown that the Ni/Al–LDH/ERGO0.05 material can be used as an electrode material for hybrid supercapacitors with interesting performance.

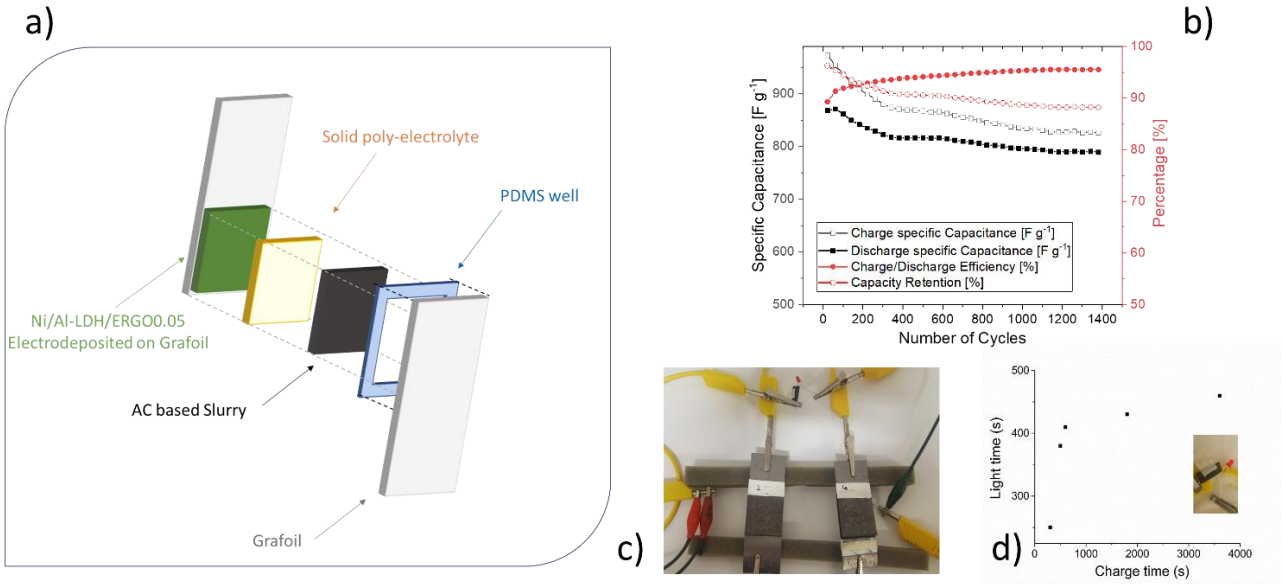

Figure 3 _ 36: a) schematic representation of the hybrid SC; b) capacitance retention of the assembled SC at 2.5 A g^{-1} for 1,400 cycles c) set up of the assembled SC to light a LED; d) plot of the light time of the LED against the charge time of the two SCs. Tests were conducted in the presence of the solid electrolytes.

3.3 Development of an ethanol sensor based on inkjet–printed carbonaceous electrodes

The electrochemical deposition of a Ni/Al–film on inkjet printed, flexible carbon nanotube (CNT) electrodes is described in this section. The CNT film was directly deposited on a polyethylene terephthalate (PET) substrate as a stand–alone CNT working electrode, thus without using a conductive support for the CNTs. Inkjet–printed electrodes are produced on large–scale, which makes them attractive to be used as disposable sensors, e.g. for healthcare and environmental analysis. The functionalization of the CNT electrodes, e.g. with hydrogels or electrocatalytically active nanoparticles, offers many possibilities in terms of selectivity and sensitivity[71,72]. Bare CNT electrodes with a working electrode area of ~1 mm^2 were printed as previously reported by Lesch et al.[71]. The working electrode area was defined by a polymeric insulator that was printed on top of the CNT pattern in the form of a window. The electrochemical response of the CNT electrodes was first tested by CV in an aqueous electrolyte solution containing 1 mM ferrocenemethanol (FcMeOH) as redox active species. An external counter electrode (Pt wire) and reference electrode (SCE) were used.

The oxidation and reduction waves of the $FcMeOH/FcMeOH^+$ redox couple were clearly identified (figure 3_37 a). Four different electrodes were tested to demonstrate the high level of reproducibility that was achieved by the inkjet printing process (variation of anodic peak less than 4%).

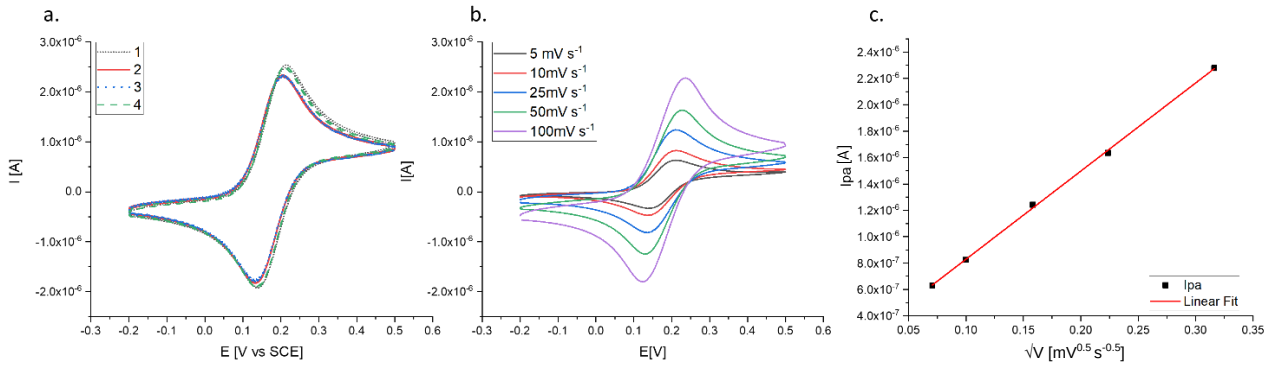

Figure 3_ 37: a) CV at 0.1 V s^{-1} of 4 different CNT electrodes. b) CVs at different scan rates. Experimental conditions: 1 mM FcMeOH and 0.1 M KNO_3. c) Linear fitting of the intensity of the anodic peak current vs the square root of the scan rate

Figure 3_37 b shows the voltammetric response at different scan rates and figure 3_37 c a plot of the intensity of the anodic peak against the square root of the scan rate. The

behaviour of FcMeOH can be described as quasi reversible displaying a ΔE_p = 71 mV and a I_{pa}/I_{pc} = 1.1 at a scan rate of 100 mV s^{-1}. Furthermore, the plot of Ip_a vs the square root of the scan rate gives a line with a slope value of 6.6 · 10^{-6} A.

Prior to the electrodeposition of the Ni/Al–film, the CNT electrodes were cycled in 0.1 M KOH until the CV curves became stable. Apart from capacitive currents, the voltammograms did not show any signals so the response corresponded to a pure blank signal, as expected for a CNT–based electrode (result not shown).

Key parameters for the potentiodynamic deposition, such as scan rate, potential window and number of cycles, were optimized, similarly to what described in the previous chapters, in order to obtain reproducible films (Table 2_2). A representative CV of the electrodeposition in a solution of Ni and Al nitrates is shown in figure 3_38a.

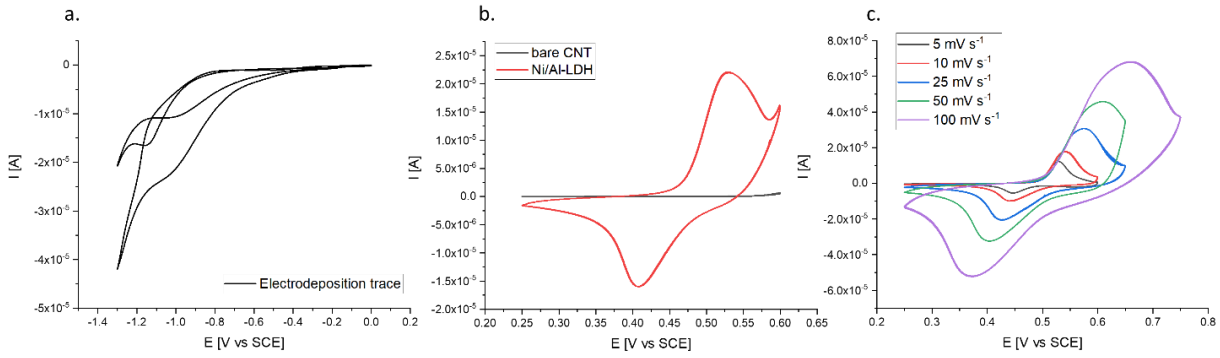

Figure 3_ 38: a) Potentiodynamic deposition of a Ni/Al film on a CNT electrode, scan rate: 25 mV s^{-1}. b) Comparison of the CVs of the bare inkjet printed electrode (black curve) and of the Ni/Al film electrodeposited on CNT electrodes (red curve) in 0.1 M KOH, scan rate: 0.01 V s^{-1}. c) CVs at different scan rates of the Ni/Al–film–modified CNT electrode, in 0.1 M KOH.

The oxidation and reduction peaks in the potential window between +0.45 V and +0.6 V are related to the redox couple Ni(III)/Ni(II) in 0.1 M KOH (figure 3_38 b), thus suggesting the presence of an oxide or hydroxide–based Ni/Al film[18]. As it can be seen clearly from the comparison with the bare CNT electrode, the CV of the latter does not show any redox peaks, confirming that the modification of the CNT electrode surface with a film of Ni/Al was successful.

The CVs at different scan rates are reported in figure 3_38 c, and characterize the Ni(III)/Ni(II) redox couple as quasi reversible, since ΔE_p is not constant but increases with the scan rate.

From optical images of the electrodes it is possible to observe macroscopically the difference between a bare CNT electrode and a modified one. The bare CNT electrode is transparent with a slightly greyish appearance (figure 3_39 a).

The CNT layer remains transparent also when the electrode is electrochemically cycled in alkaline media. On the contrary, the colour of the CNT area that is exposed to the electrolyte solution turns to brownish when the inorganic clay is present and when the electrode is immersed or cycled in KOH solution (figure 3_39 b).

HR SEM images of a bare CNT electrode (figure 3_3 9c) and of the Ni/Al–film/CNT electrode (figure 3_39 d) suggest that the Ni/Al–based film was electrodeposited as round nano–sized particles covering homogenously the CNT electrode.

EDX analysis confirms the presence of Ni and Al in the surface film with normalized mass concentrations of 25% and 14%, respectively. The Ni:Al ratio is compatible to a Ni/Al–LDH structure.

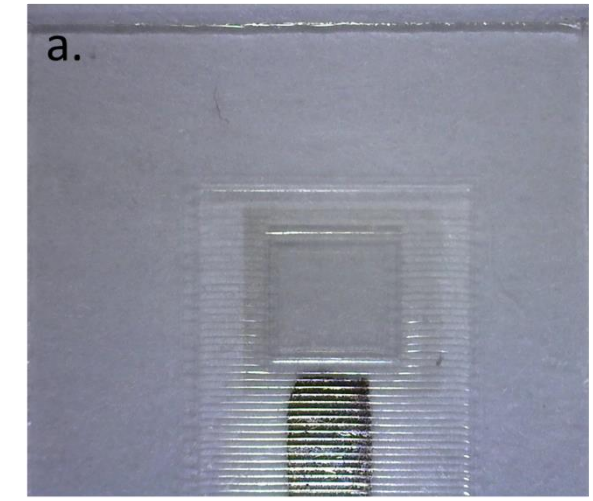

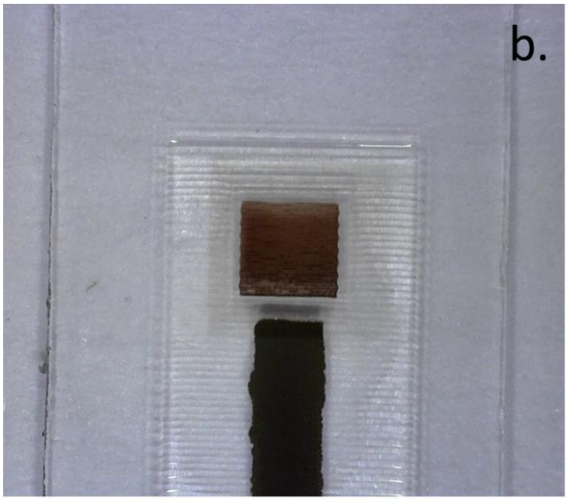

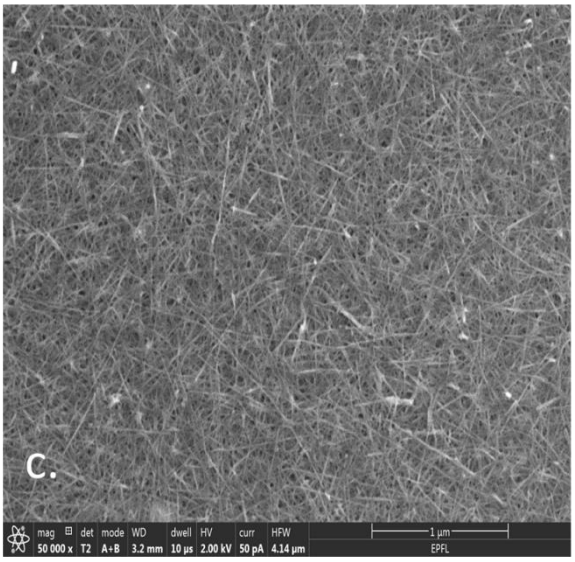

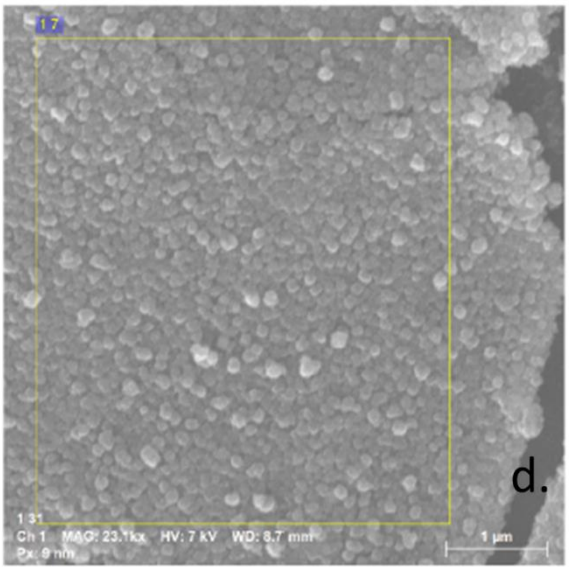

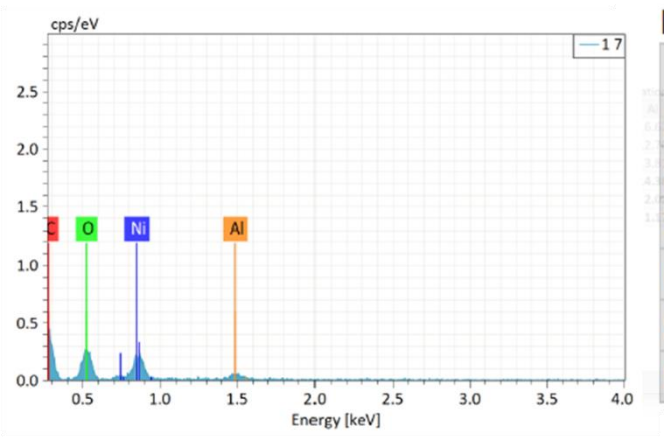

e.

Normalized mass concentration [%]

Spectrum	C	O	Al	Ni
2 2	7.57	49.25	16.62	26.56
2 3	22.23	40.35	12.70	24.73
2 4	19.58	42.72	13.81	23.88
Mean	**16.46**	**44.11**	**14.38**	**25.06**
Sigma	**7.81**	**4.61**	**2.02**	**1.37**
SigmaMean	**4.51**	**2.66**	**1.17**	**0.79**

f.

Figure 3_ 39: Optical microscope images of a) bare and b) Ni/Al–modified CNT electrode (after oxidation in 0.1 M KOH). FE–SEM micrographs obtained for c) a bare and d) a Ni/Al–modified CNT electrode. e) EDX spectrum and f) EDX analysis of the electrodeposited Ni/Al–film on the CNT electrode. (c) is taken and adapted from ref 66.

In order to evaluate the applicability of the as–prepared electrodes as disposable amperometric sensors with reproducible performance in real systems, the electrodeposition of the Ni/Al–LDH was performed in triplicate employing three electrodes of the same geometrical area and produced with the same fabrication procedure. Then the electrocatalytic properties of the Ni/Al film on the CNT electrode were investigated by using ethanol (EtOH) as analyte.

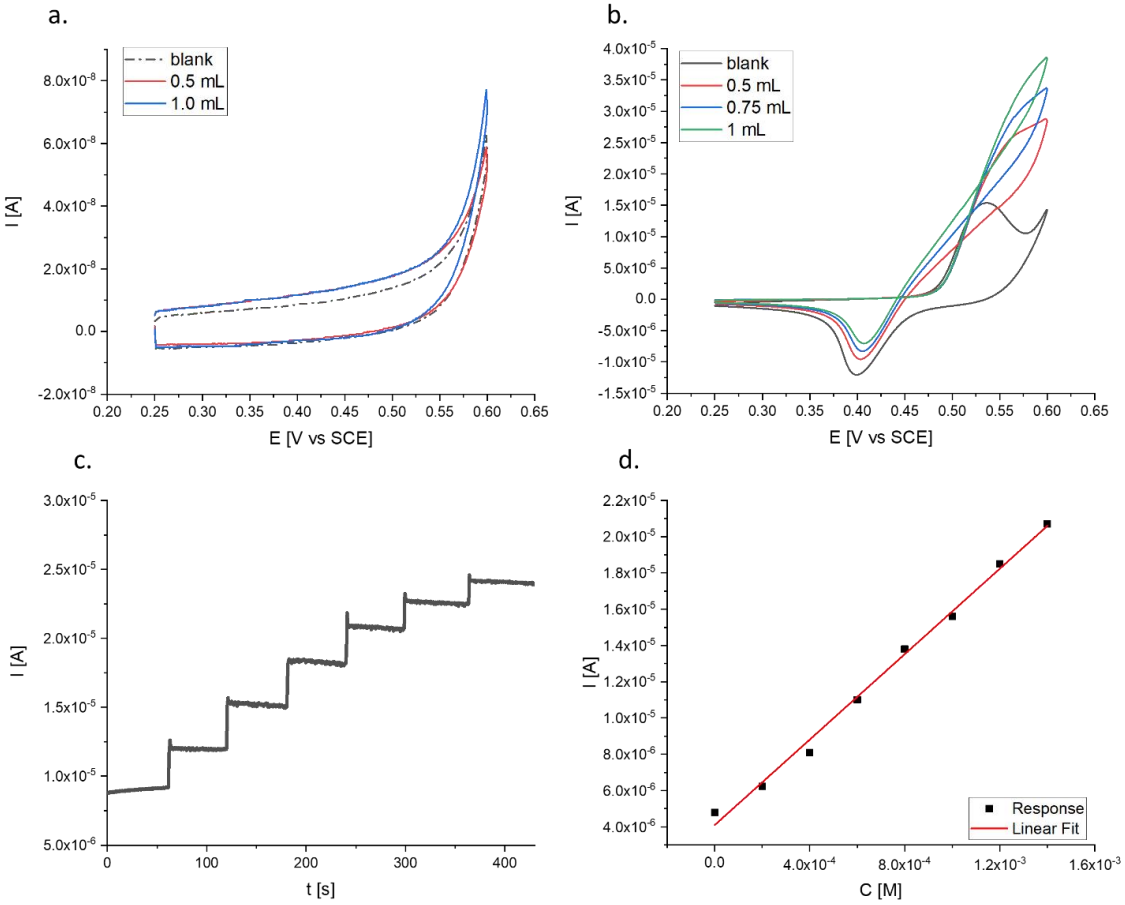

Figure 3_ 40: a) CVs recorded at an inkjet–printed bare CNT electrode in 0.1 M KOH, without EtOH and with EtOH at different concentrations, scan rate: 0.01 V s^{-1}. b) CVs recorded at CNTs inkjet printed electrode coated with Ni/Al–LDH in 0.1 M KOH, containing EtOH at different concentrations, scan rate: 0.01 V s^{-1} c) I vs. time plot obtained for the same Ni/Al–LDH modified electrode biased at +0.55 V in 0.1 M KOH under magnetic stirring, while the EtOH concentration was increased by progressive additions of a concentrated solution; d) Calibration line for EtOH determination.

Figure 3_40 a shows the CVs recorded at a bare CNT electrode following the additions of different amounts of EtOH to a 0.1 M KOH solution. An increase of the anodic current due

to the oxidation of EtOH is barely detected. However, when the electrode is modified with a Ni/Al–film, a clear oxidation signal is detectable as an anodic current peak or wave, which is proportional to EtOH concentration. In order to evaluate sensitivity of the Ni/Al–film/CNT electrodes for the detection of EtOH, chronoamperometry was carried out under stirring in 0.1 M KOH by adding aliquots of an EtOH stock solution. The chronoamperometric response was obtained by setting the electrode potential at +0.55 V (Fig. 3_ 40 c), as determined from the CV experiments. The sensitivity and LOD (Table 3_9) were measured with three Ni/Al–film/CNT electrodes and calculated by using the corresponding calibration lines. Ni/Al–LDHs display satisfactory performances. Notably, the performances of the three electrodes were very close to each other, as can be seen from the values reported in the Table, so demonstrating a good reproducibility of the inkjet printing process combined with optimized electrosynthetic protocols.

Table 3_ 9: LOD values and sensitivities obtained from the calibration lines for EtOH determination by chronoamperometry using Ni/Al–modified CNT electrodes.

	Sensitivity ($AM^{-1}\,cm^{-2}$)	**LOD (M)**
1	0.0259 ± 0.0003	$1{\cdot}10^{-4}$
2	0.0261 ± 0.0002	$1{\cdot}10^{-4}$
3	0.0266 ± 0.0005	$1{\cdot}10^{-4}$

The results obtained in this preliminary study demonstrate the promising combination of inkjet printing and electrochemical modification of carbonaceous electrodes, such as carbon nanotubes. A detailed spectroscopic analysis of the films obtained will be carried out in the continuation of this work. In the future, the sensor shall be made more compact by printing a RE/CE electrode next to the working electrode to produce a two–terminal device. This will also offer further application possibilities, such as to change the analyte matrix from liquid to gas phase for EtOH sensing. In fact, solid–state gas sensors play an important role in environmental monitoring, chemical process control and personal safety, and electrochemical gas sensors are attractive thanks to their compactness and high performance.

3.4 Ex–situ study of Co–based LDHs oxidation

The application of LDHs in a wide range of fields is largely due to their properties such as simple methods of synthesis, low cost, large specific surface areas, high number of active sites and ability to interact with various catalytic supports, as already widely discussed.

Determining the correct structure–property–function relationships require a detailed description of the material in its working state.

Recent technological advances allow us to evaluate materials with a range of *in situ* techniques that have been developed to follow the evolution of materials in the presence of an external stimulus.

To date, the structural transformations which occur to a LDH while cycling in alkaline media, are not fully understood.

Utilizing *in situ* or *ex situ* techniques can help to answer the underlying questions regarding the transformations of the LDH material from a macro to a nano – scale perspective. These behaviours can be monitored and analysed in real time, thus providing a further understanding and optimization of the related processes.

For example, in literature, in situ TEM was applied to extensively characterize the thermal evolution of Ni/Fe–LDH nanomaterials. The combinative approach of TEM and SAED yielded both to a morphological and crystallographic understanding of such processes. As the Ni–Fe LDH nanomaterials were heated *in situ*, an amorphization occurred at 250 °C, followed by a transition to a heterogeneous structure of NiO particles embedded throughout a $NiFe_2O_4$ matrix at 850 °C, confirmed by high–resolution TEM and scanning TEM[73].

More recently, Dionigi et al.[74] combined electrochemical measurements, operando X–ray scattering and absorption spectroscopy, and density functional theory (DFT) calculations to elucidate the catalytically active phase and the mechanism for OER. In spite of previous reports on the *ex situ* crystal structure of the as–synthesized precursors of M/Fe LDH catalysts and *in situ* local structure based on XAS measurements, little was before known about the long–range crystal structures of the catalytically active phase under OER conditions.

The *in situ* crystal structures of Ni/Fe and Co/Fe LDHs under OER conditions were indirectly inferred from the crystal structures of the host Ni and Co oxyhydroxides,

respectively. More specifically, for Ni/Fe LDH, a γ–NiOOH phase, in which water and cations are intercalated between layers, has long been speculated. However, no direct evidence was observed to confirm the hypothesis, as previous in–situ structural studies could not provide the characteristic interlayer spacing that can be used to differentiate between the γ–NiOOH phase and other common phases, such as the anhydrous β–NiOOH phase.

For Co/Fe LDH, in analogy to Ni/Fe LDH, a transformation similar to the one above described can be hypothesized under OER conditions. However, there is no analogous γ–CoOOH phase with species intercalated between layers; the other two known β–CoOOH and CoO_2 phases show no intercalation. As a consequence, a Fe– doped β–CoOOH has been proposed as the active phase of Co/Fe LDH under OER conditions. Density functional theory (DFT) calculations allowed to examine all of the above hypotheses and to extract atomic–scale details by screening suitable candidate phases and comparing their relative stability with that of known phases. Actually, even the atomic–scale structure of the γ–NiOOH phase itself is still unclear. The lack of these atomic–scale details has, in turn, made it highly challenging to choose appropriate models for DFT–based mechanistic studies. Although significant efforts have been made to explain the high activity of M/Fe LDHs, all the studies suggest that large uncertainties exist concerning the relationship between the active site structure and the catalytic mechanism. These uncertainties, resulting from an incomplete consideration of this ensemble of factors, have hindered the mechanistic understanding of the high activity of Ni/Fe and Co/Fe–LDHs for OER, which further hampers the prediction of new catalysts with improved performance.

Combining electrochemical measurements with *operando* wide–angle X–ray scattering (WAXS) and XAS data, as well as *ab initio* molecular dynamic simulations, and a synergistic DFT approach that was benchmarked specifically for the strongly correlated Fe, Co, and Ni oxides and (oxy)hydroxides, they were able to unravel the crystal structures and electrocatalytic OER mechanisms of the active phases of Ni/Fe and Co/Fe LDH catalysts. They provided the first direct atomic–scale evidence that, under OER conditions, both Ni/Fe and Co/Fe LDHs transform from the as–prepared α–phase to a deprotonated γ–phase. The oxidative phase transitions are characterized by ~8% contractions in both the in–plane lattice constant and the interlayer distance, which are induced by the oxidation of Fe and M(II)

(Ni or Co), and by the anion–to–cation switching of intercalated ions, respectively. Then, they adopted the *in situ* identified γ–phases to study the OER mechanism through DFT–based calculations.

Considering the great applicability of LDHs, it is necessary to elucidate all the possible structural modifications in order to comprehend and optimize their properties.

The following section arises from a specific scientific question: "what does it happen to the structure of a Co based– LDH upon oxidation?" One can understand where this doubt comes from looking at Figure 3_41.

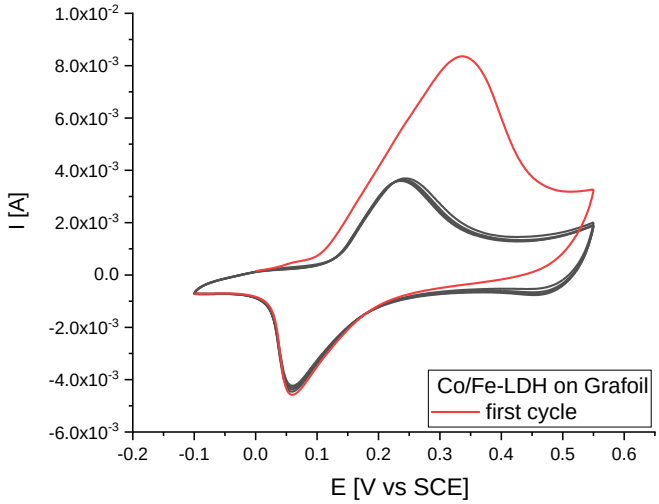

Figure 3_ 41: CV of a Co/Fe–LDH in 0.1M NaOH recorded at 0.01 V s^{-1}.

Several papers report that the first CV cycle recorded for Co based–LDHs is remarkably different from the following ones: in fact, during the first cycle an irreversible reaction occurs involving Co(II) sites.

Our group has already performed PXRD analysis in order to identify the structure of the various electrodeposited thin films, also upon oxidation in alkaline media[75]. PXRD of the pristine Co/Al–LDH showed the typical patterns of a structure with a low crystallinity. All reflections were indexed as those typical of a hydrotalcite–like structure. The structural characterization was also made on the material submitted to one CV cycle, with the potential stopped at 0.0 V where it appears stable. Compared to the starting LDH structure, the XRD pattern of the phase obtained after potential scan revealed a deep modification. Despite the poor crystallinity of the phase, it is clearly observed that all the diffraction lines, i.e., the basal and higher order (00l) reflections and the non–basal h k l reflections are shifted at

higher angles. In particular, the (003) diffraction line characteristic of the interlayer distance shifts from 7.68 Å for the Co/Al–CO_3 phase formed in basic medium to 6.89 Å for the oxidized phase whereas the (00l) reflection evolves from 1.53 Å to 1.43 Å. Such a displacement of the diffraction lines cannot be explained by a simple partial oxidation of the Co(II) into the layer leading to a $Co^{II}Co^{III}Al^{III}$ – LDH phase associated with an anion intercalation to balance the charge in excess produced by the oxidation process. Yet, the partial modification of the Co oxidation state induces only a slight modification of this lattice parameter, which is systematically described in the range of 1.53 ± 0.1 Å, in good agreement with a maintenance of the brucite–like structure. In that work, the XRD pattern modifications, and particularly the shift of the (00l) reflection clearly evidenced that the first irreversible oxidation process of Co/Al–LDH precursor phase led to the formation a new layered Co/Al–based phase which appeared comparable to the γ–CoOOH–like phase and is involved in the subsequent electrochemical processes.

Starting from all the previous studies, we performed *ex situ* XPS and XAS experiments with the aim to better understand the modifications of cobalt based LDHs in alkaline media.

3.4.1 Pristine Materials

The evaluation of Co/Al(Fe) electrodeposited films has been carried out by XPS and XAS in order to gather complementary information, i.e. surface and bulk, respectively.

The XPS detailed spectrum of cobalt hydroxide, cobalt oxyhydroxide, and cobalt oxide are very well known and taken as references[28]. Starting from literature, same values of FWHM (both Gaussian and Lorentzian), positioning, number of satellites of cobalt hydroxide have been fitted for the pristine materials and adjusted to the recorded spectra. Of course, high–resolution Co 2p spectrum shows spin–orbit splitting into $2p_{1/2}$ and $2p_{3/2}$ components, and both components qualitatively contain the same chemical information. The whole signal has been fitted and not only the $2p_{3/2}$, including the shake–up satellites of the cobalt ions. From standards[28], the intense main peaks are at 781.5 eV for $Co^{II}(OH)_2$, and at 780.3 eV for $Co^{III}O(OH)$. In the higher BE region, three peaks are required to fit the satellites for each material. In addition to the normal core photoelectron lines, a satellite line structure can be always observed in the late 3d transition metal compounds. These additional spectral lines have been related either to a coupling between unpaired electrons in the atom (multiplet

splitting) or to a multiple electron excitation (the so–called "shake–up"). They result from the interaction with metal valence electrons and provide chemical environment information about the metal ions. It is also worthy to highlight that cobalt(II) compounds are high spin complexes (s=3/2), whilst all the Co(III) complexes are diamagnetic (s=0). As a consequence, the Co(II) compounds show intense and very broad satellites, while these additional peaks are not observed in the case of Co(III).

In particular, it is evident from figure 3_42 that the Co sites of the pristine LDHs can be well fitted as reported for a $Co(OH)_2$ phase, and this is true for both samples, i.e., independently from the nature of the trivalent metal.

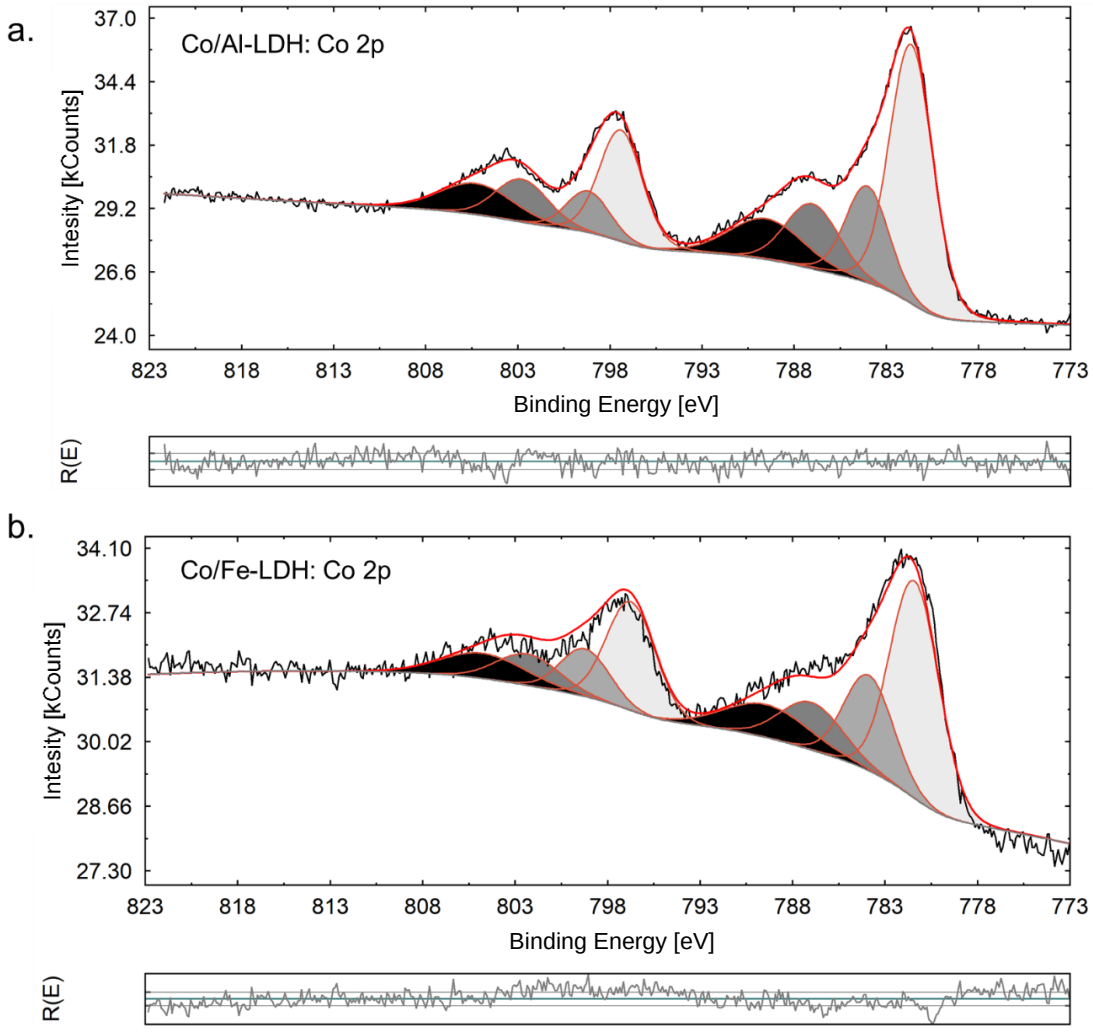

Figure 3_ 42: High–resolution Co 2p spectrum for a) pristine Co/Al and b) Co/Fe LDHs

As trivalent metals, Al and Fe have been studied. As far as Al 2p is concerned (figure 3_43a), a single signal is registered and can be described as $Al(OH)_3$. In this case, it fits well with gibbsite–like $Al(OH)_3$, in which each Al cation is octahedrally coordinated by 6 OH groups

and each hydroxyl group is coordinated by two Al cations with one octahedral site vacant (BE=74,5 eV)[51].

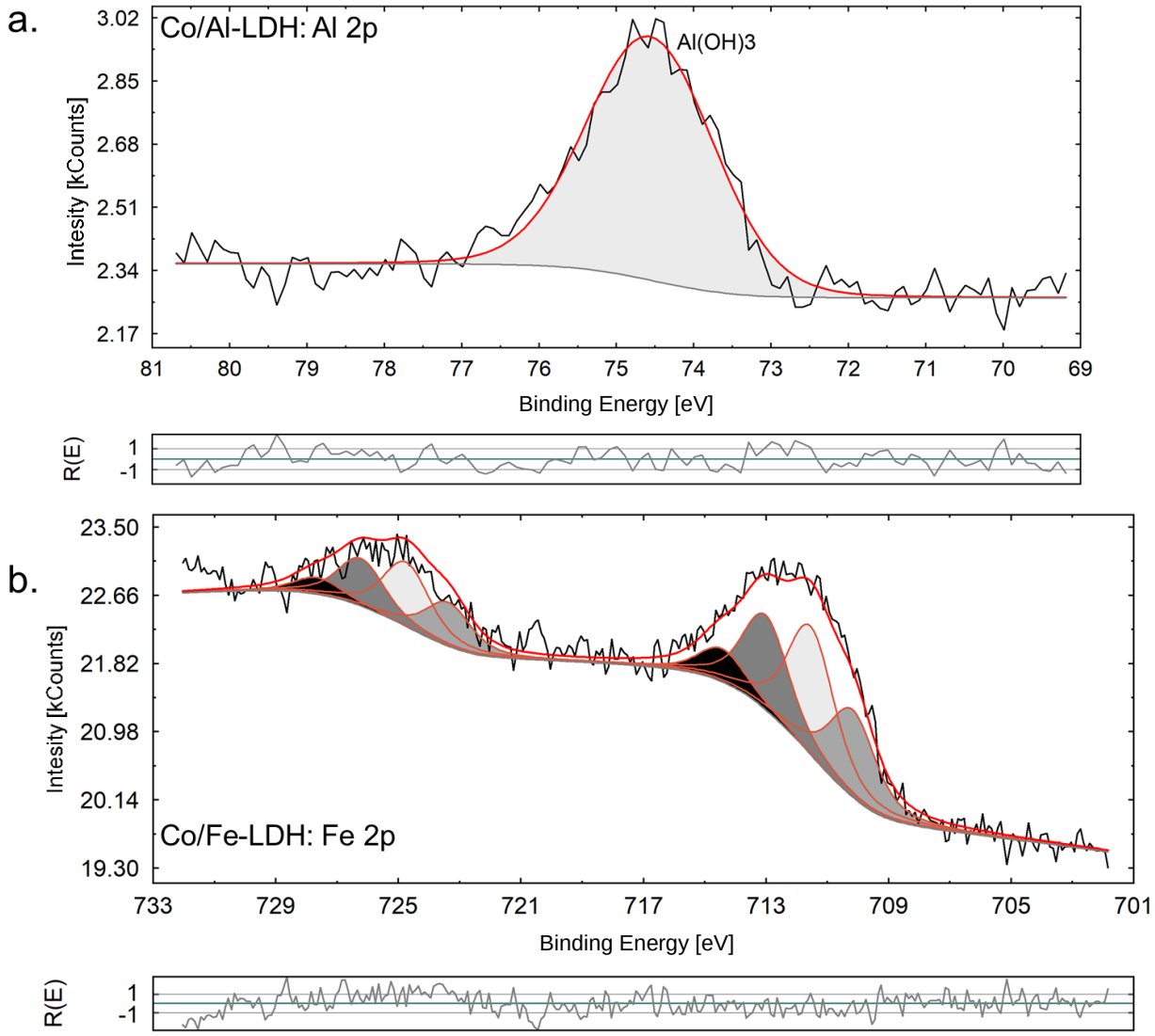

Figure 3_ 43: High–resolution spectrum for a) Al 2p in pristine Co/Al and b) Fe 2p in pristine Co/Fe LDHs

For the analysis of photoelectron spectra of Fe, several references need to be employed[76]. A comparison of peak shapes to the theoretically calculated multiplet split peak shapes needs to be taken into account: multiplet FWHM, splittings and weightings are usually plausible. An analysis of satellite to main peak separation is valuable. All Fe(II) (which can be described as high spin, since low spin Fe(II) does not exhibit multiplet splitting) and Fe(III) species can be fitted with multiplet structure. Variation in peak spacing and intensity occurs when different ligands are used. Broad satellite peaks of varying intensities at binding energies above the main Fe $2p_{3/2}$ structure are present in the spectra for all high spin

compounds. FWHM values are reported only for 10 eV pass energy, therefore 10 eV pass energy was employed also for LDH samples. For example, it can be seen that various Fe(III) compounds have a similar range of Fe 2p binding energies and vary mostly in peak shape and satellite intensities as the one reported in figure 3_43b. Any attempt to fit two or more Fe(III) species to a spectrum will consequently contain an inherent degree of error. As well, overlap of the Fe(III) satellite structure with the Fe(0) and Fe(II) Fe $2p_{1/2}$ portion of the spectrum will result in setting the higher binding energy background endpoint placement at a point that will not cover the satellite structure of the Fe(III) species. This requires any fitting of mixed chemical state systems containing Fe(III) species to omit the higher binding energy Fe(III) satellite from the envelope of peaks; this will again increase the error associated to the curve fitting. Therefore, we can describe our spectra as dominated by Fe(III)–like species, since it is also corroborated by XAS data (figure 3_44b).

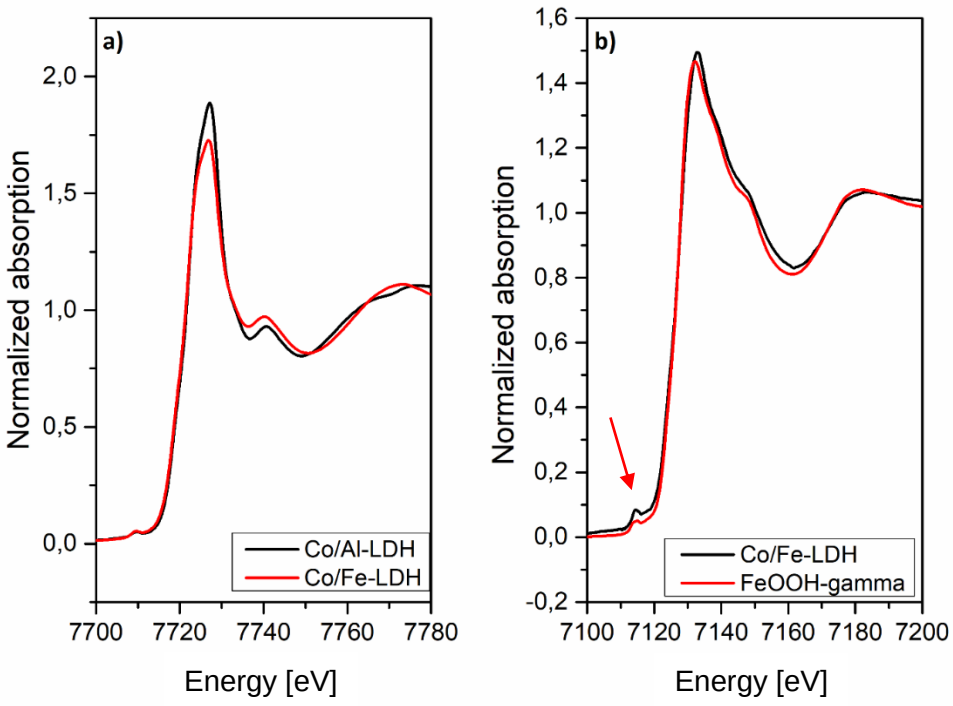

Figure 3_ 44: Comparison of the XANES spectra recorded for Co/Fe and Co/Al–LDHs at Co K–edge (a) and comparison of Co/Fe–LDH with FeOOH at the Fe K-edge (b).

Due to its strong sensitivity for the metal site, local structural and electronic information can be gained looking at the XAS spectra of the electrodeposited LDHs at both Fe and Co sites, as we are interested also in bulk characterization of the synthesized materials. Fig. 3_44 shows the comparison of the XANES spectra at Co K–edge recorded for both Co/Fe

and Co/Al LDHs. Both traces are almost super imposable, and, therefore, the local structure and charge associated to the Co site appear identical in the two electrodeposited LDHs. The state of charge can be evaluated by looking at both pre–edge peak position and overall shape of previously published Co(II) XANES data, which indicated a Co(II) formal oxidation state of an atom in an octahedral environment. Fig. 3_44b displays the XANES at the Fe K–edge of the Co/Fe LDH. The curve is characterized by a pre–edge peak at about 7114 eV which is related to the 1s–3d electronic transition and can be used as a fingerprint for the local charge around Fe. The position and the intensity of such a peak indicate mainly the occurrence of Fe(III) oxidation state in an octahedral environment. Confirmation of such an assignation comes from a comparison with a FeOOH reference sample.

To explore more deeply the local structure around the metals an EXAFS analysis has been performed at both Co and Fe K–edge. Figure 3_45 displays details of the best fit procedure for the Co/Fe LDH. Due to the presence of two metals sites, the structure of this material has been analyzed from the two photoabsorbers, i.e., Co and Fe. The Fourier Transforms (FTs) of the corresponding EXAFS signals are depicted in the panels (c) and (d). This plot displays the pseudo–radial distribution of the atoms surrounding the central one and suggests that two main peaks contribute majorly to the experimental photo–absorption process at both metal sites. They are related to the typical LDH structure, and the first peak is due to the first atomic shell surrounding the Co, and the second peak, at about 2.6 Å, is associated with the second coordination shell, formed by 6 metal atoms (4 Co and 2 Fe). The same coordination is observed at the Fe site. Therefore, only these signals have been used in the fitting procedure. This is clearly shown in the panels (a) and (b) of the Figure for both Co and Fe K–edges, respectively. These plots report various theoretical contributions to the total EXAFS signal. The Co–O and Fe–O first shells largely contribute to the total signal in their respective panels but the metal–metal signal in the second shell is rather important for the interpretation of the total experimental one. It is also interesting to notice that the two–body $\gamma^{(2)}$ Fe — Co signal has a smaller intensity when compared to that of the $\gamma^{(2)}$ Co — Co one. This can be ascribed to a structural disorder at the Fe site.

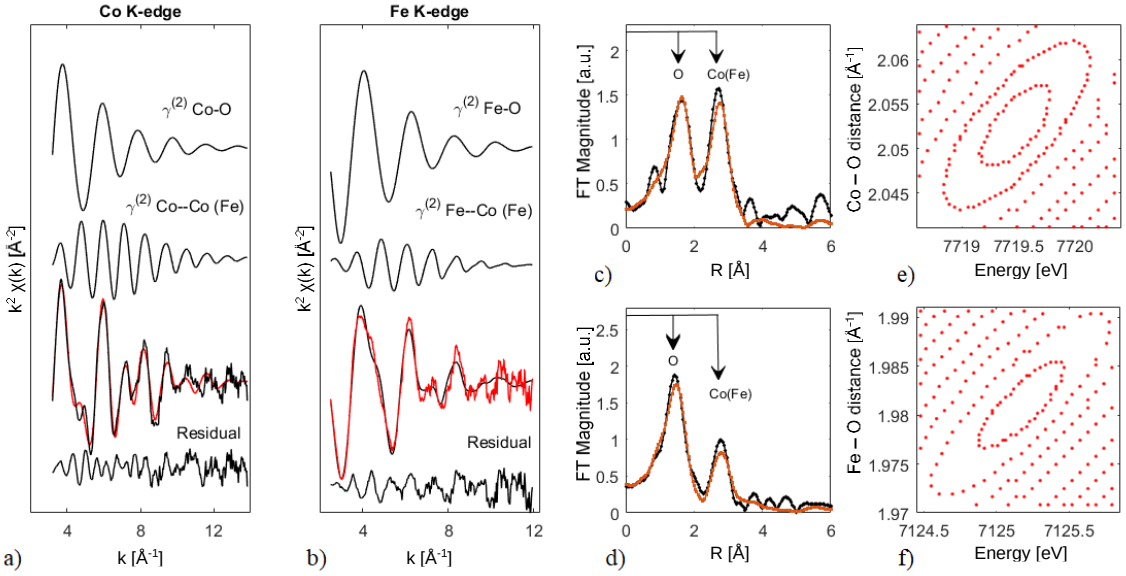

Figure 3_ 45: Best fit of Co/Fe LDH at both Fe and Co K–edges. Panels (a) and (b) show the details of the EXAFS analysis for the Co and Fe edge, respectively, in terms of individual EXAFS contributions to the total theoretical signal. The comparison of the total theoretical signal (black curve) with the experimental one (red curve) is also shown. The residual signal is reported at the bottom. Panels (c) and (d) display the fit of the corresponding FTs of EXAFS signals. Panels (e) and (f) display the contour plots for the error determination of the Co–O and Fe–O first shell distances.

Table 3_10 reports the inter–atomic distances and the corresponding EXAFS Debye–Waller factors (σ2, best–fit) of the investigated LDHs. The statistical errors associated with the parameters are indicated in parentheses. They were determined by correlation maps (contour plots) for each pair of parameters. These plots were selected among the parameters having a strong correlation to reflect the highest error. The inner elliptical contour corresponds to the 95% confidence level. Panels (e) and (f) report two examples for the highly correlated Co–O and Fe–O variables. The trivalent metal (Fe or Al) has an effect on the local structure of the electrodeposited LDHs, even at the Co site. The Co–O interaction significantly enhances from 2.053 to 2.082 Å by substituting Fe^{3+} with Al^{3+}, while the interaction at the second shell holds at a value of about 3.11–3.13 Å for both Co—Co and Co—Al (only in the Co/Al–LDH case). Lower EXAFS bond variances are observed in Al–based LDHs, as seen from both σ2 Co–O and σ2 Co—Co comparison. This suggests a more regular and crystalline structure of the Co/Al with respect to the Co/Fe–LDHs, probably because less strain is

induced by the smaller Al atomic size, in good agreement with the better crystallinity pointed out by XRD data (section 3.1.3). A comparison of the EXAFS bond variance of the Co/Fe–LDH second shell reveals a large contribution from the structural disorder at the Fe site with respect to the Co one, as previously suggested by Figure 3_45 panel (a) and (b). This fact can be extended to other LDHs (e.g. Ni/Fe LDH) where the trivalent site is found to be more structurally disordered than the divalent one.

Table 3_ 10: EXAFS Analysis. Atomic first and second shell distances and corresponding EXAFS Debye–Waller factors of the pristine LDHs. Errors (in parentheses) were determined by Contour plots (see Fig. 3_45 e and f).

Parameter	**Co–Al/LDH**	**Co–Fe/LDH**	
	Co K–edge	**Fe K–edge**	**Co K–edge**
Co–O /Å	2.053 (4)		2.082(8)
$\boldsymbol{\sigma^2_{Co-O}}$ **/Å²**	0.008 (1)		0.006(1)
$\mathbf{CN_{Co-O}}$	6		6
Co–Co /Å	3.135(6)		3.11(1)
$\boldsymbol{\sigma^2_{Co-Co}}$ **/Å²**	0.010(1)		0.0064
$\mathbf{CN_{Co-Co}}$	6		4
Co–Al /Å			3.11(2)
$\boldsymbol{\sigma^2_{Co-Al}}$ **/Å²**			0.005(2)
$\mathbf{CN_{Co-Al}}$			2
Fe–O /Å		1.981(5)	
$\boldsymbol{\sigma^2_{Fe-O}}$ **/Å²**		0.010(1)	
$\mathbf{CN_{Fe-O}}$		6	
Fe–Co(Fe)/Å		3.116(8)	
$\boldsymbol{\sigma^2_{Fe-Co(Fe)}}$ **/Å²**		0.017(2)	
$\mathbf{CN_{Fe-Co(Fe)}}$		6	
$\mathbf{E_0}$ **/ eV**	7719.4(5)	7125.1(5)	7722.1(8)
$\mathbf{S_0^2}$	0.70(4)	0.71(5)	0.70(3)

Finally, the signal of the oxygen was also evaluated through XPS (Figure 3_46). Oxygen signal is not very reliable due to the fact that an Auger line of cobalt, i.e. Co(LMM), lies nearby and compromises the background and the fitting of the oxygen signal, as can be easily seen. In any case, the signal is completely dominated by OH^- and interstitial water.

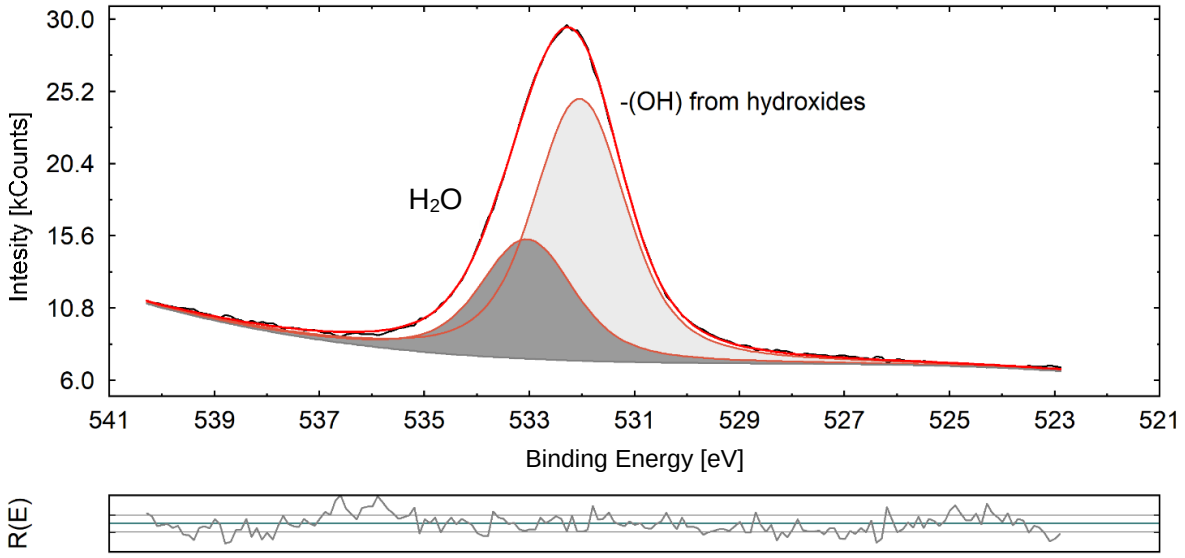

Figure 3_ 46: High–resolution O 1s spectrum for Co/Al LDH.

3.4.2 Cycling of electrodes

Figure 3_47 reports CVs relevant to Co based LDHs. As already mentioned, Co is the electroactive centre and its peak undergoes a great change during the first sweep: in particular, *ex situ* XAS and XPS were recorded at the potentials indicated by the arrows on Figure 3_47 a and b considering only the first two cycles. Therefore, the indicated voltages represent the values at which the voltammetric wave was stopped in order to acquire spectra. Typically, in literature, Co is believed to follow these redox reactions[19]:

9. $Co(II)\text{-}LDH + OH^- sol \rightarrow Co(III)(OH)\text{-}LDH + e^-$
10. $Co(III)(OH)\text{-}LDH + OH^- sol \rightarrow Co(IV)(OH)\text{-}LDH + e^-$

Therefore, it was expected to detect at least a mixed valence in the spectra.

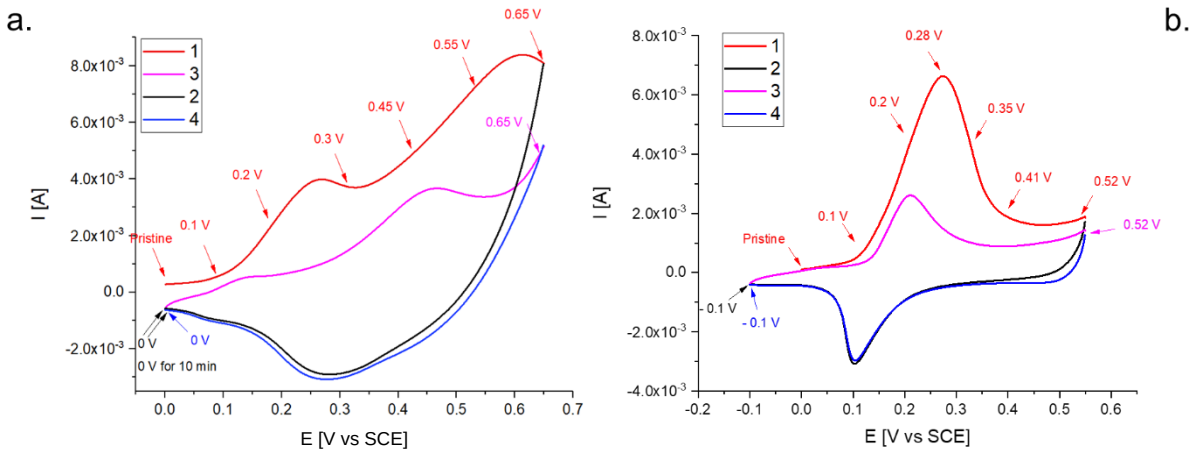

Figure 3_ 47: CVs of first four segment of a) Co/Al and b) Co/Fe–LDHs in 0.1 M NaOH. The numbers present in the legend indicates the segment of the CVs.

Figure 3_48 reports the high–resolution spectra of Co in a fully oxidized sample, namely Co/Al (note that the same considerations are valid also for the Co/Fe–LDH). From a first sight, it is possible to see the great difference with Figure 3_42 a, i.e., the deconvoluted spectrum suggests that the oxidized Co sites can be well fitted as a CoO(OH)–like phase.

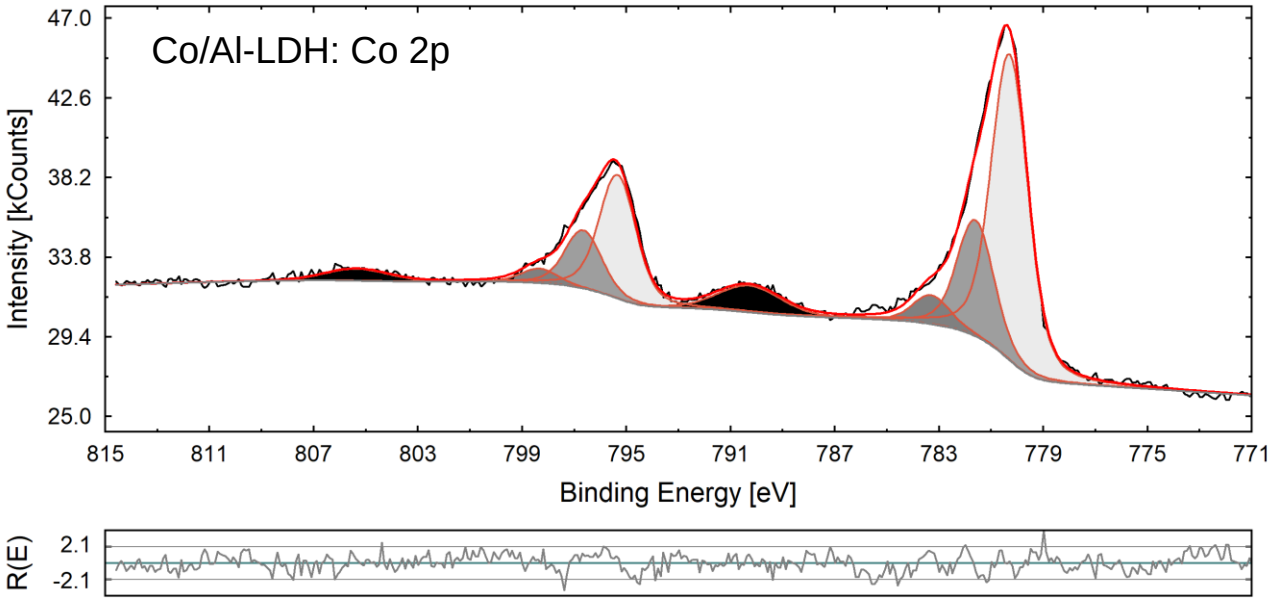

Figure 3_ 48: High–resolution Co 2p spectrum for Co/Al LDH

In the first cycle an irreversible change from a cobalt hydroxide to a cobalt oxyhydroxide–like phase occurs. The material is not able to go back to the initial state. Figure 3_49 reports the evolution of Co 2p signal over cycling. The oxyhydroxide–like phase seems to be stable during cycle and no big shifts are seen from oxidized or reduced state (light BE shift). It is

worth mentioning that maybe the CoO(OH) is not a pure phase, but a really small peak intensity due to Co(II) presence can be seen (around 782 eV), leading a mixed state valence Co(II)/Co(III) whose ratio can change between the oxidized and reduced states. In general, a mixed Co(II)/Co(III) valence for all the cycled samples can be highlighted.

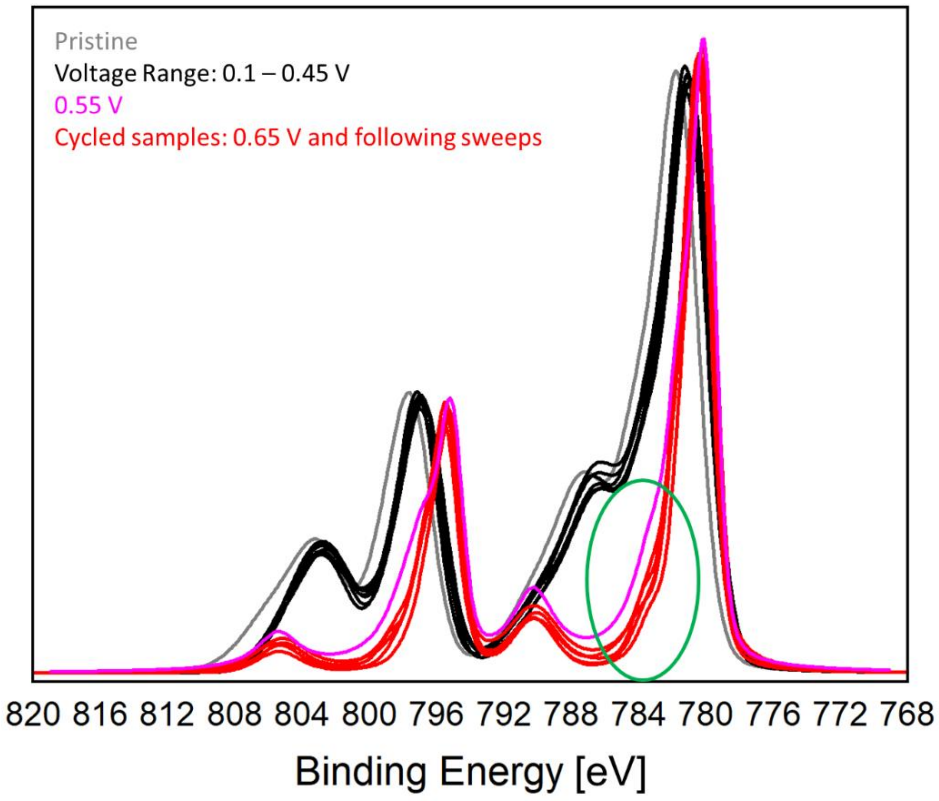

Figure 3_ 49: Co 2p peaks (the peak indicated by green circle is located at about 782 eV). Black lines refer to the potential range 0.1-0.45 V, in which no transformation occurs to the structure. The change is evident from 0.55 V on, with no apparent shape modification in further reduction/oxidation of the activated phase.

From the article by Scavetta et al.[75] about electrochemical behaviour of Co/Al–LDHs it is also reported that almost 80% of the Co(II) cations are involved in the oxidation reaction, indicating an almost total oxidation of the LDH phase in the first sweep. This finding suggested the idea of a quite high electrochemical accessibility to the Co cations within the LDH layer. Moreover, the two broad peaks present in the CV (typical of a Co/Al–LDH) have been assigned to the oxidation of Co(II) to Co(III) and then to Co(IV). Due to the highly capacitive shape of the CV response in the analysed potential region, it was not trivial to correctly extract the Faradaic contribution and, therefore, to accurately calculate the number of Co cations involved in the second electron transfer process. Anyway, the authors

estimated that 4.2×10^{-9} mol were furtherly involved, which corresponds to only 2% of the Co(III) generated in the first oxidation process. These results already published by our research group were considered still valid.

Therefore, the purpose of this section is to start to unravel the real mechanism from both electronic and structural points of view through the "suitable" analytical techniques.

From quantification of XPS spectra, it is possible to highlight that 75% of Co(II) cations are transformed in Co(III) during the first oxidation segment, i.e. in good agreement with what was stated before. It also possible to affirm that the Co sites which actually undergo further redox reaction are around 2%. This value was obtained comparing the spectra of the fully oxidized LDHs with the one of pristine materials, and again confirms what previously reported. However, no signal relevant to Co(IV) can be fitted.

It is noteworthy that the modification of the structure seems to be abrupt and not gradual. From a potential equal to 0.55 V for Co/Al (and 0.35 V for Co/Fe–LDH), the structure has almost completely changed. The newly formed phase is also the one active in the further redox process.

The application of XAS, considered a more suitable analytical bulk technique with a strong selectivity for the atomic species, allowed to corroborate the main results pointed out by the XPS study.

Figure 3_50 displays the comparison of the spectra obtained for Co/Al–LDH while multiple oxidations and reductions take place. In the panel (a) the XANES curves behaviour suggests that the charge of the probed metal, i.e., Co, is varied, whereas the structure formed at the end of the first oxidation segment is conserved. This means that, from the second segment onward, the charge variations are associated to the redox couple (Co^{2+}/Co^{3+}), but in the frame of the newly formed active phase.

In addition, panel (b), which displays the Fourier Transform (FT) of the EXAFS part of the spectra, adds a quantitative content to the structure determination: all the peaks are in the same position, indicating the same structure, but with a variable structural disorder, highlighted by different peak intensities.

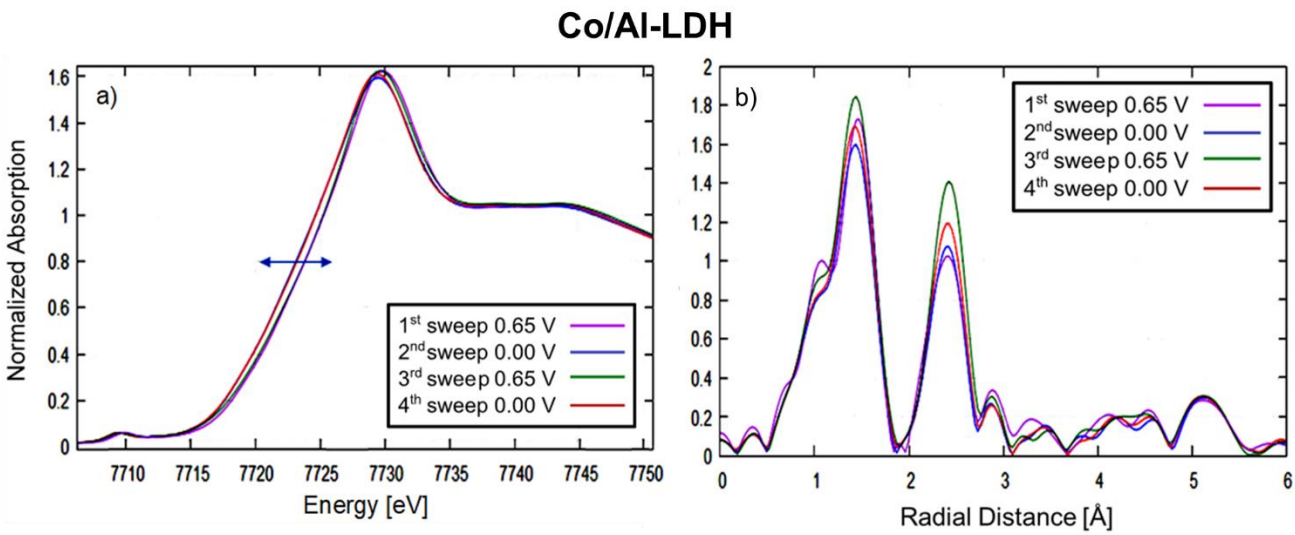

Figure 3_ 50: Panel (a) displays Co/Al-LDH XANES curves behaviour which suggests a charge modification of Co between oxidized and reduced forms (visible from the arrow, which indicates small differences in energy) and (b) shows the fit of FTs of EXAFS.

Similar consideration can be made for the Co/Fe–LDH case as the evaluation of Co K–edge in XAS show analogous features. The behaviour upon oxidation is illustrated in Figure 3_ 51. The XANES curve confirms that the modification of the structure seems to be abrupt and not gradual (see the arrow) as already seen in XPS for what concerned both LDHs.

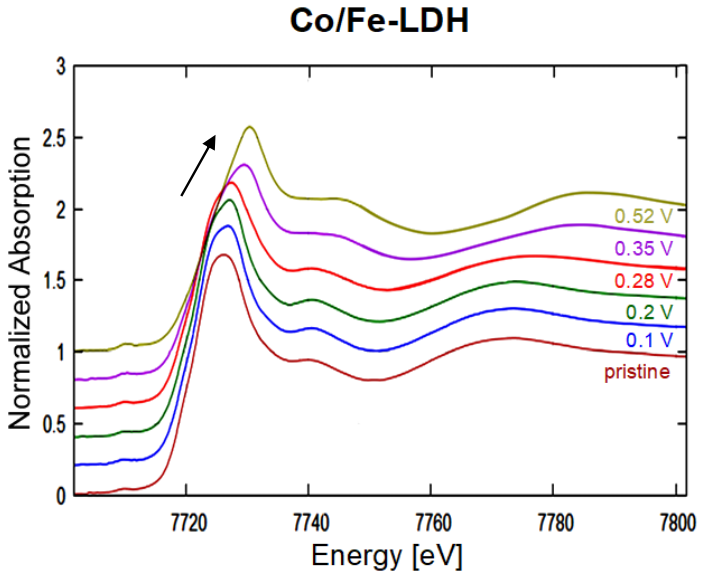

Figure 3_ 51: XANES spectra recorded for the Co/Fe–LDH at Co K–edge upon oxidation in 0.1 M NaOH.

Summarizing the findings highlighted for Co sites with both techniques, we can state that:

1. An irreversible change from a cobalt hydroxide to a cobalt oxyhydroxide–like structure happens during the first oxidation segment.
2. The structure can be considered a sort of activated material which does not get back to the pristine structure after one CV cycle and it is always retained afterwards.
3. After the structure modification, it is again important to highlight that the charge associated to the Co sites changes according to the potential applied within the new activated form (see fig. 3_41).

Moreover, in the Co/Fe–LDH, the presence of this second metal in the structure allowed to monitor the formal oxidation state of Fe as well, by both XPS and XAS.

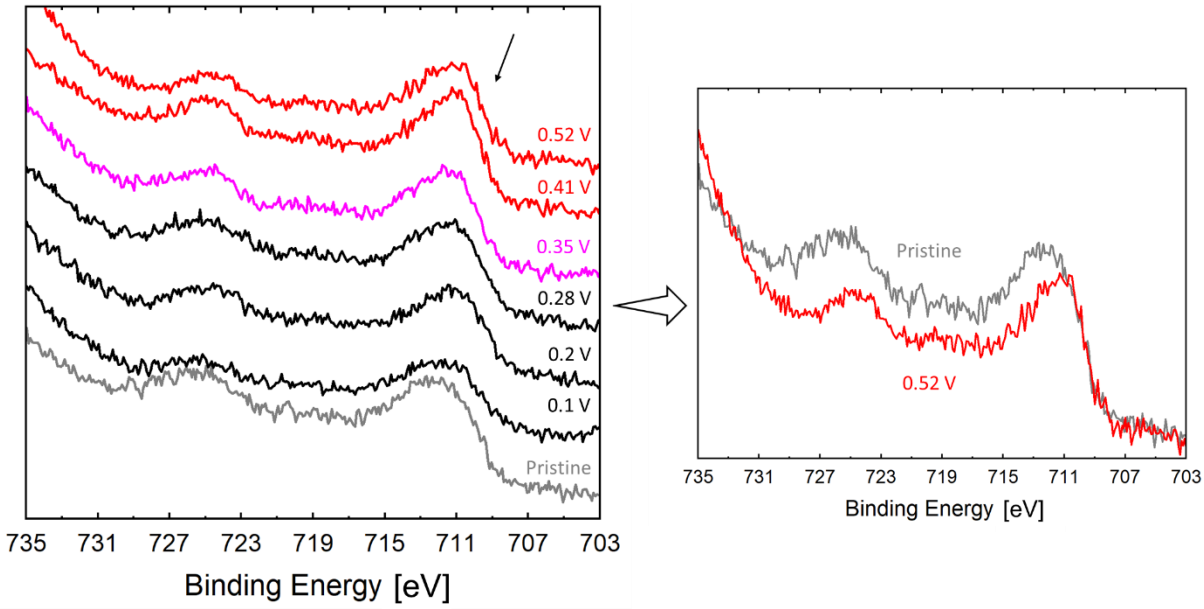

Figure 3_ 52: On the left, the modifications of Fe 2p signal recorded by XPS for the Co/Fe LDH during the first oxidation segment. The arrow indicates the small shift toward lower BEs of the spectra; on the right the difference between a pristine and a fully oxidized electrode is highlighted.

Figure 3_ 52 displays the unfitted (but charge corrected) signal of Fe 2p during the first CV segment. It is quite evident that, upon LDH oxidation, a shoulder at lower BE appears due to the formation of Fe(II), also visible from the shift of the maximum indicated by the arrow. This feature is even more evident looking at the Figure on the right, which compares the pristine and the fully oxidized electrodes. This finding corroborates the idea that Fe behaves synergistically in the redox reaction. This small reduction is also evident by the XANES

spectroscopy applied to the Fe K–edge case. A small shift toward lower energy of the pre–edge 1s–3d transition can be detected in the oxidized LDH with respect to the pristine one, as reported in figure 3_ 53, panel (a). Panel (b) displays the FTs of both pristine and oxidized Co/Fe–LDH samples. A very similar structure of the oxidized and reduced forms is found with a concomitant structural disorder contribution (higher disorder in the Co/Fe oxidized sample in respect to the Co/Al one). Unlike the Co case, the structure modification is strongly evident only in the case of the higher shell.

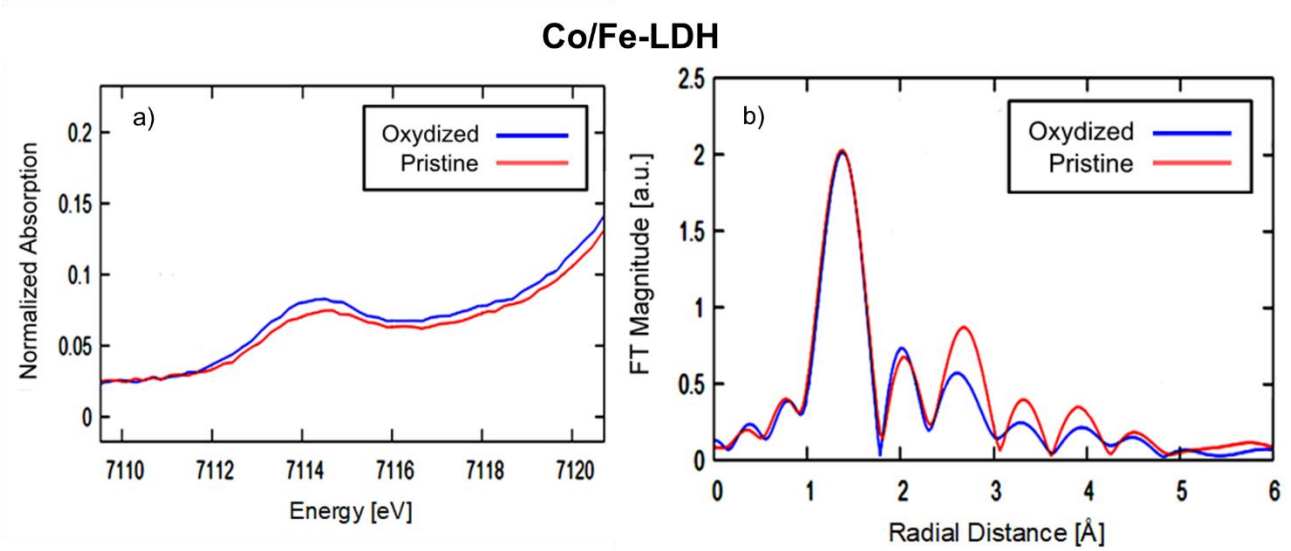

Figure 3_ 53: Panel (a) displays the comparisons between Co pre–edge parts of XANES spectra in the case of a Co/Fe–LDH. The behaviour suggests a charge modification between pristine and oxidized samples. Panel (b) shows the fit of the corresponding FTs of EXAFS.

Finally, aluminium and oxygen were also evaluated with XPS only (Figures 3_54 and 55). During the LDH oxidation, Al peaks shifts firstly to 74.1 eV (probably due to the substitution of nitrate with OH^-) and then the peak appears at 73.5 eV. The latter fits well with the α boehmite–like AlO(OH): its structure consists of double layers of oxygen octahedra partially filled with Al cations. The stacking arrangement of three oxygen layers is such that the double octahedral layer is in a cubic closed packing.

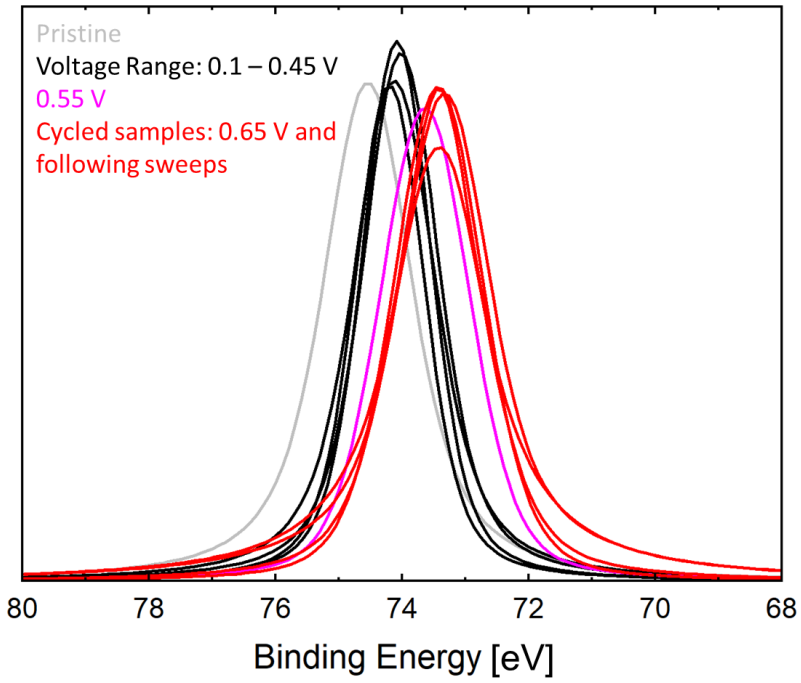

Figure 3_ 54: Al 2p sites of all samples

Finally, O1s was also considered (figure 3_55). Without over–interpreting the signal, there is an evident switch from a signal completely dominated by OH^- to a signal in which oxides and OH^- coexist (in good agreement with the model of an oxy–hydroxides like phase). Also for oxygen, the discussed features are valid both for the aluminium and the iron based LDHs.

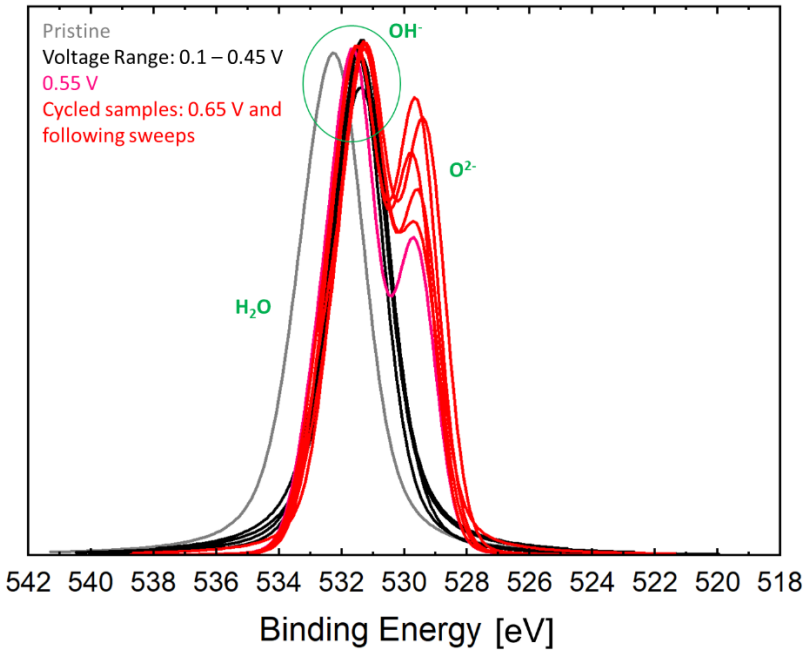

Figure 3_ 55: O 1s spectra of Co/Al LDH

Summarizing, by means of XAS and XPS techniques we investigated the modification of Co based LDHs structure upon oxidation in alkaline media. We observed that the first sweep acts as an activation step, which forms abruptly a new "phase", which is active in the further redox behaviour. Cobalt is definitively the redox active site which is involved in the deep modifications of the structure and the charge. Iron is confirmed to behave synergistically in the redox reaction, since it slightly reduces itself during oxidation of Co.

3.5 Ternary LDHs: applying chemometrics to electrochemistry

As mentioned in chapter 1, an additional metal centre can regulate the electronic structures of LDHs resulting in further synergistic effects between dopant and the host metals, forming ternary LDHs with higher electrochemical activities with respect to the binary ones.

In this section, efforts have been devoted to the controlled incorporation of cobalt into Ni/Al or Ni/Fe – LDH host layers to modulate their electronic structures, to promote the generation of metal higher valences, thus enriching the active sites and boosting the catalytic activities.

It is hereby reported a preliminary research in which the percentage of the metals in the electrolytic deposition baths was modulated, keeping always the same deposition procedure, temperature (25°C) and total metal concentration (30 mM) in order to evaluate a possible boost the LDH electrochemical response. The final aim was to find out which composition might lead to a LDH more suitable for applications in electrocatalysis (for example OER) or for energy storage.

The adopted experimental design is based on a simple ternary diagram, as can be seen in Figure 3_56. The constraint is given by the sum of components, which should be 1.

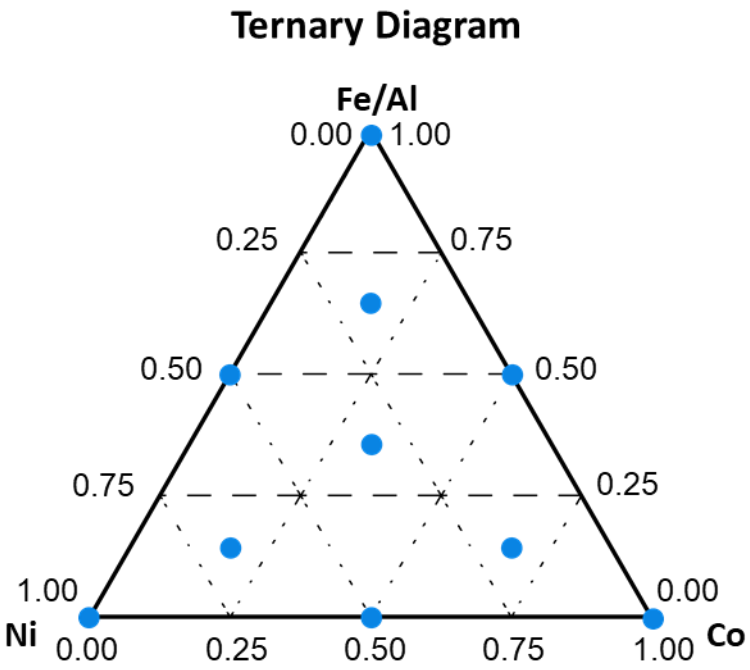

Figure 3_ 56: Experimental design based on the ternary diagram. Every angle of the diagram corresponds to a 100% in a specific metal.

The scheme of the procedure is reported in Table 3_11. Two sets of data have been considered, depending on the nature of the trivalent metal, i.e., Fe or Al. The same evaluation has been carried out for both samples. At first, when choosing the metals ratios, the existence domain of a LDH–phase was not taken into account.

Table 3_ 11: Scheme of explorative tests-

	Coded Factors			Real Factors		
Run	**A**	**B**	**C**	***Co***	***Ni***	***Fe/Al***
1	1	0	0	*0.6*	*0.2*	*0.2*
2	0	1	0	*0.2*	*0.6*	*0.2*
3	0	0	1	*0.2*	*0.2*	*0.6*
4	0.5	0.5	0	*0.4*	*0.4*	*0.2*
5	0.5	0	0.5	*0.4*	*0.2*	*0.4*
6	0	0.5	0.5	*0.4*	*0.2*	*0.4*
7	0.33	0.33	0.33	*0.33*	*0.33*	*0.33*
8	0.67	0.17	0.17	*0.67*	*0.165*	*0.165*
9	0.17	0.67	0.17	*0.165*	*0.67*	*0.165*
10	0.17	0.17	0.667	*0.165*	*0.165*	*0.67*

The experiment was divided in two parts:

- **Red experiments**: test on which the model is designed.
- **Blue experiments:** to be carried out after data treatment, in order to validate the obtained model.

Each run was made three times, in order to enable the calculation of a standard deviation. The experimental observables were considered to be position and intensity of peaks in CV, after stabilization of the responses. Samples are hereby named with the molar ratio indicated by the DOE.

In Figure 3_57 the CV responses for each set of data are reported. From Figure 3_57b, Co appears to be the main factor for the shift of the peaks to less andic potentials.

The LDH corresponding to the composition Co/Ni/Fe 020206 displays a worse behaviour than the others both in terms of peak intensity and potential values, which are quite highly

anodic. A greater amount of Ni leads to anticipated onset potentials for OER (the best LDH from various points of view seems to be CoNiFe 040402). In fact, it presents a very early onset potential (0.46 V vs SCE).

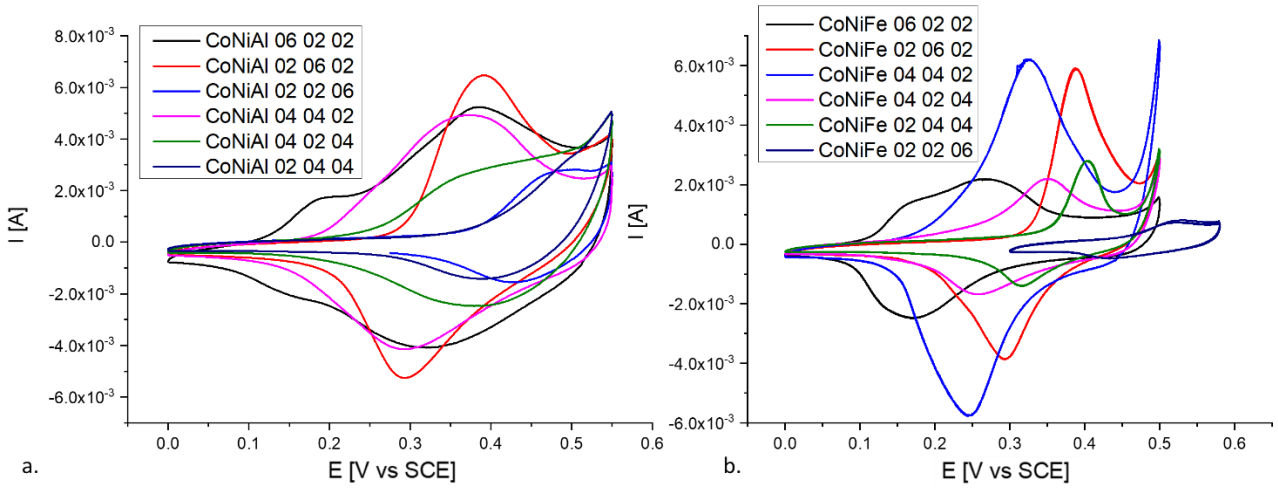

Figure 3_ 57: Red set of data relevant to a) Al – and b) Fe – based LDHs in 0.1 M KOH.

The data are more difficult to interpret "at first sight" for Al based LDHs (figure 3_57a). The results are clearly less interesting for OER. However, the shapes of the curves suggest that the LDHs could be interesting as modifiers of electrodes for capacitors development or for sensing purposes.

Table 3_12 summarizes the data obtained from CVs shown in Figure 3_57.

Table 3_ 12: Values of both position and intensity of peaks in CV for Al– and Fe– based LDHs.

Real Factors			**E_{pa}**	**I_{pa}**
Co	***Ni***	***Al***	**V vs SCE**	**A**
0.600	0.200	0.200	0.38	0.0052
0.200	0.600	0.200	0.39	0.0064
0.200	0.200	0.60	0.48	0.0027
0.400	0.400	0.200	0.36	0.0048
0.400	0.200	0.400	0.39	0.0028
0.200	0.400	0.400	0.5	0.0032

Co	*Ni*	*Fe*	V vs SCE	A
0.600	0.200	0.200	0.267	0.00222
0.200	0.600	0.200	0.387	0.00587
0.200	0.200	0.600	0.515	0.000783
0.40	0.400	0.200	0.322	0.00623
0.400	0.200	0.400	0.348	0.00218
0.200	0.400	0.400	0.403	0.00218

To check the structure of the obtained films, PXRD analysis has been carried out on samples which should display a metals ratio compatible with a LDH structure, assuming that the metals molar ratio in the electrolytic bath is maintained in the LDH. The patterns of all Al based samples, reported in Figure 3_58, show the main peaks typical of LDH phase, indexed as 003 and 006 reflections[35]. On the contrary, for Fe based materials reflections are in general less evident, confirming the trend already observed in Figure 3_9 for binary LDHs containing Co and Fe. It is reported that Al^{3+} can increase the M–O (M = Ni, Co) binding energy and offer a stable scaffold for the active sites to anchor the metal ions, which is beneficial for the redox reaction of LDH nanosheets. In fact, the incorporation of Al^{3+} into LDH layers can increase the crystallinity and hydrophilicity of the LDHs[77].

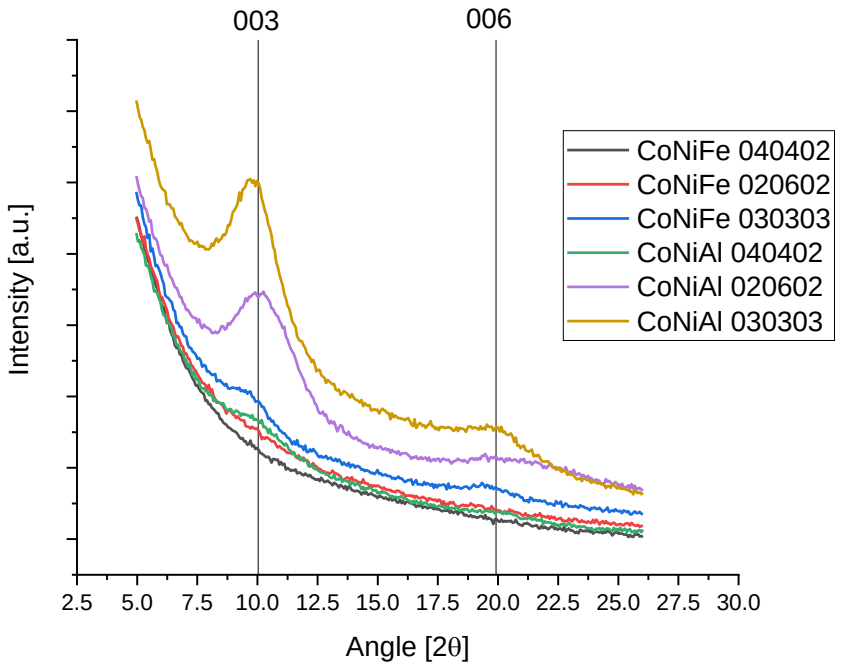

Figure 3_ 58: Example of PXRD analysis for the chosen LDHs among the data–set.

Preliminary consideration on the models

The three-dimensional models have been derived from the Scheffè's treatment in which four reference models are proposed[78-80]:

Linear $$E(y) = \sum_{i=1}^{q} \beta_i x_i$$

Quadratic $$E(y) = \sum_{i=1}^{q} \beta_i x_i + \sum \sum_{i<j=2}^{q} \beta_{ij} x_i x_j$$

Full Cubic $$E(y) = \sum_{i=1}^{q} \beta_i x_i + \sum \sum_{i<j=2}^{q} \beta_{ij} x_i x_j + \sum \sum_{i<j=2}^{q} \delta_{ij} x_i x_j (x_i - x_j) + \sum \sum \sum_{i<j<k=3}^{q} \beta_{ijk} x_i x_j x_k$$

Special Cubic $$E(y) = \sum_{i=1}^{q} \beta_i x_i + \sum \sum_{i<j=2}^{q} \beta_{ij} x_i x_j + \sum \sum \sum_{i<j<k=3}^{q} \beta_{ijk} x_i x_j x_k$$

In these models the presence of an offset (an intercept) is not expected. However, it is possible to include it, eliminating one of the variables (reparametrization).

Most available regression software packages fit a model with the intercept term suppressed. This option produces the correct estimates of the β 's in a canonical mixture model, but it results in an incorrect value for the model or regression sum of squares, because the non-intercept option does not correct the sum of squares for the overall mean. As a result, the F-test, R^2, and the adjusted R^2 will be incorrect. Reparametrizing the model will result in correct output for the regression or model sum of squares, R^2, and the adjusted R^2 [81].

In conclusion, the next section will describe the general approach employed, without the reparametrization. These reparameterization, which will also result in the estimation of the error associated with the models themselves, will be carried out in the prosecution of the work.

Model development and validation

In figure 3_59, the model representation is reported regarding the peaks position (a,b) and intensities (c,d) for Co/Ni/Al–LDHs. Analogous evaluation has been carried out also for iron containing ternary LDHs.

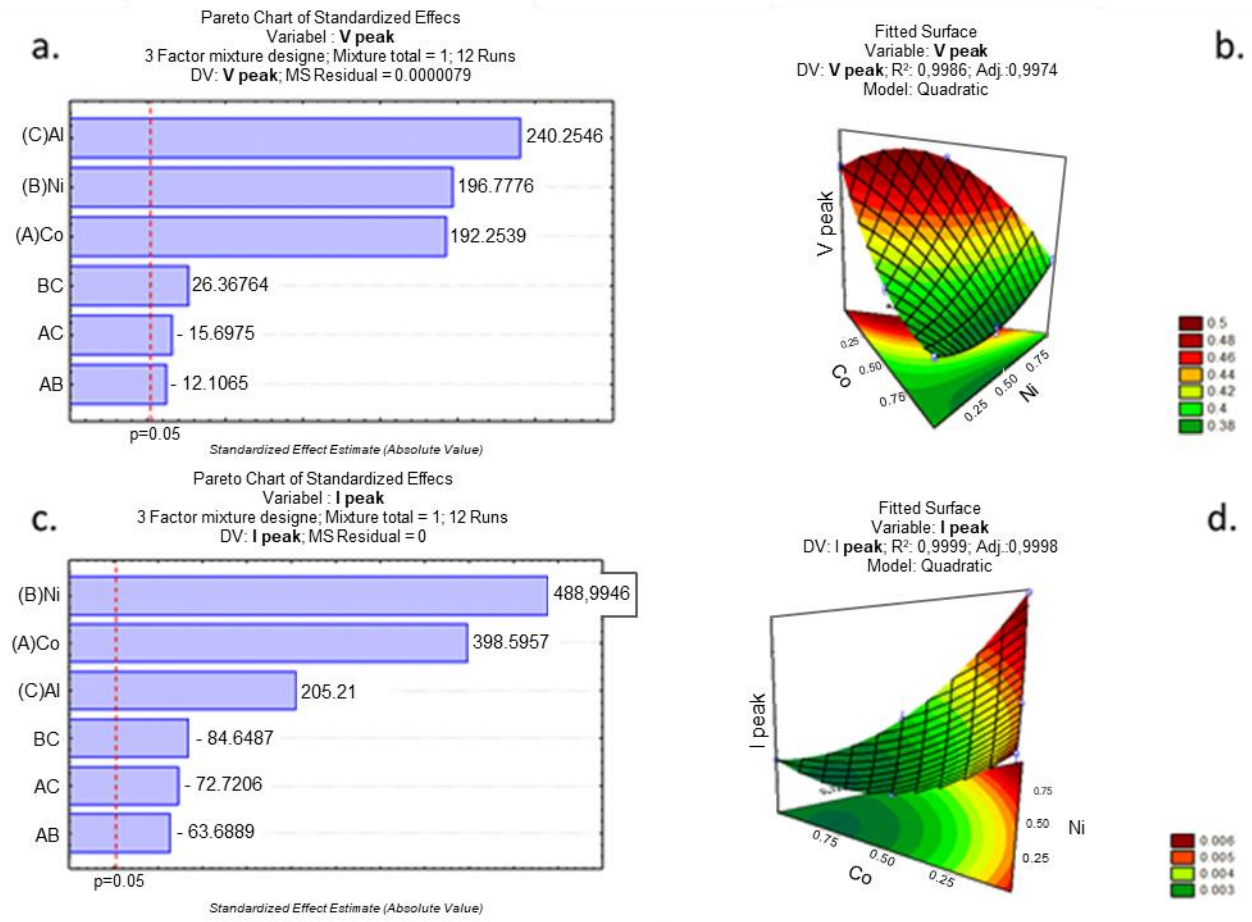

Figure 3_ 59: Polynomial models obtained for Co/Ni/Al containing LDHs relative to the prevision of peaks potentials (a,b) and current intensities (c,d).

To properly describe the analyzed systems, polynomial fitting has been chosen and precisely the equations are:

- **Co/Ni/Al:**

$$E_{pa} = 0.3825 \cdot x + 0.3915 \cdot y + 0.478 \cdot z - 0.118 \cdot x \cdot y - 0.153 \cdot x \cdot z - 0.257 \cdot y \cdot z$$
$$\mathrm{I}_{pa} = 0.005225 \cdot x + 0.00641 \cdot y + 0.00269 \cdot z - 0.00409 \cdot x \cdot y - 0.00467 \cdot x \cdot z - 0.005436 \cdot y \cdot z$$

- **Co/Ni/Fe:**

$$E_{pa} = 0.268 \cdot x + 0.386 \cdot y + 0.5155 \cdot z - 0.024 \cdot x \cdot y - 0.179 \cdot x \cdot z - 0.197 \cdot y \cdot z$$
$$\mathrm{I}_{pa} = 0.00223 \cdot x + 0.00586 \cdot y + 0.0007835 \cdot z - 0.00868 \cdot x \cdot y - 0.002653 \cdot x \cdot z - 0.004607 \cdot y \cdot z$$

The model was then validated with the blue set of data: table 3_13 reports the data which can be predicted by the model to be compared with the experimental ones. It is possible to highlight that, generally, the proposed methodology has a good prevision capability. However, since the here presented work is an early stage one, there is still room for improvement.

Table 3_ 13: Comparison between data predicted by the model and the experimental ones

Electrodeposited Film	Calculated I_{pa}	Experimental I_{pa}	Calculated E_{pa}	Experimental E_{pa}
CoNiAl 030303	0.0032	0.0038	0.44	0.42
CoNiAl 067017017	0.0039	0.0040	0.38	0.39
CoNiAl 017067017	0.0044	0.0046	0.42	0.44
CoNiAl 017017067	0.0025	0.0017	0.46	0.50
CoNiFe 030303	0.0055	0.0052	0.32	0.30
CoNiFe 067017017	0.0012	0.0016	0.31	0.34
CoNiFe 017067017	0.0028	0.0031	0.36	0.39
CoNiFe 017017067	0.00083	0.00078	0.40	0.38

Model development: a possible application to OER?

Finally, it has been explored the possibility to obtain a model for the prediction and the analysis of the electrocatalytic properties toward the oxygen evolution reaction for both sets of data.

Electrochemical tests involving LSV are reported in Figure 3_60.

As mentioned in section 3.2.2, the important data to be extrapolated for OER catalysts are onset potential and Tafel slop: Table 3_14 summarizes such data obtained from the Figure.

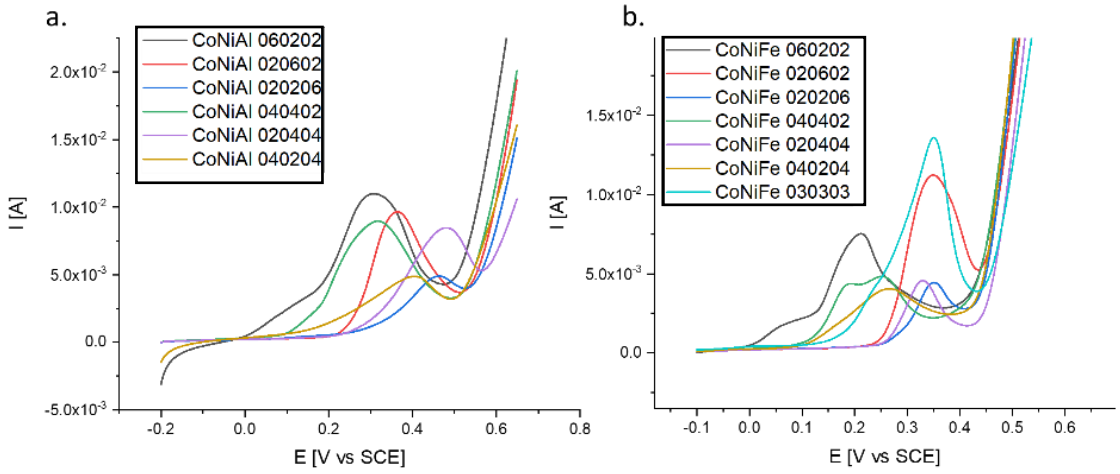

Figure 3_ 60: Evaluation of OER activity in 1 M KOH for a) Co/Ni/Al and b) Co/Ni/Fe sets of data.

Table 3_ 14: Catalytical performances for both sets of data.

	Co/Ni/Fe		**Co/Ni/Al**	
	Onset (V vs SCE)	**Tafel Slope (mA/cm^2)**	**Onset (V vs SCE)**	**Tafel Slope (mA/cm^2)**
060202	0.402	62.6	0.497	76.15
020602	0.438	53.15	0.529	73.15
020206	0.443	209.6	0.541	86.6
040402	0.426	59.1	0.512	72.85
020404	0.434	66.8	0.573	117.05
040204	0.416	77.4	0.504	85.1

Similarly to what has already been reported, a quadratic model has been proposed:

- **Co/Ni/Al:**

$$Onset(V) = 0.49605 \cdot x + 0.52805 \cdot y + 0.54005z + 0.01494 \cdot x \cdot y + 0.23494 \cdot x \cdot z - 0.10506 \cdot y \cdot z$$
$$\text{Tafel } (\text{mA/cm}^2) = 76.2292 \cdot x + 73.22912 \cdot y + 86.6792 \cdot z - 0.7833332 \cdot x \cdot y + 141.117 \cdot x \cdot z + 19.31667 \cdot y \cdot z$$

- **Co/Ni/Fe:**

$$Onset(V) = 0.40177 \cdot x + 0.43776 \cdot y + 0.44276z + 0.02870 \cdot x \cdot y - 0.050697 \cdot x \cdot z - 0.09330 \cdot y \cdot z$$
$$\text{Tafel } (\text{mA/cm}^2) = 62.4572 \cdot x + 53.0072 \cdot y + 209.4572 \cdot z - 7.7561 \cdot x \cdot y + 274.34391 \cdot x \cdot z - 213.04394 \cdot y \cdot z$$

The model will be validated in the prosecution of the work.

Summary

The results obtained in this preliminary study (section 3.5) demonstrate the promising application of chemometric techniques to the field of electrochemistry, in particular for the prediction of LDHs peak intensities and potentials.

The validation of the model and the detailed evaluation of the OER catalytic activity on predicted LDHs will be carried out in the continuation of this work. In the future, the model will guide us in the development of a water splitting system, where the ternary LDH with the best performances will be employed.

Furthermore, as already stated, modelling a system will also offer further application possibilities, such as for the employment of LDHs in the fields of energy storage and sensing.

3.6 References

1 Y. Vlamidis, E. Scavetta, M. Giorgetti, N. Sangiorgi and D. Tonelli, *Appl. Clay Sci.*, 2017, **143**, 151–158.

2 A. Khenifi, Z. Derriche, C. Forano, V. Prevot, C. Mousty, E. Scavetta, B. Ballarin, L. Guadagnini and D. Tonelli, *Anal. Chim. Acta*, 2009, **654**, 97–102.

3 I. Gualandi, M. Monti, E. Scavetta, D. Tonelli, V. Prevot and C. Mousty, *Electrochim. Acta*, 2015, **152**, 75–83.

4 S. C. Sekhar, G. Nagaraju and J. S. Yu, *Nano Energy*, 2017, **36**, 58–67.

5 M. T. De Groot and M. T. M. Koper, *J. Electroanal. Chem.*, 2004, **562**, 81–94.

6 I. Gualandi, A. G. Solito, E. Scavetta and D. Tonelli, *Electroanalysis*, 2012, **24**, 857–864.

7 J. W. Boclair and P. S. Braterman, *Chem. Mater.*, 1999, **11**, 298–302.

8 J. W. Boclair, P. S. Braterman, J. Jiang, S. Lou and F. Yarberry, *Chem. Mater.*, 1999, **11**, 303–307.

9 E. Bernardi, M. Monti, D. Tonelli, P. H. Ho, P. Benito, A. Vaccari, L. Nobili, G. Fornasari and E. Scavetta, *Electrochim. Acta*, 2016, **222**, 1335–1344.

10 I. Gualandi, Y. Vlamidis, L. Mazzei, E. Musella, M. Giorgetti, M. Christian, V. Morandi, E. Scavetta and D. Tonelli, *ACS Appl. Nano Mater.*, 2019, **2**, 143–155.

11 W. Yang, Z. Gao, J. Wang, J. Ma, M. Zhang and L. Liu, *ACS Appl. Mater. Interfaces*, 2013, **5**, 5443–5454.

12 C. C. L. McCrory, S. Jung, J. C. Peters and T. F. Jaramillo, *J. Am. Chem. Soc.*, 2013, **135**, 16977–16987.

13 C. C. L. L. McCrory, S. Jung, I. M. Ferrer, S. M. Chatman, J. C. Peters and T. F. Jaramillo, *J. Am. Chem. Soc.*, 2015, **137**, 4347–4357.

14 Orfino, F. P. *Microscopy and Microanalysis,* 2005, 11, 422-423.

15 H. H. Chien, C. Y. Liao, Y. C. Hao, C. C. Hsu, I. C. Cheng, I. S. Yu, J. Z. Chen, *Electrochimica Acta,* 2018, 260, 391-399.

16 X. L. Wei, N. Li, J. F. An, C. F. Huo, H. Liu, R. C. Yang, X. Li, Z. S. Chao

CrystEngComm, 2020, 22, 205-212

17 C. Santoro, M. Guilizzoni, J.P. Correa Baena, U. Pasaogullari, A. Casalegno, B. Li, S. Babanova, K. Artyushkova, P. Atanassov, *Carbon*, 2014, 67, 128-139.

18 F. Cavani, F. Trifirò and A. Vaccari, *Catal. Today*, 1991, **11**, 173–301.

19 D. Totir, Y. Mo, S. Kim, M. R. Antonio and D. A. Scherson, *J. Electrochem. Soc.*, 2000, **147**, 4594.

20 M. Morishita, *J. Low Temp. Phys.*, 2011, **162**, 638–644.

21 N. Zamel, X. Li and J. Shen, *Energy and Fuels*, 2009, **23**, 6070–6078.

22 C. Brasquet, B. Rousseau, H. Estrade-Szwarckopf and P. Le Cloirec, *Carbon N. Y.*, 2000, **38**, 407–422.

23 G. W. Yang, C. L. Xu and H. L. Li, *Chem. Commun.*, 2008, 6537–6539.

24 F. Yang, K. Sliozberg, I. Sinev, H. Antoni, A. Bähr, K. Ollegott, W. Xia, J. Masa, W. Grünert, B. R. Cuenya, W. Schuhmann and M. Muhler, *ChemSusChem*, 2017, **10**, 156–165.

25 J. Pérez-Ramírez, G. Mul, F. Kapteijn and J. A. Moulijn, *J. Mater. Chem.*, 2001, **11**, 821–830.

26 J. T. Kloprogge, D. Wharton, L. Hickey and R. L. Frost, *Am. Mineral.*, 2002, **87**, 623–629.

27 E. Musella, I. Gualandi, E. Scavetta, A. Rivalta, E. Venuti, M. Christian, V. Morandi, A. Mullaliu, M. Giorgetti and D. Tonelli, *J. Mater. Chem. A*, 2019, **7**, 11241–11249.

28 J. Yang, H. Liu, W. N. Martens and R. L. Frost, *J. Phys. Chem. C*, 2010, **114**, 111–119.

29 E. Musella, I. Gualandi, E. Scavetta, M. Gazzano, A. Rivalta, E. Venuti, M. Christian, V. Morandi and D. Tonelli, *Chem. - A Eur. J.*, 2019, **25**, 16301–16310.

30 S. Deabate, F. Fourgeot and F. Henn, *J. Power Sources*, 2000, **87**, 125–136.

31 J. Hu, G. Lei, Z. Lu, K. Liu, S. Sang and H. Liu, *Chem. Commun.*, 2015, **51**, 9983–9986.

32 L. Zhang, J. Wang, J. Zhu, X. Zhang, K. San Hui and K. N. Hui, *J. Mater. Chem. A*, 2013, **1**, 9046–9053.

33 P. H. Ho, M. Monti, E. Scavetta, D. Tonelli, E. Bernardi, L. Nobili, G. Fornasari, A. Vaccari and P. Benito, *Electrochim. Acta*, 2016, **222**, 1335–1344.

34 A. I. Khan and D. O'Hare, *J. Mater. Chem.*, 2002, **12**, 3191–3198.

35 K. H. Goh, T. T. Lim and Z. Dong, *Water Res.*, 2008, **42**, 1343–1368.

36 C. Ehrhardt, M. Gjikaj and W. Brockner, *Thermochim. Acta*, 2005, **432**, 36–40.

37 J. Pérez-Ramírez, G. Mul, F. Kapteijn and J. A. Moulijn, *J. Mater. Chem.*, 2001, **11**, 2529–2536.

38 S. J. Palmer, R. L. Frost, G. A. Ayoko and T. Nguyen, *J. Raman Spectrosc.*, 2008, **39**, 395–401.

39 I. D. Dobrea, C. E. Ciocan, E. Dumitriu, M. I. Popa, E. Petit and V. Hulea, *Appl. Clay Sci.*, 2015, **104**, 205–210.

40 J. L. Bantignies, S. Deabate, A. Righi, S. Rols, P. Hermet, J. L. Sauvajol and F. Henn, *J. Phys. Chem. C*, 2008, **112**, 2193–2201.

41 N. Lu, L. Lia, W. Banerjee, P. Sun, G. Nang and M. Liu, *J. App. Phys.*, 2015, **118,** 045701.

42 W. P. Wuelfing, S. J. Green, J. J. Pietron, D. E. Cliffel, R. W. Murray, C. Hill, N. Carolina, R. V June, V. Re, M. Recei and V. September, J. Am. Chem. Soc., 2000, **122**, 11465–11472.

43 E. Scavetta, I. Gualandi, D. Tonelli, C. Mousty, V. Prevot and M. Monti, *Electrochim. Acta*, 2014, **152**, 75–83.

44 V. V. Sharma, I. Gualandi, Y. Vlamidis and D. Tonelli, *Electrochim. Acta*, 2017, **246**, 415–423.

45 A. Shalaby, D. Nihtianova, P. Markov, A. D. Staneva, R. S. Iordanova and Y. B. Dimitriev, *Bulg. Chem. Commun.*, 2015, **47**, 291–295.

46 D. S. Hall, D. J. Lockwood, C. Bock and B. R. MacDougall, *Proc. R. Soc. A Math. Phys. Eng. Sci.*, 2015, **471** (2174).

47 N. S. Mcintyre and M. G. Cook, *Anal. Chem.*, 1975, **47**, 2208–2213.

48 J. W. Lee, T. Ahn, D. Soundararajan, J. M. Ko and J. D. Kim, *Chem. Commun.*, 2011, **47**, 6305–6307.

49 J. Liang, M. Renzhi, N. Iyi, Y. Ebina, K. Takada and T. Sasaki, *Chem. Mater.*, 2010, **22**, 371–378.

50 H. Jiang, Y. Guo, T. Wang, P. L. Zhu, S. Yu, Y. Yu, X. Z. Fu, R. Sun and C. P. Wong, *RSC Adv.*, 2015, **5**, 12931–12936.

51 J. T. Kloprogge, L. V. Duong, B. J. Wood and R. L. Frost, *J. Colloid Interface Sci.*, 2006, **296**, 572–576.

52 O. Böse, E. Kemnitz, A. Lippitz and W. E. S. Unger, *Fresenius. J. Anal. Chem.*, 1997, **358**, 175–179.

53 L. Zhang, H. Yao, Z. Li, P. Sun, F. Liu, C. Dong, J. Wang, Z. Li, M. Wu, C. Zhang and B. Zhao, *J. Alloys Compd.*, 2017, **711**, 31–41.

54 G. Greczynski and L. Hultman, *Angew. Chemie*, 2020, **59** (13), 5002-5006.

55 N. F. Chiu and C. Du Yang, *RSC Adv.*, 2018, **8**, 11557–11565.

56 I. Gualandi, E. Scavetta, S. Zappoli, D. Tonelli, *Biosens Bioelectron.* 2011, 26 (7), 3200-3206

57 A. M. Ullman, C. N. Brodsky, N. Li, S. L. Zheng and D. G. Nocera, *J. Am. Chem. Soc.*, 2016, **138**, 4229–4236.

58 Y. Vlamidis, E. Scavetta, M. Gazzano and D. Tonelli, *Electrochim. Acta*, 2016, **188**, 653–660.

59 X. Li, L. Yu, G. Wang, G. Wan, X. Peng, K. Wang and G. Wang, *Electrochim. Acta*, 2017, **255**, 15–22.

60 B. Wang, Q. Liu, Z. Qian, X. Zhang, J. Wang, Z. Li, H. Yan, Z. Gao, F. Zhao and L. Liu, *J. Power Sources*, 2014, **246**, 747–753.

61 S. Li, P. Cheng, J. Luo, D. Zhou, W. Xu, J. Li, R. Li and D. Yuan, *Nano-Micro Lett.*, 2017, **9**, 1–10.

62 E. Scavetta, A. Casagrande, I. Gualandi and D. Tonelli, *J. Electroanal. Chem.*,

2014, **722–723**, 15–22.

63 B. Wang, Q. Liu, Z. Qian, X. Zhang, J. Wang, Z. Li, H. Yan, Z. Gao, F. Zhao and L. Liu, *J. Power Sources*, 2014, **246**, 747–753.

64 M. Shao, F. Ning, Y. Zhao, J. Zhao, M. Wei, D. G. Evans and X. Duan, *Chem. Mater.*, 2012, **24**, 1192–1197.

65 J. Wang, Y. Song, Z. Li, Q. Liu, J. Zhou, X. Jing, M. Zhang and Z. Jiang, *Energy and Fuels*, 2010, **24**, 6463–6467.

66 X. M. Liu, Y. H. Zhang, X. G. Zhang and S. Y. Fu, *Electrochim. Acta*, 2004, **49**, 3137–3141.

67 Y. Wei, X. Zhang, X. Wu, D. Tang, K. Cai and Q. Zhang, *RSC Adv.*, 2016, **6**, 39317–39322.

68 L. Zhang, M. Ou, H. Yao, Z. Li, D. Qu, F. Liu, J. Wang, J. Wang and Z. Li, *Electrochim. Acta*, 2015, **186**, 292–301.

69 L. Zhang, K. N. Hui, K. S. Hui, X. Chen, R. Chen and H. Lee, *Int. J. Hydrogen Energy*, 2016, **41**, 9443–9453.

70 X. Ge, C. Gu, Z. Yin, X. Wang, J. Tu and J. Li, *Nano Energy*, 2016, **20**, 185–193.

71 A. Lesch, F. Cortés-Salazar, V. Amstutz, P. Tacchini and H. H. Girault, *Anal. Chem.*, 2015, **87**, 1026–1033.

72 V. Costa Bassetto, M. Mensi, E. Oveisi, H. H. Girault and A. Lesch, *ACS Appl. Energy Mater.*, 2019, **2**, 6322–6331.

73 C. Hobbs, S. Jaskaniec, E. K. McCarthy, C. Downing, K. Opelt, K. Güth, A. Shmeliov, M. C. D. Mourad, K. Mandel and V. Nicolosi, *npj 2D Mater. Appl.*, 2018, **2**, 4.

74 F. Dionigi, Z. Zeng, I. Sinev, T. Merzdorf, S. Deshpande, M. B. Lopez, S. Kunze, I. Zegkinoglou, H. Sarodnik, D. Fan, A. Bergmann, J. Drnec, J. F. de Araujo, M. Gliech, D. Teschner, J. Zhu, W. X. Li, J. Greeley, B. R. Cuenya and P. Strasser, *Nat. Commun.*, 2020, **11**, 1–10.

75 E. Scavetta, B. Ballarin, C. Corticelli, I. Gualandi, D. Tonelli, V. Prevot, C.

Forano and C. Mousty, *J. Power Sources*, 2012, **201**, 360–367.

76 M. C. Biesinger, B. P. Payne, A. P. Grosvenor, L. W. M. Lau, A. R. Gerson and R. S. C. Smart, *Appl. Surf. Sci.*, 2011, **257**, 2717–2730.

77 M. Zhao, Q. Zhao, B. Li, H. Xue, H. Pang and C. Chen, *Nanoscale*, 2017, **9**, 15206–15225.

78 H. Scheffé, *Journal of the Royal Statistical Society, Series B,* 1958, 20, 344–366.

79 H. Scheffé, *Journal of the Royal Statistical Society, Series B*, 1959, 23, 171–172.

80 H. Scheffé, Journal of the Royal Statistical Society, B, 1965, 25, 235–263.

81 R. H. Myers, D. C. Montgomery, C. M. Anderson-Cook. *Response Surface Methodology. Process and Product Optimization Using Designed Experiments.* Fourth Edition. Wiley 2016

CHAPTER 4: CONCLUSIONS

"νόμωι (γάρ φησι) γλυκὺ καὶ

νόμωι πικρόν,

νόμωι θερμόν,

νόμωι ψυχρόν,

νόμωι χροιή,

ἐτεῆι δὲ ἄτομα καὶ κενόν"

- Democritus

LDHs are fascinating materials with high performances for several electrochemical applications.

Electrodeposition is a one-step and rapid (minutes) procedure that allows at the same time for the synthesis of LDHs and modification of the electrode surface. However, the widely employed potentiostatic protocol exhibits a low control on the film composition with a consequent constrain to the chemical tunability, which is a key advantage of these materials. Therefore, an alternative electrochemical synthetic route, based on a potentiodynamic approach, has been here proposed to deposit thin films of LDHs materials with the following features:

- high reproducibility (independently of the adopted substrate)
- well-controlled M(II)/M(III) ratio
- suitability to large anions intercalation.

In particular, films of Co and Ni based-LDHs were prepared on several conductive substrates, comprising Pt, Ni-foam and carbon-based materials. All characterizations confirmed the LDH structure of the electro-synthesised materials. Furthermore, the kinetics of the reactions involved in LDHs precipitation was demonstrated to be essentially dependent on the nature of the electrode surface, whatever was the strategy adopted for the synthesis. The most relevant result was that when the potentiodynamic approach was used, the substrate was homogeneously covered, and no detachment of the film was highlighted in any case (better adhesion), as confirmed by SEM. Moreover, PXRD suggested better-formed crystal domains with respect to the potentiostatic approach which often led to LDH films displaying also breakages and detachments.

As to the metal molar ratio, an extensive characterization confirmed that the LDH structure was successfully obtained with all the M(II)/M(III) molar ratios (from 1:1 to 4:1) tested in the electrolytic solution. The composition of the LDHs reflected the one of the synthetic baths, and, therefore, the potentiodynamic synthesis has proved effective in exercising a precise control on the stoichiometry of the final structure.

The protocol was also tested for the electrosynthesis of Ni/Al-LDHs intercalated with electrochemically reduced graphene oxide. The procedure has been optimized by varying the

electrolytic solution composition. The ERGO intercalation has been proven also in this case by a comprehensive multi-technique approach demonstrating for the first time the possibility of electrosynthesis of LDHs intercalated with big anions. The cyclic voltammetric characterization of Ni/Al-LDH/ERGO0.05 showed a higher reversibility than Ni/Al-LDH/NO_3 due to a boosted charge transfer that is enhanced by the ERGO presence.

The above mentioned LDHs were tested for different applications. Firstly, electrodes modified with Co/Fe and Co/Al-LDHs (3:1 molar ratio) were employed successfully for the electro-oxidation of HMF, so suggesting the importance of a further investigation for applications in the field of industrial catalysis. Co based-LDH films (different M(II)/M(III) ratios) were tested also as OER catalysts, obtaining results comparable to those of the similar LDHs synthesised by the classical co-precipitation method which requires very long times (hours). LDHs coming from the potentiostatic and potentiodynamic deposition methods have also been compared, finding that the latter displays a higher OER catalytic activity.

A hybrid capacitor has been fabricated both in solution and in solid-state coupling Ni based LDH with nanomaterials and activated carbon. The robust structure of the composite with ERGO ensured a long cycle life, making Ni/Al-LDH/ERGO0.05 very attractive as electrode material for hybrid supercapacitors. The device had a starting discharge specific capacity of 880 F g^{-1} which decreased and stabilized at 820 F g^{-1} after 300 cycles. The potential applicability of the supercapacitor was demonstrated by powering a red light-emitting diode. Moreover, as a proof of concept, another two terminal device was tested, using Grafoil modified with the LDH as cathode and Grafoil modified with PEDOT:PSS as anode, which displayed interesting performance. The most important result is that water solutions have been employed, without harmful substances and binders, and thus the proposed application goes towards a sustainable chemistry.

Ni/Al-LDH was also tested as modifier of an ink-jet printed electrode for ethanol sensing. The preliminary results demonstrated a promising combination of inkjet printing and electrochemical modification of carbonaceous electrodes, such as carbon nanotubes. In the future, the sensor will be made more compact by printing a RE/CE electrode next to the working electrode so to produce a two-terminal device. This will also offer further application

possibilities, such as to change the analyte matrix from liquid to gas phase, for ethanol sensing.

The Co-based LDHs were also evaluated by means of an *ex situ* study through XPS and XAS. The utilization of such complementary techniques (surface *versus* bulk) helps to answer to the questions regarding the transformations of the LDH material upon oxidation in alkaline media. As previously reported, an irreversible structural change has been observed for the LDHs containing Co from the as-prepared to an oxyhydroxide-like phase which is stable, and it is supposed to be the long-term electroactive material. The conversion to the active phase is abrupt and not gradual upon oxidation, as demonstrated from both the techniques employed. Even if a low amount of the total Co of the starting Co/M(III)-LDH phase is still electroactive, after the formation of the new phase, these materials remain highly interesting for their activity in a great number of applications.

At last, a preliminary study on ternary LDHs has been carried out employing chemometric tools. The results obtained sustain the hypothesis that the application of chemometric techniques to the field of electrochemistry can be fruitful. The method has revealed to be predictive for the position and intensity of the CV peaks. However, a detailed evaluation of the OER catalytic activity on predicted LDHs will be carried out in the continuation of this work. In the future, the model will guide us in choosing the composition of the electrolytic solution which should lead to the ternary LDHs with the best predicted catalytic activity for OER. The same approach will be useful also for the electrosynthesis of LDHs usable for energy storage and sensing.

Summarizing, this work was devoted to find efficient strategies to enlarge the spectrum of LDHs that can be successfully prepared by electrodeposition and applied in many fields, such as energy storage and conversion, catalysis, and sensing.

APPENDIX: Analytical methods – fundamentals and techniques

Dato che le teorie vengono continuamente modificate per tener conto di nuove osservazioni, non vengono mai debitamente assimilate o semplificate in modo tale che la gente comune possa capirle.

- *Steven Hawking*

This section describes the techniques exploited to characterize the materials employed in the research.

However, only characterizations I personally carried out will be discussed in detail.

Techniques (such as chemometrics, SEM, TEM and Raman spectroscopy) which have been performed in collaboration with other research groups will be shortly discussed.

Chemometrics

Chemometrics is the science of extracting relevant information from chemical systems. It is interdisciplinary and employs methods frequently exploited by data–analytic disciplines (for examples: statistics, mathematics and computer science) in order to optimize analytical methods, and solve problems in applied science, such as chemistry, biochemistry, medicine, biology and chemical engineering[1].

Among the topics generally faced by chemometrics it is possible to cite: the selection of the relevant variables and the elimination of those that are useless or bearer of noise only, and therefore harmful; the evaluation of the quality of the chemical data and, therefore, of the analytical method or the study of the dependence of a model performance on the factors by which it is affected[2].

The usefulness of the information is obviously relevant to the problem. In general, problems of a chemical or partially chemical nature utilize information for:

- exploration, with the aim of improving the knowledge of the chemical system in view of subsequent decisions.
- classification (qualitative chemometric), with the aim of assigning objects (samples, individuals) to a class.
- regression (quantitative chemometric), with the aim of extrapolating a quantity (chemical, physical, ...) from other more easily measurable quantities.

It is certainly true that chemometrics uses procedures from statistics, applied mathematics, computer science; but it has also developed its own procedures, or adapted procedures born in other disciplines to chemical problems. Since the invention of chemometrics in the years between 1970 and 1980, this discipline was identified as autonomous in the framework of Analytical Chemistry. However, the initial definition has been variously modified, adapting it frequently to non–analytical sectors of chemistry in which statistics and/or mathematics

are of great importance[2]. Elements of chemometrics are met in many phases of the chemical–analytical process. Chemometric methods prepare mathematical models, in particular models for classification and regression. Each strategy must start with the preparation of the simplest models, which are also the cheapest in the sense that they are described by as less as possible parameters. The principle of maximum parsimony serves as a guide to obtain stable models. Chemometrics essentially studies (in relation to the first objective, i.e., extraction of the maximum useful information) sets of multivariate data which are the result of experiments in which many chemical or physical quantities have been determined on a chemical sample (object). In relation to the second aim (optimization of methods), chemometrics considers methods whose performance depends on several factors. In this case, the techniques and strategies are those of Experimental Design[2]. Experimental design and optimization are tools which are used to systematically evaluate problems that can arise within research. The idea is that when experiments are performed randomly the obtained outcome will also be random. Therefore, it is a necessity to plan the experiments which can result in interesting information[3]. Real problems involve many quantities which need to be determined on a chemical sample. An analytical method always depends on a series of factors, and conditions that the operator can set within certain intervals at will (temperature, time, pressure, concentration, electric potential, ...) and on whose value the quality of the analytical result depends[2].

A screening experiment is usually performed in order to set the experimental variables and interactions that have significant influence on the result, measured in one or several ways[3]. When a series of variables to be investigated has been highlighted as significant, an experimental design is chosen. This needs to estimate the influence of the different variables on the result. In screening tests, linear or second order interaction models are common, such as full factorial or fractional factorial designs. The former design is limited to the determination of linear influence of the variables, while the latter allows for interaction terms among variables to be evaluated as well. Eventually, the variables with the largest influence on the procedure should be identified[3].

X–Ray techniques

Since their discovery by Röntgen[4] over 100 years ago in his laboratory in Würzburg, X–Rays have provided a non–destructive characterization of a large variety of materials. X–Ray methods cover many techniques based on scattering, emission, and absorption properties of the X–Ray radiation[5]. In general, spectroscopic techniques are used in order to gather chemical information about surfaces. As shown in Fig. A_1, a beam is incident on the surface and penetrates to some depth within the surface layer. A second beam exits from the sample and ultimately is analysed by a spectrometer[6].

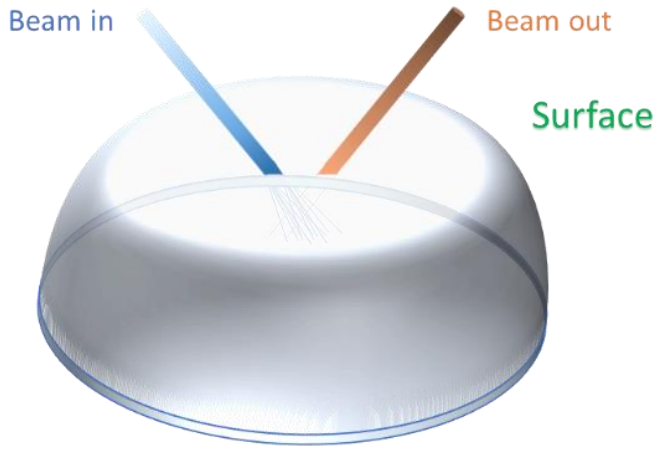

Figure A_ 1: Relationship of probe and analysed beams in surface spectroscopy

By varying the nature of the beams in and out, one can generate a large number of surface analytical techniques as seen in the Table A_1[6]. The techniques that are shown in bold are the one used in this work. When probing a surface with any beam, one must be concerned, of course, with the effect of the probe beam on the surface:

- Photons are the least destructive: in more than 95% of the cases no decomposition of the surface occurs.
- Electrons are more destructive; their effect varies from insulators to conductors. Electron beams are particularly destructive for organic materials. In addition to chemical effects, electron beams cause serious sample charging for many insulators.
- Ion beams cause sputtering of all materials[6].

Table A_ 1*: X–Rays techniques*

Beam in	**Beam out**		
	Photons	**Electrons**	**Ions**
Photons	X–Ray Fluorescence **Extended X–Ray Absorption Fine Structures**	**X–Ray Photoelectron Spectroscopy** Proton–Induced Auger Electrons	Laser Mass Spectrometry
Electrons	Electron Microprobe Appearance–Potential Spectroscopy Catholuminescence	**Auger Electron Spectroscopy** Low–Energy electron Diffraction Electron Microscopy Electron–Impact Spectroscopy	Electron–Induced Ion Desorption
Ions	Ion Microprobe: X Rays Ion Induced X–Rays	Ion Neutralization Spectroscopy Ion–Induced Auger Electrons	Secondary–Ion Mass Spectrometry Low–Energy Ion Scattering Spectroscopy High Energy Ion Scattering Spectroscopy Ion–Microprobe: Ions

X–Ray diffraction

X–Ray diffraction (XRD) is undoubtedly the most important and powerful technique to elucidate crystal and molecular structures, and many of the most important scientific advances in the 20th Century have come from the use of this technique[7].

This method is based on the Bragg's diffraction law which expresses the condition of constructive reflection. Since the energy of a photon is related to its wavelength ($\epsilon = h\nu = hc/\lambda$), photons with energy from 10 to 50 keV are required for the study of crystals. The X–Rays are usually emitted during the friction of accelerated electrons or by inelastic excitation of the inner electrons of the target. From the latter process thin lines are normally obtained, superimposed to a broad emission band, which are used as analytical beam (the ones which are most commonly used are the $K_{\alpha 1}$ and $K_{\alpha 2}$ lines of copper). Considering the crystalline material as an infinite recurrence of parallel atoms planes (with

interplanar distance d), reflected beams interact constructively only if the Bragg condition ($2dsin\theta = n\lambda$) is respected (θ is the incident angle, and n must be an integer number). The copper $K_{\alpha 1}$ line corresponds to 1.541 Å. A block diagram of a typical diffractometer is reported in Figure A_2. The intensity of a single peak of the pattern expresses the probability of a single diffraction order n of the diffraction pattern from a crystalline solid, the positions of the diffraction maxima depend on the periodicity of the structure (i.e., the dimensions of the unit cell), whereas the relative intensities of the diffraction maxima depend on the distribution of scattering matter (i.e., the atoms, ions, or molecules) within the repeating unit. Crystal structure determination from diffraction data can be divided into three stages[7]:

1) Unit cell determination (indexing) and symmetry determination (space–group assignment),
2) structure solution,
3) structure refinement.

Determination of the unit cell requires consideration of the peak positions, whereas space–group assignment, structure solution, and structure refinement also require consideration of the relative intensities of diffraction maxima. In structure solution, the aim is to derive an approximate description of the crystal structure, starting from no knowledge of the actual arrangement of atoms, ions, or molecules in the unit cell. If the approximate structure solution is a sufficiently good representation of the real structure, a good quality structure may be then obtained by refinement of this structural model against the experimental diffraction data, during the structure refinement stage. For powder diffraction data, refinement of crystal structures can be carried out fairly using the Rietveld profile refinement technique[7].

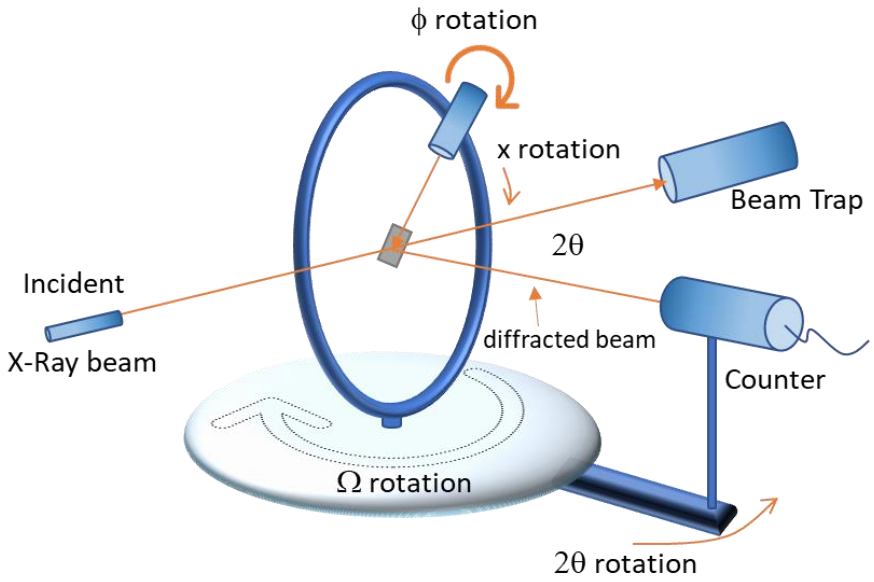

Figure A_ 2: Scheme of 4–circle diffractometer; the angles between the incident Ray, the detector and the sample are shown.

X–Ray Photoelectron Spectroscopy

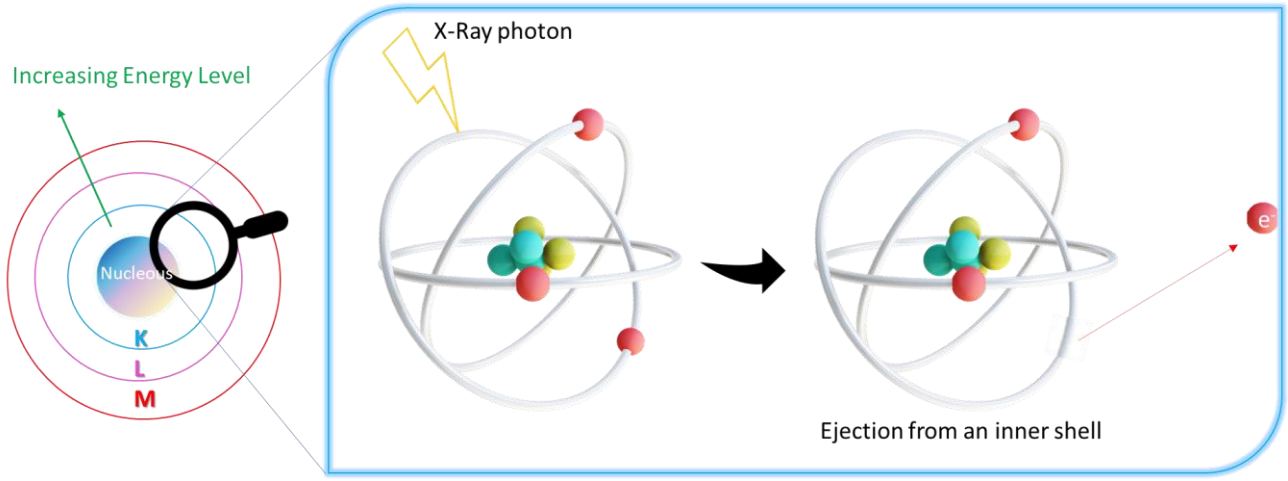

Figure A_ 3: Schematic representation of X–Ray photoelectron spectroscopy process.

X–Ray photoelectron spectroscopy (XPS) in a non–destructive technique in which incident photons excite the atoms in the samples to produce electrons[8].

XPS is based on the photoelectric effect, i.e. an incident X–Ray causes ejection of an electron from an atom, usually from a core electron energy level (as shown in Figure A_3). This primary photoelectron, which is bound to the atom with binding energy E_B (for solids referenced to the Fermi energy), is detected in XPS. To be detected in XPS, the primary electron must have sufficient kinetic energy to overcome, in addition to E_B, the overall

attractive potential of the spectrometer described by its work function Φ_{SP}. Thus, the kinetic energy E_{kin} of the photoelectron is given by:

$$E_{kin} = h\nu - E_B - \Phi_{SP}$$

If the energy of the X–Rays and the spectrometer work function are known, the measured kinetic energy can be used to determine the binding energy E_B from:

$$E_B = h\nu - E_{kin} - \Phi_{SP}$$

This E_B is characteristic for each energy level in the element and can be used to establish which is the element from which the electron originated.

The sensitivity of XPS towards certain elements is dependent on the intrinsic properties of the observed photoelectron lines. The parameter governing the relative intensities of these core–level peaks is the photoionization cross section σ. This parameter describes the relative efficiency of the photoionization process for each core electron as a function of element atomic number.

XPS is a surface–sensitive technique, as opposed to bulk techniques, because electrons cannot travel without interaction, so the depth from which the electron information is obtained is limited by "the escape depth" of the photo–emitted electrons[8]. The typical escape depth for XPS with the parameters used in this work is 20 Å[6].

In this sense, XPS can firstly be applied as a simple qualitative tool to establish the presence or absence of elements on a surface. It is sensitive to all elements except H and He. The typical information that we can gather from an XPS measurement are[9]:

- oxidation state
- bonding information

In addition to the generation of core photoelectron lines in XPS, certain outgoing photoelectrons undergo characteristic energy losses as they are ejected from the atom, ion or molecule. Such well–defined losses should not be confused with the general cascade of inelastic collisions or secondary electrons that occur once an electron has been ejected and gives rise to a step–like background but involve promotion of electrons within the atom to a higher energy level: the consequential loss of kinetic energy by the photoelectron is observed in the XPS spectrum as a minor peak at the higher binding energy side of the characteristic core level[123]. Such phenomena include shake–up and shake off–satellites.

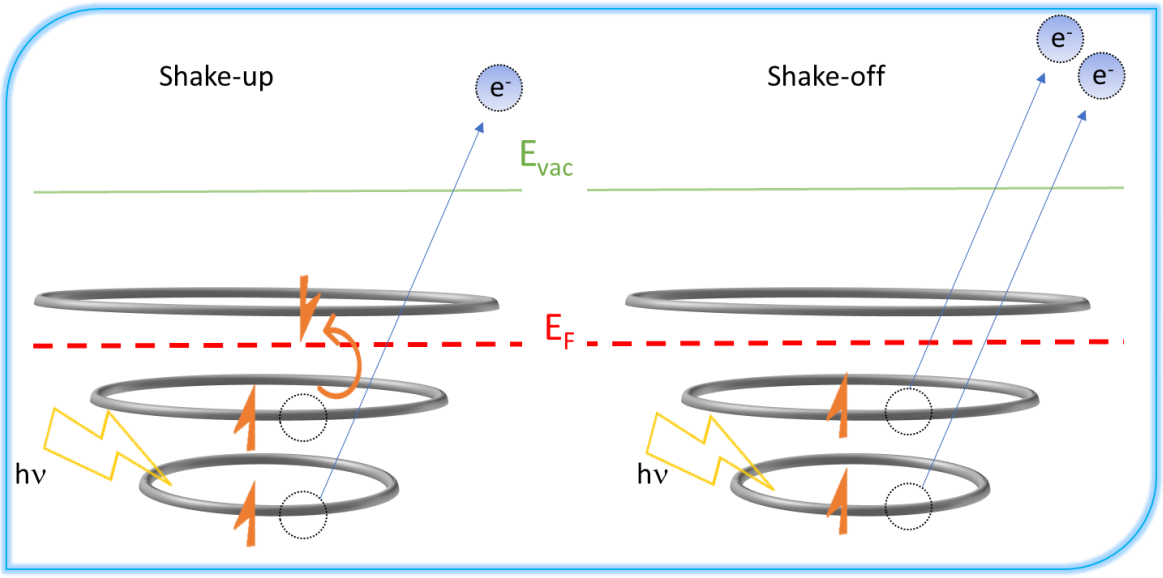

Figure A_ 4: Examples of energy loss phenomena

Figure A_4 shows a schematic to describe the processes involved. Shake–up satellites occur when the outgoing electron interacts with a valence electron and promotes it to a higher energy level. The kinetic energy of the core electron is slightly reduced and consequently appears at slightly higher binding energy within the photoelectron spectrum as a characteristic satellite structure. A related occurrence is that of shake–off in which the valence electron is ejected completely from the atom. Another phenomenon that may happen is multiplet splitting. Multiplet splitting of a photoelectron peak may occur in a compound that has unpaired electrons in the valence band and arises from different spin distributions of the electrons of the band structure. This manifests itself as a core line that appears as a multiplet rather than the expected simple core line structure[10]. XPS spectra also bear a relationship between photo–electron intensity and number of atoms sampled. Quantification of these data can be achieved with a precision within ≈10%. For a homogeneous sample analysed in a fixed geometry, the relationship between XPS intensity and number of atoms is given by:

$$I_A = \int \sigma_A n_A K F_{\hbar\omega} e^{\left(\frac{-z}{\lambda_A cos\theta}\right)} dz$$

where I_A is the XPS intensity line of the substance A, σ_A is the cross section for A excitation, n_A is the density of the A substance, K is the instrument factor (comprehensive of acceptance angle, detection sensitivity, transmission function and illuminated area), $F_{\hbar\omega}$ is the photon flux, λ_A is the mean free path for the measured line and θ is the emission angle.

In Figure A_5, the block diagram of the employed XPS is reported.

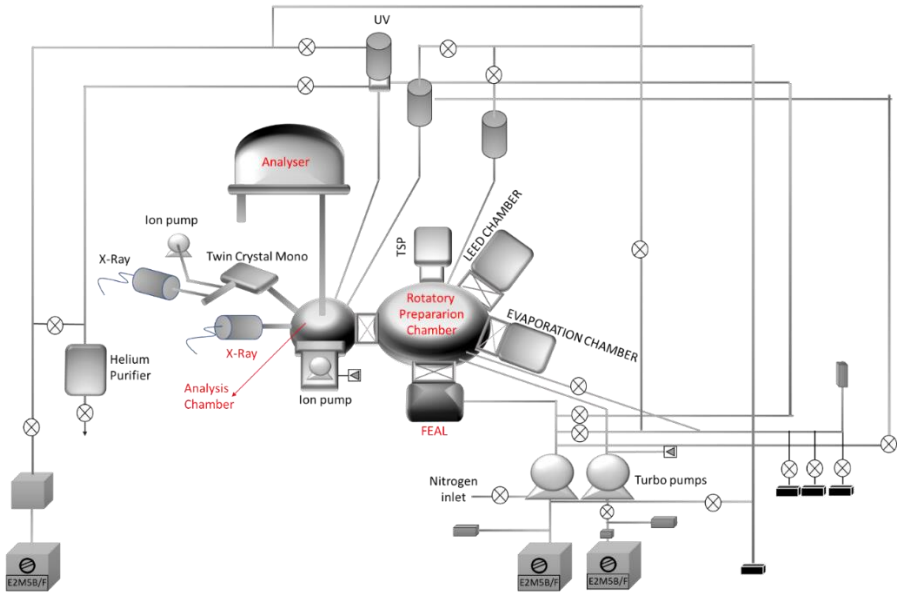

Figure A_ 5: block diagram of the used XPS

Auger Spectroscopy

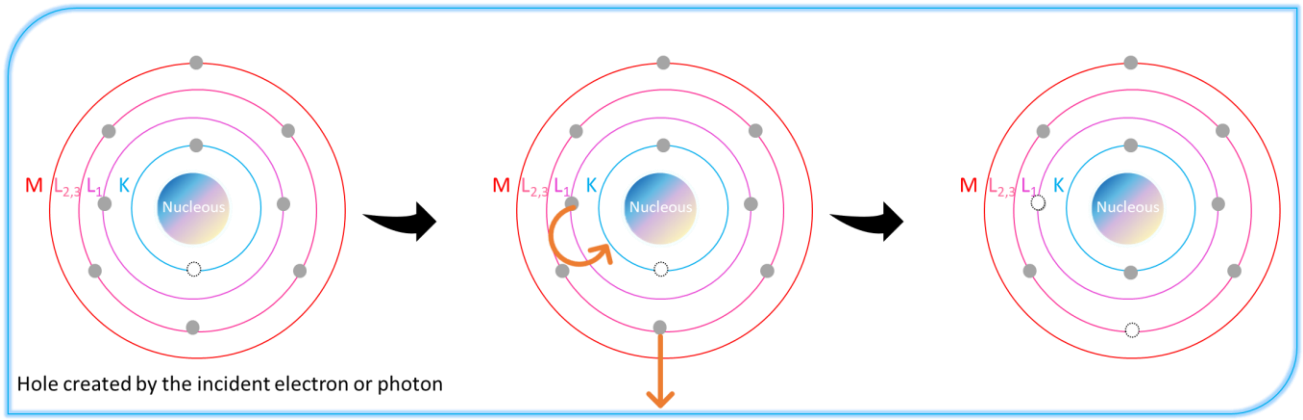

Figure A_ 6: Scheme of the Auger electron emission process induced by creation of a K–level electron hole.

An Auger electron spectroscopy (AES) spectrum is always recorded while measuring with XPS. AES is also based on an electron ejection process like XPS, but the electrons that are monitored in AES are secondary electrons. The secondary electrons called Auger electrons arise from a process shown schematically in Figure A_6. The process occurs after primary electron emission when such a core–level hole exists. Incident electrons are usually used in AES to stimulate primary electron emission, although incident X–Rays can also be used as in XPS. The presence of the core–level electron hole results in electron relaxation from an outer core level or a valence level to fill the core–level hole. When this relaxation occurs, the excess energy that is released stimulates ejection of a secondary or Auger electron from

another core or valence electron energy level. The final state of the atom after Auger electron emission is thus doubly ionized; however, the final doubly ionized state is more stable than the initial singly ionized state. The energy of the Auger electron is independent of the energy of the incident electron beam (or photon energy) and depends only on the energies of the three electron levels involved in the process. The kinetic energy of the Auger electron is given by the difference in energy between the primarily ionized core level and the level from which the electron filling the core–level vacancy comes, minus the energy that it takes to remove the Auger electron from the singly ionized atom, and the spectrometer work function Φ_{SP}. The Auger transition is identified by a three–letter label in which the first letter indicates the core level in which the initial electron vacancy resides, the second letter represents the electron level from which the electron filling the initial vacancy comes and the third letter indicates the electron level from which the ejected Auger electron comes. Thus, for a KLL Auger electron:

$$E_{kin\_KL(1)L(2,3)} = E_K - E_{L(1)} - E^*_{L(2,3)} - \Phi_{SP}$$

where $E_{kin\_KL(1)L(2,3)}$ is the kinetic energy of the Auger electron, E_k is the energy of the K core level, $E_{L(1)}$ is the energy of the electron level from which the electron comes to fill the K–level core vacancy, and $E^*_{L(2,3)}$ is the binding energy of the $L_{(2,3)}$ level in the presence of a hole in the $L_{(1)}$ level. Any three subshells within an atom can be involved in the Auger process as long as the final state is significantly more stable than the initial state[8].

X–Ray Absorption Spectroscopy

X–Ray absorption is a synchrotron–based characterization technique that can be divided into near edge spectroscopy (XANES) and extended X–Ray absorption fine structure (EXAFS)[11]. The general preference is to use either XAS or XAFS to refer to the entire spectrum, which comprises the XANES (within 30 eV or so), and EXAFS to refer to the extended part. (Therefore XAS = XAFS =XANES +EXAFS as can be seen in Figure A_ 7)[5].

Because XAS does not require long–range crystalline order, it has been used with great success in many research fields, and the basic principles and several applications of the XAS spectroscopy have been illustrated in several books since the 80s[5].

In the X–Ray absorption process, a core electron is excited to an empty state and, as such, X–Ray absorption probes the unoccupied part of the electronic structure of the system[11].

In particular, an X–Ray absorption spectrum is an accurate measure of the X–Ray absorption coefficient as a function of incident X–Rays, in an energy range that is below and above the absorption edge of the selected element of the material under investigation. Thus, it is element–specific and comprises electron transition and features that are modified by electron scattering with nearest neighbor atoms.

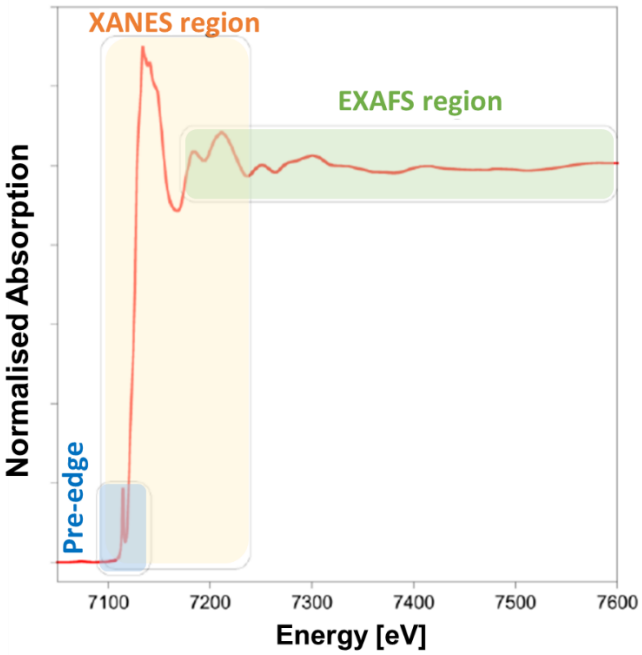

Figure A_ 7: XAS spectrum near–edge of iron. The main regions of the spectra are evidenced.

The absorption coefficient (m) depends on the atomic number Z, density r, atomic mass A and energy E ($m = rZ^4/AE^3$). It gives the probability of the absorption of X–Rays and is related to the X–Ray intensity by Beer's Law:

$$I_T = I_0 e^{-\mu x}$$

where I_0 is the incoming X–Ray intensity to the sample, I_T is the intensity transmitted through the sample and x is the sample thickness; if x is expressed in cm, μ results in cm^{-1}. The absorption coefficient has a characteristic value depending on both the atomic number of the element and the wavelength of the incident X–Ray radiation.

As already mentioned, an X–Ray absorption spectrum can be divided into two regions which originate with different physical–chemical mechanism: XANES and EXAFS, even though the two structures can be recorded simultaneously in one X–Ray absorption spectrum. The

XANES region, comprising the absorption edge itself and the features immediately beyond the edge (to ~100 eV after the edge), is strongly sensitive to oxidation state and coordination chemistry of the absorbing atom of interest. The EXAFS region has been largely exploited to gain quantitative structural information such as first shell distance of the metal site and coordination number. EXAFS comprises periodic undulations in the absorption spectrum that decay in intensity as the incident energy increases well over (~1000 eV) the absorption edge. These undulations arise from the scattering of the emitted photoelectron with the surrounding atoms[5].

As stated above, to perform XAS experiments it is necessary to employ X–Rays sources with high energy and with very collimated beams, i.e. synchrotron radiations. Synchrotron radiation is the name given to the radiation which occurs when charged particles are accelerated in a curved path or orbit. In Figure A_8 a schematic image of a synchrotron is shown. The main elements which constitute the apparatus are the bending magnets, which are placed at a number of locations on the ring to guide the beam along the reference path, the wiggler and the undulators magnets, that deflect the electron beam in alternate directions, producing an angular excursion of the beam. Synchrotron radiation emitted by electrons in particle accelerators is extremely intense and extends over a broad energy range from the infrared through the visible and ultraviolet, into the soft and hard X–Ray regions of the electromagnetic spectrum. Due to these and other characteristics, nowadays synchrotron radiation is used to study many aspects of the structure of matter at the atomic and molecular scale, from surface properties of solids to the structure of protein molecules[12].

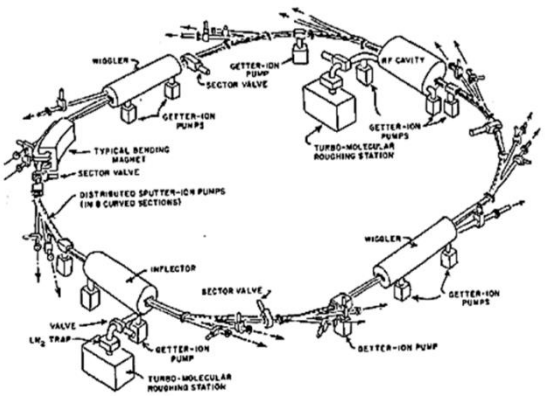

Figure A_ 8: Schematic image of a synchrotron

Electron Microscopy

The techniques of primary importance in surface and interface imaging are the electron microscopies. These techniques take advantage of the fact that accelerated beams of electrons typically have higher energies than commonly available photon beams, and therefore, they can be focused more tightly[8].

Electron microscopy is carried out mainly in two ways: SEM (Scanning Electron Microscopy) or TEM (Transmission Electron Microscopy). STEM is simply TEM carried out in a scanning mode.

Scanning Electron Microscopy

SEM is certainly one of the most common microscopies employed for the imaging of surfaces. This technique is based on the interaction with a surface of a primary beam of electrons with energy typically in a range of 0.5 – 40 keV. SEM must be performed under vacuum condition: electrons need to travel unimpeded for the necessary distances. Modern SEMs can achieve a resolution of 1.5 nm at a primary electron voltage of only 1.5 keV. In most SEM analyses, secondary electrons, which are created near the position of the primary beam, are detected. However, surface images can also be obtained through backscattered primary electrons. The secondary electrons, which result from ionization of the sample atoms in the near–surface region by the incident or backscattered primary electrons, have much smaller energies of ≈ 0 – 20 eV. Due to their very low energies, secondary electrons have escape depths of only a few nanometers. Therefore, SEM is a highly surface–sensitive tool, even if the primary beam electrons may penetrate the sample to depths up to 5 mm for higher voltages. Therefore, images can be definitively obtained by collection of either secondary electrons or backscattered primary electrons. Both approaches have strengths and weaknesses depending on the information desired. Generally, images from secondary electrons have higher resolution, because they depend only on the primary beam diameter. Secondary electron images also have higher contrast than backscattered electron images. However, backscattered electron images have their own set of advantages. The main one is that backscattered electron images are generally more sensitive to topography than secondary electron images, because backscattering increases significantly at sharp edges on a surface. Moreover,

backscattered images have a pronounced dependence on the elemental composition of the sample surface.

SEM can also be equipped with additional instrumentation for electron–excited X–Ray analysis. In many systems, this is performed in the mode known as energy dispersive spectroscopy (EDS). EDS is based on the emission of X Rays with energies characteristic of the atom from which they originate following the secondary electron emission. Thus, these techniques can be used to provide elemental information about the sample. In SEM, this process is stimulated by the incident primary beam of electrons. SEM/EDS typically occurs in a volume of sample larger than that from which backscattered electrons are observed. Thus, SEM/EDS samples the surface to a greater depth than SEM imaging does. Signals typically result from the upper several microns of the near–surface region[8].

Transmission Electron Microscopy

A second important technique relative to electron microscopy is TEM. This method provides a magnified image of a transparent sample with an electron beam using objective and projector lenses. Obviously, the requirement of an electron beam–transparent sample is the most important limitation of this approach. For most materials, this means that the sample thickness must be of the order of $\approx 20 - 200$ nm. Given the extremely small thickness of TEM samples, the surface area–to–bulk volume is rather large; therefore, TEM contains some information of the surface as well. The final image is typically recorded on a fluorescent or phosphorescent screen where it can be captured by a video camera for viewing. TEM is a very powerful surface imaging tool with atomic resolution in the most modern equipment, providing sample magnifications between 100 and 500,000 times. One of the main applications in materials science is the study of the atomic structure of interfaces by ‘‘looking’’ edge–on to the interface along atomic rows in carefully prepared and adjusted samples. Chemical analysis of the interfaces, typically with nanometer resolution, is also common. By generation of a core–level hole of an atom, the primary electron of a well–defined energy suffers an energy loss characteristic of the element, which is usually determined with an electrostatic sector analyzer attached below the image plane[8].

Electrochemical Techniques

Electrochemistry is the branch of chemistry that studies the relation between electrical and chemical effects. This field deals with chemical changes caused by the passage of an electric current and the production of electrical energy by chemical reactions. This section is a summary of what can be found in ref.[13].

There is a variety of reasons to make electrochemical measurements on chemical systems. There may be interest in obtaining thermodynamic data about a reaction or in generating an unstable intermediate and studying its decay rate or its spectroscopic properties. It is also possible to analyze a solution for trace amounts of metal ions or organic species. In these examples, electrochemical methods are employed as tools in the study of chemical systems: there are also investigations where the electrochemical properties of the systems themselves are of primary interest, for example, in the design of a new power source or for the electrosynthesis of some products.

Typically, an electrochemical measurement (with current passage) is conducted in a three–electrode cell connected to an instrument known as a *potentiostat* (Figure A_9). This instrument has the control of the voltage across the working electrode–counter electrode pair, and it adjusts this voltage to maintain the potential difference between the working and reference electrodes in accord with the program defined by a function generator. The three electrodes are so defined:

- **the working electrode (WE):** the actual electrode at which the voltage is applied and the response as current is registered.
- **the reference electrode (RE):** the potential of this electrode is fixed; it is used to measure the real potential at the WE
- **the counter electrode (CE):** this allows to measure the current flowing in the system

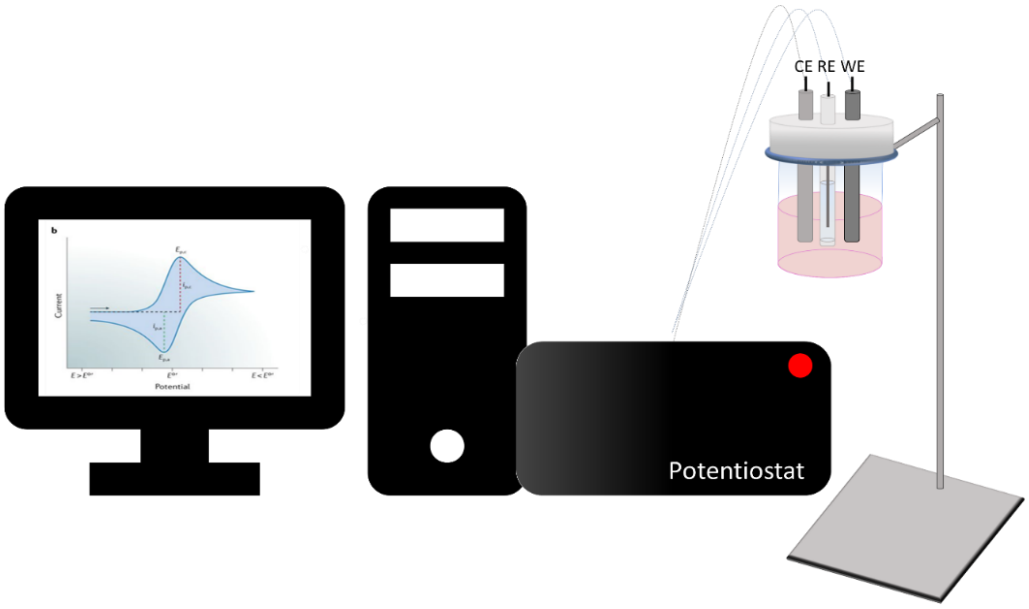

Figure A_ 9: sketch of the typical set–up used for an electrochemical experiment

There are plenty of electrochemical techniques depending on the waveform of the applied potential. The functional processes on which cells work are:

1. oxidized/reduced species diffusion from bulk to electrode–surface
2. their charge–transfer reaction with electrode
3. oxidized/reduced species diffusion from electrode–surface to bulk

Diffusion phenomena are related to the rate of the mass transfer, whereas the electrode reaction has a velocity which depends on the applied potential: the system can, therefore, be dominated by charge transfer, mass transfer or both. When a Faradaic process occurs at the electrode, a current flows and it is expressed by $i(t) = nFAJ_{(0,t)}$ (with A is electrode area and J is the flux of the species).

For a reversible process, when a potential (for example a cathodic one) is applied to an electrode, the oxidized species close to the electrode surface starts to reduce, leading to a concentration ratio between oxidized and reduced species imposed by **Nernst equation**:

$$E = E^0 + \frac{RT}{nF} ln \frac{C_0}{C_R}$$

Where E is the electrode potential (V), E^0 is the standard potential of the redox couple, R is the ideal gas constant 8.314 J $(mol\ K)^{-1}$, T the temperature (K), which is generally 25 °C

(298 K), n is the number of electrons transferred in the balanced equation and F is Faraday constant, the charge carried by a mole of electrons equal to 95,484 C/mol.

When the Faradaic process occurs, the value of C_O at electrode surface is different with respect to the one in the solution bulk as a consequence of the consumption of the electroactive species. Since the solution tends to homogeneity, which implies diffusion from more to less concentrated regions, a concentration gradient is generated. The wideness of the diffusion layer depends on both the time and the applied potential. Of course, each electrochemical technique displays a typical diffusion profile due to the different shapes of the employed potential waves.

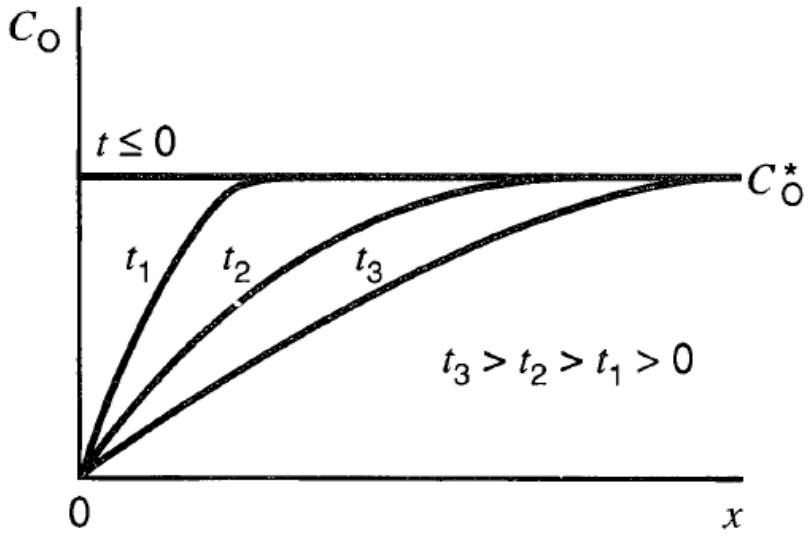

Figure A_ 10: Concentration profiles for various times into the experiment

If the potential is so cathodic to reduce all the oxidized species, the electrochemical reaction is fast, and the kinetics is under mass transfer control. As an example figure A_10 shows the concentration profiles when the $C_O(0)$ is about 0.

In the following section the electrochemical techniques used during the thesis work will be briefly discribed[13].

Chronoamperometry

Chronoamperometry (CA) is an elemental electrochemical technique in which the potential of the working electrode is stepped and the resulting current from Faradaic processes occurring at the electrode is monitored as a function of time. The relationship between

current response and time is measured after applying a potential step to the working electrode of the electrochemical system.

Let's consider the general redox reaction:

$$O^- + e^- \rightleftarrows R$$

Where O and R are the oxidized and reduced forms of a redox couple. The potential is here stepped from a value in which only O is the stable form, i. e., $C_O(0) = C_O^*$, to a potential at which $C_O(0) \sim 0$. As a consequence, also high charging currents, which decay exponentially with time, are generated. The Faradaic current – which is due to electron transfer events and which is almost often the current component of interest – decays as described by the **Cottrell equation**[13]:

$$i(t) = i_d(t) = \left(\frac{nFAD_0^{1/2}C_0^*}{\pi^{1/2}t^{1/2}} \right)$$

where C_O^* is the bulk concentration the analyte and t is the time (sec).

The Cottrell equation describes the case for an electrode that is planar but analogues equations can also be derived for spherical, cylindrical, and rectangular geometries by using the corresponding Laplace operator and boundary conditions in conjunction with Fick's second law of diffusion.

Cyclic Voltammetry

Cyclic voltammetry (CV) is an electrochemical technique that has become very popular to start electrochemical studies of new systems and has proven very useful in obtaining information about complex electrode reactions.

The information can be gained in a single experiment by sweeping the potential with time and recording the i–E curve directly. It is a reversal technique since once the potential is scanned in one direction, for example from 0 V to 1 V, the direction of polarization is inverted (back from 1 V to 0). The potential is varied linearly with time (the applied signal is as a matter of fact a voltage ramp) with sweep rates ν ranging from 0.01 mV s^{-1} to about 1000 V s^{-1} with conventional electrodes (Figure A_11a).

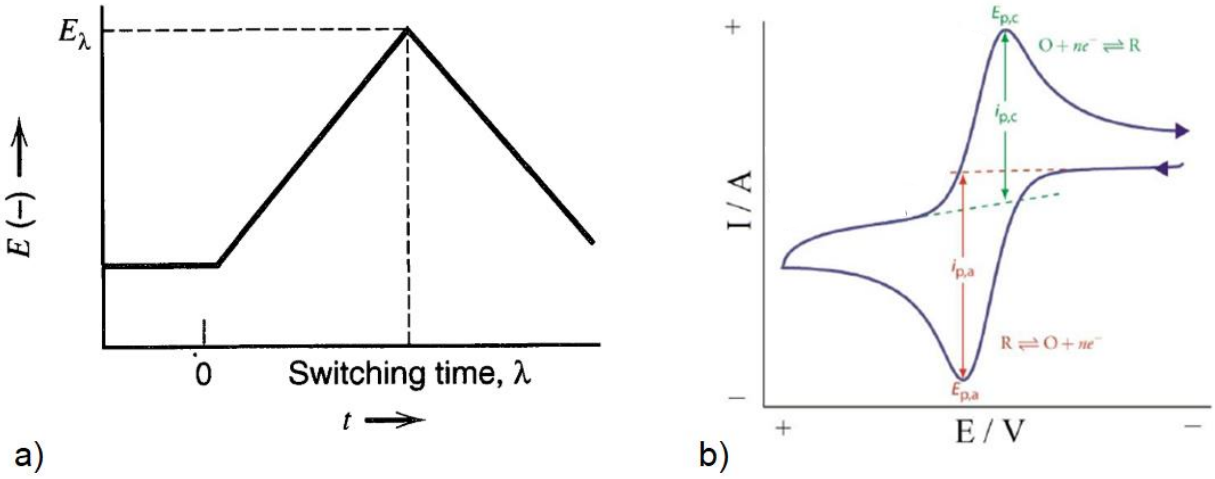

Figure A_ 11: a) Cyclic potential sweep b) resulting cyclic voltammogram.

As the voltage is swept to the right (to more reductive values in figure A_11b), a current begins to flow and, eventually, reaches a peak before dropping. To rationalize this behaviour, it is necessary to consider the influence of voltage on the equilibrium established at the electrode surface. Here the rate of electron transfer is fast in comparison to the voltage sweep rate. Therefore, at the electrode surface an equilibrium is established identical to that predicted by thermodynamics (Nernst equation).

The exact form of the voltammogram can be rationalized by considering the voltage and mass transport effects. As the voltage is swept from the initial value, only non Faradaic currents flow for a while. When the voltage reaches a value near to E° the reduction begins and the Faradaic current starts to flow. The current rises as the equilibrium position is shifted further to the right–hand side, thus converting more reactant. The peak occurs, since at some point the $C_O(0)$ drops nearly to zero and so the mass transfer reaches a maximum rate, then it declines as depletion effect sets in. For a reversible process, at potentials higher about 180 mV than the peak maximum value the drop–in current follows the same behaviour as that predicted by the Cottrell equation.

For a reversible electrochemical reaction, the recorded CV has certain well–defined characteristics:

- The voltage separation between the current peaks.
- The positions of peak voltage are not altered by the voltage scan rate.
- The ratio of the peak currents is equal to one.

- The peak currents are proportional to the square root of the scan rate.

The Randles–Sevcik equation well describes the effect of the scan rate on the current for a reversible system:

$$i_p = 0.4463nFAC\sqrt{nF\nu D/RT}$$

where ν is the scan rate (V s^{-1}).

This leaves the question as to what would happen if the electron transfer processes were "slow" (relative to the voltage scan rate). For these cases the reactions are referred to as quasi–reversible or irreversible electron transfer reactions.

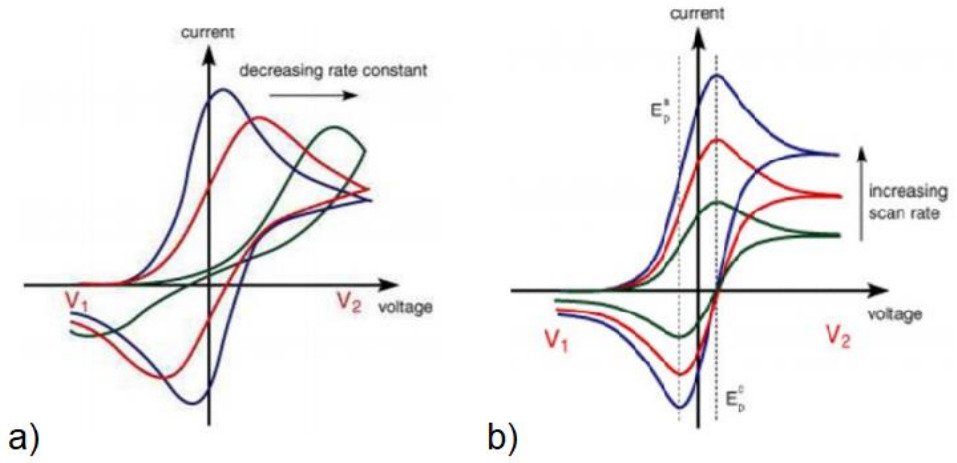

Figure A_ 12: Effect of the rate constant for a) quasi–reversible and b) reversible system.

Figure A_12 a shows a series of voltammograms recorded at a single voltage scan rate for different values of the reduction rate constant. In this situation the voltage applied will not result in the generation of the concentrations at the electrode surface predicted by the Nernst equation. This happens because the kinetics of the reaction is "slow" and thus the equilibria are not established rapidly (in comparison to the voltage scan rate). In this situation the overall form of the voltammogram recorded is similar to that of Figure A_12 a (red and green traces), and unlike the reversible behaviour (Figure A_12 b) the position of the current maximum shifts depending upon the reduction rate constant (and also the voltage scan rate). This occurs because the electron transfer is not so fast in response to the applied voltage as it occurs in the reversible case.

In conclusion, cyclic voltammetry is used both to characterize any kind of electrochemical reaction and to evaluate the electron transfer kinetics.

Galvanostatic Charge–Discharge Curves

Chronopotentiometry (CP) is the most basic constant current experiment. In CP, a current step is applied across an electrochemical cell (without stirring).

The potential changes when a value, at which the flux of the electroactive species is enough to supply the applied current, is reached. After a certain time, the flux of redox species to the surface cannot sustain this current and the potential changes rapidly to a new value at which another species (often solvent or electrolyte) is reduced (or oxidized). This time, termed the transition time, follows the Sand equation:

$$\tau^{1/2} = \left(\frac{nFAD_0^{1/2}C_0^*}{\pi^{1/2}t^{1/2}} \right)$$

Galvanostatic techniques are suitable for the characterization of supercapacitors and/or battery–like materials. Charge–discharge measurements are critical for the analysis of the active materials performance. The main parameters obtained from this experiment are the capacity of the electrode, the change of potential as a function of the state of charge, the cyclability and the estimation of the ohmic drop.

A pure capacitive behaviour leads to the same charge–discharge times with a triangular shape. Otherwise, if a Faradaic reaction occurs the curve displays a plateau.

Long term cycling is often employed to test the cycling stability and Faradaic efficiency over long periods of time. This kind of measurements is considered more reliable than CV for the determination of capacitance during charge and discharge because the current can be kept rigorously constant and time can be evaluated with accuracy.

Bulk electrolysis methods

The methods previously described generally employ conditions featuring a small ratio of electrode area to solution volume (A/V). These allow the experiments to be carried out over fairly long time periods without appreciable changes of the concentrations of the reactant and the products in the bulk solution.

There are circumstances where it is desired to alter the composition of the solution bulk appreciably by electrolysis; these include analytical measurements, techniques for removal or separation of solution components, and electrosynthetic methods. These bulk electrolysis

methods are characterized by large A/V conditions and as effective mass–transfer conditions as possible. Consequently, large currents are generally recorded and the experimental time scales are of the order of minutes and hours.

In the case of a potentiostatic method the potential applied to the working electrode is fixed with respect to a reference electrode. Since the potential of the working electrode controls the degree of completeness of an electrolytic process in most cases, the potentiostatic approach is usually the most desirable for bulk electrolysis. If i–E curves are recorded repeatedly during an electrolysis (assumed to be taken at such a rapid rate that no appreciable change of C_0^* occurs during the potential scan) they will show a continuously decreasing current as C_0^* decreases.

Rotating Disk Electrode

The rotating disk electrode (RDE) is an electrode system which undergoes a rotative movement (Figure A_13). The hydrodynamic equations and the convective–diffusion equation have been solved for the steady state. This system is quite simple to construct and consists of a disk of the electrode material embedded in a rod of an insulating material, typically Teflon, epoxy resin, or another plastic.

Even if the literature suggests that the shape of the insulating mantle is critical and that exact alignment of the disk is important, these factors are usually not problematic in practice, except perhaps at high rotation speeds, where turbulence and vortex formation may occur. What is important is that no space is present between the electrode material and the insulator so that the electrolytic solution cannot rise by capillarity.

The rod is attached to a motor and is rotated at a certain frequency, f (revolutions per second). The more useful description of the rotation rate is the angular velocity, (s^{-1}), where $\omega = 2\pi f$.

Electrical connection is made to the electrode by means of a brush contact; the noise level observed in the current at the RDE depends on this contact. RDEs are available commercially.

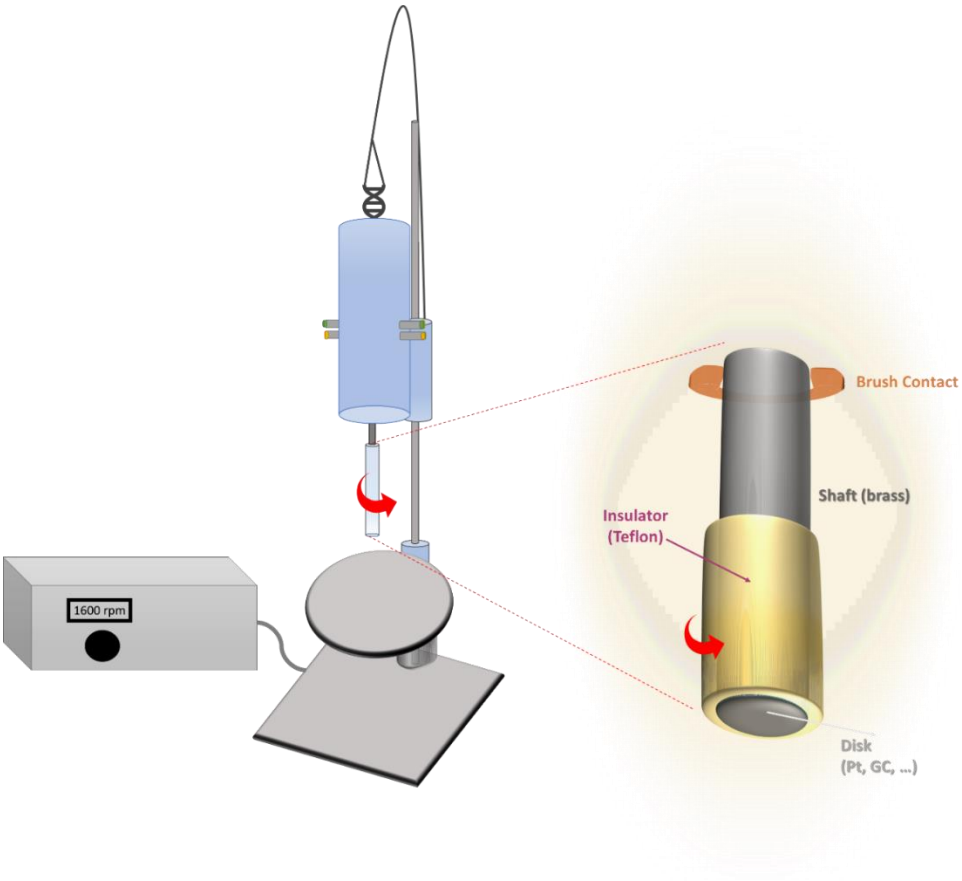

Figure A_ 13: Rotating disk electrode sketch

Electrochemical Impedance Spectroscopy (EIS)

In this technique the basic approach is to perturb the cell with an alternating signal of small magnitude and to observe the way in which the system follows the perturbation at the steady state. Many advantages arise from the technique:

- ✓ high–precision measurements are obtained since the response may be indefinitely steady and can, therefore, be averaged over a long term,
- ✓ the response can be treated theoretically by linearization of current–potential characteristics,
- ✓ measurement over a wide time (or frequency) range (10^4 to 10^{-6} s or 10^{-4} to 10^6 Hz).
- ✓ since one usually works close to equilibrium, detailed knowledge about the behaviour of the i–E response curve over wide ranges of overpotential is not required. This advantage leads to important simplifications in treating kinetics and diffusion.

The typical experiment is the Faradaic impedance measurement, in which the cell contains a solution with both forms of a redox couple, so that the potential of the working electrode

is fixed. The technique where the cell or electrode impedance is plotted against frequency is called electrochemical impedance spectroscopy. Here, the impedance is measured as a function of the frequency of the AC source. The job of theory is to interpret the equivalent resistance and capacitance values in terms of interfacial phenomena. Measurements can be made at other potentials by preparing additional solutions with different concentration ratios. EIS is capable of high precision and is frequently used for the evaluation of heterogeneous charge–transfer parameters and for studies of double–layer structure. EIS normally involves excitation signals, E_{ac}, of very low amplitude, and they depend essentially on the fact that current–overpotential relations are virtually linear at low overpotentials. In a linear system, excitation at the frequency ω provides a current also of frequency ω (and only of frequency ω). On the other hand, a nonlinear i–E relation gives a distorted response that is not purely sinusoidal; but it is still periodic and can be represented as a superposition of signals at frequencies ω, 2ω, 3ω[13].

The variation of the impedance with frequency is often of interest and can be displayed in different ways. In a Bode plot, the logarithm of the total impedance and Φ (log of the phase shift) are both plotted against log(ω). An alternative representation, the Nyquist plot, displays the imaginary part, Z_{Im}, as a function of the real part, Z_{Re}, of the complex impedance for different values of ω.

Raman Spectroscopy

Raman spectroscopy is based on the so–called Raman effect, i.e., the inelastic scattering of a monochromatic radiation interacting with a sample. When this interaction occurs, the wavelength of the incident radiation undergoes a shift directly connected to the vibrations of the molecules and of the crystal lattice. This produces a characteristic spectral profile of the species under examination[14]. In the case of Raman scattering there are three possible types of interaction:

- If there is an elastic collision, the energy $h\nu_0$ of the photon, as well as that of the molecule, do not change following the collision. The elastic scattering of the photon is called Rayleigh scattering.
- If the diffused energy of the molecule is increased with the collision, the energy of the scattered photons will be decreased by the same amount and will, therefore be detected, at longer wavelengths. The corresponding spectral lines are referred to as Stokes shifts.
- If the diffused energy of the molecule is decreased with the collision, the energy of the scattered photons will be increased by the same amount and will, consequently, be detected at shorter wavelengths. The corresponding spectral lines are called anti–Stokes shift.

It is possible to theoretically determine the active vibrations in Raman and IR by exploiting the respective selection rules, selected on the symmetry of the normal modes of vibration. The result is that in many cases the information obtained from the two spectroscopies are complementary.

Raman spectroscopy is virtually practicable in a wide spectral region from UV–VIS to near IR and it covers a wide range of applications, from the identification of functional groups of a molecular structure to characterizations in materials science.

The types of information that can be obtained with this technique can be summarized in the following points[14]:

- Study the "intramolecular" modes (molecular properties) and of the intermolecular modes (properties of the crystal lattice);

- Measure the polarized light to investigate the molecular order, anisotropy, alignment and self–organization of molecular and crystal domains;
- Map the sample surfaces to monitor the spatial distribution of structural inhomogeneities (chemical, physical, phasic, etc.) with a spatial resolution of one μm order.

References

1 S. D. Brown, T. B. Blank, S. T. Sum and L. G. Weyer, *Anal. Chem.*, 1994, **66**, 315–359.

2 M. Forina, G. Drava and R. Leardi, *Chemometrics in transparencies*, Università di Genova, 1997.

3 R. A. Olivero, J. M. Nocerino and S. N. Deming, *Handb. Environ. Chem.*, 1995, **2**, 73–122.

4 W. C. Röntgen, *Nature*, 1896, **53**, 274–276.

5 M. Giorgetti, *ISRN Mater. Sci*, 2013, **2013**, 938625.

6 D. M. Hercules and S. H. Hercules, *J. Chem. Educ.*, 2009, **61**, 402.

7 K. D. M. Harris, M. Tremayne and B. M. Kariuki, *Angew. Chemie - Int. Ed.*, 2001, **40**, 1626-1651.

8 S. Hofmann, Y. Liu, W. Jian, H. L. Kang, J. Y. Wang, Surface and Interface Analysis, 2016, **48** (13), 1354-1369.

9 D. M. Hercules and S. H. Hercules, *J. Chem. Educ.*, 1984, **61**, 483.

10 J. F. Watts, *Vacuum*, 1994, **45**, 653–671.

11 F. De Groot, *Chem. Rev.*, 2001, **101**, 1779–1808.

12 D. Norman, *J. Synchrotron Radiat.*, 2001, **8**, 72–75.

13 A. J. Bard and L. R. Faulkner, Electrochemical Methodes - Fundamentals and Applications, 2001: 632-658.

14 P. Vandenabeele, *Practical Raman Spectroscopy – An Introduction*, 2013, John Wiley & Sons.

ACKNOWLEDMENTS

Innanzitutto, ringrazio di cuore la prof.ssa Domenica Tonelli per la dedizione, la competenza e la disponibilità sempre mostrata e per avermi accolta nel suo laboratorio dandomi la possibilità di crescere professionalmente grazie questa importante esperienza. La ringrazio anche per la sua umanità e aver ricoperto per me un ruolo che va ben oltre quello di un supervisore e che si avvicina molto a quello di un mentore.

Ringrazio anche il mio co-supervisore, il prof. Marco Giorgetti, per avermi accompagnata in questo viaggio.

Ringrazio inoltre molto la prof.ssa Erika Scavetta, il prof. Sergio Zappoli per l'aiuto e per i preziosi consigli, e tutte le persone che hanno contribuito alla realizzazione delle ricerche condotte durante il dottorato, quali il prof. Massimo Gazzano (ISOF-CNR), la dott.ssa Meganne Christian e il dott. Vittorio Morandi (IMM-CNR), la prof.ssa Elisabetta Venuti e la dott.ssa Arianna Rivalta.

Grazie ai ragazzi del laboratorio, in particolare Isacco, Federica, Andreas, Martina, Giacomo, Stefano, Danilo, Alessandro e Luca per le gioie e i dolori condivisi.

Un immenso grazie va agli amici e soprattutto alla mia famiglia che è stata costantemente il mio punto di riferimento.